



**Development of High Force Dense Linear  
Generators for Wave Energy Converters**

Mohammad Abdul Hakim Raihan

A thesis submitted for the degree of  
*Doctor of Philosophy*

School of Engineering

Newcastle University  
United Kingdom

February 2020

## **Abstract**

The main concern of this thesis is the development of force dense linear generators for a Direct Drive Wave Energy Converter. Linear machines for direct drive power take-off systems are required to deliver very high force in order to harness the significant amount of power from the low velocity oscillation of an ocean wave. Therefore, the linear Vernier Hybrid Machine is investigated for its simple design structure and high force density at low speed, due primarily to the inherent magnetic gearing. Attention is focused on improving the performance of the existing linear Vernier Hybrid Machine and developing new variant topologies with higher force density.

An improved E-core stator design, optimised permanent magnet dimensions and new segmented translator structure have been proposed which improve the machine performance in terms of mass and magnet utilisation. The implementation of a pole shifting method is shown to provide a significant reduction in the cogging force. Two cylindrical variants with three-dimensional flux paths are also developed from the improved E-core Vernier Hybrid Machine, which further improves the force with similar magnet mass and current density. Furthermore, a new combination of Halbach magnets arrays and Consequent Pole topology are employed in the flat E-core structure, known later as Halbach Consequent Pole Vernier Hybrid Machine, which significantly improves the flux density by reducing the inherent pole-to-pole leakage and thus further improve the force density and power factor of the machine. A cylindrical variant of the flat Halbach Consequent Pole topology has been designed and analysed to prove the performance improvement of the cylindrical versions compared to the flat.

The flat Halbach Consequent Pole and two small scale cylindrical variants of the E-core Vernier Hybrid Machines have been built and tested in the laboratory. The flat prototype is built from laminated steel and both the cylindrical machines are made of Soft Magnetic Composites to allow the three-dimensional flux path. All the experimental results are shown to provide good agreement with the static and dynamic generator performance predictions.

Finally, this thesis compares the performance of three flat and three cylindrical Vernier Hybrid Machine topologies for various axial lengths and air-gap diameters and investigate the feasibility of using them for a wave energy device

## Acknowledgments

Firstly, all praises and thanks to Allah, the Almighty God, the Benevolent, the Merciful.

I would like to thank my supervisors Dr. Nick Baker and Dr. Kristopher Smith, who have tirelessly given advice, guidance, and support throughout the past three years and patiently reviewed and remarked my work to improvement.

I gratefully received technical advice and supports from IT guys; Chris, Sam, Alan, and John from the mechanical workshop and James and Gordon in the UG lab, who also helped me build, put together and test all the prototype machines.

Heartily thanks to my friend, brother and well-wisher Ahmed, who has generously shared his thoughts and knowledge with me and has graciously contributed to my publications. I will always cherish the time we spent together with great laughs and arguments, innovative, interesting and crazy! discussions and obviously our friendship. I am also thankful to Yerasimos, Aslan, Ramin, Reza, Liam, Iago, Yang, Mehmet, Sana, Osama and many more in the UG lab (Electrical Power Group). It has been an exciting journey and great pleasure to work with creative, dedicated and talented colleagues.

I am deeply indebted to my parents who, throughout my life, have shown me unconditional love and support. I would also like to mention my sister (Bona) and brother-in-law (Tarek) at this point, who have always encouraged me in my work and life choices. Finally, without the unconditional support from my brother (Rana) and delicious homemade food and care from my sister-in-law (Madhuri), I couldn't imagine finishing my Ph.D. Thank you all for the wonderful support.

A special thanks to the woman I shared fights and arguments, ups and downs, hugs and kisses, smiles and frowns – my wonderful wife (Feroza). You always fill my heart with love and affection and supported me during my hardest moments with pure patience and perseverance. I am also very grateful to my father-in-law and mother-in-law, who had believed in me.

When God made nephews and nieces, I got the best ones. Tanaz, Tarneem, Rayeed, Srijita, Tanisha, Raya & Mannita have always filled my heart with love. Last but not least, my 'Titto-Rayeed & Raya' have always the fountain of energy and joy to me throughout my journey. To be a hero to them is the best achievement of my stay in the UK.

This thesis is dedicated to my Parents– Abdul Gani Sarder and Razia Gani.

## Table of Content

<b>Abstract</b> .....	<b>i</b>
<b>Acknowledgments</b> .....	<b>ii</b>
<b>Table of Content</b> .....	<b>iii</b>
<b>List of Figures</b> .....	<b>xi</b>
<b>List of Tables</b> .....	<b>xix</b>
<b>Nomenclature</b> .....	<b>xxi</b>
<b>Chapter 1: Introduction</b> .....	<b>1</b>
1.1 Problem Statement and Motivation .....	1
1.2 Aims and Objectives.....	2
1.3 Thesis Overview .....	3
1.4 Published Works.....	4
<b>Chapter 2: Literature Review</b> .....	<b>6</b>
2.1 Introduction .....	6
2.2 History & Technological Developments of Ocean Energy Conversion.....	6
2.3 Ocean Energy Resource.....	9
2.3.1 Ocean Wave Energy.....	10
2.4 Wave Energy Converters.....	10
2.4.1 Oscillating Water Columns (OWC) .....	11
2.4.2 Overtopping Devices:.....	12
2.4.3 Oscillating Body System.....	13
2.5 Power Take-Off (PTO).....	14
2.5.1 Hydraulic.....	15
2.5.2 Pneumatic & Hydro Turbine .....	16
2.5.3 Direct Drive.....	17
2.6 Linear Generators for Wave Energy Converter.....	18
2.6.1 State of the Art .....	19

2.6.2	Archimedes Wave Swing (AWS) .....	19
2.6.3	Seabased Industry AB (SIAB) & Uppsala University (UU).....	20
2.6.4	Columbia Power Technologies .....	21
2.6.5	Trident Energy.....	22
2.6.6	C-Gen .....	23
2.6.7	Vernier Hybrid Machine (VHM) .....	24
2.7	Selection of Machine for Further Development .....	26
2.8	Conclusion.....	27
<b>Chapter 3: Vernier Hybrid Machine.....</b>		<b>28</b>
3.1	Introduction .....	28
3.2	Initial Design .....	28
3.2.1	Operation Principle .....	28
3.2.2	Design Dimensions .....	29
3.3	Machine Layout Development .....	31
3.3.1	Integrated 3-Phase E-core Design.....	31
3.4	Finite Element Analysis & Optimisation .....	33
3.4.1	Magnet Height Optimisation.....	34
3.4.2	Translator Optimisation.....	35
3.4.2.1	Translator tooth pitch.....	35
3.4.2.2	Translator tooth width.....	36
3.4.2.3	Translator core .....	37
3.4.3	Cogging Reduction by Harmonic Analysis.....	39
3.5	Final Design Analysis and Comparison .....	42
3.5.1	No Load Flux Linkage .....	42
3.5.2	Back EMF .....	43
3.5.3	Thrust Force .....	44
3.6	Conclusion.....	45

<b>Chapter 4: Linear Halbach Consequent Pole Vernier Hybrid Machine .....</b>	<b>46</b>
4.1 Introduction .....	46
4.2 Halbach Consequent Pole Vernier Hybrid Machine (HCVHM).....	47
4.2.1 Motivation for the New Machine Topology .....	48
4.2.2 Operation Principles.....	50
4.3 Finite Element Analysis & Optimisation .....	52
4.3.1 Translator Teeth Width Optimisation .....	53
4.3.2 Translator Core Thickness Optimisation.....	55
4.3.3 Stator Split Teeth Analysis.....	57
4.3.4 Transition Magnet Width Optimisation .....	58
4.3.5 Magnet Thickness Analysis .....	59
4.4 Simulation Result Analysis .....	60
4.4.1 Open Circuit Field Variation.....	61
4.4.2 Open Circuit Back EMF.....	62
4.4.3 Electromagnetic Excitation .....	64
4.4.4 Cogging Force .....	65
4.4.5 Thrust Force .....	66
4.4.6 Inductance Measurement.....	68
4.4.6.1 Inductance equivalent circuit – Method A.....	68
4.4.6.2 Electromagnetic excitation – Method B .....	69
4.4.6.3 Step function method – Method C.....	71
4.4.6.4 Synchronous inductance – Method D.....	72
4.4.7 Power Factor Analysis .....	72
4.4.8 Concluding Remark.....	74
4.5 Prototype Building and Construction .....	75
4.5.1 Stator Construction.....	75
4.5.1.1 Laminated E-core stator .....	75

4.5.1.2	Stator support .....	76
4.5.2	Coils .....	77
4.5.3	Permanent Magnets Assembly .....	79
4.5.4	Translator Construction.....	80
4.5.4.1	Translator segments .....	80
4.5.4.2	TUFNOL I-beam structure .....	81
4.5.4.3	Translator segments assembly .....	82
4.5.4.4	Aluminium I-beam caps.....	83
4.5.4.5	Shaft and carriage assembly on translator support .....	84
4.5.5	Machine Housing Development & Construction.....	85
4.5.6	Machine Assembly .....	87
4.6	Prototype Machine Testing.....	89
4.6.1	Thermal Testing .....	89
4.6.2	Force Measurement.....	92
4.6.2.1	Description of Test rig set-up .....	92
4.6.2.2	Cogging Force.....	92
4.6.2.3	Thrust Force .....	94
4.6.3	Electrical Performance .....	96
4.6.3.1	Open circuit test .....	96
4.6.3.2	Short circuit test.....	99
4.6.4	Resistance Measurement.....	100
4.6.5	Single Coil Inductance Measurement .....	101
4.6.6	Phase Inductance Measurement .....	102
4.7	Conclusion.....	103
<b>Chapter 5: The Cylindrical Vernier Hybrid Machine-I.....</b>		<b>105</b>
5.1	Introduction .....	105
5.2	Single Sided Flat VHM-I Topology .....	106

5.3	Cylindrical VHM-I Topology.....	106
5.3.1	Motivation .....	106
5.3.2	Soft Magnetic Composite (SMC).....	107
5.3.3	Design Development .....	108
5.3.4	Principle of Operation .....	109
5.4	Simplified Geometrical Analysis.....	109
5.4.1	Flat Topology .....	109
5.4.2	Cylindrical Topology .....	110
5.5	Electromagnetic Performance.....	112
5.5.1	Flux Density .....	113
5.5.2	Flux Linkage .....	114
5.5.3	No-load Back EMF .....	115
5.5.4	Electromagnetic Forces .....	116
5.5.5	Phase Inductance .....	117
5.5.6	Comparison .....	118
5.6	Prototype Construction .....	120
5.6.1	SMC Stator Design.....	120
5.6.2	Arc Magnets .....	121
5.6.3	Coils .....	122
5.6.4	Stator Housing.....	123
5.6.5	SMC Translator Construction .....	124
5.6.5.1	Translator design.....	124
5.6.5.2	Bearing and translator support .....	125
5.6.6	Final Assembly.....	126
5.7	Prototype Testing.....	126
5.7.1	Test Rig .....	127
5.7.2	Resistance Measurement .....	128

5.7.3	Inductance Measurement.....	128
5.7.4	Open Circuit Test .....	128
5.7.5	Static Force Measurement.....	131
5.7.5.1	Cogging force.....	131
5.7.5.2	Thrust force .....	132
5.8	Power Factor.....	134
5.9	Conclusion .....	134
<b>Chapter 6: Cylindrical Vernier Hybrid Machine-II.....</b>		<b>135</b>
6.1	Introduction .....	135
6.2	Machine Specification .....	136
6.3	Development of the Cylindrical Topology .....	136
6.4	Principle of Operation .....	138
6.5	Finite Element Analysis & Machine Performance .....	138
6.5.1	Reduction of Cogging by Pole Shifting .....	139
6.5.2	Flux linkage.....	142
6.5.3	Back EMF .....	143
6.5.4	Thrust Force .....	145
6.5.5	Inductance .....	145
6.6	Prototype Machine Building & Testing .....	148
6.6.1	SMC Stator Design.....	148
6.6.2	Permanent Magnets .....	149
6.6.3	Coils .....	150
6.6.4	Stator Housing and Final Machine Assembly.....	151
6.7	Prototype Testing.....	152
6.7.1	Resistance Measurement.....	152
6.7.2	Inductance Measurement.....	153
6.7.3	No Load Test.....	153

6.7.3.1	Open circuit test – per coil .....	153
6.7.3.2	Open circuit test – per phase .....	154
6.7.3.3	Non-uniform air-gap distribution.....	155
6.7.3.4	Open Circuit Test at varying speed.....	157
6.7.4	Static Tests .....	157
6.7.4.1	Cogging force.....	157
6.7.4.2	Thrust force .....	158
6.8	Conclusion .....	158
<b>Chapter 7: Generalised Linear Machine and Comparison.....</b>		<b>160</b>
7.1	Introduction .....	160
7.2	Cylindrical Halbach Consequent Pole Vernier Hybrid Machine .....	160
7.2.1	Flux Linkage .....	161
7.2.2	Back EMF .....	162
7.2.3	Thrust Force .....	163
7.3	Machine Performance Comparison .....	163
7.4	Generalised Linear Machines .....	166
7.5	Comparison of Machine Volume .....	168
7.6	Conclusion .....	170
<b>Chapter 8: Conclusion and Future Work.....</b>		<b>172</b>
8.1	Introduction .....	172
8.2	Contribution to Knowledge & Technical Achievements .....	172
8.3	Suggestions for Future Work.....	173
8.4	Conclusion.....	174
<b>References .....</b>		<b>175</b>
<b>Appendix A: Flat Stator and Support Structure.....</b>		<b>181</b>
<b>Appendix B: Cylindrical Machines and Structural Support .....</b>		<b>182</b>
<b>Appendix C: Flanged Carriage (L1016.F) .....</b>		<b>184</b>

<b>Appendix D: Linear Guide Rail.....</b>	<b>186</b>
<b>Appendix E: Calibration Certificate of Force Transducer .....</b>	<b>187</b>
<b>Appendix F: Tufnol Sheet (Whale grade) .....</b>	<b>188</b>
<b>Appendix G: Neodymium-Iron-Boron Magnet (N42H) .....</b>	<b>189</b>
<b>Appendix H: Stator and translator lamination (M270-35A) .....</b>	<b>190</b>
<b>Appendix I: Soft Magnetic Composite (SMC) Material.....</b>	<b>191</b>

## List of Figures

Figure 2. 1: Outline of Japanese navigation buoy equipped with air turbine [15].....	7
Figure 2. 2: (a) Utilisation of wave energy converters with Pelamis [22] (b) exploitation of wave energy at the port of Pecem Ceará – Brazil.....	8
Figure 2. 3: Wave Hub - Infrastructure for development and testing of wave energy converters in Cornwall – England [28].....	9
Figure 2. 4: Approximate wave power level is given in KW/m of wave front [34] .....	10
Figure 2. 5: Classification of Wave Energy Converter (WEC) extraction technologies: (a) oscillating water column, (b) overtopping devices, and (c) oscillating bodies [43, 44] .....	12
Figure 2. 6: Principle of operation of an Overtopping system (Wave Dragon).....	13
Figure 2. 7: On the left: Schematic of a converter AWS. On the right: converter with concept Seabased AB. Both use a linear generator as a way of taking power. ....	13
Figure 2. 8: Block diagram of different Power take-off methods .....	14
Figure 2. 9: Hydraulic PTO system for wave energy conversion [22] .....	15
Figure 2. 10: AWS linear generator topology and its translator assembly.[27, 47].....	20
Figure 2. 11: On the left, the inside of the converter of Seabased AB. On the center, floating buoy with the WEC device and a detail of the excitation winding system. On the right, the real prototype of the WEC device[60] .....	21
Figure 2. 12: (a) SeaBeav-I with integrated permanent magnet linear generator on the linear test bed [63] (b) 2D crosssectional view of the generator component [61] .....	22
Figure 2. 13: Schematics details of the slot-less linear generator for the converters of Trident Energy being installed for testing at the sea [64-66].....	23
Figure 2. 14: On the left, a module of translator C-Gen. In the centre, characterisation of the module. On the right, the distribution of the magnetic flow lines in a module [67].....	24
Figure 2. 15: 2D Schematic diagram between modules of the linear generator, C-Gen a) Double-sided generator with magnet pairs separated into modules (b)&(c) magnetic flux distribution in a module (d) coil mounted on the c-core module [67].....	24
Figure 2. 16: Prototype C-Gen 25kW [67].....	24
Figure 2. 17: The 3kW prototype VHM generator and the 2D cross-section of a C-core unit [7] .....	25
Figure 3. 1: Single phase of the baseline C-core double sided Vernier Hybrid Machine .....	28

Figure 3. 2: Analytical analysis of Magnet Thickness and width for maximum shear stress on the baseline VHPM machine.....	30
Figure 3. 3: Three phase VHM a) Initial C-core design b) Modified integrated core design c) Isolated E-core design .....	32
Figure 3. 4: Flux contour plot (a) baseline C-core model (b) integrated core model (c) isolated E-core model .....	33
Figure 3. 5: Refined 2D mesh for the E-core model. ....	34
Figure 3. 6: Effect of magnet thickness on back-EMF and average force in the E-core VHM model.....	34
Figure 3. 7: Translator tooth and slot optimisation method .....	35
Figure 3. 8: Translator tooth pitch analysis with equal tooth and slot .....	35
Figure 3. 9: Translator tooth width analysis of the VHM with constant translator pitch.....	36
Figure 3. 10: Translator core thickness optimisation in terms of average force and cogging .	37
Figure 3. 11: Flux density plot under phase-A a) translator with core back b) segmented translator.....	38
Figure 3. 12: Flux density comparison of the E-core VHM between the cored and coreless translator.....	38
Figure 3. 13: E-core VHM model with a segmented translator. ....	39
Figure 3. 14: No load flux contour plot for the E-core VHM model with segmented translator .....	39
Figure 3.15: Lower stator shifted model to reduce cogging. ....	40
Figure 3. 16: Harmonic analysis of cogging force between shifted and non-shifted lower stator model.....	40
Figure 3. 17: Cogging reduction by implementing lower stator pole shifting .....	41
Figure 3. 18: Cogging reduction technique by shifting lower stators. ....	41
Figure 3. 19: Thrust force comparison between shifted and non-shifted lower stator.....	42
Figure 3. 20: No load flux linkage comparison between C-core baseline model and the optimised E-core model with the segmented translator over an electrical cycle. ....	43
Figure 3. 21: Back-EMF comparison between C-core baseline model and the optimised E-core model over an electrical cycle.....	43
Figure 3. 22: Average thrust force comparison between C-core baseline and improved the E-core VHM models over an electrical cycle. ....	44

Figure 4. 1: Proposed HCVHM with magnet orientation and three phase windings (a) 2D (b) 3D cross section .....	47
Figure 4. 2: Schematics of PM array development of proposed HCVHM machine from baseline VHM.....	48
Figure 4. 3: Magnetic flux contour under stator pole a) VHM b) Consequent Pole VHM c) HCVHM topology.....	48
Figure 4. 4: a) flux contour of the HCVHM and VHM machine b) flux linkage variation between HCVHM and VHM.....	49
Figure 4. 5: Operation principle at different translator positions (a) Position ‘0’ or ‘1’ (b) Position ‘1/4’ (c) Position ‘1/2’ (d) Position ‘3/4’.....	51
Figure 4. 6: Single phase no-load flux linkage and back EMF of the top and bottom stator coils under the same phase.....	53
Figure 4. 7: No load flux contour plot with a segmented translator (a) translator teeth align with pole magnets of the top stator (b) translator teeth align with pole magnets of the bottom stator. ....	53
Figure 4. 8: Average force and back EMF variation with translator teeth width.....	54
Figure 4. 9: Effect of magnetic flux saturation on translator teeth at rated current (a) 6mm (b) 8.5mm.....	54
Figure 4. 10: Phase-A back EMF for different translator teeth width.....	55
Figure 4. 11: No load flux contour path of HCVHM (a) solid translator (b) segmented Translator .....	55
Figure 4. 12: Average force and back EMF variation by varying translator core thickness....	56
Figure 4. 13: Cogging and force ripple variation by varying translator core thickness.....	56
Figure 4.14: a) Cogging and back EMF variation by varying split teeth width b) Flux contour plot at split tooth width of 2mm.....	58
Figure 4. 15: Average force and back EMF variation with the transition PM width.....	59
Figure 4. 16: Average force and back EMF variation with PM thickness variation.....	60
Figure 4. 17: (a) Final 3D model with segmented translator (b) 3D mesh. ....	61
Figure 4. 18: Active air gap flux density of the HCVHM model over the active machine length. ....	62
Figure 4. 19: Leakage air gap flux density ( $B_x$ ) comparison.....	62
Figure 4. 20: a) Three phase back EMF for the proposed HCVHM. b) Harmonic analysis of phase back EMF.....	63

Figure 4. 21: Flux linkage map of an entire phase at the various position for different current levels.....	64
Figure 4. 22: Flux contour plot at different translator position at different DC excitation current. ....	65
Figure 4. 23: (a) Cogging force for the final design (b) harmonic analysis of the cogging force. ....	66
Figure 4. 24: Average force variation with peak current. ....	67
Figure 4. 25: Thrust force at various translator positions. ....	68
Figure 4. 26: Simple per phase equivalent circuit.....	68
Figure 4. 27: Variation of phase flux linkage with only excitation current, without magnetic excitation. ....	69
Figure 4. 28: Self-inductance at a different position for different current levels.....	70
Figure 4. 29: Equivalent circuit model for step variable inductance .....	70
Figure 4. 30: Simple per phase equivalent circuit model with a trapezoidal DC voltage source .....	71
Figure 4. 31: Flux linkage variation with the current in one phase.....	71
Figure 4. 32: Phase inductance between three phases.....	72
Figure 4. 33: Variation of the power factor with respect to the machine axial length.....	73
Figure 4. 34: (a) Lamination stack and bonding structure (b) wire eroded laminated stator ...	75
Figure 4. 35: Aluminium support structure for the stator assembly.....	76
Figure 4. 36: (a) Machining of the aluminium support plate for the stator (b) Stator with aluminium cap support. ....	77
Figure 4. 37: Winding configuration for top and bottom stator.....	78
Figure 4. 38: Hand winding process and finished coils. ....	78
Figure 4. 39: Rectangular Neodymium Iron Boron (N42H) magnets (a) transition magnets (b) Pole magnets .....	79
Figure 4. 40: Magnet assembly and curing stage in a stator. ....	80
Figure 4. 41: Segmented translator teeth from laminated steel.....	81
Figure 4. 42: Machining of TUFNOL I-beam structure.....	81
Figure 4. 43: (a) Machined TUFNOL I-beam structure with slots for translator segments (b) cross-section of the slot. ....	82
Figure 4. 44: Assembly of translator teeth segments inside the TUFNOL I-beam structure...	83
Figure 4. 45: Assembly of the translator teeth segments inside the TUFNOL I-beam structure. ....	83

Figure 4. 46: Attaching the aluminium I-beam caps on the TUFNOL Structure.....	84
Figure 4. 47: Complete translator assembly.....	84
Figure 4. 48: Initial design for the steel housing structure.....	85
Figure 4. 49: Final design of the aluminium housing. ....	86
Figure 4. 50: Aluminium housing (a) solid Aluminium block (b) machined structure. ....	86
Figure 4. 51: Assembling the translator and the stators in the aluminium housing.....	87
Figure 4. 52: Air-gap controlling by adjustment screws.....	87
Figure 4. 53: Fully assembled linear HCVHM with segmented translator.....	88
Figure 4. 54: Position of thermocouples on the stator assembly.....	89
Figure 4. 55: Thermal testing of three-phase winding. ....	89
Figure 4. 56: Temperature rise of the coil center at different DC current level.....	90
Figure 4. 57: The coil temperature rises for 250 minutes. ....	91
Figure 4. 58: Test rig setup for the prototype machine (a) schematic drawing (b) laboratory assembly.....	93
Figure 4. 59: Cogging force variation with the translator displacement after removing offset. .....	93
Figure 4. 60: Electrical circuit connection for the static force measurement.....	95
Figure 4. 61: Static force test at different translator position during 8A DC excitation (air- gap=1mm).....	95
Figure 4. 62: Static force test at different translator position during 8A DC excitation (air- gap=2mm).....	96
Figure 4. 63: Measured no-load EMF for two coils under the same phase at 0.2m/s.....	96
Figure 4. 64: Measured no-load EMF results (a) AG=1mm (b) AG=2mm. ....	97
Figure 4. 65: Measured no-load EMF at variable speed (a) for single mechanical stroke (b) compared with simulation over one electrical cycle. ....	98
Figure 4. 66: Measured no-load EMF variation with speed (a) different air-gap (b) at 1mm air- gap. ....	99
Figure 4. 67: Short circuit current test.....	100
Figure 4. 68: Comparison of experimental and simulation predicted self-inductance of an entire phase.....	101
Figure 4. 69: Inductance measurement setup for transient trapezoidal voltage input.....	102
Figure 4. 70: Flux linkage plots against the current for three phases.....	103
Figure 5. 1: Flat E-core VHM-I topology .....	106

Figure 5. 2: Cylindrical VHM-I topology .....	106
Figure 5. 3: Cylindrical VHM-I model development from flat VHM-I.....	108
Figure 5. 4: Simple geometry of flat VHM used to build a simple mass model.....	110
Figure 5. 5: Simple geometry of flat VHM used to build a simple mass model.....	110
Figure 5. 6: Simple geometry of cylindrical VHM used to build a simple mass model .....	111
Figure 5. 7: Equivalence of flux density in the stator core back for (a) Cylindrical VHM-I (b) Flat VHM-I.....	112
Figure 5. 8: The cylindrical prototype design in 3D FEA, a) magnetic flux distribution and b) 3D mesh.....	112
Figure 5. 9: Flux density comparison under full stator tooth length during maximum flux linkage .....	114
Figure 5. 10: Flux density harmonics comparison for one translator pitch.....	114
Figure 5. 11: Three flux linkage comparison between flat and cylindrical VHM-I.....	115
Figure 5. 12: Three back EMF comparison between flat and cylindrical VHM-I.....	115
Figure 5. 13: Back EMF harmonics of flat and cylindrical VHM-I.....	116
Figure 5. 14: Cogging force comparison between flat and cylindrical VHM-I.....	116
Figure 5. 15: Thrust force comparison between flat and cylindrical VHM-I .....	117
Figure 5. 16: Three phase inductance of the cylindrical machine.....	117
Figure 5. 17: Cylindrical SMC stator construction processes .....	121
Figure 5. 18: Arc-shaped PMs and magnet assembled stator .....	122
Figure 5. 19: Completed three phase windings in the stator .....	123
Figure 5. 20: (a) Stator housing components (b) stator assembly.....	124
Figure 5. 21: (a) 40mm long SMC block (b) translator construction in the milling machine.....	125
Figure 5. 22: (a) Translator assembly components (b) PTFE bearing support and end cap bearings. ....	125
Figure 5. 23: Final Machine assembly on the bed plate.....	126
Figure 5. 24: Fully assembled cylindrical VHM-I mounted on the test rig. ....	127
Figure 5. 25: Measured EMF for single mechanical stroke. ....	129
Figure 5. 26: Back EMF comparison between experimental and simulation results over two electrical cycles .....	129
Figure 5. 27: The three air-gap regions of the prototype under three stator teeth.....	130
Figure 5. 28: Air-gap imbalance (a) translator shifted up by 0.4mm (b) translator shifted down by 0.4mm.....	130

Figure 5. 29: Measured (exp) and simulated (FEA) results for two values of offset translator. .....	130
Figure 5. 30: Comparison between experimental and predicted results. ....	132
Figure 5. 31: Experimental results for the static force test.....	133
Figure 5. 32: Peak force comparison between simulation and experimental results for varying current.....	133
Figure 6. 1: (a) Flat double sided E-core VHM-II (b) cylindrical VHM-II .....	135
Figure 6. 2: Cylindrical Vernier machine topology development.....	137
Figure 6. 3: 2D flux path representation of the separated three phases of the cylindrical machine .....	138
Figure 6. 4: 3D model of cylindrical VHM-II, a) Magnetic flux density distribution b) 3D mesh .....	139
Figure 6. 5: Stator teeth geometry of the cylindrical topology for cogging reduction.....	140
Figure 6. 6: Harmonic distribution for different pole shifted models. ....	141
Figure 6. 7: Cogging force variation by pole shifting. ....	141
Figure 6. 8: No load armature coil flux linkage .....	142
Figure 6. 9: No load armature coil back EMF.....	143
Figure 6. 10: Three-phase back EMF comparison between flat and cylindrical topology ....	143
Figure 6. 11: EMF harmonics comparison between flat and cylindrical .....	144
Figure 6. 12: Thrust force comparison between flat and cylindrical VHM-II at rated current .....	145
Figure 6. 13: Phase inductance for 3D FEA.....	146
Figure 6. 14: (a) Cylindrical SMC block (b) single piece stator structure .....	148
Figure 6. 15: PM assembly and the stator. ....	149
Figure 6. 16: coils assembled stator .....	150
Figure 6. 17: components of the stator housing. ....	151
Figure 6. 18: Assembled stator on the bed plate and the full machine assembly.....	151
Figure 6. 19: Prototype cylindrical VHM-II is driven by a ball screw actuator and being tested. .....	152
Figure 6. 20: No-load EMF for coil A12 and A34 under phase-A .....	153
Figure 6. 21: No-load EMF for coil B12 and B34 under phase-B.....	154
Figure 6. 22: No-load EMF for coil C12 and C34 under phase-C .....	154
Figure 6. 23: Three-phase EMF comparison between measured and predicted results.....	155

Figure 6. 24: Uneven mechanical air-gap regions of the prototype. ....	155
Figure 6. 25: Uneven mechanical air-gap regions (a) simulation (b) geometry. ....	156
Figure 6. 26: Measured three phase no load back EMF for three mechanical strokes for linear reciprocating motion, peak linear speed of 1.4m/s.....	157
Figure 6. 27: Cogging comparison between experimental and predicted results.....	157
Figure 6. 28: Peak force comparison between simulation and experimental results for varying current.....	158
Figure 7. 1: Cylindrical Halbach Consequent Pole VHM.....	161
Figure 7. 2: No load magnetic flux distribution plot of the cylindrical HCVHM.....	161
Figure 7. 3: No load magnetic flux linkage comparison between flat and cylindrical model	162
Figure 7. 4: No load three phase back EMF comparison between flat and cylindrical model	162
.....	
Figure 7. 5: Electromagnetic thrust force comparison between flat and cylindrical model...	163
Figure 7. 6: Cross-section of a conventional linear tubular PM machine .....	165
Figure 7. 7: 3D view (a) cylindrical VHM-I with a non-segmented translator (b) Cylindrical VHM-II with a non-segmented translator (c) Cylindrical HCVHM with a segmented translator (d) flat HCVHM.....	166
Figure 7. 8: General linear machine dimensions, including stroke length, x (a) Single sided flat topology (b) double-sided flat topology with a shorter axial length (c) Cylindrical topology. ....	167
Figure 7. 9: Comparison of active machine volume with different topologies of cylindrical and flat machines for fixed axial length, copper mass, and magnet mass .....	169
Figure 7. 10: Force density against equivalent axial length plot for all six machine topologies. ....	169

## List of Tables

Table 2- 1: Pros and cons of different power take-offs.....	17
Table 2- 2: Different types of generator used in existing WEC devices and their power take-off the system.....	18
Table 2- 3: Overview of the state of the art of linear synchronous generators applied to recover wave energy [69].....	25
Table 3- 1: Initial design dimensions of the baseline VHM [7].....	31
Table 3- 2: Comparison of machine performance between baseline C-core and pole shifted E-core model.....	44
Table 4- 1: Main machine parameters and specifications	46
Table 4- 2: Specification of the final design parameters	60
Table 4- 3: Specification of the final design parameters	74
Table 4- 4: Thermal test with various excitation current.	91
Table 4- 5: Synchronous phase inductance for three phases	103
Table 5- 1: Initial design specification and model parameters.....	105
Table 5- 2: Basic machine dimensions for flat and cylindrical geometry.....	111
Table 5- 3: Definition of radii in cylindrical VHM-I.....	111
Table 5- 4: Model parameters for both machines does .....	113
Table 5- 5: Three phase inductance for the cylindrical machine .....	118
Table 5- 6: FEA performance comparison between flat and cylindrical VHM-I .....	119
Table 5- 7: Phase resistance measurement.....	128
Table 5- 8: Comparison between measured and simulated inductance results .....	128
Table 5- 9: Simulated and measured performance of the cylindrical VHM-I .....	131
Table 6- 1: Main machine parameters for the cylindrical VHM-II.....	136
Table 6- 2: Model Parameters for both Machines.....	138
Table 6- 3: three phase inductances for the cylindrical machine .....	146
Table 6- 4: FEA performance comparison between flat and cylindrical VHM-II.....	147
Table 6- 5: comparison between measured and simulated inductances.....	153
Table 6- 6: Simulated and measured no-load performance at 0.3m/s velocity .....	156
Table 7- 1: Machines' performance and parameters comparison .....	164



## Nomenclature

UK	United Kingdom
PTO	Power Take-Off
DD-WEC	Direct Drive Wave Energy Converter
WEC	Wave Energy Converter
LVHPM	Linear Vernier Hybrid Permanent Magnet
PM	Permanent Magnet
VHM	Vernier Hybrid Machine
VHM-I	Single-Sided Linear Vernier Hybrid Machine
VHM-II	Double-Sided Linear Vernier Hybrid Machine
HCVHM	Halbach Consequent Pole Vernier Hybrid Machine
SMC	Soft Magnetic Composite
EMEC	European Marine Energy Centre
NaREC	National Renewable Energy Centre
PF	Power Factor
OWC	Oscillating Water Columns
EDF	Electricité de France
R&D	Research and Development
TISEC	Tidal In-Stream Energy Conversion
EPRI	Electric Power Research Institute
LIMPET	Land Installed Marine Power Energy Transmitter
MOWC	Multi-resonant Oscillating Wave Column
AWS	Archimedes Wave Swing
DD-PTO	Direct drive power take-off
TU Delft	Technical University of Delft
SIAB	Seabased Industry AB
NdFeB	Neodymium-Iron-Boron
CPT	Columbia Power Technologies
OSU	Oregon State University
FS	Flux Switching
VR	Variable Reluctance

PMSM	Permanent Magnet Synchronous Machine
TFM	Transverse Flux Machine
FSM	Flux-Switching Machine
VRPM	Variable reluctance permanent magnet
FEA	Finite Element Analysis
3D	Three-dimensional
2D	Two-dimensional
EMF	Electro-Motive Force
MMF	Magneto-Motive Force
KVL	Kirchhoff's Voltage Law
RMS	Root Mean Square
DC	Direct current
$\sigma_{peak}$	Maximum shear stress
$B_t$	Flux density under the tooth
$B_{root}$	Flux density at the root of the tooth,
$B_r$	Residual flux density of the magnet material,
$\mu_0$	Permeability of free space,
$\mu_r$	Relative permeability of rare earth magnets,
$g$	Air gap length,
$t_m$	Magnet thickness
$w_m$	Width of the magnet poles.
$H_c$	Coercive force of the magnets
$L_{PM}$	Magnet thickness
$\mu_0$	Permeability of magnets which is approximately equal to that of air
$B_0$	Average flux density
$B_1$	Fundamental flux density
$n$	Number of turns per coil
$i_a$	Instantaneous current
$l_a$	Axial or stack length of the machine
$N$	Number of translator teeth per stator tooth
$\tau_t$	Tooth pitch.
$\alpha$	Air gap geometry function

$D_P$	Shift between stator teeth under same phase.
$\tau_P$	Translator tooth pitch.
$PPP$	Stator pole pair pitch
$PM_{lv}$	PM Pole width
$FT_l$	Split tooth width
$PM_{lh}$	Transition PMs Width
$E$	Electro-Motive Force
$N$	Number of winding turns
$F_{avg}$	Average thrust force
$F_x$	Instantaneous thrust at translator position $x$
$X$	Translator position
$f_r$	Force ripple
$\psi_i$	Flux linkage due to the only electrical excitation.
$L_i$	Inductance at a position.
$E_{open}$	No load back EMF per phase
$R$	Phase resistance
$V$	Stator phase voltage
$L_{i,x}$	Inductance due to the electromagnetic excitation for various position.
$\psi_{total}$	Total flux linkage per phase
$L_{i,x}$	Value of inductance at different translator position, $x$ .
$\tau$	Time constant of the per phase equivalent LR circuit
$V(t)$	Instantaneous value of voltage per phase.
$\psi(t)$	Instantaneous value of flux linkage per phase.
$I(t)$	Instantaneous value of current per phase.
$\psi(0)$	Flux linkage per phase due to magnetic excitation only at $t=0$ .
$T_0$	Initial temperature
$L_{phase}$	Phase inductance
$\tau_t$	Translator tooth pitch
$l_a$	Axial length,
$L$	Stator length,
$\sigma$	Shear stress capability
$F_i$	Specified force requirement

$D_s$	Outer diameter of the cylindrical stator,
$D_t$	Translator outer diameter
$L_c$	Active length of the machine

## Chapter 1: Introduction

### 1.1 Problem Statement and Motivation

Fossil fuels like coal, oil, and gas make up more than three-quarters of the world's energy use while having the problem of being non-renewable, limited in supply and will deplete in the near future. There is a great demand for the development and increase of global energy generation from alternative naturally replenished sources like wind, solar and waves. There has been a great deal of research into wind and solar energy, which are the most popular renewable energy sources nowadays. While being widely used renewable energy sources, wind and solar energy have lower power density and efficiency than wave energy, which is comparatively new in this field [1]. However, it has a plentiful supply and remarkable possibilities to meet the global challenge of ever-growing power demand.

Wave energy research in the United Kingdom (UK) started in the 1970s and focused on large single devices. Initial cost calculations showed these large structures were unlikely to be economic. Focus shifted to smaller devices, fueled in part by the discovery of the point absorber effect, whereby a resonating device which is small relative to the wavelength can capture more energy than that contained in a wavefront of its own width [2]. The effect is achieved with the device resonating at the predominant wave frequency, the wave force continuously in phase with the device velocity and the assumption of zero viscous losses. Devices must be small (~10m) relative to the wavelength (~100m). Since 2000, there has been a broad range of devices proposed, mostly between these size extremes, some of which have been optimised and tested. European Marine Energy Centre (EMEC), Wave Hub, National Renewable Energy Centre (NaREC), and various universities meant the UK had seen thriving wave energy converter testing. Sadly, in recent years, several of the more commercially advanced devices have folded, such as Pelamis, Aquamarine, and WaveDragon. Many factors have caused this, of which a lack of supply chain of appropriate power take-off technology is one until recently. Devices were forced either to develop their own bespoke components, such as the Pelamis power module [3] or rely on power take of components developed for a completely different market.

Electrical machines have traditionally been designed to be driven at high-speed rotary motion, typically from an internal combustion engine. For example, a 3000rpm electrical machine with an active diameter of 200mm has an air gap speed of 30 m/sec. A typical wave energy converter, however, can expect to produce oscillatory motion with velocities in the region of 0.5-2m/s. This discrepancy of velocity profile can be accommodated by a range of mechanical

linkages used in devices, predominantly hydraulic or pneumatic in the systems demonstrated to date due to their availability off the shelf. There are concerns about the limitations of hydraulic Power Take-Off (PTO) including low efficiency at part load, ability to control over a wide range of frequencies and displacement leading to potential end-stop problems. The efficiency of a hydraulic PTO is dependent upon pressure and flow rate, with values quoted as high as 90%, but also as low as 40% at part load, where a device will spend much of its time [4].

The alternative to hydraulics is an all-electric direct drive, whereby the linear electrical machine is coupled directly to the moving part of the wave energy device. Linear generators are used in Direct Drive Wave Energy Converters (DD-WECs) as the number of moving parts required in the drive train of the converters can be reduced. The removal of the mechanical interface between the prime mover and the high-speed rotary generator could contribute to a robust system with significant improvement of the overall system efficiency and a reduction of the maintenance cost.

The natural motion of many Wave Energy Converters (WECs) presents two key challenges for the electrical machine designer: it is slow speed and reciprocating. As,  $Power = force \times velocity$ , for the same rated power, the required force needs to be high for the slow speed WECs. This leads to the use and development of high force density linear machines such as a Variable Reluctance Machine (VRM) [5, 6]. This thesis relates to the development of linear Vernier Hybrid Machines (VHM), which is a member of VRM and capable of high force density at a low operational speed suitable for DD-WECs.

## 1.2 Aims and Objectives

The principal goal of this project is to design and develop high force dense permanent magnet linear generators for the DD-WEC system. The main objectives of this research are as follows:

- To design, analyse and optimise the existing VHM for better performance, simpler structure and assembly, and substantial reduction of translator and magnet mass.
- To improve the force density, power density, and power factor by implementing new Permanent Magnet (PM) array design topology.
- To develop cylindrical machine designs from the flat topology.
- To develop and build a custom test rig from scratch for laboratory testing. Testing of the prototype linear generators is not straightforward as linear drive systems are not conventional in traditional electrical machine laboratories.

- To build, test and validate selected lab-scale prototypes.
- To perform a comparative study between flat and cylindrical machine topologies.

### 1.3 Thesis Overview

This thesis unites diverse topics separated into chapters and a brief summary as to their content may prove convenient to the reader. The contents of the thesis can be briefly described as:

Chapter 2: This chapter provides a brief literature review on wave energy resources, existing and most recent wave energy technologies including direct drive power take-off systems and state of art of linear generators to harness wave energy. A suitable high force dense linear permanent magnet machine topology is selected for further analysis and development for DD-WEC application at the end of this chapter.

Chapter 3: This chapter describes the development and optimisation of the E-core design of a Double-Sided Linear Vernier Hybrid Machine (VHM-II) from an existing flat C-core design. The focus is, however, reduction of magnet mass and the influence of employing the segmented translator on the machine performance. Furthermore, deep electromagnetic performance analysis and comparison of the baseline C-core and developed E-core machine is presented in detail in this chapter.

Chapter 4: A novel Halbach Consequent Pole Vernier Hybrid Machine (HCVHM) with a combination of Halbach and Consequent Pole magnet arrays, providing a flux concentration effect has been developed and presented in this chapter. It utilises the same E-core stator which is developed in the previous chapter. The feature of combining Halbach and Consequent Pole PM array results in a reduction in flux leakage and hence improving the air gap flux density, which leads to a better force density than the surface mounted variant presented in chapter 3. Further description of the lab-scale prototype manufacturing and construction process, practical assembly techniques, experimental testing, and validation are also presented in this chapter.

Chapter 5: A cylindrical Vernier Hybrid Machine is proposed as an evolution from a flat Single-Sided Linear Vernier Hybrid Machine (VHM-I) adopting only one E-core. Electromagnetic performance analysis and comparison between the flat and the cylindrical models have been performed. Finally, a small lab-scale prototype of the cylindrical VHM-I has been constructed from Soft Magnetic Composite (SMC) materials and tested to validate the concept.

Chapter 6: In this chapter, another lab-scale cylindrical Vernier Hybrid Machine prototype is built, which is developed from a flat Double-sided Linear Vernier Hybrid Machine (VHM-II) presented in chapter 3. Similar electromagnetic analysis, comparison, testing and validation of the experimental results are performed.

Chapter 7: This chapter presents a cylindrical model of the HCVHM presented in chapter 4. It also gives a detailed performance comparison study between all the machines presented in this thesis for different power ratings.

Chapter 8: Main research findings are summarised along with the recommendations for further work in this chapter.

#### 1.4 Published Works

- Raihan M.A.H., Baker N.J., Smith K.J., Almoraya A.A., **“Development and Testing of a Novel Cylindrical Permanent Magnet Linear Generator”** in *IEEE Transactions Industrial Applications Society*, 2019, under review.
- Almoraya A.A., Baker N.J., Smith K.J., Raihan M.A.H. **“A New Configuration of a Consequent Pole Linear Vernier Hybrid Machine with V-shape Magnets,”** *IEEE Transactions Industrial Applications Society*, 2019, Accept for Final Submission.
- Baker N.J., Raihan M.A.H., Almoraya A.A., Burchell J.W. and Mueller M.A., 2018. **“Evaluating Alternative Linear Vernier Hybrid Machine Topologies for Integration into Wave Energy Converters,”** in *IEEE Transactions on Energy Conversion*, 33(4), pp.2007-2017.
- Baker N.J., Raihan M.A.H., Almoraya A.A., **“Development of a Cylindrical Linear Permanent Magnet Vernier Hybrid Machine for Wave Energy,”** in *IEEE Transaction on Energy Conversion*. 2018.
- Raihan M.A.H., Baker N.J., Smith K.J., Almoraya A.A., **“Development and Testing of a Novel Cylindrical Permanent Magnet Linear Generator,”** In *2018 IEEE XIII International Conference on Electrical Machines (ICEM)* (pp. 2137-2143).
- Raihan M.A.H., Baker N.J., Smith K.J., Almoraya A.A.. **“Development of a Linear Vernier Machine with Low Mover Mass for Wave Energy Converter,”** In: *The 7th International Conference on Renewable Power Generation (RPG2018)*. Lyngby, Copenhagen, Denmark: IET.

- Raihan M.A.H., Baker N.J., Smith K.J., Almoraya A.A., “***A linear Consequent Pole Halbach array flux reversal machine,***” In: *9th International Conference on Power Electronics, Machines and Drives (PEMD 2018)*. 2018, Liverpool: IET.
- Raihan M.A.H., Baker N.J., Smith K.J. and Almoraya A.A., “***Investigation of a doubly salient Halbach array linear permanent magnet machine for wave energy converters,***” In *Electrical Machines and Systems (ICEMS), 2017 20th International Conference on* (pp. 1-5). IEEE.
- Raihan, M.A.H., Baker, N.J., Smith, K.J. and Almoraya, A.A., “***An E-core linear Vernier hybrid permanent magnet machine with a segmented translator for direct drive wave energy converter,***” in *IEEE Electric Machines and Drives Conference (IEMDC), 2017 IEEE International* (pp. 1-6).

## Chapter 2: Literature Review

### 2.1 Introduction

Ocean waves are vast, to a great extent undiscovered energy resources, and the potential for extracting energy from waves is significant. Ocean energy consists of wave energy, the energy of marine currents and tidal energy. This chapter gives a brief description of the history and development of these renewable energy resources in the world, mostly in the UK. It also gives an overview of the existing and most recent wave energy converter technologies including pneumatic, hydraulic and direct drive power take-off system. State of the art of linear generators to harness wave energy are also presented from different kinds of commercially available direct drive linear generators. In the end, after considering electromechanical perspectives, the Vernier Hybrid Machine (VHM) topology is selected for further research and development in the next chapters.

### 2.2 History & Technological Developments of Ocean Energy Conversion

Throughout history, there have been several efforts to harness power from the ocean. The first patent about the use of the ocean wave's motion to drive a mechanical system was awarded to Girard and his son in France in 1799 [8]. They utilised the oscillation of waves to move large wooden beams for driving pumps. Similar patents are also found in the United Kingdom in 1855, according to the work of Leishman and Scobie [9]. In the last decade of the 19th century in San Francisco, California, begin to appear one of the first experiments to use wave energy for electricity generation [10].

Despite daunting challenges and failures, technologies to harness the power of the waves and tides are now being deployed around the world. The emergence of the first modern technology of Wave Energy Converters (WECs) occurred in 1945. Japanese pioneer, Yoshio Masuda had designed several floating buoy systems later known as Oscillating Water Columns (OWC), with the purpose of providing electricity from the wave's motion for navigation [11-13]. In this system, a pneumatic closed chamber is placed in contact with the water. So, the oscillatory movement of the wave pressurises and depressurises the air within the chamber. This variation in pressure actuates a unidirectional air turbine which required a system of rectifying valve, coupled to an electric generator [14, 15]. OWC will farther be described in detail later in this chapter. In 1966, Electricité de France (EDF) developed a 240MW hydroelectric Tidal power plant in La Rance, France, which was installed with 24 turbines of 10MW each [16, 17].

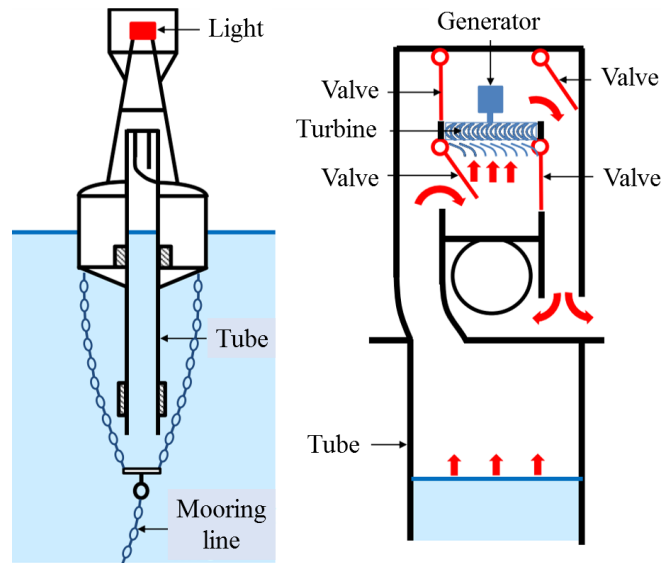


Figure 2. 1: Outline of Japanese navigation buoy equipped with air turbine [15]

The oil crisis of 1973 caused a severe impact on world economies that "alarmed" the world to the problems related to the dependence on fossil fuels. This awareness drove more research into alternative forms of energy. In this scenario, the possibility of ocean wave energy was seen to be an attractive option, which triggered a new phase of research to take advantage of this feature. To exploit this form of renewable energy, United Kingdom (UK) government called for industries and research institutes to come up with plans and, funded larger research and development (R&D) projects during the late 1970s. In 1974, Professor Stephen Salter of "Institute for Energy Systems" at the University of Edinburgh, Scotland, invented the first Wave Energy Converter (WEC) of oscillating bodies named 'Salter Duck' [15, 18]. In the 1980s, the oil and petroleum price went down, which caused wave-energy funding to be reduced. However, a small number of first generation wave energy prototypes were tested at the sea during this period. Over the next two decades, following the growing concern about climate change and protocols on the reduction of CO<sub>2</sub> emission, the R&D projects in wave energy started to grow again in many other countries. European Commission had played a vital role in boosting innovation and cooperation between countries.

In 2008 in Agucadoura, Portugal, the first wave energy park was constituted by three WECs developed by Scottish technology, *Pelamis Wave Power* - with a total capacity of 2.25 MW [19, 20]. Each *Pelamis* converter was composed of four tubes interconnected and floating in the direction of wave propagation. Its passage of the wave causes a relative displacement between the pipes, resisted by hydraulic pistons pumping a high-pressure oil to an accumulator. This fluid at high pressure is then used by a hydraulic motor to drive a conventional electrical generator. While active, the system was interlocked with the Portuguese electrical network [21].

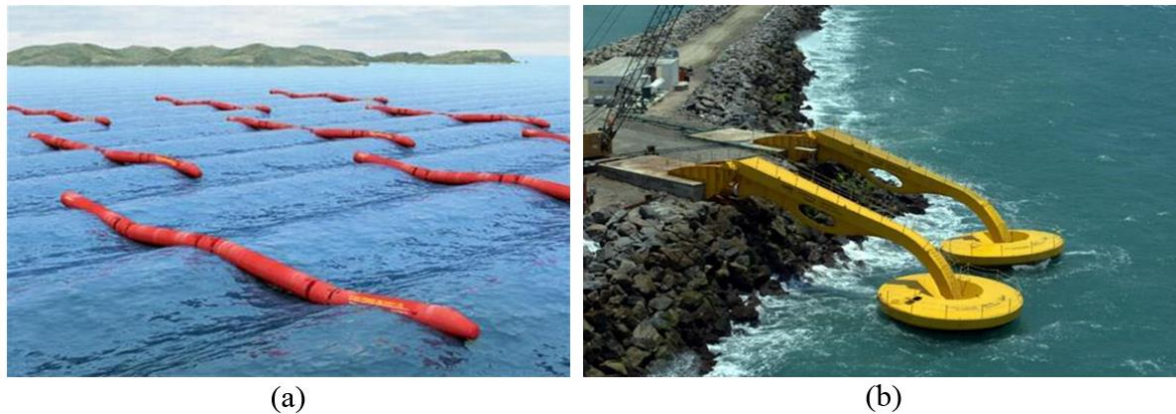


Figure 2. 2: (a) Utilisation of wave energy converters with Pelamis [22] (b) exploitation of wave energy at the port of Pecem Ceará – Brazil

In 2012, Alberto Luiz Coimbra Institute of Graduate Studies and Research in Engineering (often referred to as *Coppe*) in Brazil developed a WEC in order to pump water for a conventional hydroelectric generator to be consumed by the port itself [23]. There are other systems of wave energy converters, with different topologies, installed over the world.

The investments of the United Kingdom for the technology of wave energy conversion deserve to be highlighted. UK is the headquarters of the *European Marine Energy Center* (EMEC) and companies that have become increasingly influential in the sector, such as the *AWS Ocean Energy* and the *Pelamis Wave Power*. The UK is also one of the world's largest importers of coal and natural gas [24]. The dependence of its energy on fossil fuels - 70% composed of coal and natural gas - and the continuous decline of its reserves of fossil makes the situation even more dramatic [25, 26]. In a region where there is not much land available, the sea becomes an attractive alternative.

In Cornwall, southeast England, the 'Wave Hub' is a project funded by the South West of England Regional Development Agency (SWRDA) and European Regional Development Fund Convergence Programme for Cornwall and the Isles of Scilly. The 'Wave Hub' is a shared infrastructure to assist in the development and systems demonstrations of wave energy converters. It was installed on the seabed in September 2010, consists of submarine-8 cabling that reaches a distance of 16 km from the north coast of Cornwall with a transmission capacity of 20 MW connected to the electrical system of the UK [27].

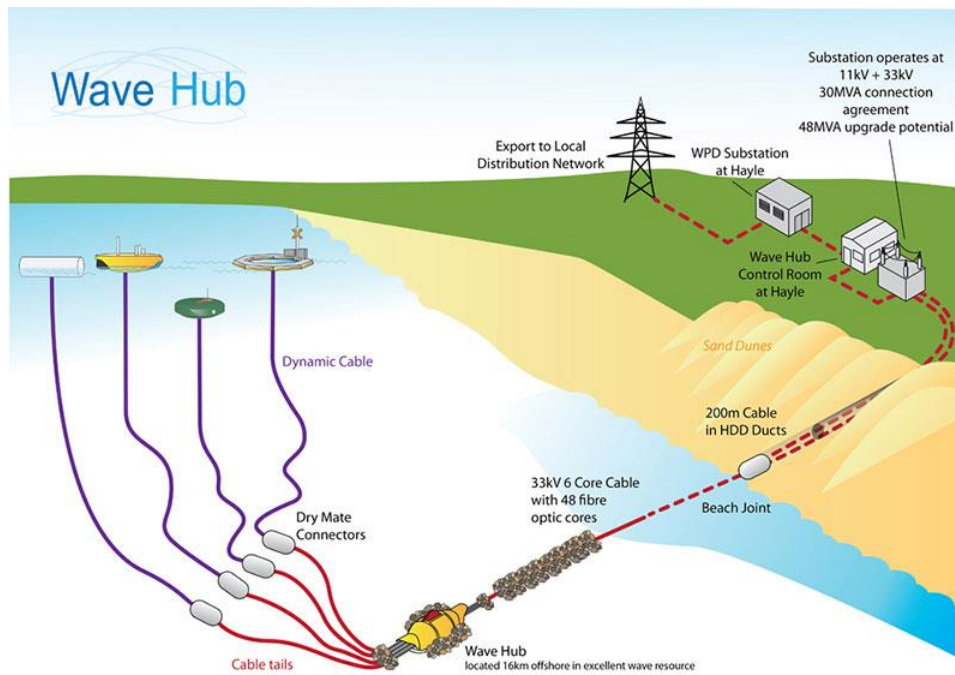


Figure 2. 3: Wave Hub - Infrastructure for development and testing of wave energy converters in Cornwall – England [28].

The “Scottish Power Renewables” had tested a 750kW *Pelamis* wave energy converter prototype of the second generation (P2-002) from 2014 – 2016, which weighs 1350tons. Currently, P2-002 seeking ideas on future learning opportunities and R&D projects. Furthermore, it may benefit from utilising P2-002 prototype with another project in partnership with *Andritz Hydro Hammerfest*, to take advantage of the marine current power of 10 MW [29].

The energy systems of waves and currents are still pre-commercial. The marine energy in the UK has indicated a promising potential with a healthy number of projects that have been through to the planned and operational development.

### 2.3 Ocean Energy Resource

In most of the cases, the exploration of the sea as an energy resource can be performed without conflicting with their other forms of use. The abundance of this feature of energy on the surface of the earth, about 70%, making the sea a renewable source of high availability for the production of electricity. However, the marine environment presents very aggressive characteristics which, in addition to increasing costs, complicate the operation and maintenance of the energy generation systems. It is also difficult to comment on the environmental impacts of the systems, as they are still small-scales with a limited time of operation. Furthermore, the results of environmental studies conducted so far are practically inconclusive [30, 31].

### 2.3.1 Ocean Wave Energy

It is estimated by the Electric Power Research Institute (EPRI) that the total wave energy resource along the outer continental shelf is 2,640TWh/yr [32]. That is an enormous amount of energy, considering the total electric energy consumption by the world was just over 23,000TWh in 2018 [102]. Therefore, the focus on generating electricity by extracting wave energy is an important area of research.

The interaction between the wind and the surface of the sea generates the waves that propagate for long distances. The breaking of the wave means the release of its energy and this usually happens in the vicinity of the coast. As there is not an isolated propagation of the waves of the sea, the energy contained therein is defined as the set of waves incidents in the region. Therefore, the estimate of the available power considers the values of speed and height of the wave that can represent the joint interaction of wave incidents.

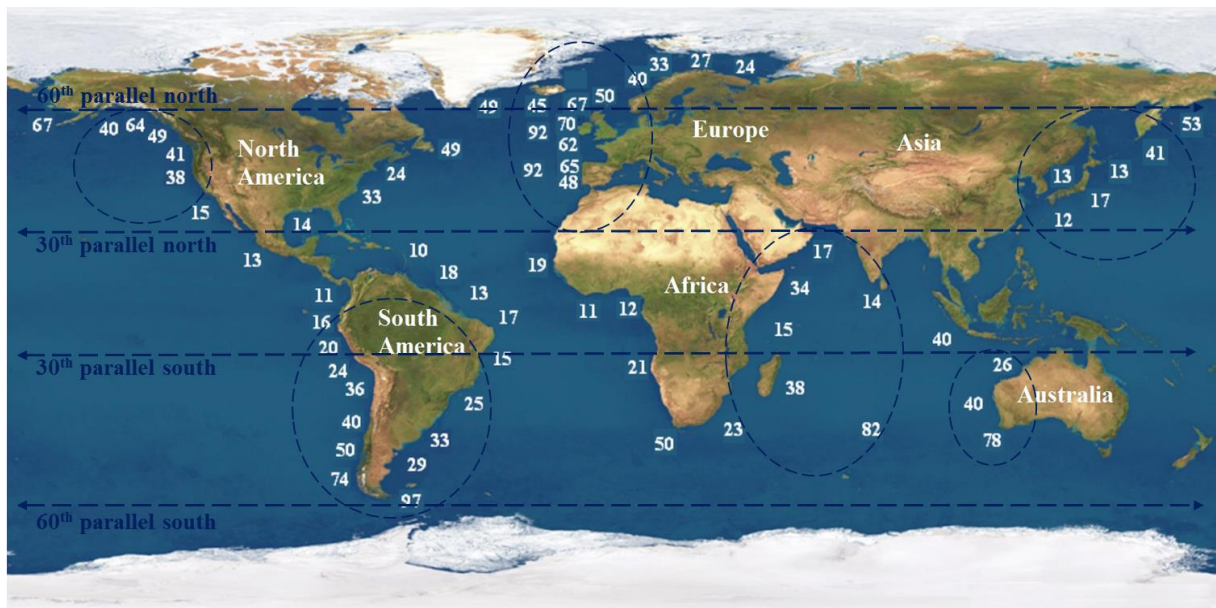


Figure 2. 4: Approximate wave power level is given in KW/m of wave front [34]

Figure 2.4 shows that the world's best wave energy potential is located between the latitudes of 30° and 60°. When comparing with the European potential, the UK coast seems to be an attractive area to exploit the wave power. Therefore, it directed research and development to optimise wave energy conversion technologies and move towards convergence of design and commercialisation of wave devices in Scotland, Wales and Northern Ireland [35].

## 2.4 Wave Energy Converters

Generally, Wave Energy Converters (WECs) are the devices which can generate electricity by exploiting the ocean wave energy. There have been almost 1000 techniques of wave energy

conversions patented around the world [36]. In a broader aspect, the WECs can be classified in three ways based on the location. Firstly, the wave energy devices which are on the shoreline, have the benefit of being near the grid and utility system network and are easy to manage the maintenance work. The waves are weakened as they travel through shallower water, while the devices have a lower chance of being damaged in extreme conditions. However, this results in a disadvantage of having lower wave power for the shore mounted wave energy conversion devices. Although this can partially be compensated by choosing a natural energy concentrated location [36]. Tidal range can likewise be an issue. Furthermore, there are also location specific requirements including shoreline geometry, safeguarding of shoreline view, and protection of natural habitat that can cause the device not to be designed for mass production.

Secondly, the nearshore device can be placed in the shallow water with a depth of less than one-quarter of the wavelength [37]. Typically, the device is embedded in the seabed in the 10-25m depth of water by means of a pillar or tensioned cable, which provides the stationary base stability and datum to react the force against the oscillating body [38]. Again, this nearshore device suffers from the same low power waves near the shore that limits the harvesting energy.

The third category is the offshore deepwater or slack moored device which doesn't have any direct connection with the seabed and is generally floating in the water with a 40m to 100m depth, normally exceeding the one-third of the wavelength [37, 39, 40]. The benefit of placing a WEC offshore is that it can harness greater available energy content in deep-water [37]. Conversely, deep water devices are increasingly hard to build and maintain. It also needs to withstand the most extreme conditions of the wave, which increase the cost of the device development and construction. Regardless of this, it is contended that with the more dominant waves, offshore floating devices offer greater structural economy in terms of energy yield [41].

The wave energy converters tend to be classified into three main types based on their operation:

#### ***2.4.1 Oscillating Water Columns (OWC)***

The Oscillating Water Column (OWC) is one of the earliest methods to harness the potential of an ocean wave. A brief history and operation principle of OWC are presented earlier in this chapter. The heaving movement of the waves is used to pressurise and depressurise the air which then drives a turbine, and then the turbine runs the generator, as can be seen in figure 2.5(a). Numerous real scale prototypes have been installed all around the world, for example: 400 kW OWC plant on the island of Pico, Portugal; 500kW Islay Land Installed Marine Power

Energy Transmitter (LIMPET) on the Island of Islay, Scotland; 1MW Kvaerner Brug's Multi-Resonant Oscillating Wave Column (MOWC) power station, Norway [42] etc.

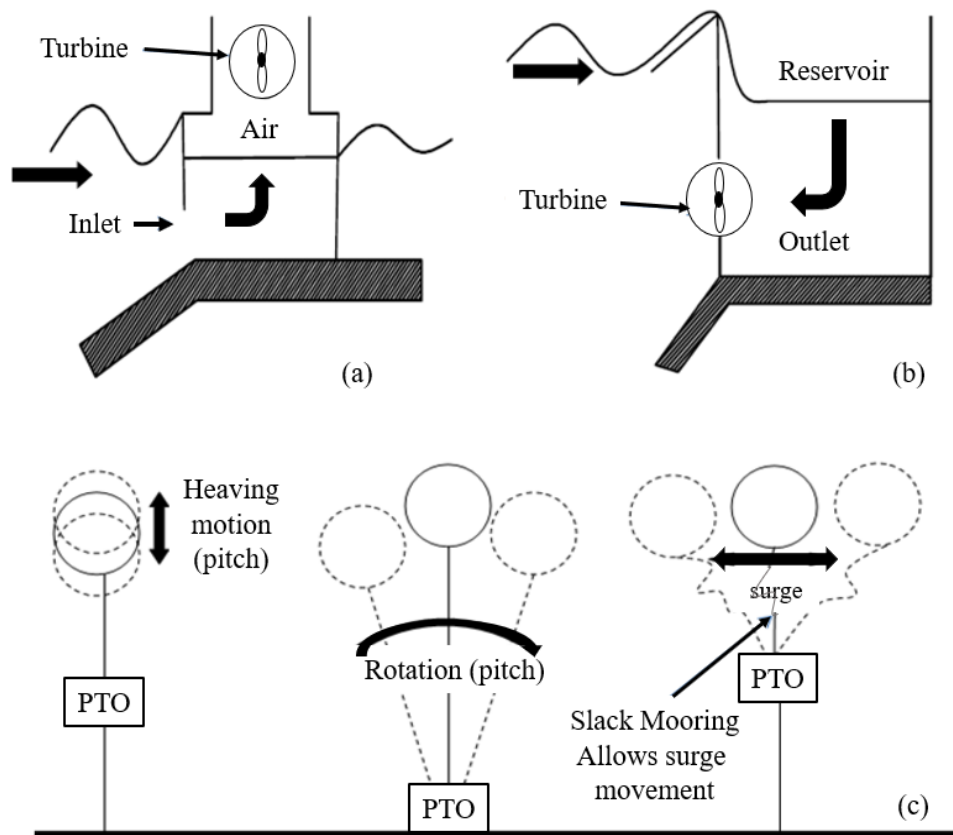


Figure 2. 5: Classification of Wave Energy Converter (WEC) extraction technologies: (a) oscillating water column, (b) overtopping devices, and (c) oscillating bodies [43, 44]

#### 2.4.2 Overtopping Devices:

These technologies work with a reservoir above the sea level that is regulated to store water from the sea with the incidence of waves. This stored water is then flowing out through the small head hydro turbines which operate conventional hydroelectric generators and returning the water back to the sea. By these steps the potential energy obtained by the overtopping water is converted into electrical energy. Example of a system that operates in this manner is the Wave Dragon that has been developed in partnership with the University of Aalborg in Denmark. Figure 2.6 represents the operation principle of the overtopping system of Wave Dragon. Among the few other overtopping WEC devices built and tested are Wave Plane, Sucking Sea Shaft, Power Pyramid, Seawave Slot-cone Generator (SSG) and Tapered Channel (TAPCHAN) [45].

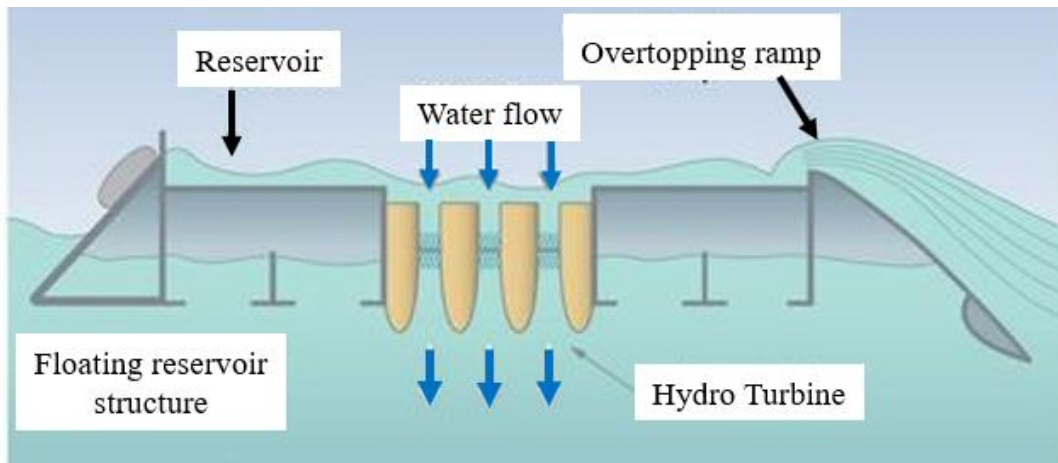


Figure 2. 6: Principle of operation of an Overtopping system (Wave Dragon).

### 2.4.3 Oscillating Body System

These structures directly use the oscillatory movement of the waves for the electromechanical conversion. Figure 2.7 shows the basic principle of operation of the Oscillating Body System. The air filled chamber moves up and down with the oscillation of wave which provides the mechanical input for a direct driven Power Take-off (PTO) system to produce electricity. Some systems such as the Pelamis and the Oyster of the Aquamarine Power [46] take advantage of this movement to pressurise fluid, store it, and then through hydraulic turbines, engage conventional electrical generators. AWS, Ocean Power and the Seabased AB use the oscillation of waves to drive a linear generator for direct drive power take-off.

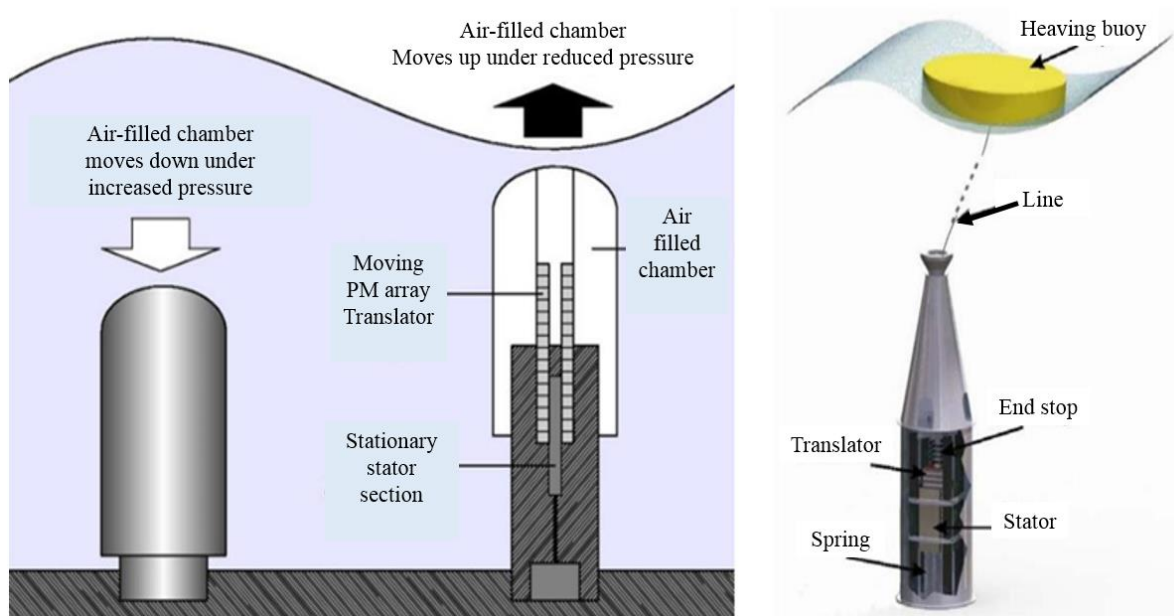


Figure 2. 7: On the left: Schematic of a converter AWS. On the right: converter with concept Seabased AB. Both use a linear generator as a way of taking power.

### 2.5 Power Take-Off (PTO)

The main objective of the wave energy conversion process is to absorb the energy of the wave and convert it into electrical power, to be transferred into the grid. The PTO of any WEC is the mechanism to convert the primary kinetic and potential energy of wave (linear motion) into electrical energy. The PTO system should be robust, efficient, reliable, and require minimum maintenance. Diversity in the PTO systems reflects the lack of industrially standard WEC devices, unlike the wind energy sector. The selection of the PTO for a WEC device is strongly correlated with the type of the converter. A simple flow diagram for wave energy to electricity generation via different types of PTO system is shown in Figure 2.8.

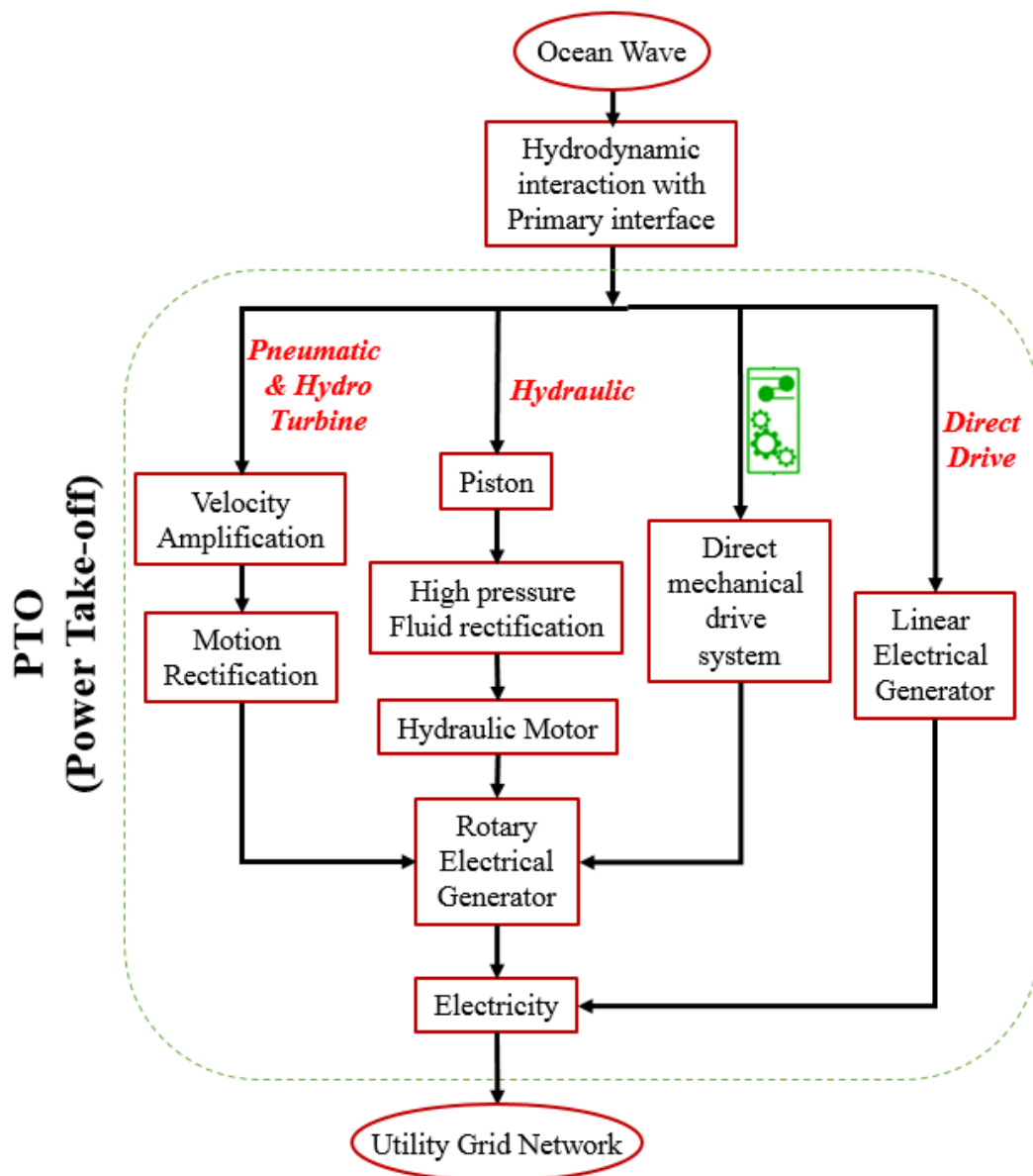


Figure 2. 8: Block diagram of different Power take-off methods

Most technologies developed for the utilisation of wave energy need relatively complex systems to transform the natural oscillatory movement of waves in a rotating movement and, thus, allow the use of conventional rotary generators of fixed or variable speeds [47]. The ‘Direct mechanical drive system’ comprises of gearbox, pulleys, cable, and flywheel can be integrated into a rotation-based system to drive a conventional rotary generator. Direct drive linear generator can also convert the linear motion of waves into electricity.

Although the systematic comparison between different PTO systems is difficult, three major categories are briefly described in the following subsections.

### 2.5.1 Hydraulic

The process of converting wave energy into electrical energy by using the hydraulic system, for example, the *Pelamis*, is accomplished through several steps. Figure 2.9 shows a schematic of the Hydraulic PTO system for wave energy conversion. The point absorber (buoy) is connected to a linear actuator, which pressurise or depressurise the fluid through the controlled hydraulic manifold to the hydraulic motor. The motor then rotates the generator to produce electricity. The accumulators are also added in the system to level the fluid pressure in the system by either delivering or accumulating the fluid energy when necessary.

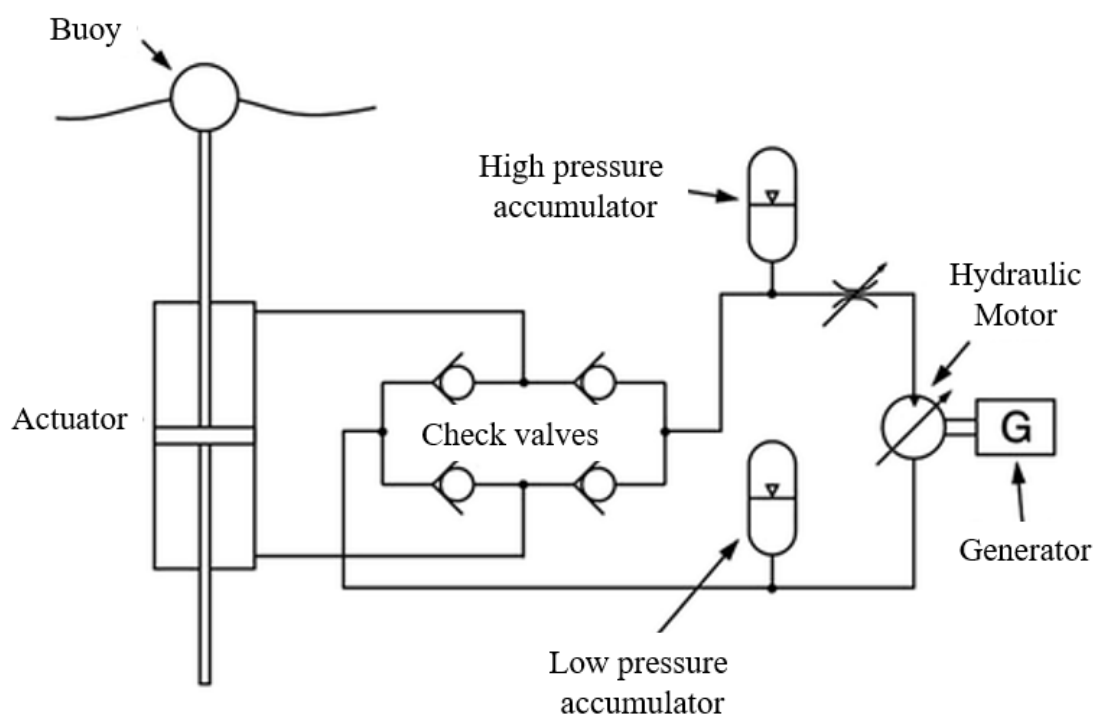


Figure 2. 9: Hydraulic PTO system for wave energy conversion [22]

The hydraulic pistons have been sensitive points to the operation of these converters. In practice, different components i.e. hydraulic accumulator, motor, multiple moving parts, etc. have presented reduced durability compared to what was expected, and malfunction may impair the operation and start oil leaks. Despite the complexity of the system, the peak efficiency of these converters at the ideal operating point is relatively high, at around 80% [22].

### ***2.5.2 Pneumatic & Hydro Turbine***

Devices using fluid to drive the hydro-turbine, which is directly connected to the generator, include OWCs and overtopping devices. One of the significant advantages is the leakage of working fluid (ocean water) causes no harm to the surrounding environment. Disadvantages include complex and volatile constituents, coarse particles in sea water which can cause damage to the valves and seal for near shore device. Again, maintaining appropriate pressure in near shore device is a challenge and propeller type Kaplan turbines are often used in such conditions.

The advantage of Pneumatic PTO is the conversion of slow velocity wave to high velocity air flow. It utilises a fixed or floating structure to trap the air between the free surface and air turbine. Islay LIMPET (Land Installed Marine Power Energy Transmitter) is an OWC converter that also use a pneumatic system in conjunction with a Wells turbine to drive the electric generator [13, 48]. The Wells turbine is an axial flow turbine that can self rectifies to rotate continuously in one direction independent of the direction of air flow. One of the major drawbacks of these systems, compared to hydraulic power take-off systems is the efficiency of the pneumatic system in conjunction with the stall problems in air flow through the Wells turbine. The detachment of air flow in the guide vanes causes stall problem, which increases the turbulence of the fluid, introducing vibration problems and reducing the efficiency of conversion. The vibration was one of the biggest problems faced by central OWC Pico in the Azores, Portugal, which caused the turbine not to reach its maximum speed [44]. Another difficulty faced in the OWC is the great inertia of the Wells turbine, which makes the process of braking performed by an exhaust valve relatively slow. In cases of waves with excessive heights, this increases the risk of the system packaging and, due to the problems of vibration, damaging the structure.

According to a *Carbon Trust* report, the central LIMPET had observed the efficiency of 64% in the pneumatic chamber, 40% in the Wells turbine and 32% in the electrical generator [49]. The total efficiency measured was very low, 8%. In both cases, this efficiency has been

hampered by the low yield of electrical generator installed in the possible conditions of operation.

### 2.5.3 Direct Drive

Direct Drive Power Take-off (DD-PTO) or all electric power take-off refers to the system that directly couples the moving part of the linear generator to the mechanical energy captured from the point absorber or primary converter. The use of linear generators simplifies the conversion process, leveraging directly the oscillatory movement of the waves of the sea. It represents the minimisation of the number of processes for the conversion of energy and decreases not only the quantity of equipment involved in power take-off but also the number of sensors in this process. It is expected that this option needs least corrective maintenance activities and that its lower efficiency and higher cost per kW installed in relation to the rotating machines are justified by the reduction in the revenue cost.

Table 2- 1: Pros and cons of different power take-offs.

Power Take-off	Pros	Cons
Hydraulic	<ul style="list-style-type: none"> <li>• Well suited for absorbing high forces.</li> <li>• Incorporated energy storage within the PTO.</li> <li>• Low environmental challenge.</li> </ul>	<ul style="list-style-type: none"> <li>• Low efficiency and high maintenance cost.</li> <li>• complex fluid containment system.</li> <li>• Wear and tear in sealing.</li> </ul>
Pneumatic & Hydro Turbine	<ul style="list-style-type: none"> <li>• Speed multiplication</li> <li>• Working fluid (ocean water) causes no harm to the surrounding environment.</li> </ul>	<ul style="list-style-type: none"> <li>• Low turbine efficiency</li> <li>• Alternating air-flow.</li> <li>• Volatile constituent and coarse particles can cause harm to the valves and seal.</li> </ul>
Direct Drive	<ul style="list-style-type: none"> <li>• Higher system efficiency</li> <li>• No complicated intermediate mechanical linkage system.</li> <li>• Simple system architecture, Higher reliability and lower maintenance.</li> </ul>	<ul style="list-style-type: none"> <li>• Non-conventional electrical machine with high force density.</li> <li>• Large machine size to react large forces and expensive permanent magnets.</li> </ul>

However, there are new challenges, because linear generators are not generally used to produce electricity in other areas, there is no consensus on how best to build them and it is a low-speed

application. Some phenomena that are attenuated in conventional rotary machines at low speed may have their relevance enhanced, among them is the parasitic forces. Although one of the advantages of linear generators is reducing the need for corrective maintenance, they also have difficulties in operation. Among them, translator bearings can be caused by electromagnetic forces perpendicular to the motion, as, for example, by forming an angle between the rope and the converter at the sea-based system. The need for corrective maintenance of the system for monitoring the environmental parameters remains a weakness.

*Table 2- 2: Different types of generator used in existing WEC devices and their power take-off the system*

<b>WEC Device</b>	<b>Power Take-off (PTO)</b>	<b>Generator topology</b>
PELAMIS (UK)	Attenuator/Hydraulics	Induction generator
SEAREV (France)	Point Absorber	Permanent Magnet Synchronous Generator
OYSTER (UK)	Oscillating Wave Surge Converter	Induction generator
LIMPET (UK)	OWC & Wells turbine	Induction generator
PICO (Portugal)	OWC & Wells turbine with guides vanes	Doubly-Fed Induction Generator
WAVE DRAGON (Denmark)	Overtopping & Kaplan turbine	Permanent Magnet Synchronous Generator
AWS (USA)	Direct Drive	Linear Permanent Magnet generator

## 2.6 Linear Generators for Wave Energy Converter

Linear generators are rarely used in the conversion of mechanical energy into electrical energy. Conventional power plants (coal, gas, oil, nuclear, hydro, wind, etc.) employ high speed rotating electrical generators. The natural motion of many wave energy converters presents a few key challenges for conventional generators, which are the major requirements for the linear generators in this application:

- It is slow speed and reciprocating in nature.
- High force density and peak force.
- Cost-efficient
- Irregular motion

### 2.6.1 State of the Art

Different topologies of conventional linear generators could be used for DD-WECs [50]:

- Linear induction machines
- Linear electrically excited synchronous machines
- Linear permanent-magnet synchronous machines
- Linear switched reluctance machines

Linear permanent magnet synchronous machines are proved to be the most suitable generators for the wave energy application [25]. To present the state of the art of the permanent magnet linear generators applied to recover wave energy, the emphasis is given to some prototypes that were tested at sea conditions. Examples of WECs tested on the marine environment with linear generators include *AWS*, *Columbia Power Technologies*, *Seabased AB* and the *Trident Energy*. Moreover, two other technologies developed by the University of Edinburgh (VHM) and the University of Durham (C-Gen) also have distinct characteristics, which will be discussed at the end of this chapter

### 2.6.2 Archimedes Wave Swing (AWS)

The development of a linear generator for Archimedes Wave Swing (AWS) was conducted in partnership with the Technical University of Delft (TUDelft) in the Netherlands. The AWS converters consist of linear permanent magnet generators with double-translator structure (Figure 2.10). The stator is positioned between the PM mounted translators and is composed of ferromagnetic material. This converter had a nominal power of 1 MW. Currently, the company AWS does not work with this concept, the most recent prototype - AWS-III - operates with a system of the pneumatic power socket, similar to the "*Sea Clam*" [27, 51, 52]. However, a recurrent factor in articles of the developers of the AWS system refers to the high forces on the axis perpendicular to the movement, which generate heavy stress in the bearings of translator and hinders the maintenance of the air gap, especially in longer machines (the generator AWS had an 8 m length) [33]. Another converter with double side flat topology and the ferromagnetic translator core is the "*Snapper*" which integrated with a system of springs that amplifies the speed of the translator [53-55].

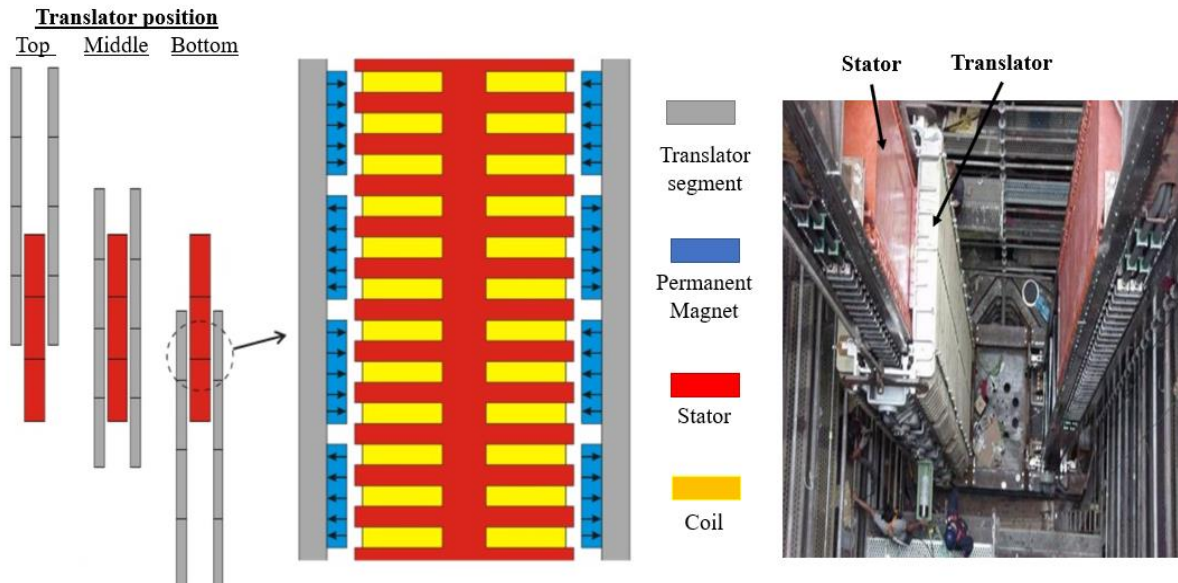


Figure 2. 10: AWS linear generator topology and its translator assembly.[27, 47]

### 2.6.3 Seabased Industry AB (SIAB) & Uppsala University (UU)

The WECs of *Seabased Industry AB (SIAB)* is developed in partnership with the University of Uppsala in Sweden. The WECs consist of a linear generator enclosed by a water-tight pressurized hull connected with a point absorber buoy systems that are placed in a concrete foundation on the seabed (Figure 2.11). Although the underlying idea of the WEC has been developed at the Division of Electricity of Uppsala University (UU) [56], it is promoted by the Swedish organisation SIAB, who are currently collaborating in a number of research projects with the UU [57].

The translator and the stator of this linear generator have four sides. The translator accommodates powerful Neodymium-Iron-Boron (NdFeB) magnets spaced by non-magnetic aluminum on each side, which develops a longitudinal distribution of magnetic flux and is surrounded by four stators. The distribution of the coils in the grooves of the ferromagnetic stator is made in order to mitigate the parasitic forces [58]. The concept of SIAB consists of having low power converters, but build with many units. These converters have a nominal power of 30 or 50 kW according to the document of ‘*Strategic Initiative for Ocean Energy*’ [59]. This document also mentions that the SIAB has already received funding for the construction of a park of energy waves of 10 MW with approximately 420 converters in Sweden.

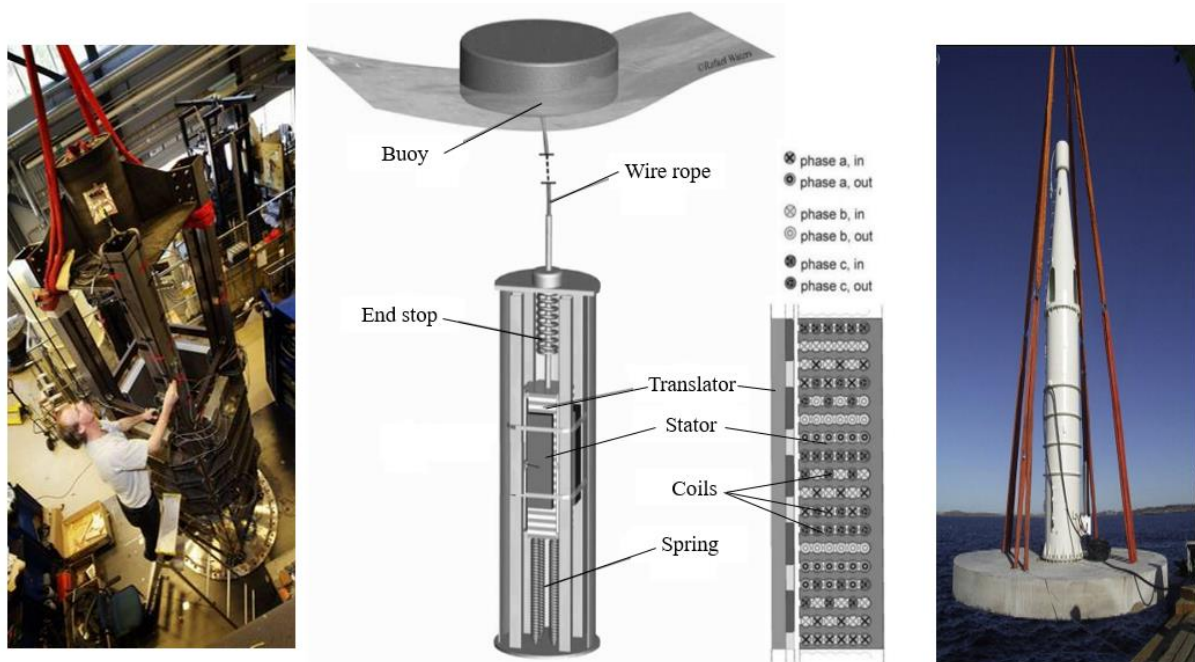


Figure 2. 11: On the left, the inside of the converter of Seabased AB. On the center, floating buoy with the WEC device and a detail of the excitation winding system. On the right, the real prototype of the WEC device[60]

#### 2.6.4 Columbia Power Technologies

The linear generator of *Columbia Power Technologies (CPT)* was developed in partnership with *Oregon State University (OSU)* in the United States. It is a three-phase generator of tubular geometry with ferromagnetic core and magnetic excitation produced by NdFeB magnets that develop a longitudinal distribution of magnetic flux. The nominal power of the second generation converter was 10 kW [61]. After the tests at sea, the *CPT* saw the need to rethink the topology of the system. Their third-generation converters no longer use linear generators. The new technology, according to the company's website, consists of a DD-PTO system consisting of a PM rotary generator [62]. Figure 2.12 shows the linear generator of *CPT* in operation and its inner part for a second generation device.

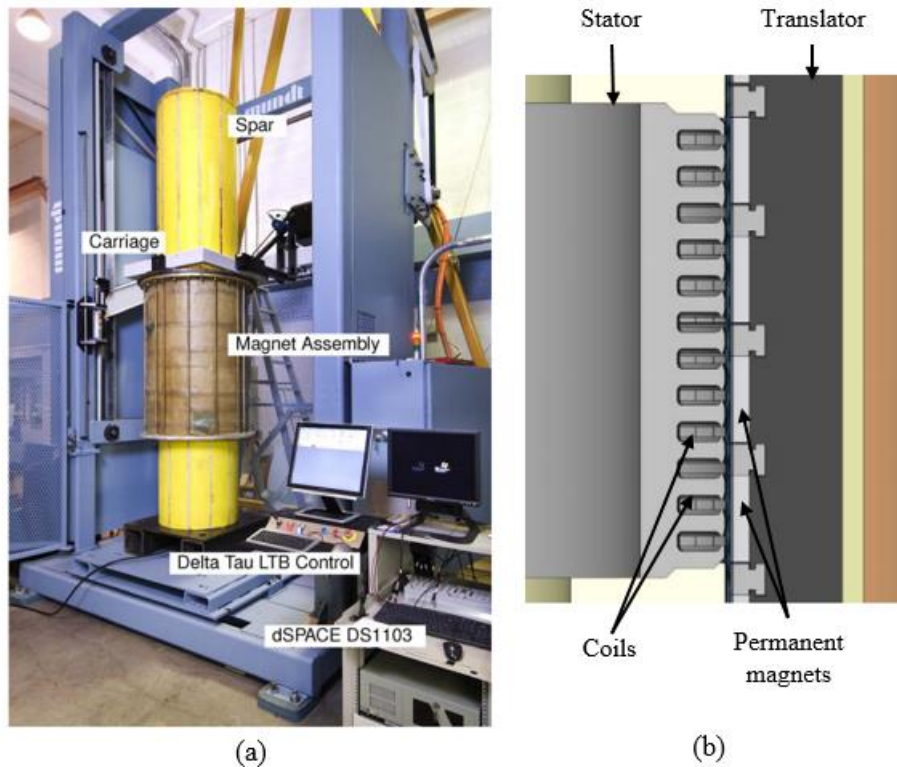


Figure 2. 12: (a) *SeaBeav-I* with integrated permanent magnet linear generator on the linear test bed [63] (b) 2D crosssectional view of the generator component [61]

### 2.6.5 Trident Energy

The topology proposed by *Trident Energy* consists of a slotless tubular generator. The stator of this converter is composed of NdFeB magnets, separated from each other by ferromagnetic material, which develops a longitudinal distribution of magnetic flux. The translator, which in this case encompasses the stator, has no teeth ("slotless") but has a layer of steel behind the coils (reducing the magnetic reluctance). For this reason, it is said that this machine has an air core. Each converter of the *Trident Energy* in its interior has six generators whose translators move in synchronisation. This topology has a positive feature to reduce the forces of attraction between the stator and the translator, bringing benefits to its mechanical operation. On the other hand, the *slotless* topology significantly reduces the magnetic flux density in the stator coils and, thus, these machines are working with a low density of strength and must have minimum air gaps [64]. Figure 2.13 shows an air cored slotless linear generator from the 'WaveDrive' project of Trident Energy [65].

Other prototypes with tubular air-core topologies are presented by the University of Durham in [29] and the University of Stellenbosch in [64].

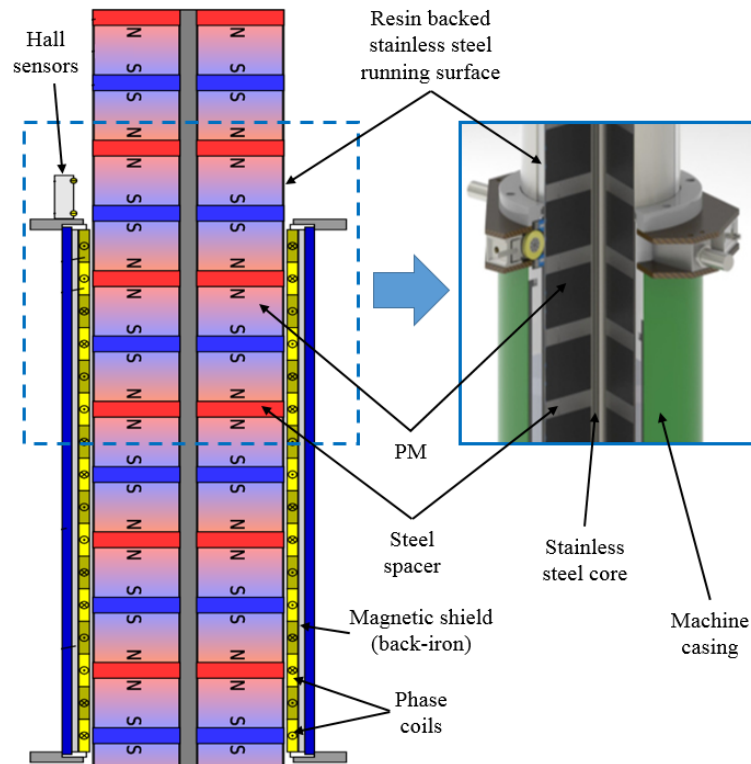


Figure 2. 13: Schematics details of the slot-less linear generator for the converters of Trident Energy being installed for testing at the sea [64-66]

### 2.6.6 C-Gen

According to the developers of the C-Gen, this linear generator is thought to be used by a wave power converter from AWS concept [67]. The translator is composed of modules each with two C-core ferromagnetic parts, which can accommodate magnets. The distribution of the magnetic flux lines is three-dimensional – longitudinal flux path between different modules and transverse flux paths within the same module. The stator is flat, internal to the modules comprising of air-core. This topology has advantages that the attraction force between the stator and the translator can be eliminated due to the absence of stator core and the possibility of modular construction of the energy converter [67, 68]. In contrast, the magnetic flux density and field strength in the coils are reduced.

Figure 2.14 shows the topology and flux path of a module. Figure 2.15 allows observing the closing of the magnetic flow lines between modules (longitudinal flux path), and the physical winding layouts. Figure 2.16 shows a 25 kW prototype.

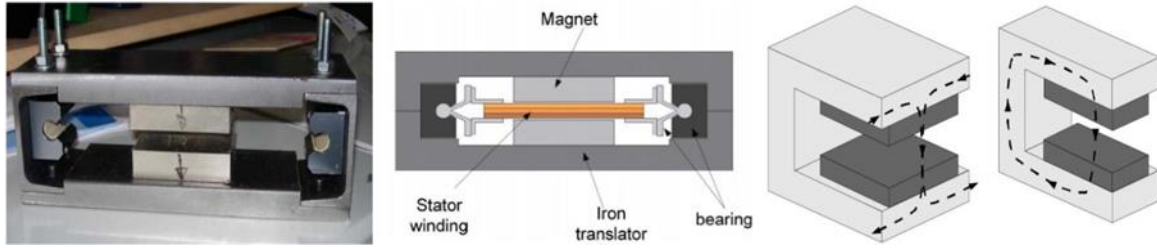


Figure 2. 14: On the left, a module of translator C-Gen. In the centre, characterisation of the module. On the right, the distribution of the magnetic flow lines in a module [67].

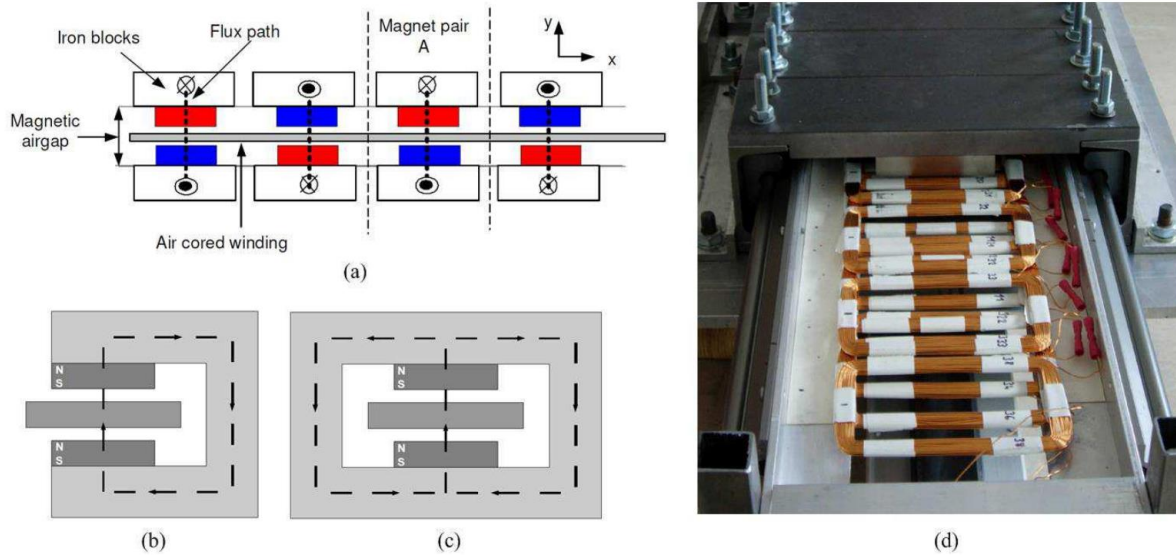


Figure 2. 15: 2D Schematic diagram between modules of the linear generator, C-Gen a) Double-sided generator with magnet pairs separated into modules (b)&(c) magnetic flux distribution in a module (d) coil mounted on the c-core module [67]



Figure 2. 16: Prototype C-Gen 25kW [67]

### 2.6.7 Vernier Hybrid Machine (VHM)

The Vernier Hybrid Machine (VHM) is a member of the variable reluctance machine family and is reported in various articles including [5, 7, 38]. The research on VHM started at Durham University as an efficient alternative of conventional linear generators for their high force density and slow speed application. The three-phase VHM composed of three sets of double-sided stators properly spaced. Each set composed of two laminated C-core stators, which consist of both coils and the permanent magnets (Figure 2.17). There are multiple magnets with alternating polarities mounted on each stator pole face. The translator is a laminated

ferromagnetic core with salient teeth. The basic concept is that multiple small pitch magnets link a single coil so that a small physical displacement of the translator is amplified to a high rate of change in magnetic flux, which induces voltages in the coils. The voltage has its frequency determined by the dimensions of the teeth and the magnets.

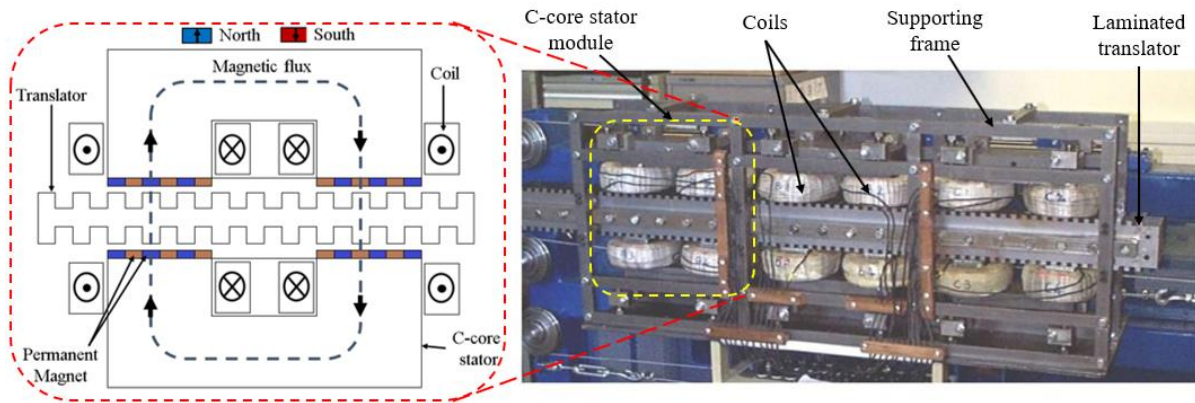


Figure 2. 17: The 3kW prototype VHM generator and the 2D cross-section of a C-core unit [7]

Like the other member of the Flux Switching (FS) or Variable Reluctance (VR) machine family, this topology facilitates the operation with higher values of electrical frequency, force, and power density application. On the other hand, the attraction forces between the stator and the translator are high and the air gap must be small so that the magnetic flux between adjacent magnets do not come in short circuit, increasing the leakage flux and thus reducing the performance.

An overview of the current state of the art of linear synchronous generators applied to recover energy from waves is presented in Table 2-3.

Table 2- 3: Overview of the state of the art of linear synchronous generators applied to recover wave energy [69]

Force Density	Generator type	Company / Developer	Power
High	Vernier Hybrid Machine (VHM)	University of Durham [25]	3 kW
	Variable Reluctance Machine (VRM)	Wedge Global [70]	160 kW peak
Average	Permanent Magnet Synchronous Machine (PMSM)	Seabased AB in cooperation with Uppsala University[58, 71-73]	30/50 kW
	Permanent Magnet Synchronous Machine (PMSM)	Snapper consortium [53-55]	1.4 kW

Low	Air Cored, Flat- Permanent Magnet Synchronous Machine (PMSM)	U. Edinburgh, C-Gen [67, 68]	25 kW
	Air Core, Tubular, Permanent Magnet Synchronous Machine (PMSM)	University of Durham [29], University of Stellenbosch [64]	1.6 kW, 1 kW
	Tubular, Permanent Magnet Synchronous Machine (PMSM)	Trident Energy [65]	30kW/45kW/60kW

## 2.7 Selection of Machine for Further Development

Several linear machine topologies have been proposed for wave energy, many of which capitalise on rare earth permanent magnets, such as the air-cored topologies of [65, 74, 75]. Alternatively, magnetic gearing is employed such as the Transverse Flux Machine (TFM) [25], Flux-Switching Machine (FSM) [26], and the Vernier Hybrid Machine (VHM) [5]. These Variable Reluctance Permanent Magnet (VRPM) machines provide higher power density and require the smaller machines to react to a given force compared to the conventional PM synchronous machines. Among the VRPM machines, the linear TFM with flux concentration appeared to be cheaper and considerably more efficient than the currently applied linear PM synchronous generator [25]. The drawbacks of this kind of machines are — the complicated design due to their configuration of stator and translator, their complex three-dimensional (3D) flux pattern that takes a long time to analyse and optimise in Finite Element Analysis (FEA), high cogging, low magnet utilisation and poor power factor.

The investigation into linear machines for other applications has shown that among the topologies, where the magnets are located on the stator, they give a less efficient magnet use on short-stroke machines [76]. Thus, are likely to prove favorable for long stroke machines as it cost no additional expensive magnets on the longer translator compared to the conventional linear machines with PM on the translator.

The VHM utilises the minimal quantity of PM mounted on the shorter stator, has a simple 2D flux pattern, rigid mechanical structure with a simple translator design and easily scalable into single-sided or multi-sided topologies. However, the VHM suffers from a low power factor, which requires overrated power electronic converters to be employed. The main reasons behind the low power factor in this kind of machine are the high phase inductance and the high magnetic flux leakage as only half of the PM poles contribute to the active flux linkage [77-79].

Another important disadvantage of the VHM is the high attraction force or the air-gap closing forces between the stator and the translator which have an adverse effect on the bearings. The problem becomes severe especially for the single-sided flat topology, while theoretically, the double-sided topologies with identical air-gaps on both sides have zero net attraction force, as both stators counterbalance forces on the translator. However, the smallest non-identical air-gap variation can cause a large net attraction force between primary and secondary parts, which can cause a serious mechanical failure [80].

Therefore, strong and rigid structural support is required to keep the air-gap uniform for the flat topologies or converting the flat topology into cylindrical can reduce the attraction force and reduce the associated bearing cost. Again, cylindrical linear PM machines have been shown to have a higher force-to-weight ratio compared to flat topologies in some scenarios [81, 82]. Furthermore, a cylindrical configuration may have the potential to be more suitable for wave energy converter power take off as it removes the need for the translator to resist torsional forces and dynamic sealing is likely to be less challenging.

Consequently, it is worthwhile to investigate the VHM topology further for the wave energy converter application. All these advantages can be further improved, and the adverse effects can be minimised to an acceptable value by design, development, and optimisation, which will be discussed in the coming chapters.

## **2.8 Conclusion**

Harnessing the potential of the ocean waves for generating electricity represents an important step towards meeting the target of renewable energy. This chapter has presented a review of different types of WEC devices established and evaluated by individual companies, institutions and as collaboration projects on wave energy. Hydraulic, pneumatic and direct drive - linear generator-based PTO systems have been demonstrated in different WEC devices. Considerable research and development show high force linear permanent magnet machines are proved to be a strong contender for direct drive power take-off without the need for the mechanical linkages, which are required to facilitate the use of conventional rotary electric machines. Finally, by taking into consideration the simplicity and the rigidity of the mechanical structure, high force density at low operating speed and scopes for design improvement and optimisation, the VHM has been selected for further development and analysis among the topologies presented.

## Chapter 3: Vernier Hybrid Machine

### 3.1 Introduction

A linear Vernier Hybrid Machine (VHM) with inherent magnetic gearing had been proposed for Direct Drive Wave Energy Converter (DD-WEC) due to its high shear stress and force density [5]. Other force dense variable reluctance PM synchronous machines e.g. Transverse Flux Machine (TFM) suffer from complex 3D flux pattern, heavy translator and a high magnet volume. However, the VHM has a comparatively simple 2D flux path, simpler construction and less magnetic material [7]. In this chapter, a C-core baseline VHM is presented and an improved E-core design of VHM is developed and optimised to give a smaller size and lower magnet mass. In addition, a pole shifting method is utilised to reduce the cogging force to a great extent and a segmented translator structure is also proposed, resulting in a significant reduction in the translator mass while improving the performance. The E-core VHM is designed, analysed, optimised, and compared with the baseline VHM machine using Finite Element Analysis (FEA). The newly developed topology is proved to produce higher back EMF and average force, all with a lower cogging force.

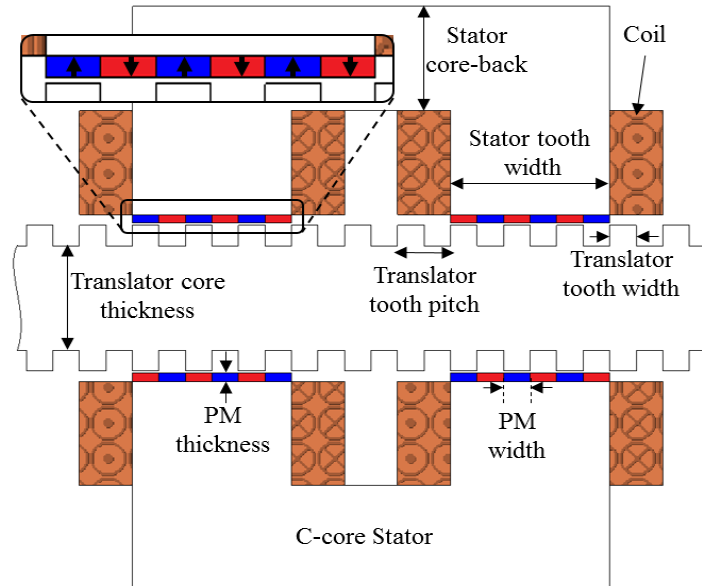


Figure 3. 1: Single phase of the baseline C-core double sided Vernier Hybrid Machine

### 3.2 Initial Design

#### 3.2.1 Operation Principle

The VHM is a variable reluctance, flux reversal machine that offers high power and force density with simple and rigid structural construction. In the initial design [7], there are two C-core stators facing each other which form a single phase, surrounding two sides of a laminated

steel-toothed translator (Figure 3.1). Translator teeth and slots are of equal widths while multiple magnet poles and armature coils are mounted on the C-core stator. Alignment and un-alignment between magnet poles and translator's teeth produce maximum and zero flux linkage respectively. Moving the teeth to an adjacent magnet produces a reverse flux flow around the machine. Physically displacing the translator by a short distance, the coils, therefore, see a large change in magnetic flux, and a corresponding high back EMF and force production - this phenomenon is called 'magnetic gearing'. This 'magnetic gearing' is a non-contact method that enables direct drive machines to reach a higher force density without a conventional mechanical gearbox [83].

### 3.2.2 Design Dimensions

The initial design dimensions of the VHM are based on a simple flux path and theoretical analysis of the equivalent reluctance network [7]. The ratio of flux densities under the slot ( $B_s$ ) and the tooth ( $B_t$ ) can be derived from the following equation [84],

$$\frac{B_s}{B_t} = \frac{g+t_m}{\sqrt{(g+t_m)^2+0.25w_m^2}} \quad (3-1)$$

Where,

$B_t$  = Flux density under the tooth

$B_s$  = Flux density under the slot region

$B_{root}$  = Flux density at the root of the tooth

$B_r$  = Residual flux density of the magnet material

$\mu_0$  = Permeability of free space

$\mu_r$  = Relative permeability of rare earth magnets

$g$  = Air gap length

$t_m$  = Magnet thickness

$w_m$  = Width of the magnet poles

The magnets will significantly distort the flux distribution around the slot-tooth region. However, the magnets are considered equivalent to armature conductors such that their effect is equivalent to armature reaction. The Maximum achievable force and the power capability of the machine can be derived from the shear stress. Peak thrust force occurs when the translator teeth are aligned with the intersection between adjacent magnets, in which case the shear stress over the full magnet area is:

$$\sigma_{peak} = (B_t - B_s)H_c \frac{t_m}{w_m} \quad (3-2)$$

$$\sigma_{peak} = H_c B_t \frac{t_m}{w_m} \left(1 - \frac{B_s}{B_t}\right) \quad (3-3)$$

Substituting the  $\frac{B_s}{B_t}$  from (3-1),

$$\sigma_{peak} = \frac{B_r}{\mu_0 \mu_r} \frac{t_m}{w_m} B_t \left(1 - \frac{g+t_m}{\sqrt{(g+t_m)^2 + 0.25w_m^2}}\right) \quad (3-4)$$

A good approximation relating the field strength under the tooth to that at the root is given [7],

$$B_t \approx \frac{B_t}{B_t + B_s} B_{root} \quad (3-5)$$

Substituting (3-1) into (3-5) hence can give the relationship between flux densities under tooth geometry and its root,

$$B_t = \frac{B_{root}}{1 + \frac{g+t_m}{\sqrt{(g+t_m)^2 + 0.25w_m^2}}} \quad (3-6)$$

Assuming zero leakage flux and an infinite depth of the slot, general peak shear stress can be expressed in terms of maximum flux density under each translator's tooth by substituting (3-6) into (3-3),

$$\sigma_{peak} = \frac{B_r}{\mu_0 \mu_r} \frac{t_m}{w_m} \left( \frac{B_{root}}{1 + \frac{g+t_m}{\sqrt{(g+t_m)^2 + 0.25w_m^2}}} \right) \left( 1 - \frac{g+t_m}{\sqrt{(g+t_m)^2 + 0.25w_m^2}} \right) \quad (3-7)$$

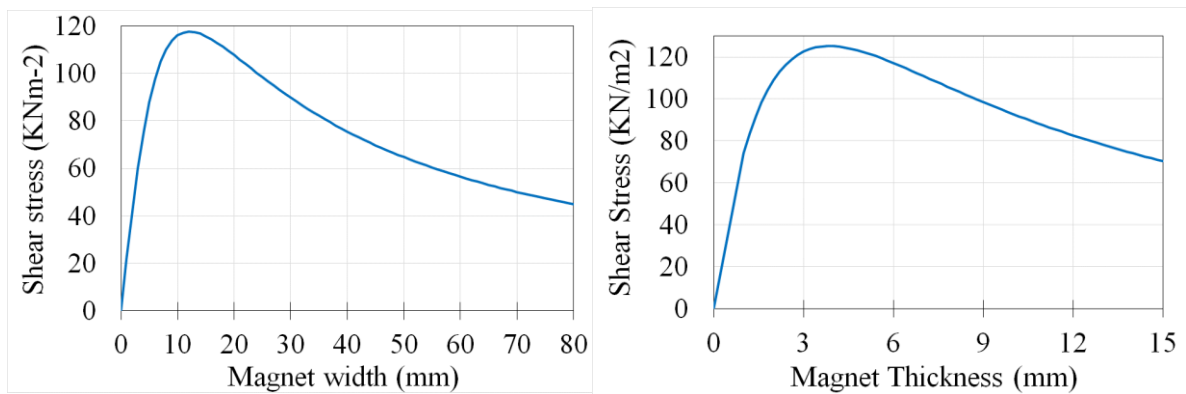


Figure 3. 2: Analytical analysis of Magnet Thickness and width for maximum shear stress on the baseline VHPM machine.

Figure 3. 2 to show that for a fixed PM thickness of 4mm, the maximum shear stress is obtained at a magnet width of 12mm. Similarly, for a fixed width of 12mm, the maximum shear stress occurs at a thickness of 4 mm. Assumed values are  $B_r = 1.2T$ ,  $B_{root} = 1.8T$ , and  $g = 1mm$ .

The VHM design developed in [5] is taken as a baseline for initial investigation and optimisation. Initially, the stator magnet pole pitch was assumed equal to the translator tooth pitch which gave translator tooth width of 12mm each. So, the total number of magnets per stator tooth was found to be 6 from the tooth area. The air-gap is assumed to be 1mm for the prototype build [5]. However, in real-world full-scale WEC devices, this 1mm air-gap may not be physically achievable given the sealing and mechanical requirement. Other parameters of the initial VHM model are given in the following table,

*Table 3- 1: Initial design dimensions of the baseline VHM [7]*

<b>Parameters</b>	<b>Values</b>
Magnet pitch (mm)	12
Translator tooth pitch (mm)	24
Magnet thickness (mm)	4
Stator core back (mm)	50
Air-gap (mm)	1
Magnets per stator pole	6
Translator slot depth (mm)	10
Machine length (mm)	100

### 3.3 Machine Layout Development

#### 3.3.1 Integrated 3-Phase E-core Design

Figure 3.3(a) shows the baseline three phase C-core VHM. Three separate C-core units can be integrated together to make a common core 3-phase integrated model which increases the robustness and mechanical stability – Figure 3.3(b). After FEA simulation, magnetic flux distribution in Figure 3.3 (b) shows that the integrated common core design acts as two separate 3-phase E-core units with a very low mutual flux linking between them. As a result, they can be separated into two magnetically decoupled E-core units with no loss of performance. So, the integrated common core design is converted into two isolated sets of E-core models with a common translator –Figure 3.3 (c). Figure 3.4 (c) presents the contour plot of the isolated E-core model.

The advantage of isolating two E-cores is a reduction in stator mass by eliminating the interconnection iron which does not provide much of a useful flux path and isolating the two E-cores is also found to increase the back EMF of the machine [85]. Furthermore, as shown in Figure 3.4, the two sets of E-cores sitting beside each other are acting independently. Therefore,

instead of four E-cores, a single set of a top and a bottom E-core can be utilised with twice the axial length for similar machine performance.

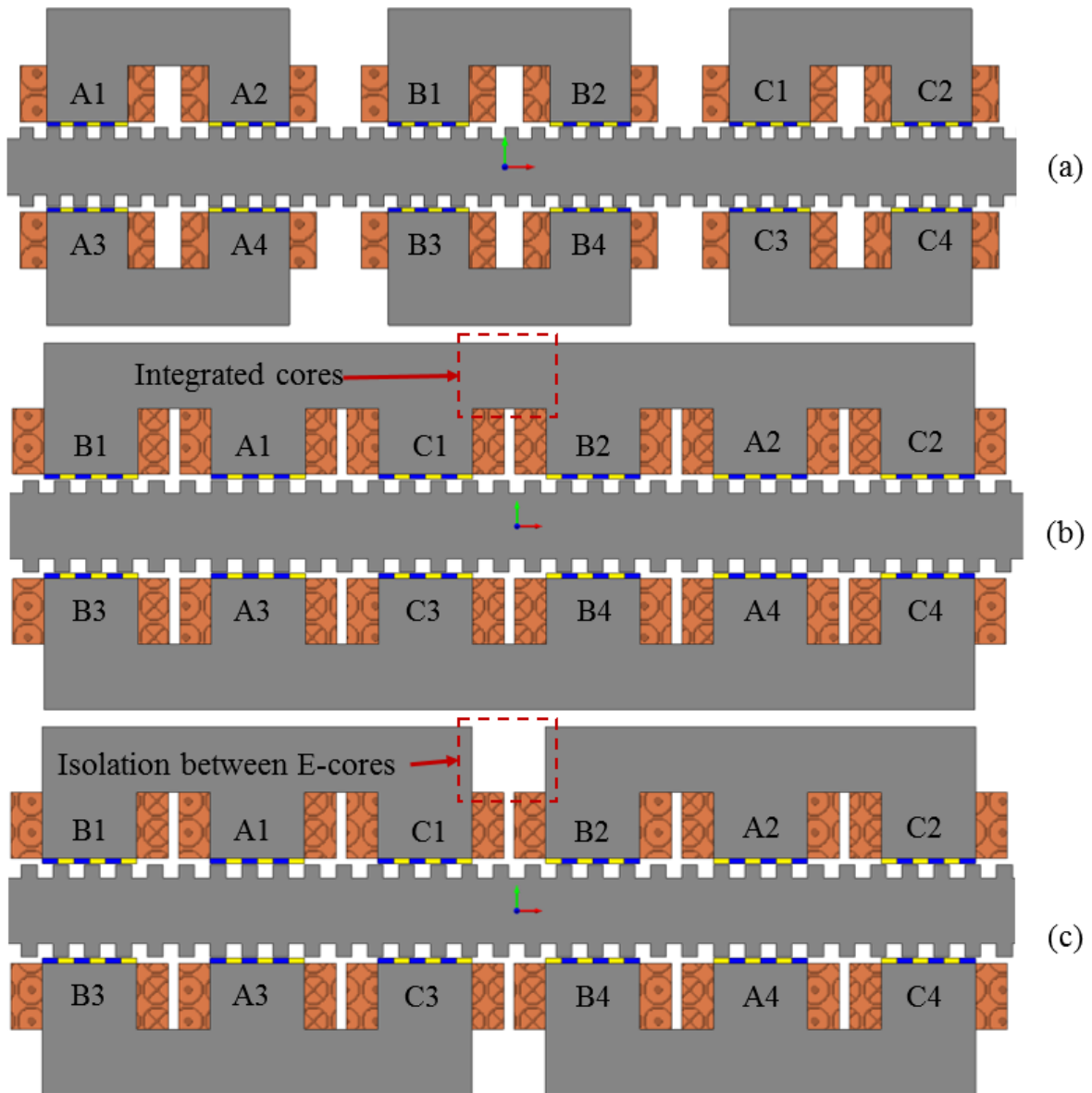


Figure 3. 3: Three phase VHM a) Initial C-core design b) Modified integrated core design c) Isolated E-core design

Although it doubles the stack length of each component, the active length and the number of components become halved which facilitates ease of the manufacturing and assembly processes. It also reduces the length of end windings, as it consists of only 6 coils instead of 12 for the four E-cores. However, this chapter analyses and optimise the 4 E-core modules to compare with the 6 C-core VHM. The next chapter will employ a single set of two E-core modules and discuss the manufacturing and assembly process of a new prototype VHM machine.

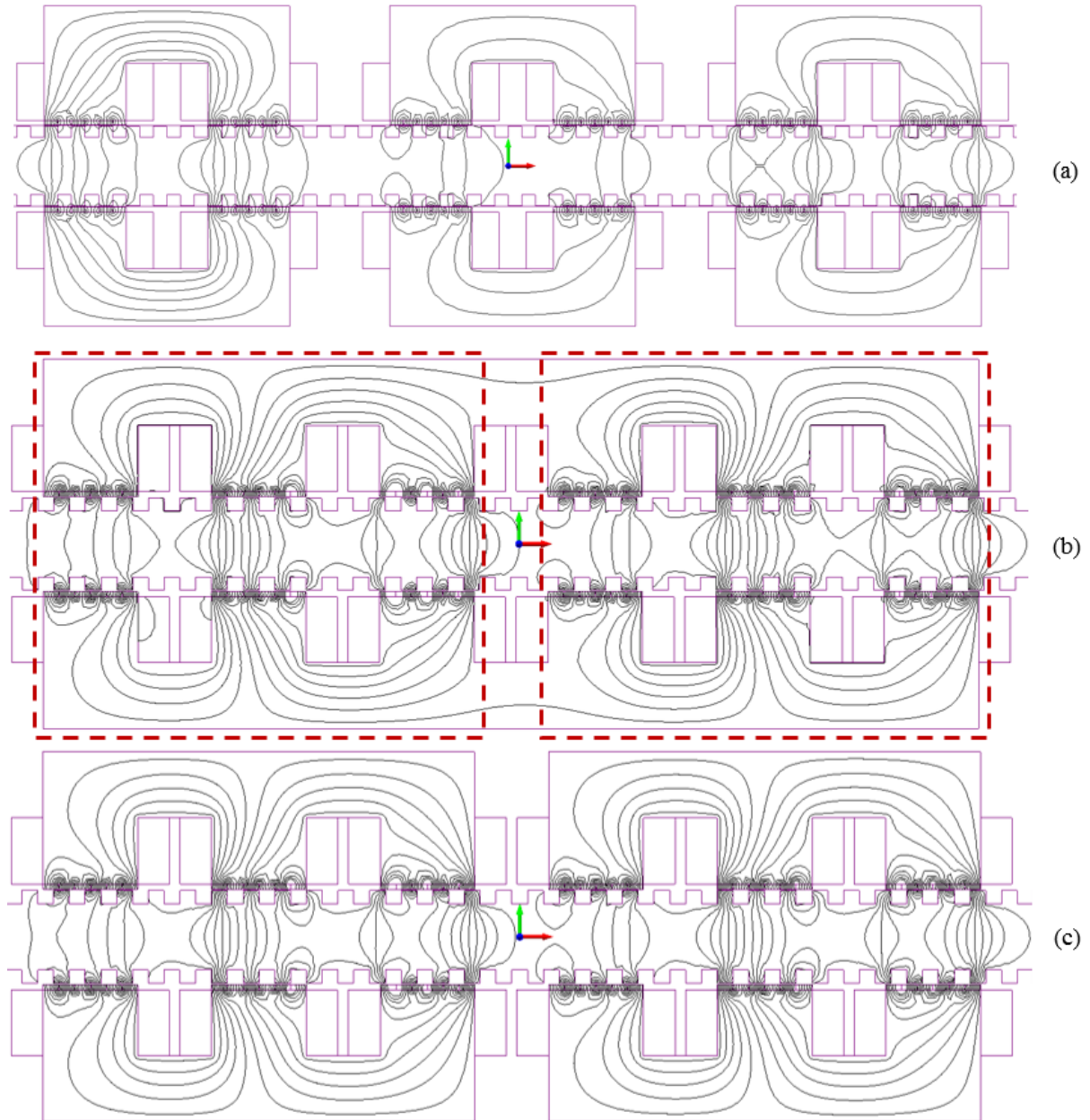


Figure 3. 4: Flux contour plot (a) baseline C-core model (b) integrated core model (c) isolated E-core model

### 3.4 Finite Element Analysis & Optimisation

Initial design dimensions and detail about the VHM mentioned in Table 3-1 are based on a simple flux path and theoretical analysis of the equivalent circuit [7]. Practically, there is a significant difference within the FEA results because of the fringing, leakage, and interference between adjacent magnets in the stator tooth. At the beginning of the design process, a simulation mesh refinement study has been done to find the suitable mesh size of the design parameters to get accurate results with the lowest possible simulation time. Figure 3.5 presents the refined 2D mesh for the E-core model.

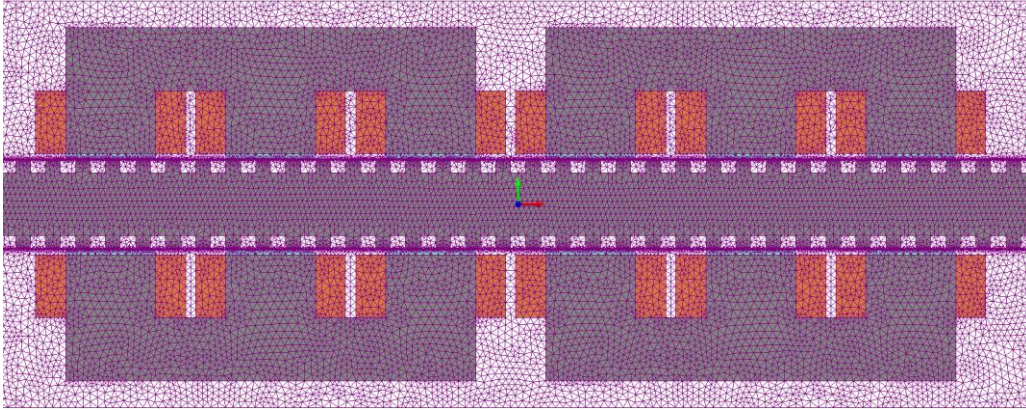


Figure 3. 5: Refined 2D mesh for the E-core model.

### 3.4.1 Magnet Height Optimisation

Magnet height has been analysed using FEA to provide optimal average thrust force and back EMF. It is shown in Figure 3.6 that a PM thickness of 2.5mm gives the best results in terms of back EMF and average force while keeping the magnet width constant at 12mm and maintaining a constant current density. Normally, force and back EMF is expected to increase with magnet thickness in conventional PM machines. In the E-core VHM machine, however, with opposite polarity adjacent magnetic poles, the ratio of magnetic flux leakage to active flux linkage becomes prevalent as magnet thickness increases further from 2.5mm. Thus, average force and back EMF start to reduce. Again, if the magnet thickness is reduced further down from 2.5mm, air-gap flux density becomes insufficient which causes EMF and force to reduce. Furthermore, thinner PMs are hard to handle, especially to assemble as they are prone to breaking and demagnetisation becomes an issue for thinner PMs.

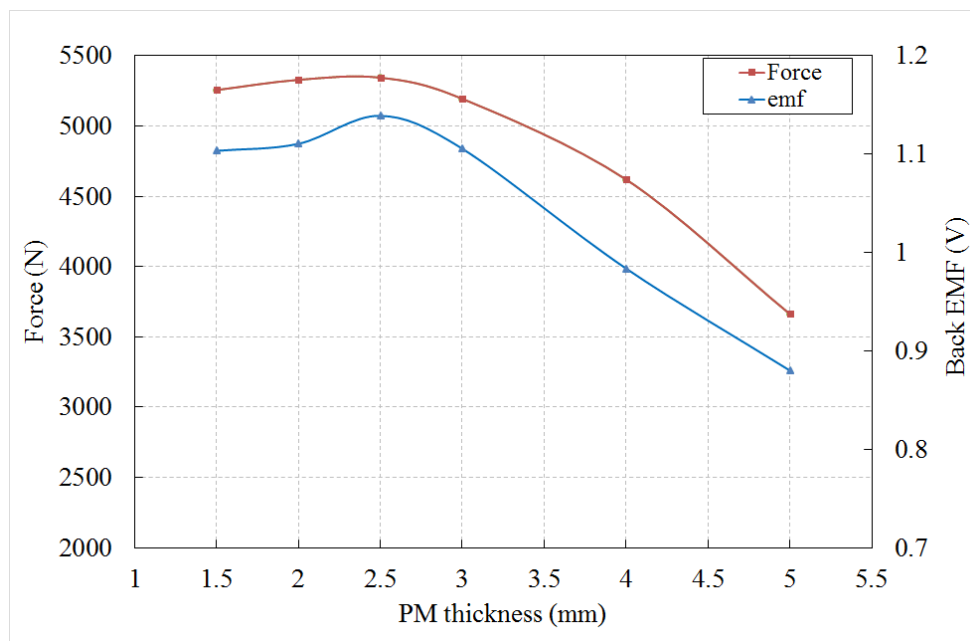


Figure 3. 6: Effect of magnet thickness on back-EMF and average force in the E-core VHM model

### 3.4.2 Translator Optimisation

Different combinations of translator tooth and slot width have been analysed whilst keeping the translator tooth pitch constant and equal to the stator pole pair pitch. Translator tooth pitch has also been varied whilst keeping the tooth and slot width equal. These two optimisation methods regarding the translator teeth, and another study regarding the translator core thickness have been investigated in this sub-section to improve the performance of the E-core model.

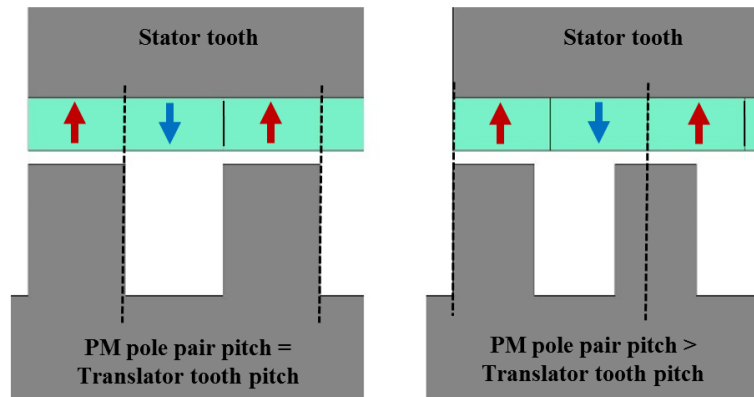


Figure 3. 7: Translator tooth and slot optimisation method

#### 3.4.2.1 Translator tooth pitch

In a *Vernier* machine, the translator tooth pitch and stator pole pair pitch should not be equal, so the alignment of magnets and teeth across the machine does not occur concurrently. As a result, cogging under each tooth is shifted a certain amount and thus resultant cogging of the machine reduced whilst not adversely affecting the performance of the machine.

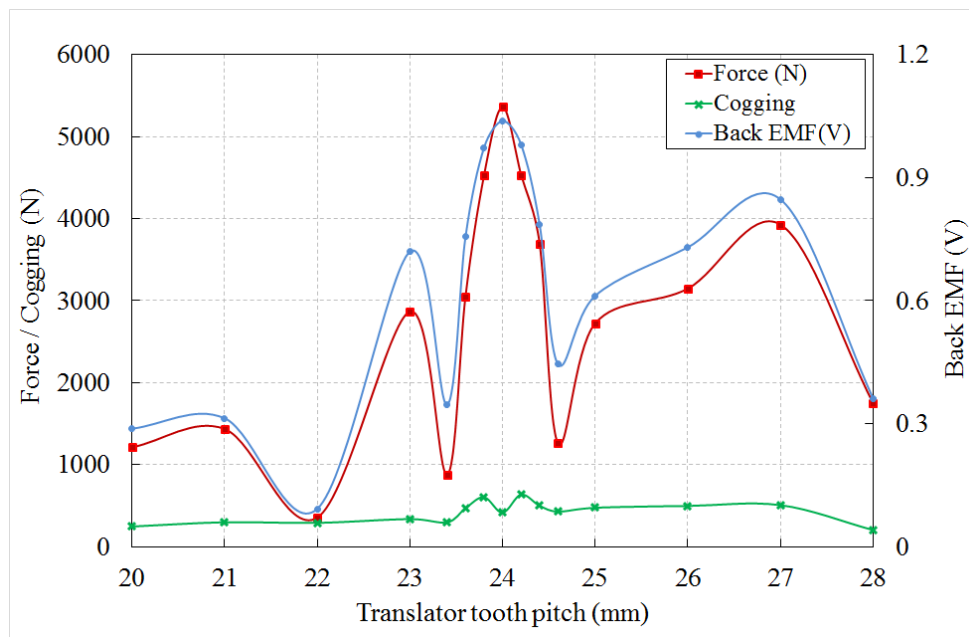


Figure 3. 8: Translator tooth pitch analysis with equal tooth and slot

'Vernier' action has been analysed in the E-core VHM by altering translator tooth pitch while maintaining constant stator pole pair pitch (Figure 3.7). After analysing the 'Vernier' action for varying translator tooth pitch, it is concluded that the 'Vernier' action is not an effective cogging reduction tool for the respective model as it degrades the performance of the machine by reducing the no-load Electro-Motive Force (EMF) and thrust force substantially. Figure 3.8 represents the analysis of cogging, back EMF and average force by varying the translator tooth pitch for a constant stator pole pitch of 24mm. During this analysis, the translator tooth and slot width were kept equal while varying the translator tooth pitch. The concurrent un-alignment between stator magnet poles and translator teeth due to the Vernier action causes the leakage flux between adjacent magnet poles to be increased and thus degrades the active flux. It is clearly seen that a translator tooth pitch equal to the stator pole pair pitch produces the best performance in terms of force and back EMF while maintaining a reasonable cogging force.

### 3.4.2.2 Translator tooth width

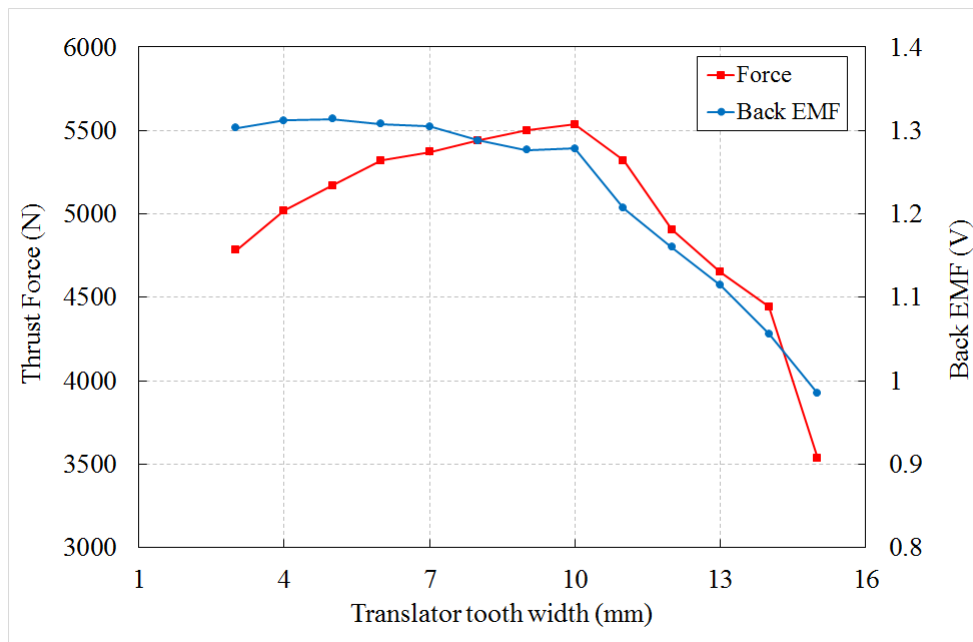


Figure 3. 9: Translator tooth width analysis of the VHM with constant translator pitch

An alternative method of investigating the effect of translator teeth and slot width is performed by fixing the translator tooth pitch to the optimised constant value whilst changing the tooth and slot widths. Translator tooth pitch has been fixed at 24mm after the analysis in the previous subsection and translator tooth and slot width was varied to analyse the back EMF and force of the machine, which is presented in Figure 3.8. It has been found that the 10mm tooth / 14mm slot provides convincing results with a high force and back EMF. The percentage increase in the back EMF is very low (0.9%) at 5mm tooth compared to 10mm tooth, while as the translator

teeth become thinner than 10mm, the average thrust force reduces due to saturation at rated current. Therefore, 10mm tooth / 14mm slot has been chosen for further machine design analysis and optimisation.

### 3.4.2.3 Translator core

In this VHM configuration, almost all the useful flux travels straight through the translator tooth from the top to the bottom stator, as shown in Figure 3.4. There is no useful flux traveling through the translator core back except for some leakage flux. The translator can hence be optimised for the core-back thickness to obtain optimal performance.

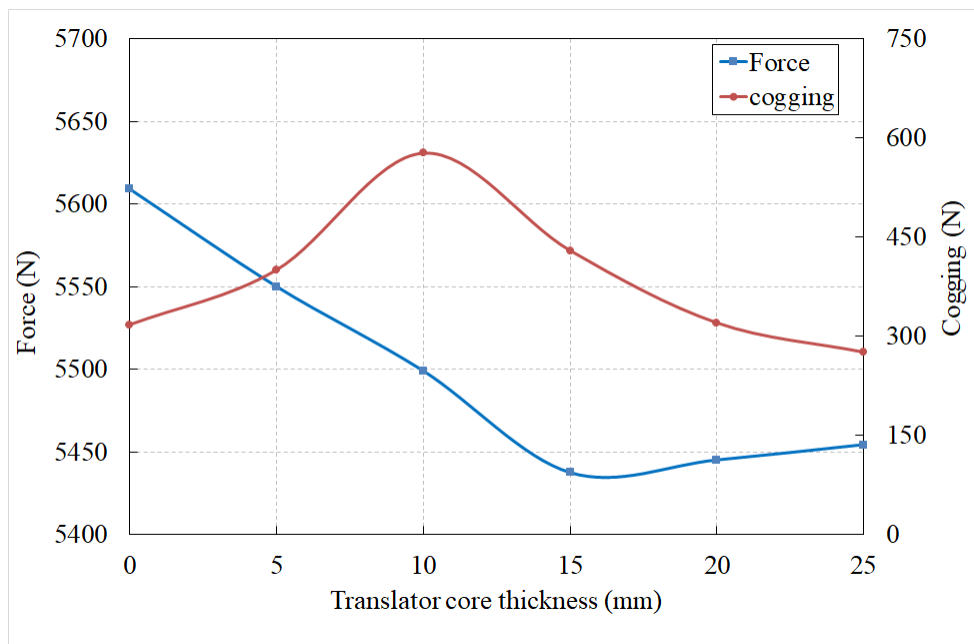


Figure 3.10: Translator core thickness optimisation in terms of average force and cogging

Figure 3.10 shows the response of average force and cogging for different translator core thickness. It indicates that the peak average force can be achieved when there is no core back on the translator (segmented translator teeth) and the average force decreases linearly by only 2% afterward by increasing the core back thickness to 15mm. The cogging is also increased until 10mm and then decreases afterward.

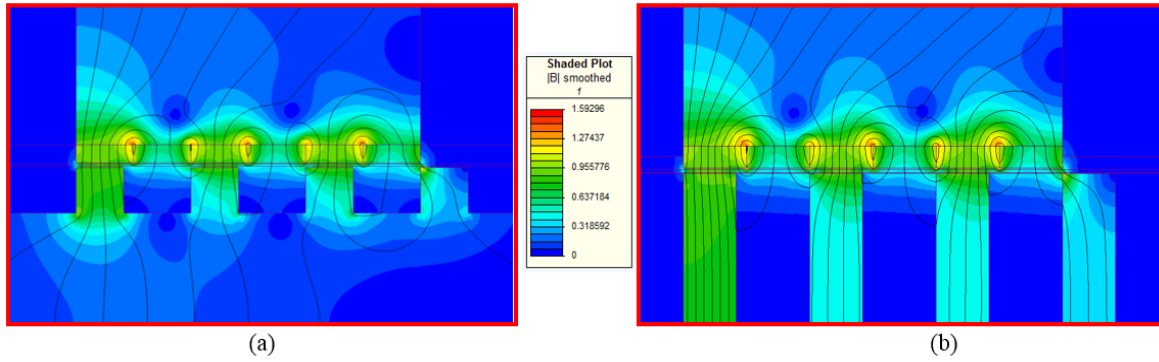


Figure 3.11: Flux density plot under phase-A a) translator with core back b) segmented translator

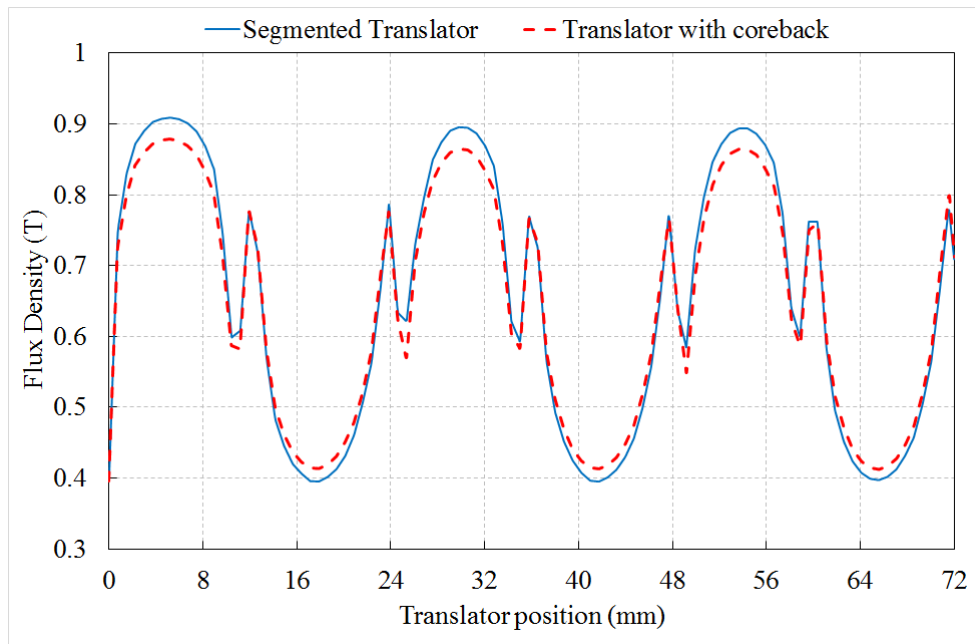


Figure 3.12: Flux density comparison of the E-core VHM between the cored and coreless translator

Figure 3.11 presents the no-load air-gap flux density contour distribution of E-core VHM with and without translator core back. Figure 3.12 compares the flux density in the air-gap between the cored and coreless translator model. It can be clearly seen that the flux density for the segmented translator model provides higher air-gap flux density and thus higher force at the constant current density. The increase of the flux density is caused by the flux concentration on the translator segments and further reduction of the leakage flux path between PM poles, adjacent translator teeth and the translator core back.

Figure 3.13 presents the E-core VHM after the development of segmented teeth without a translator core in the middle. Figure 3.14 illustrates FEA contour plots of no-load flux in the d-axis position for the E-core VHM model with a coreless translator. With no core back, individual translator teeth are independent components that would need to be mounted in a non-magnetic structure. This isolated segmented translator has a much-reduced active mass (30%), can guide the magnetic flux and improve effective electromagnetic flux distribution.

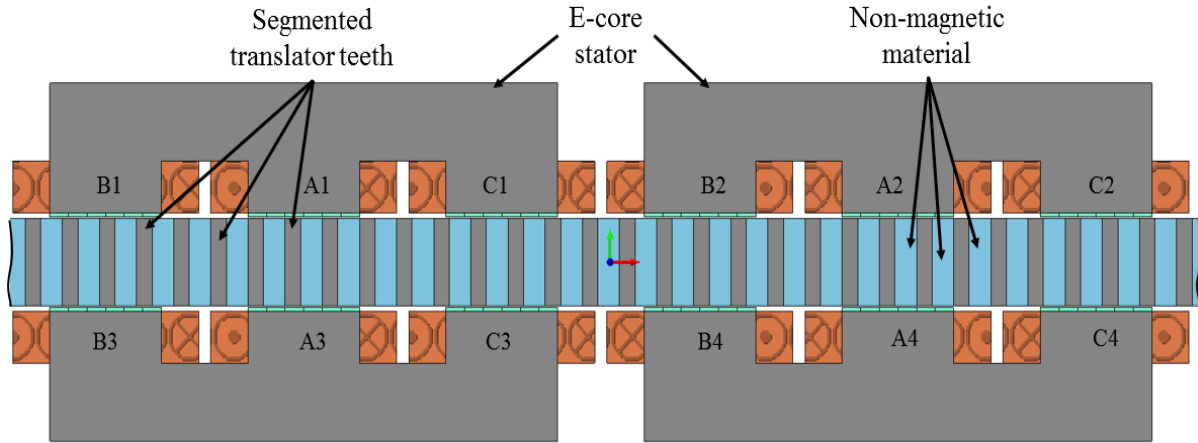


Figure 3.13: E-core VHM model with a segmented translator.

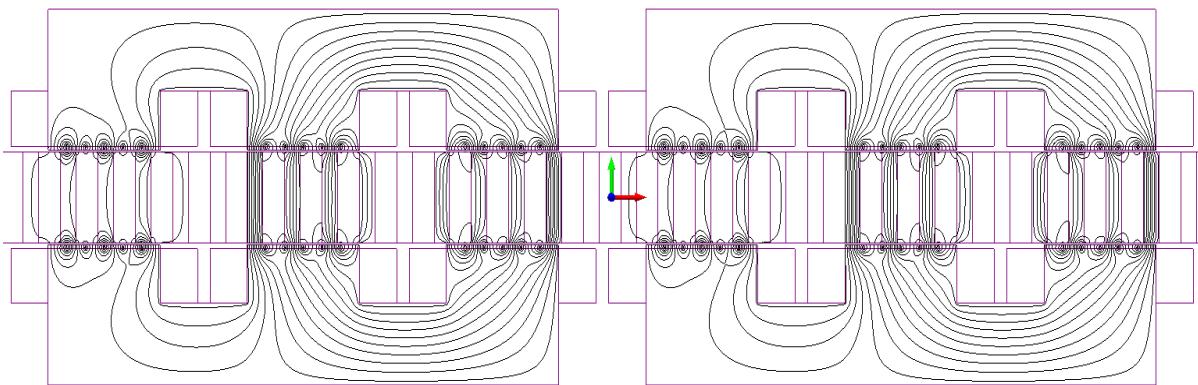


Figure 3.14: No load flux contour plot for the E-core VHM model with the segmented translator

### 3.4.3 Cogging Reduction by Harmonic Analysis

Higher order harmonics are unwanted in the machine outputs as they deteriorate the performance of the machine. In [86], the dislocation of PM pole by pole shifting method to reduce  $N^{\text{th}}$  order harmonic has been discussed. It is proved that a specific order harmonic can be reduced by shifting top and bottom stators with respect to each other by the following amount,

$$D_p = \frac{\tau_p}{2N} \quad (3-7)$$

Where,

$D_p$  = shift between stator teeth under the same phase.

$\tau_p$  = translator tooth pitch.

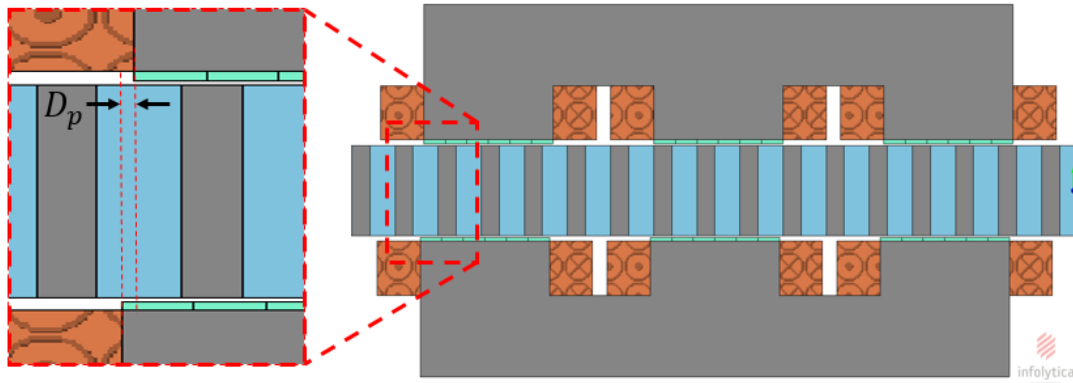


Figure 3.15: Lower stator shifted model to reduce cogging.

Figure 3.15 shows the E-core model with the shifted lower stator. Figure 3.16 represents the harmonic analysis of the optimised E-core VHM model for shifted and non-shifted lower stators. For the aligned lower and upper stator model, the 6<sup>th</sup> order harmonic is the dominant order harmonic and causes a high cogging ripple. It can be seen that shifting the lower stator by 2mm, as calculated from equation (3-7), the 6<sup>th</sup> order harmonic is substantially reduced.

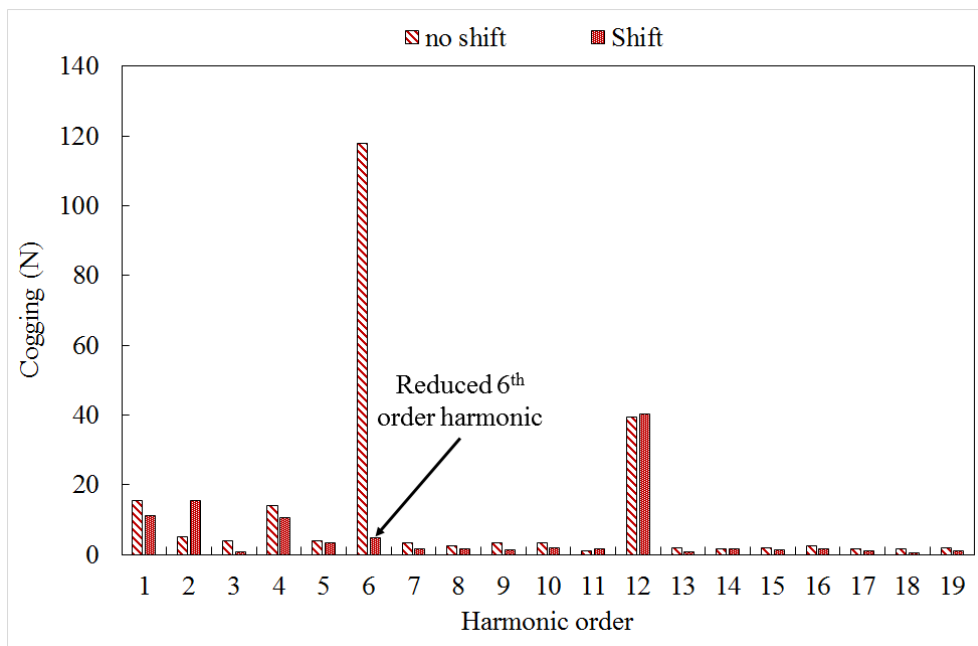


Figure 3.16: Harmonic analysis of cogging force between shifted and non-shifted lower stator model.

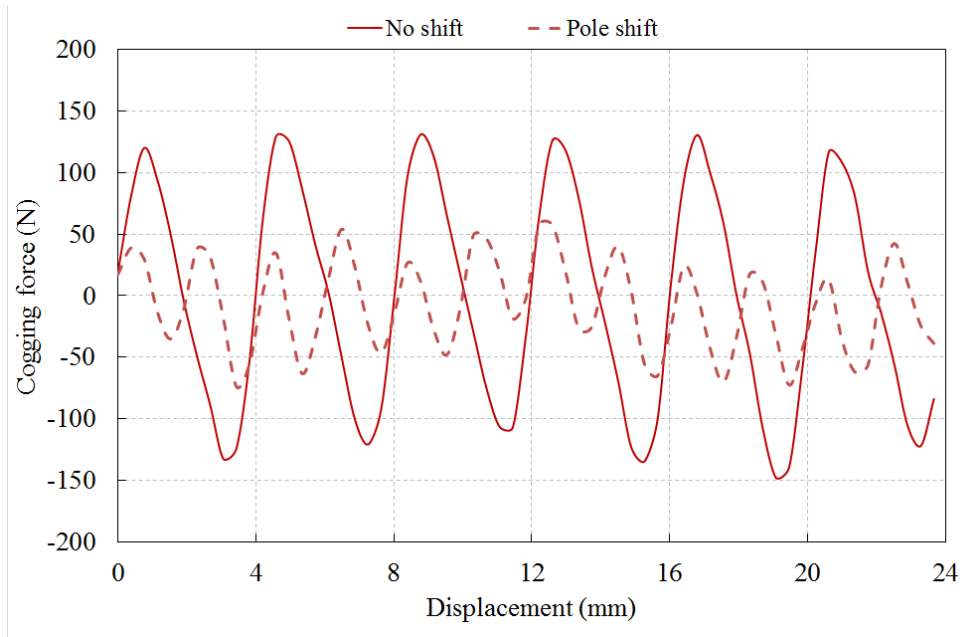


Figure 3. 17: Cogging reduction by implementing lower stator pole shifting

Figure 3.17 displays the comparison of the cogging forces between the E-core models with shifted and non-shifted lower stators. It is observed from the figure that the cogging has substantially reduced by almost 58% for the shifted model compared to the non-shifted model.

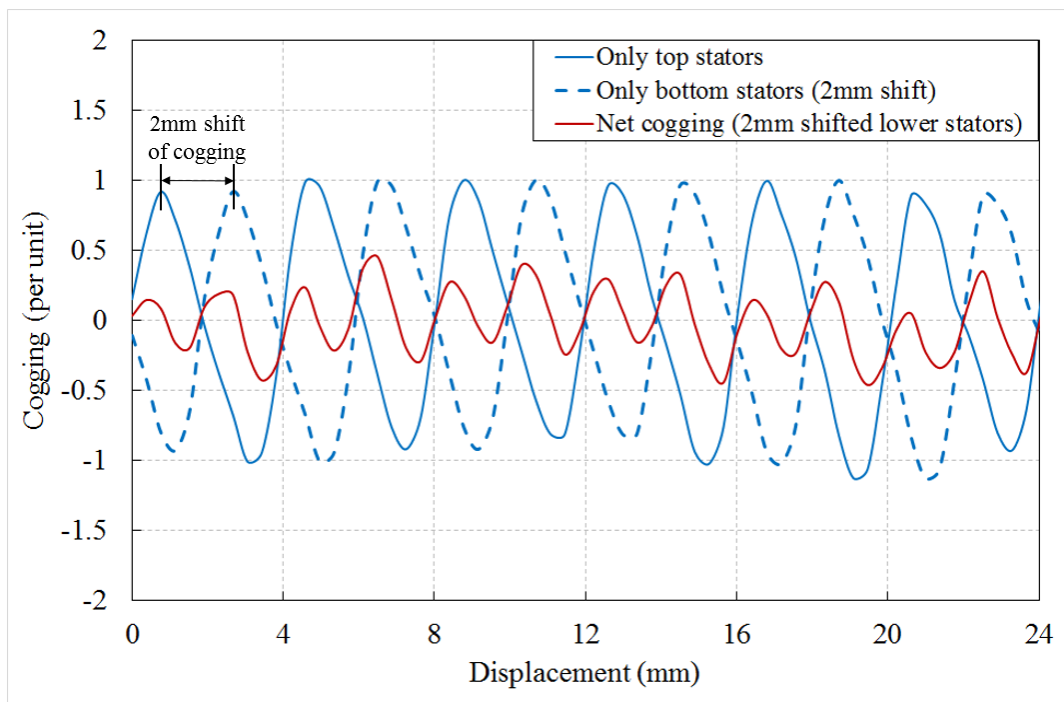


Figure 3. 18: Cogging reduction technique by shifting lower stators.

Figure 3.18 can further explain the cogging reduction by pole shifting. For the cogging with a dominant 6<sup>th</sup> order harmonic, each cycle is repeated every 1/6<sup>th</sup> of the electrical cycle, which is equivalent to 4mm displacement in this model. So, by shifting the lower stators and poles by 2mm with respect to the top stators will cause the cogging produced by the bottom stators to be

opposing top stators' (Figure 3.17). The net result is a substantial reduction in overall cogging as top and bottom stator cogging almost canceling each other.

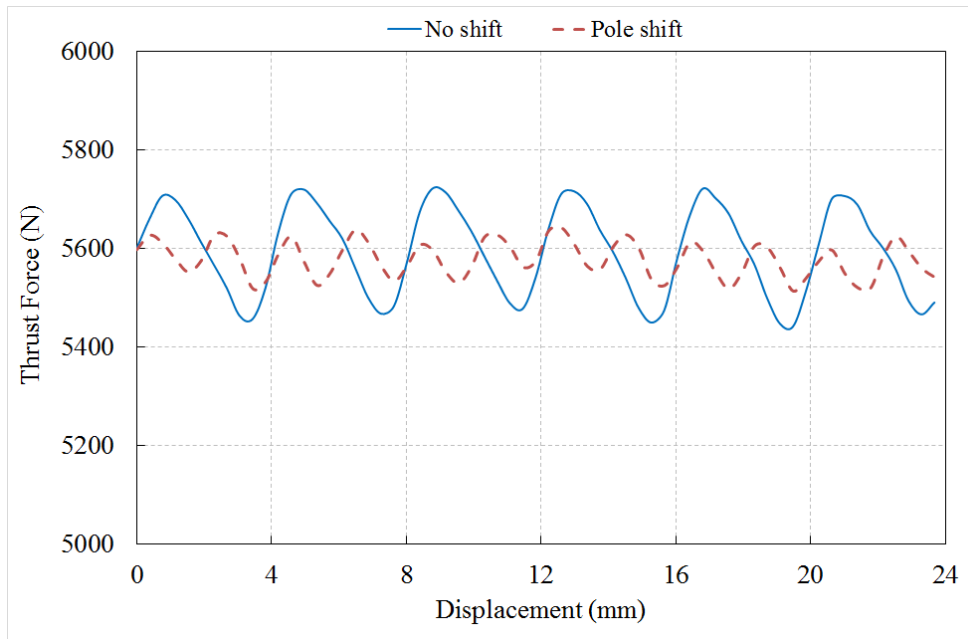


Figure 3. 19: Thrust force comparison between shifted and non-shifted lower stator.

Figure 3.19 shows the comparison of the thrust force between the shifted and non-shifted stator pole E-core models. It can be seen that the average force only drops by 0.2% while the force ripple reduced by almost 54%. Therefore, by utilising the pole shifting method, the cogging and force ripple can be substantially reduced without degrading the average force performance of the machine.

### 3.5 Final Design Analysis and Comparison

#### 3.5.1 No Load Flux Linkage

Figure 3.20 presents the three-phase no load flux linkage per turn for a C-core baseline and segmented translator E-core VHM model over an electrical cycle. It can be clearly seen that the flux linkage is almost 25% higher in the optimised E-core model. This high flux linkage caused by the reduction in the leakage flux and an increase of the active flux linkage via PM and translator optimisation.

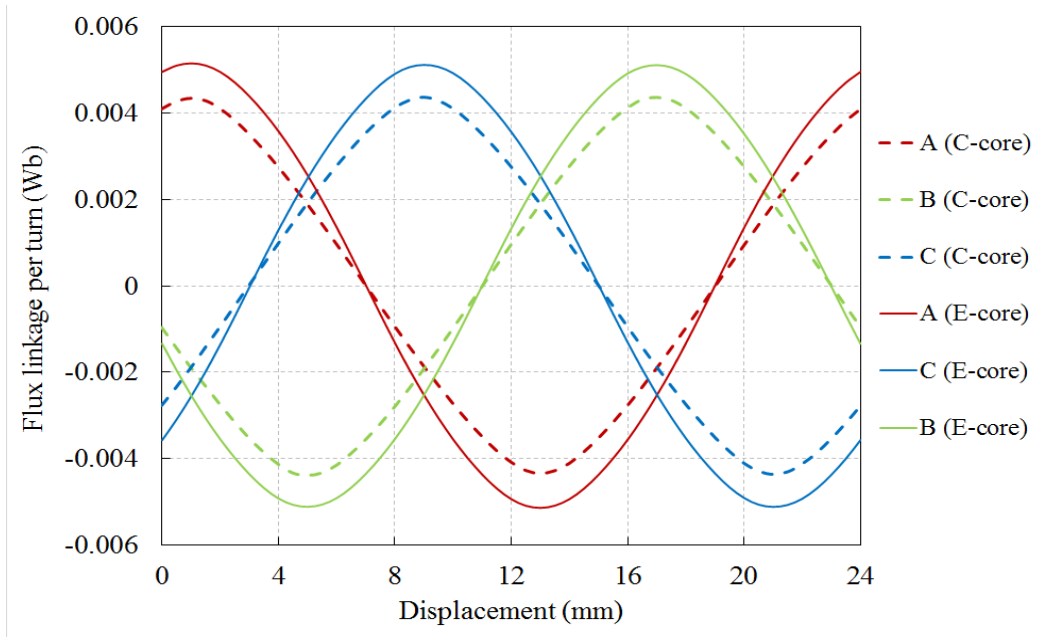


Figure 3. 20: No load flux linkage comparison between C-core baseline model and the optimised E-core model with the segmented translator over an electrical cycle.

### 3.5.2 Back EMF

The FEA simulation of back EMF per turn for both C-core and E-core models at a constant speed of 1.2 m/s are compared in Figure 3.21. As the E-core VHM has reduced the leakage flux and increased the active flux, the achieved back EMF is increased by almost 30% compared to the baseline model. It is also important to notice that the three-phase back EMFs of both models are symmetrical and shifted by 120° from each other.

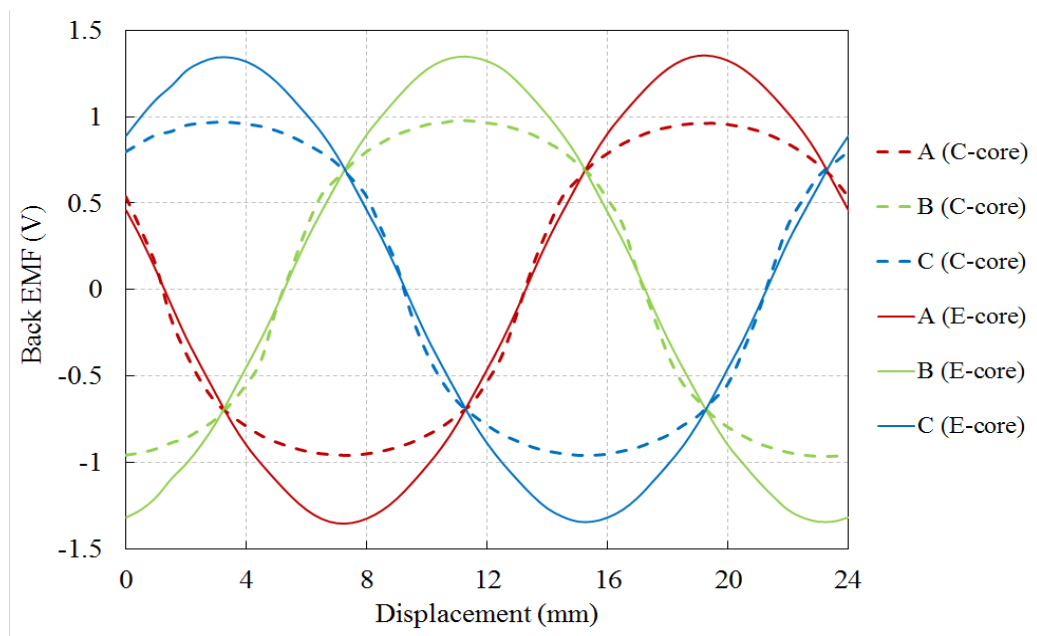


Figure 3. 21: Back-EMF comparison between C-core baseline model and the optimised E-core model over an electrical cycle.

### 3.5.3 Thrust Force

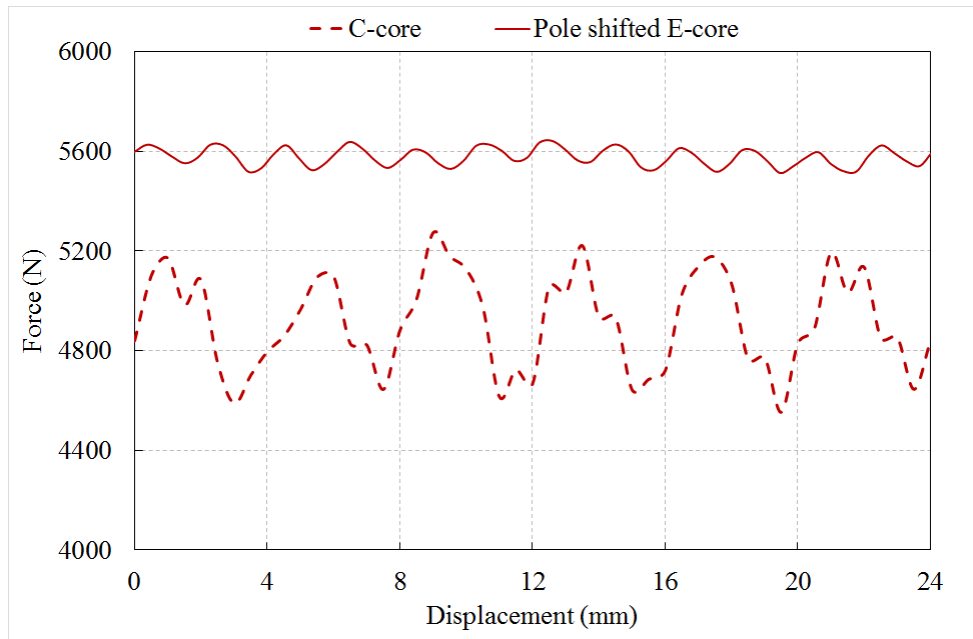


Figure 3. 22: Average thrust force comparison between C-core baseline and improved the E-core VHM models over an electrical cycle.

The machine Thrust force comparison graph in Figure 3.22 clearly shows the performance comparison between C-core and E-core models with the same rated MMF of 3000A-turns. The average thrust force of the optimised E-core machine is improved by approximately 15% compared to the C-core baseline model due to the optimum dimensioned magnet poles and segmented translator modeling. The E-core model also provides a reduction in force ripple of up to 82% by implementing a segmented translator and pole shifted lower stators. The power factor of the optimised E-core design is also improved due to the reduction of PM leakage and improve in back EMF.

Table 3- 2: Comparison of machine performance between baseline C-core and pole shifted E-core model.

Parameters	C-core VHM	Pole shifted E-core VHM
Machine axial length (mm)	100	100
Magnet poles thickness (mm)	4	2.5
Average Force (kN)	4.9	5.6
% Force ripple	14.5	2.5
Cogging (N)	312	130
Peak Back EMF / turns (V)	1	1.34
Magnet mass (Kg)	2.55	1.6
Stator mass (Kg)	82.7	68.3
Translator mass (Kg)	44	12.5

Force density (kN/m <sup>3</sup> )	230	335
Shear stress (kN/m <sup>2</sup> )	85	97.2
Power Factor	0.22	0.31

After a full investigation of the design parameters, stator teeth, translator teeth, slots, combining 3 phases within a new E-core model and introducing segmented translator teeth structure, Table 3.2 derives the key machine parameters and performance comparison between the initial C-core VHM and E-core VHM. The optimised E-core VHM presents a superior electromagnetic performance in terms of active machine mass, thrust force and back EMF with the minimum cogging force.

### 3.6 Conclusion

In this chapter, an E-core VHM has been developed from the baseline C-core VHM. A new type of segmented translator has also been introduced and analysed in FEA regarding the magnetic flux path for optimal performance. Introducing segmented translator teeth also ensures the maximum useful flux carrying capability. Electromagnetic and electrical performance comparison between baseline and E-core VHM shows that the leakage magnetic flux has been greatly reduced by using optimised magnet dimensions in the E-core model. Cogging is minimised to almost 58% of its initial value by implementing the pole shifting method. Magnet mass and translator mass are also greatly reduced in the improved E-core design, compared to the baseline. The final design is shown to deliver a 15% higher force and use 38% less PM material, and have an active mass of 78% compared to the baseline machine. It is also proved to possess improved performance and reduced mass. Finite Element Analysis (FEA) shows, it has the merit of rigid and compact stator design with a higher force and power density in terms of machine and magnet volume, while maintaining very low cogging force and force ripple over the existing model.

## Chapter 4: Linear Halbach Consequent Pole Vernier Hybrid Machine

### 4.1 Introduction

In this chapter, a linear Vernier Hybrid Machine (VHM) combining Halbach PM array and Consequent Pole topologies is introduced, developed and analysed. The Halbach Consequent Pole Vernier Hybrid Machine (HCVHM) employs Consequent Poles separating arrays of Halbach magnets. Halbach PM array has the property of producing high air-gap flux density by shaping and concentrating the magnetic field into the targeted iron part, and the Consequent Pole can reduce the fringing flux that ultimately reduces the leakage flux [87]. Therefore, a significant improvement of the air-gap flux density and hence the power factor can be achieved by combining both properties [88, 89]. The electromagnetic performance of the machine is simulated under given operating conditions. PM array development and optimisation of other structural parameters of the proposed HCVHM are analysed in this chapter for maximum thrust force. A segmented translator structure is adopted which at the same time reduces the translator mass and improves the force density of the machine. It is shown that the proposed machine has the potential to offer improved force density, lighter translator and better PM utilisation than the surface mounted variant presented in the previous chapter.

This chapter is divided into three parts: machine development and analysis; final design and prototype construction; testing and validation. Finite Element Analysis (FEA) has been performed to investigate the effect of different machine parameters and optimise machine performance. Finally, a prototype of the proposed machine has been built and tested under different operating conditions to validate the experimental results with the predicted performance. Important machine parameters and specifications are presented in Table 4-1.

*Table 4- 1: Main machine parameters and specifications*

<b>Parameters</b>	<b>Value</b>
Number of stator teeth	6
Number of phases	3
Pole pairs per stator tooth	3
Air gap length	1mm
Translator speed	1.2m/s
Current density	3.5A/mm <sup>2</sup>
Power Factor (PF)	>0.5

### 4.2 Halbach Consequent Pole Vernier Hybrid Machine (HCVHM)

Figure 4.1 presents the double-sided HCVHM, which consists of a combination of Consequent Pole and Halbach PM array to utilise the magnet poles efficiently, thus reducing the leakage and fringing flux. The E-core stator structure, which has been developed in the previous chapter, is used for the HCVHM. The proposed machine consists of three phase windings that each produce a two-pole magnetic field. Due to the slotted structure, these magnetic fields are modulated by the translator teeth.

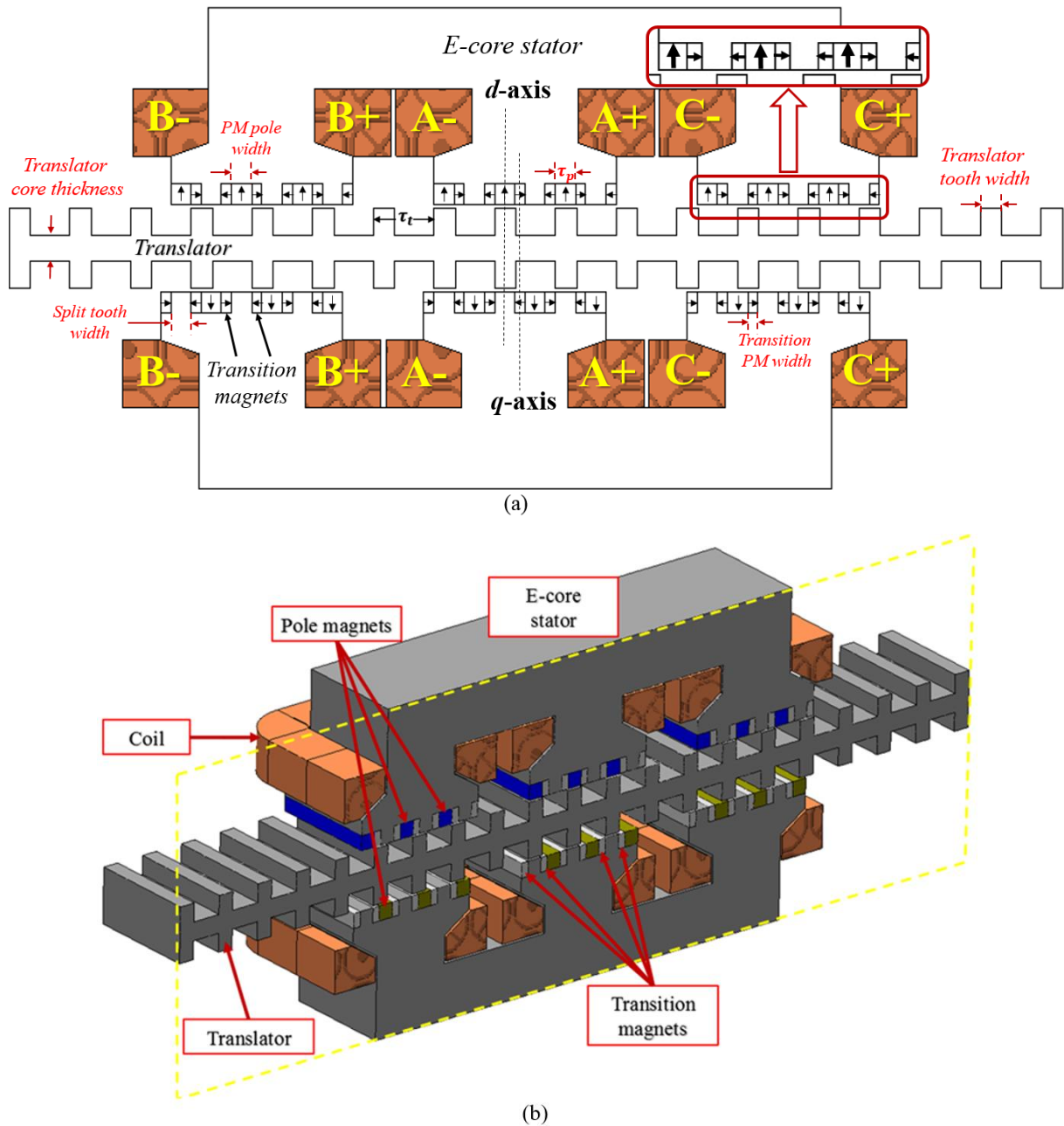


Figure 4. 1: Proposed HCVHM with magnet orientation and three phase windings (a) 2D (b) 3D cross section

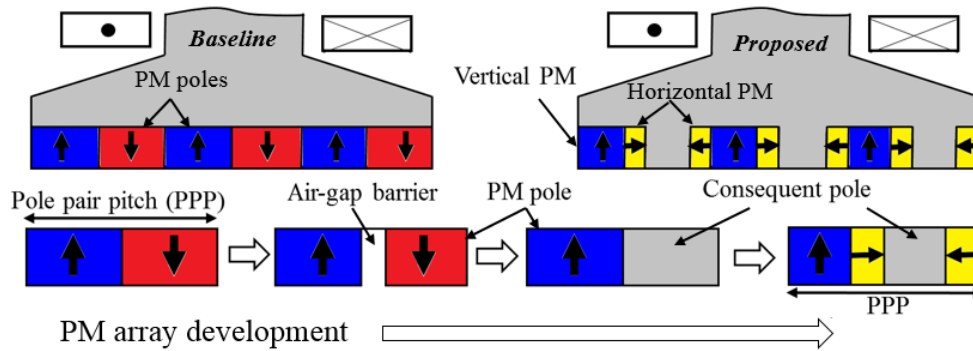


Figure 4. 2: Schematics of PM array development of proposed HCVHM machine from baseline VHM.

Figure 4.2 represents the development of PM array of the HCVHM model. One PM array has three magnets with different magnetisation directions and a ferromagnetic pole piece (split tooth). Each magnet pole consists of a surface mounted vertically magnetized (towards stator iron core) PM *pole* and two oppositely directed horizontal magnets (*transition PMs*) that sandwich the split tooth. In the double-sided model, the vertical PM *pole* of the top stator aligns with the split tooth of the bottom stator and vice versa to align the magnetic flux from the vertical PM pole to the split tooth. Therefore, it is noticeable from Figure 4.1(a) that the bottom stator is offset left by the distance of one *transition PM* width. Magnetic flux path will be shown in the coming section for better understanding about this offset.

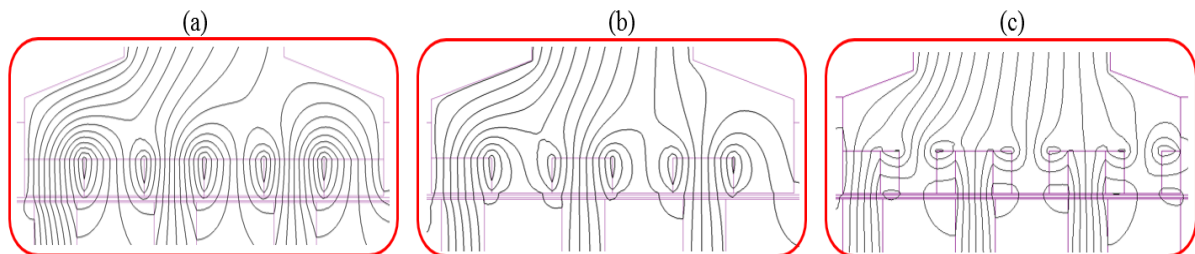


Figure 4. 3: Magnetic flux contour under stator pole a) VHM b) Consequent Pole VHM c) HCVHM topology

#### 4.2.1 Motivation for the New Machine Topology

The improved E-core VHM topology developed in the previous chapter works well, although inspection of the flux contours generated by FEA still shows significant flux leakage between poles as they are magnetising in the opposite direction. Those oppositely magnetised poles and translator teeth are connected via a low reluctance iron stator path and high reluctance air gaps. As Figure 4.3 (a) shows, some magnet pairs contribute almost zero to the main flux as almost all the flux leaks through the air gap and does not contribute to the active machine force.

Figure 4.3 (b) shows the flux path for the Consequent Pole topology which provides less leakage path by substituting the opposing PM with soft magnetic poles (teeth) [90-92]. The stator of this configuration consists of inset rectangular magnets magnetized in a common direction and

separated by soft magnetic poles. Whilst magnet saving can be realised, these consequent pole machines still suffer from magnetic flux leakage [93].

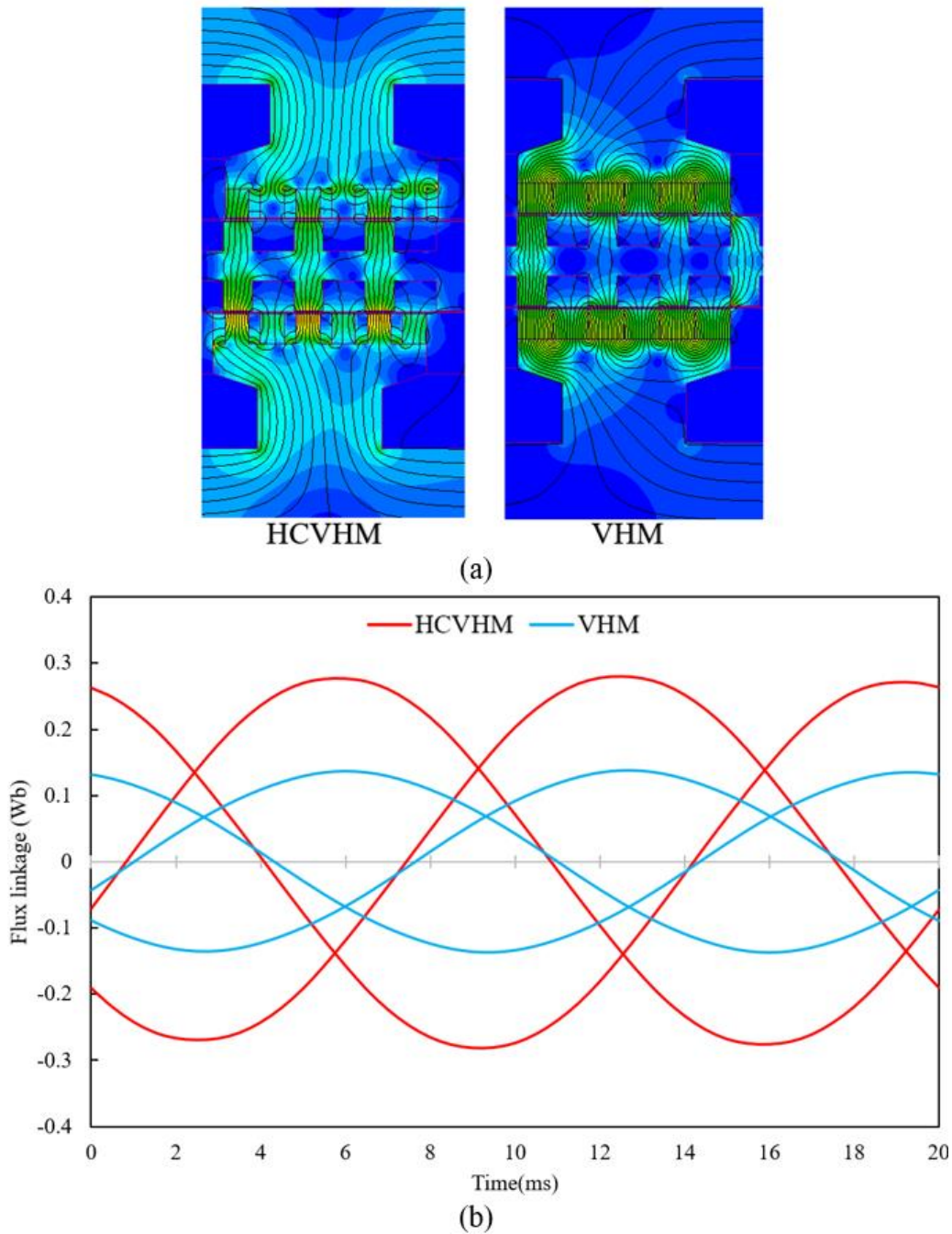


Figure 4. 4: a) flux contour of the HCVHM and VHM machine b) flux linkage variation between HCVHM and VHM.

To further reduce the leakage between the adjacent magnet pole and Consequent Pole, and to increase the reluctance path between them, the new topology of HCVHM model has been developed. Both vertically and horizontal PMs contribute to the magnetic flux, while the horizontal transition magnets serve an additional purpose to reduce the fringing leakage flux as

compared to the Consequent Pole counterpart [94]. As shown the proposed HCVHM in Figure 4.3(c), the *transition* PMs guide the flux to the split teeth and reduce the leakage flux around the edges of PMs by acting as an affective reluctance barrier, leading to a significant improvement of the air-gap flux density and hence the force density. Figure 4.4 presents the flux contour and the flux linkage variation between the HCVHM and the VHM. The HCVHM has almost double the flux linkage compared to the VHM due to the aforementioned reasons.

Mass of the translator of the linear Vernier machines for long stroke WEC application is of great importance. If all the active flux needs to pass through the translator core, the core needs to be thick enough to accommodate the flux at the rated current [7]. This makes the overall machine heavier and limited to a small current density. Therefore, optimisation of the translator structure and active flux path for a lighter machine are also considered in the proposed HCVHM.

#### ***4.2.2 Operation Principles***

Figure 4.5 demonstrates the operation principle of the proposed machine in four translator positions in terms of phase-A (middle phase). Figure 4.5(a) represents the positive maximum flux linkage (d-axis) in phase-A, where the translator teeth are aligned with the PM *poles* of the top stator and split teeth of the bottom stator. Flux linkage of phase-A becomes zero when the translator moves a quarter of its pitch (q-axis), as shown in Figure 4.5(b). The back EMF in any coil is the rate of change of flux linkage and this position (b) will give a negative maximum back EMF in the phase winding as the flux linkage goes down from maximum to zero.

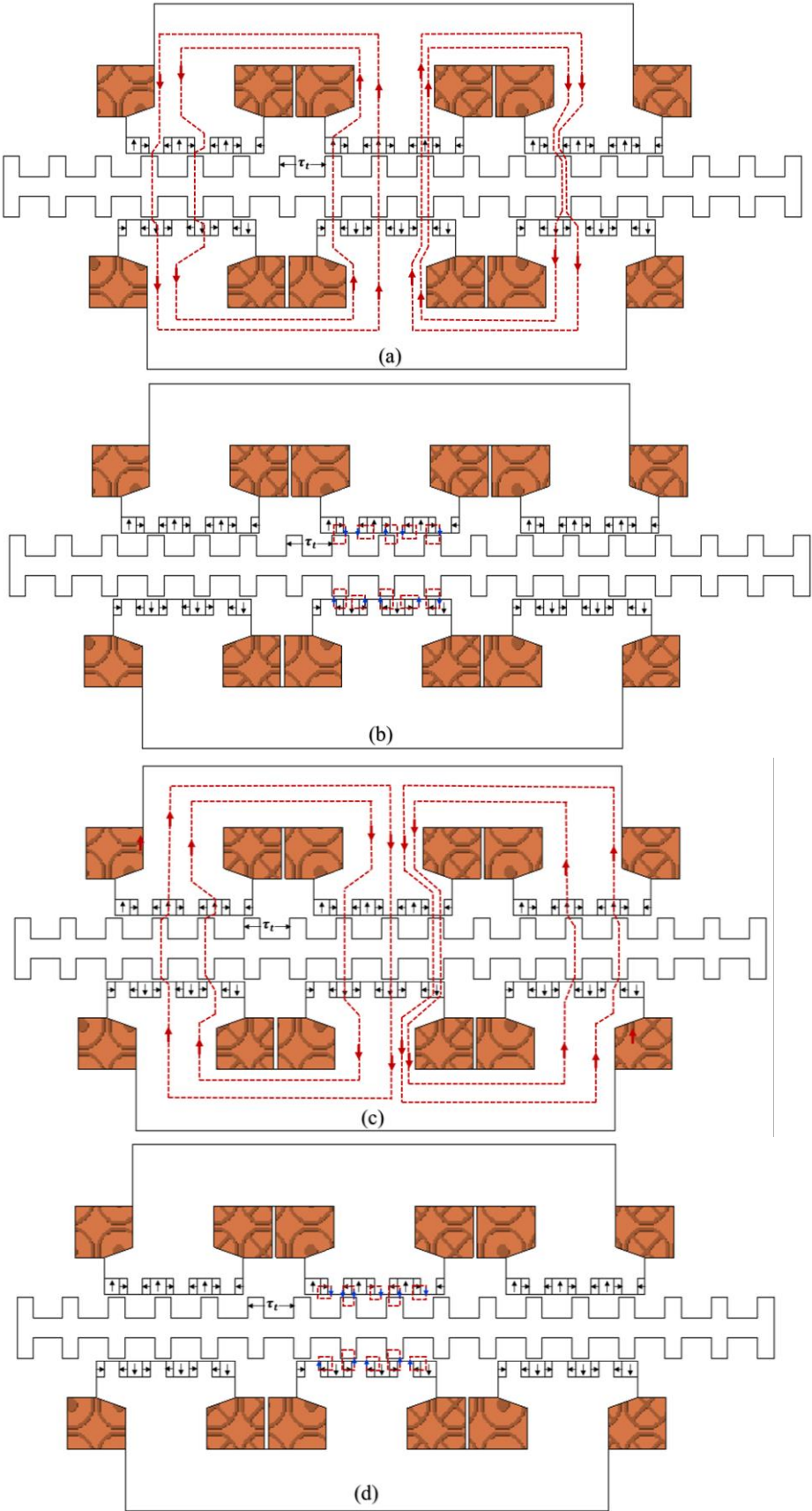


Figure 4. 5: Operation principle at different translator positions (a) Position '0' or '1' (b) Position '1/4' (c) Position '1/2' (d) Position '3/4'.

Figure 4.5(c) shows a relative displacement of half of the translator pitch from the initial position. This time, translator teeth under phase-A are aligned with split teeth of the top stator and vertical PM *poles* of the bottom stator and thus produce a negative maximum flux linkage and zero phase back EMF. The three-quarter of the translator pitch relative to the starting point shown in Figure 4.5(d). This position is identical with the position (b) when the flux linkage becomes minimum while the back EMF of phase A becomes positive maximum.

To further understand the flux distribution of the machine, the flux from *transition* magnets allow the flux to be concentrated in the iron split tooth and add up with the PM poles flux, resulting in a greater flux per pole. The vertically magnetized PM poles produce the main flux, while the horizontally magnetised *transition* magnets reduce the leakage flux around the edges of PM. The peak force is produced when the translator teeth are aligned with the *transition* magnets along the q-axis of the machine.

### 4.3 Finite Element Analysis & Optimisation

Finite Element Analysis has been performed to analyse the electromagnetic flux in the machine. Figure 4.6 presents the no-load flux linkage and back EMF from the top (A1) and bottom (A2) coils of the phase-A. Flux linkage of the upper coil is slightly higher in the positive axis than the bottom coil, while the bottom coil has a higher negative flux component for the second half. This is because of the alignment of translator teeth with the vertical *pole* magnet links slightly more flux in the respective coil than the alignment with ferromagnetic teeth. Figure 4.7 presents the magnetic flux path through the segmented translator which was described earlier in the previous chapter. The segmented translator optimisation and the half-circle extension on both sides of each translator segment developed for assembly purposes will be described later in this chapter. Figure 4.7(a) shows the segmented translator teeth aligned with vertical magnets of the top stator and ferromagnetic teeth of the bottom stator. It is clear to notice that the top stator has slightly lower flux leakage than the bottom stator and thus higher active flux linkage. On the other hand, Figure 4.7(b) shows the bottom *pole* magnets are aligned with the translator teeth during the second half cycle. This time bottom coils link more active flux compared to the top stator due to the same reason and thus have higher negative flux linkage compared to a top coil. The back EMF - the rate of change of flux linkage ( $d\psi/dt$ ) remains almost the same for both stator coils as both top and bottom coils under the same phase have a similar rate of change of flux linkage.

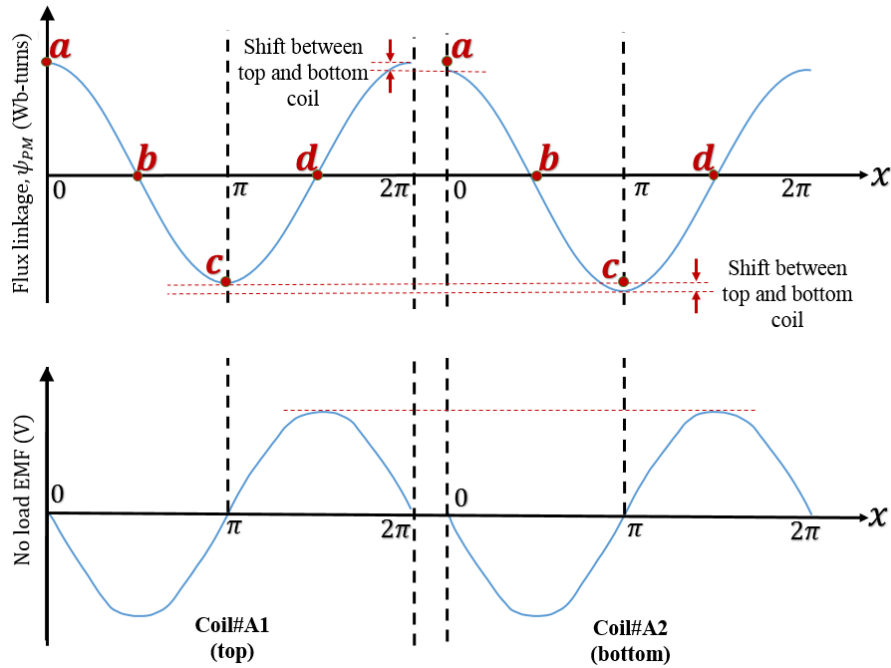


Figure 4. 6: Single phase no-load flux linkage and back EMF of the top and bottom stator coils under the same phase.

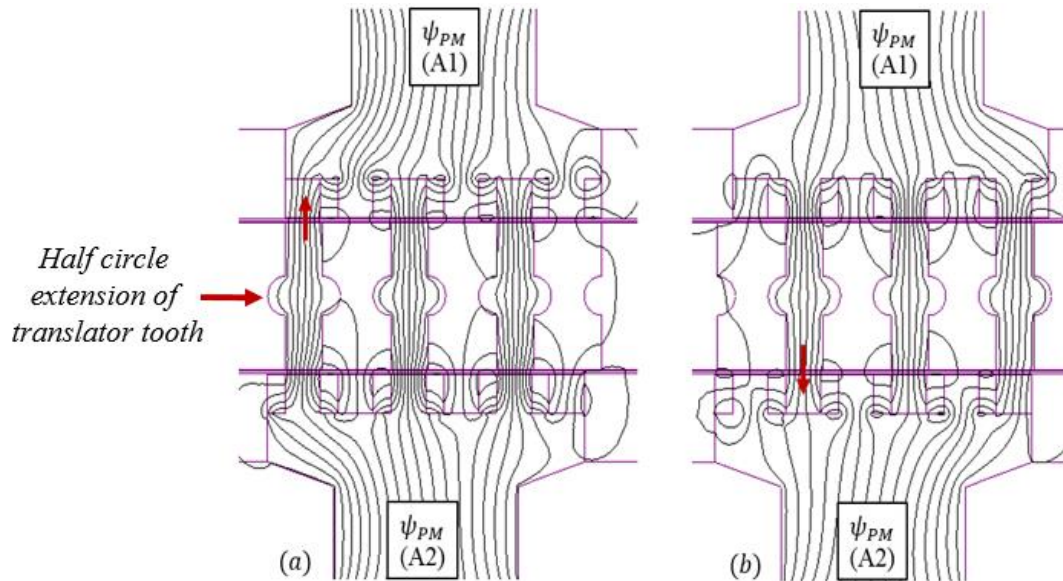


Figure 4. 7: No load flux contour plot with a segmented translator (a) translator teeth align with pole magnets of the top stator (b) translator teeth align with pole magnets of the bottom stator.

### 4.3.1 Translator Teeth Width Optimisation

Figure 4.8 shows the translator teeth optimisation for optimal thrust force and back EMF combinations. The translator tooth width was varied from 5mm to 10mm with increments of 0.5mm in the FEA simulation. The maximum force is achieved at a tooth width of 8.5mm, while the peak EMF is achieved at 6mm. However, at the width of 6mm, the force drops down by more than 12% of the maximum achievable force at rated current, because of the high magnetic saturation in the narrower teeth compared to the wider teeth. Figure 4.9 illustrates the

effect of magnetic saturation on translator teeth. As iron laminations remains unsaturated and behave linearly upto 1.5T which is limit of the linear region of the B-H curve and over this limit, it gets saturated and performance reduces. Again for saturation effect, it can be seen from Figure 4.10 that the 8.5mm wide teeth provide only 4% lower but more sinusoidal back EMF than for 6mm for the presence of higher order harmonics. Thinner tooth increases the rate of change of flux linkage which increases voltage, but also a smaller tooth increases flux density in the tooth towards saturation. Therefore, the translator teeth width has been chosen as 8.5mm for optimal performance.

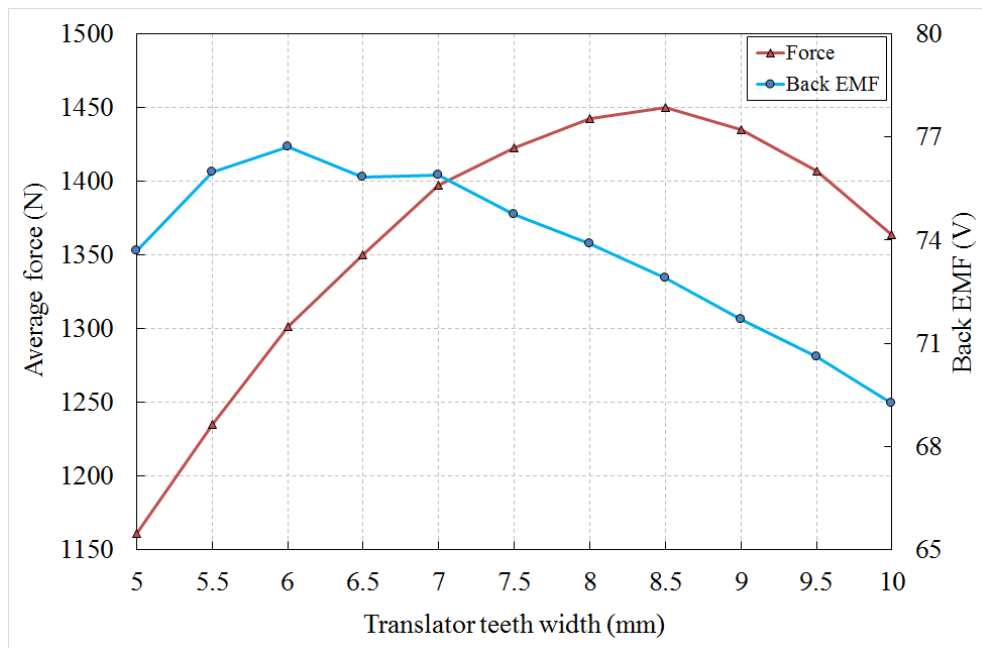


Figure 4. 8: Average force and back EMF variation with translator teeth width.

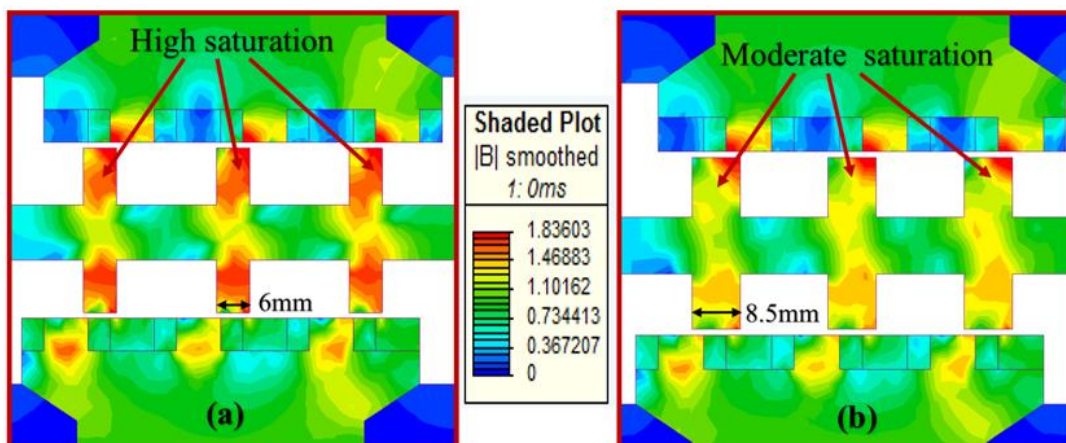


Figure 4. 9: Effect of magnetic flux saturation on translator teeth at rated current (a) 6mm (b) 8.5mm

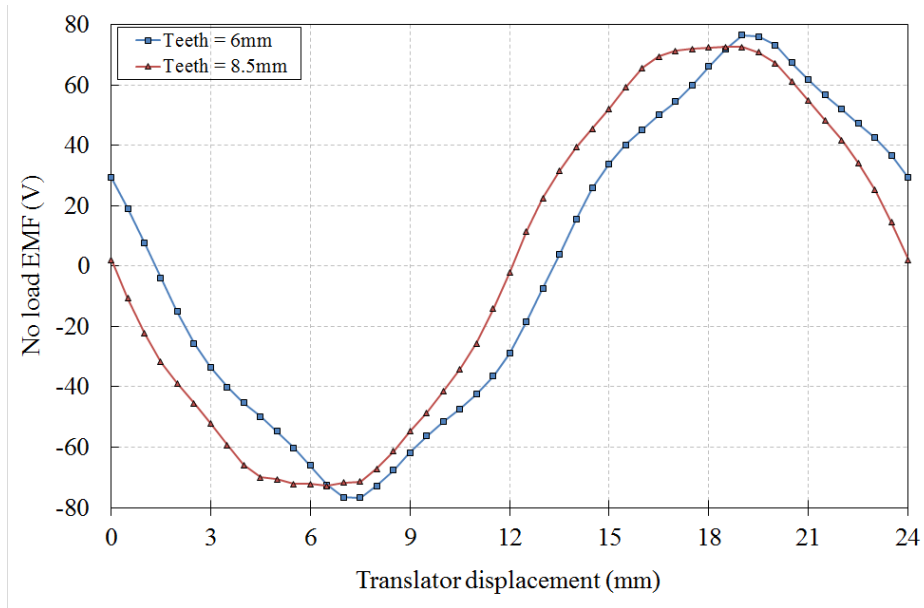


Figure 4. 10: Phase-A back EMF for different translator teeth width

### 4.3.2 Translator Core Thickness Optimisation

In the HCVHM, the majority of the useful flux travels straight through the translator teeth rather than translator core showed in Figure 4.11 (a). For long stroke applications like Direct Drive – Wave Energy Converters (DD-WEC), reducing the translator mass is important. Hence the translator core back thickness can be optimised for the high force with minimum translator mass.

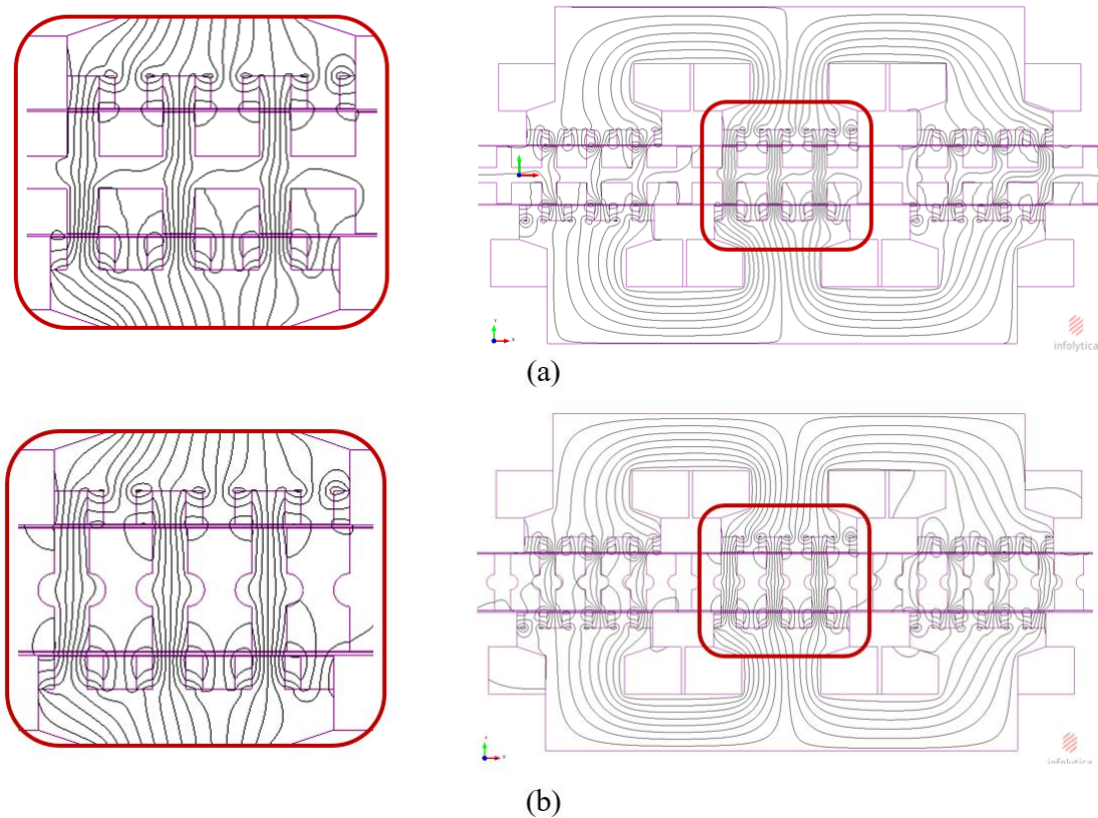


Figure 4. 11: No load flux contour path of HCVHM (a) solid translator (b) segmented Translator

Figure 4.11 shows the flux path for the machine through the translator with and without a core back. FEA is performed to find the optimal core back thickness for the maximum achievable average force. Figure 4.11(b) illustrates an FEA plot of no-load flux contour in the  $d$  axis position for the machine without a translator core back. With no core back, individual translator teeth are independent components mounted in a non-magnetic structure. This isolated segmented translator along with light weight non-magnetic structure has a much lower mass, guides the magnetic flux and improves effective electromagnetic flux distribution.

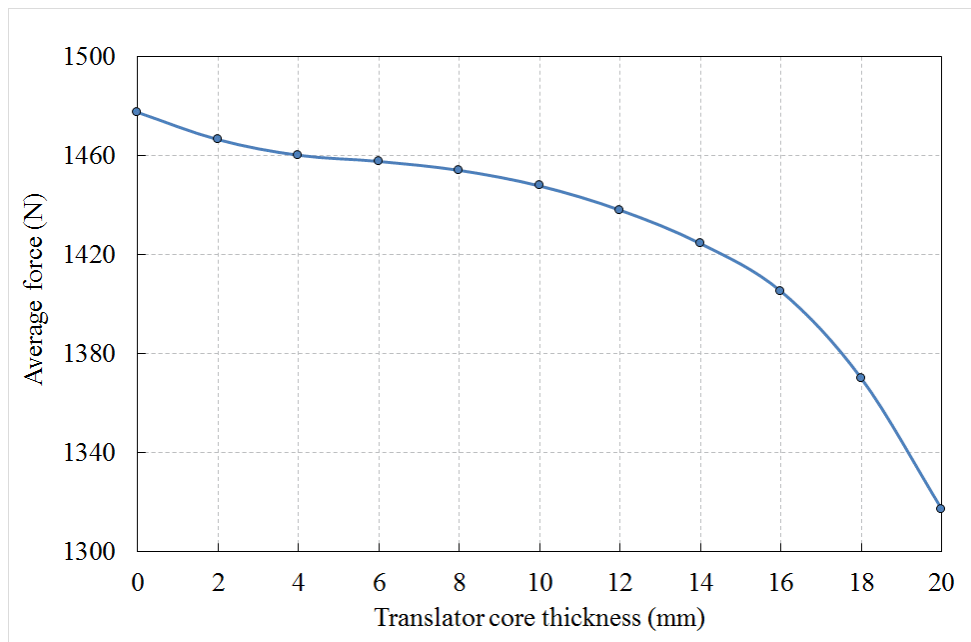


Figure 4. 12: Average force and back EMF variation by varying translator core thickness.

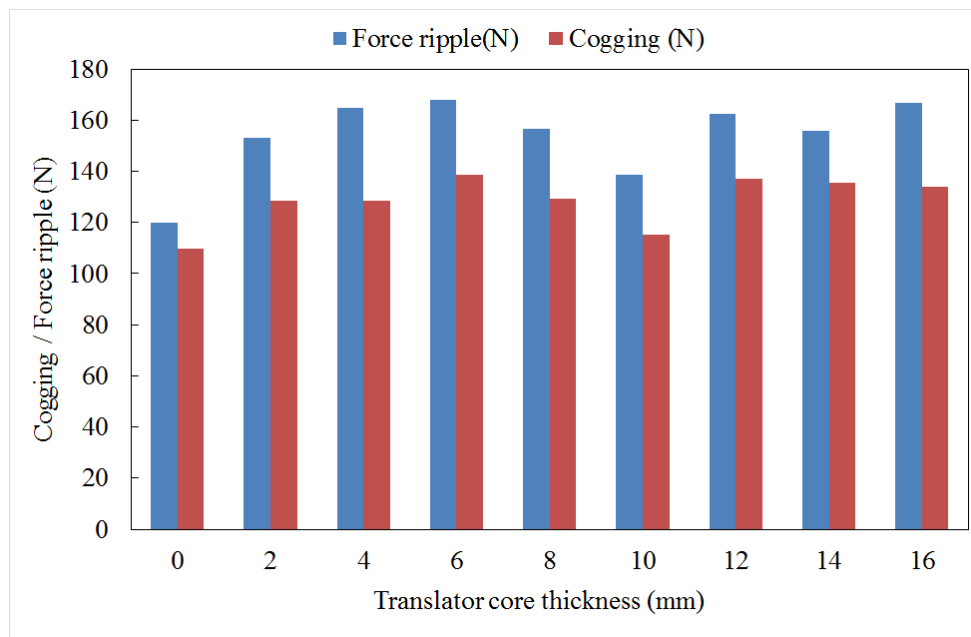


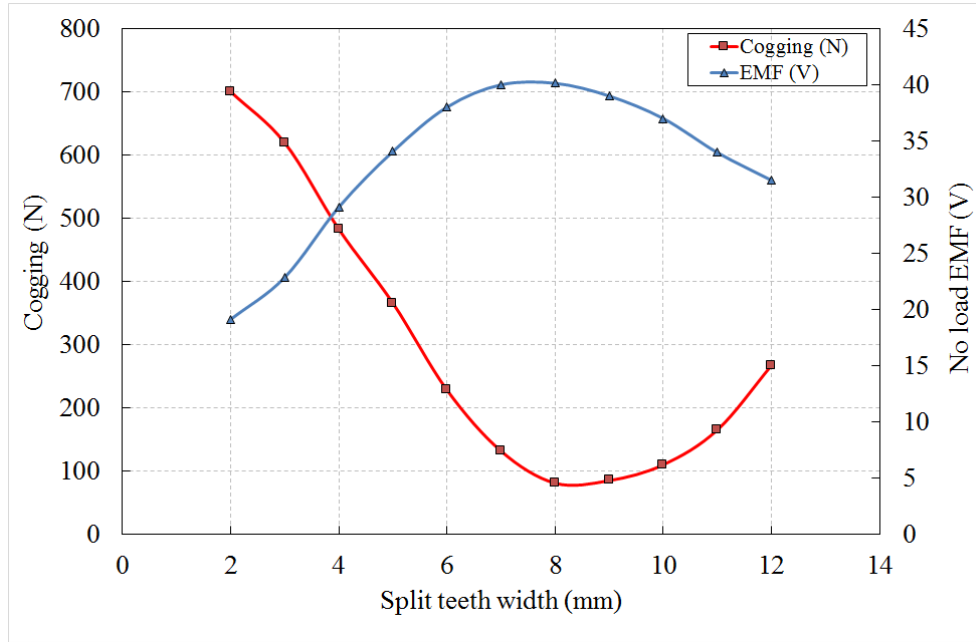
Figure 4. 13: Cogging and force ripple variation by varying translator core thickness.

Figure 4.12 shows the response of the average force for different core back thickness. The peak average force occurs with no core back on the translator and decreases by 10% when the translator core is larger than 14mm. Figure 4.13 shows the cogging force and force ripple against various translator core thickness. Therefore, a segmented translator (translator without core back) is adopted for the proposed machine for maximum force generation per active machine volume and minimum cogging.

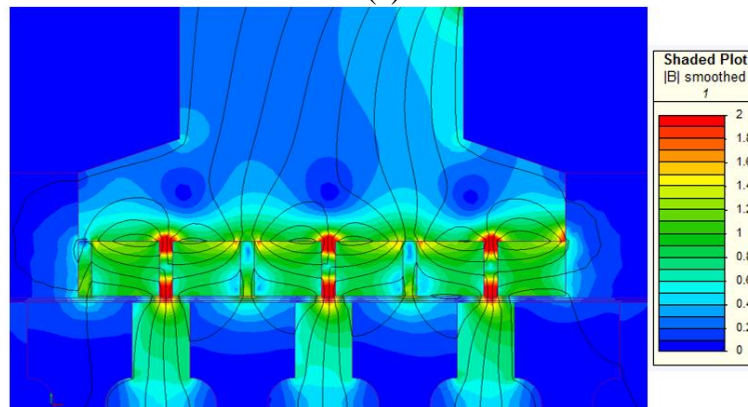
### 4.3.3 Stator Split Teeth Analysis

In the proposed machine, an important factor that has a great impact on back EMF and cogging force is the PM *poles* and the *split tooth* width. The stator pole pair pitch (*PPP*) was kept constant at 24mm to match the translator tooth pitch specification. It is shown that by keeping the vertical PM *pole* width ( $PM_{lv}$ ) same as the *split tooth* width ( $FT_l$ ), provide sinusoidal back EMF of high amplitude [94]. Therefore, only split teeth and transition magnets need to be optimised. Figure 4.14 shows the variation of peak back EMF and cogging force with respect to *split tooth* width.

It is clearly shown that an 8mm *split tooth* width produces the maximum peak back EMF with the minimum cogging force ripple. For a smaller split tooth, the main flux producing PM *poles* also get smaller and thus the net PM flux reduces and the saturation in the split teeth increases (Figure 4.14(b)). At a higher split tooth width, the *transition* PMs become smaller which reduce the effective flux barrier between PM pole and split tooth which causes leakage to increase and thus reduce the net active flux. Therefore, the optimal split tooth width is chosen to be 8mm.



(a)



(b)

Figure 4.14: a) Cogging and back EMF variation by varying split teeth width b) Flux contour plot at split tooth width of 2mm.

#### 4.3.4 Transition Magnet Width Optimisation

The optimisation of the PM array for the proposed machine has been done to achieve maximum thrust force and back EMF. As the *transition* magnets play a very important role in the performance of the machine, the ratio of the widths of vertically magnetised PM *poles* and horizontally magnetised *transition* PMs are investigated for optimal performance. *Transition PM* width ( $PM_{lh}$ ) can be derived from equation (4-1) and is changed from 1mm to 8mm with an increment of 1mm to observe the performance variation.

$$PM_{lh} = \frac{(PPP - FT_L - PM_{lw})}{2} \quad (4-1)$$

It can be seen from Figure 4.15 that the thrust force linearly increased to reach a maximum at the *transition PM* width of 4mm. Therefore, the force capability of the machine reduces above

that point – reducing by 3.5% at 5mm width and continue to drop afterward. Again, the back EMF follows a similar pattern with a peak at the ratio of *transition* to *pole* width of 4:8. As mentioned in the previous section, increasing the transition PM width from 1mm reduces the leakage flux and increases the active flux, while after 4mm, the associated vertical poles and the split teeth become too narrow for a constant pole pair pitch which causes the active flux to reduce.

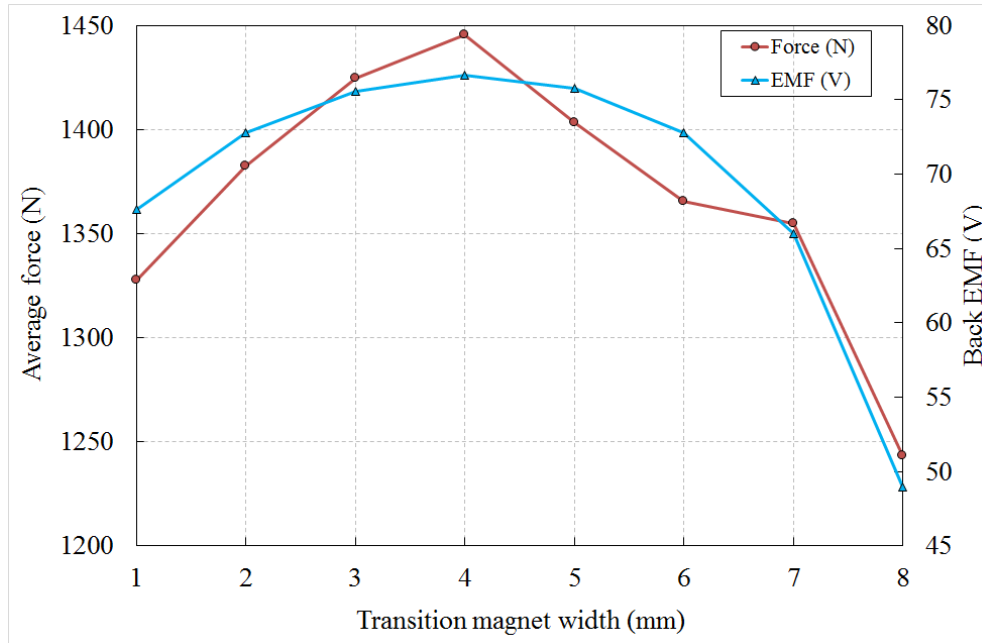


Figure 4. 15: Average force and back EMF variation with the transition PM width.

Therefore, after analysing the Permanent magnets' width, the final *transition* magnets' and *pole magnets*' width are chosen to be 4mm and 8mm respectively for maximum back EMF and thrust force application.

#### 4.3.5 Magnet Thickness Analysis

In Halbach machine topologies, the thickness of PM has a significant impact on the machine performance including the force production and its ripple. On the other hand, the length of the equivalent air-gap can be affected by the magnet thickness which may influence the power factor [89]. As magnet thickness increases, the reluctance seen by the coil MMF increases, so inductance reduces and thus power factor improves. All these factors were considered in the machine design study. The main objective of optimizing the PM thickness is to obtain the maximum achievable thrust force while keeping PM mass to an acceptable value. Figure 4.16 demonstrates the effect of PM thickness on no load back EMF and thrust force. As expected, at the beginning the back EMF and force increase almost linearly with PM thickness which is proportional to PM mass. But soon after the PM thickness reaches 4mm, a saturation effect is

noticed which becomes predominant after it passed 8mm. A further increase of the PM thickness would result in magnetic saturation in the iron poles, which reduces the magnet utilisation and increases the cost. So, optimal PM thickness is chosen to be 8mm for the final design.

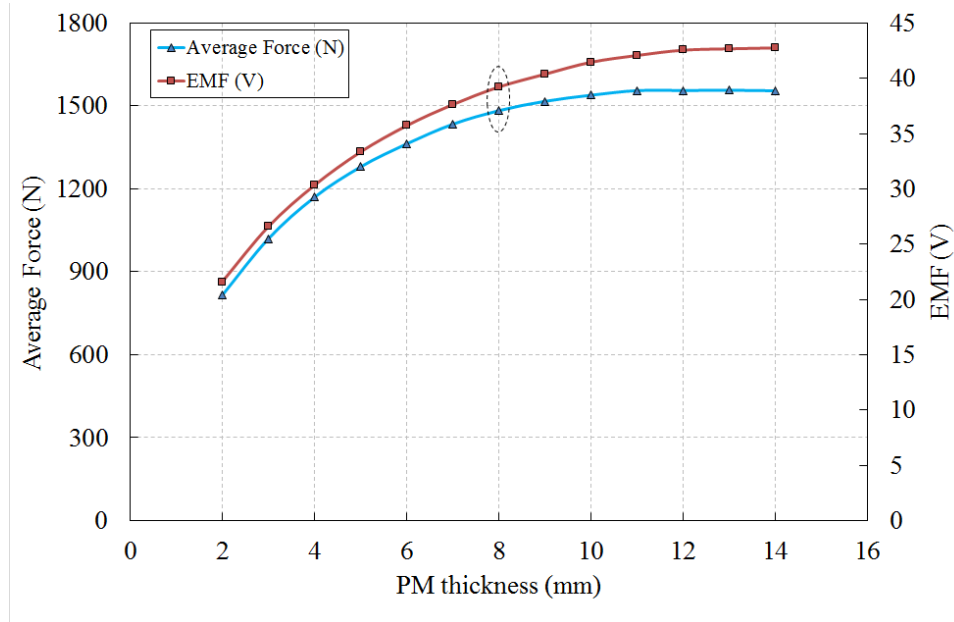


Figure 4. 16: Average force and back EMF variation with PM thickness variation.

#### 4.4 Simulation Result Analysis

A prototype of the final design of a segmented translator HCVHM, with the dimensions justified above, is built in the laboratory to validate the operation and predicted performance. All studies have so far been performed in 2D only, and so a 3D FEA model has been developed (shown in Figure 4.17(a)) with the refined mesh illustrated in Figure 4.17(b) to achieve more accurate simulation results. When moving to a 3D model, force predictions decreased by an average of 8% due to the leakage flux in the axial direction, stator end effect and coil end winding effect. The final design parameters are presented in Table 4-2.

Table 4- 2: Specification of the final design parameters

Parameters	Value
Translator teeth width (mm)	8.5
Transition PM width (mm)	4
Pole magnet width (mm)	8
PM thickness (mm)	8
Split tooth width (mm)	8
Machine axial length (mm)	60
Active machine width (mm)	280

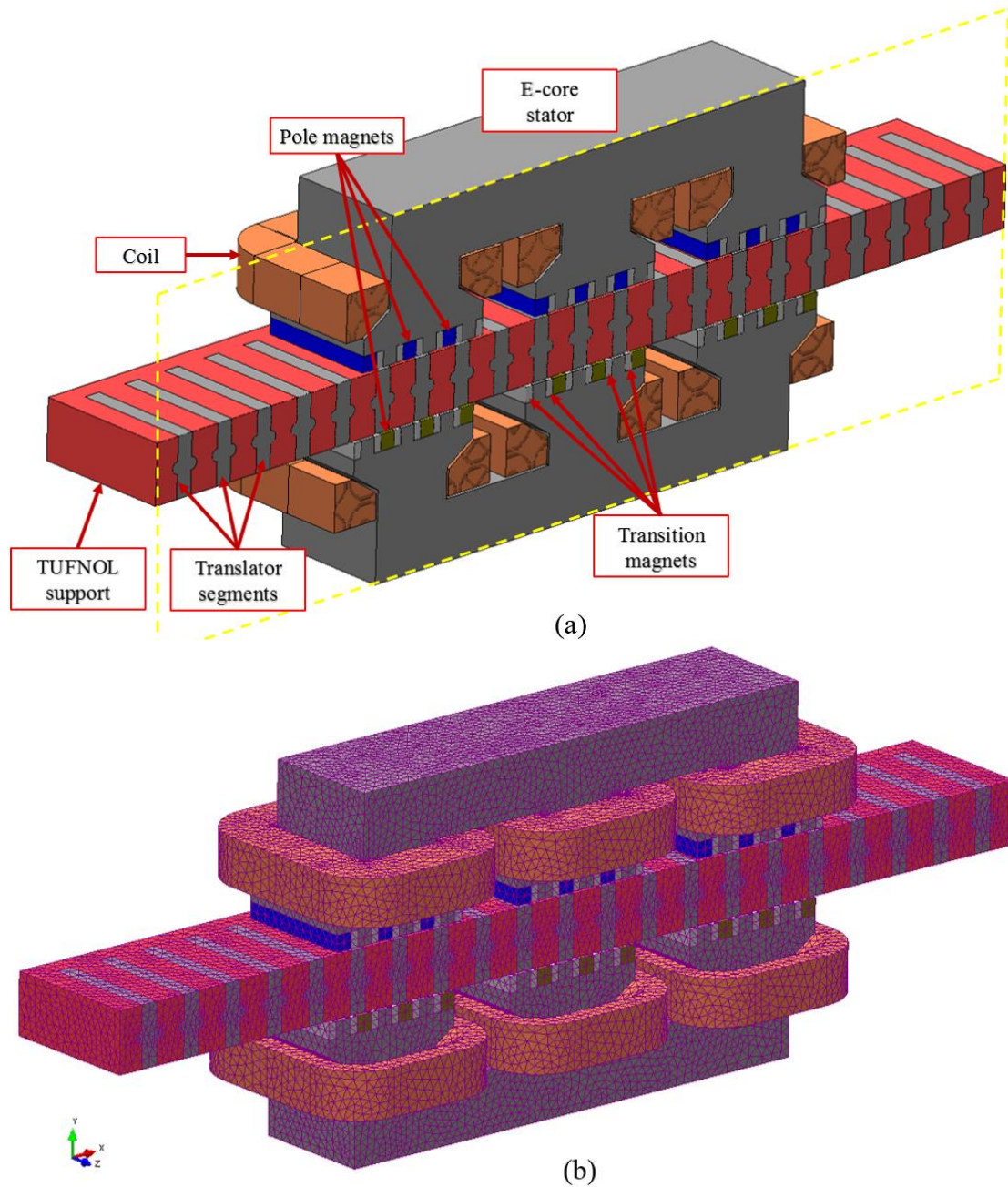


Figure 4.17: (a) Final 3D model with segmented translator (b) 3D mesh.

#### 4.4.1 Open Circuit Field Variation

Figure 4.18 presents the no-load air-gap field distribution of the proposed HCVHM under the top three phase windings over an active length of 280mm. It can also be seen from Figure 4.19 that, in the proposed HCVHM model, leakage flux is substantially reduced across the air-gap central line and converted into active flux using the horizontal magnets compared to the baseline model presented in the previous chapter. It shows that the HCVHM model has the capability to minimise more than 50% leakage flux compared to the baseline design presented in the previous chapter that boosts the active flux density of the HCVHM.

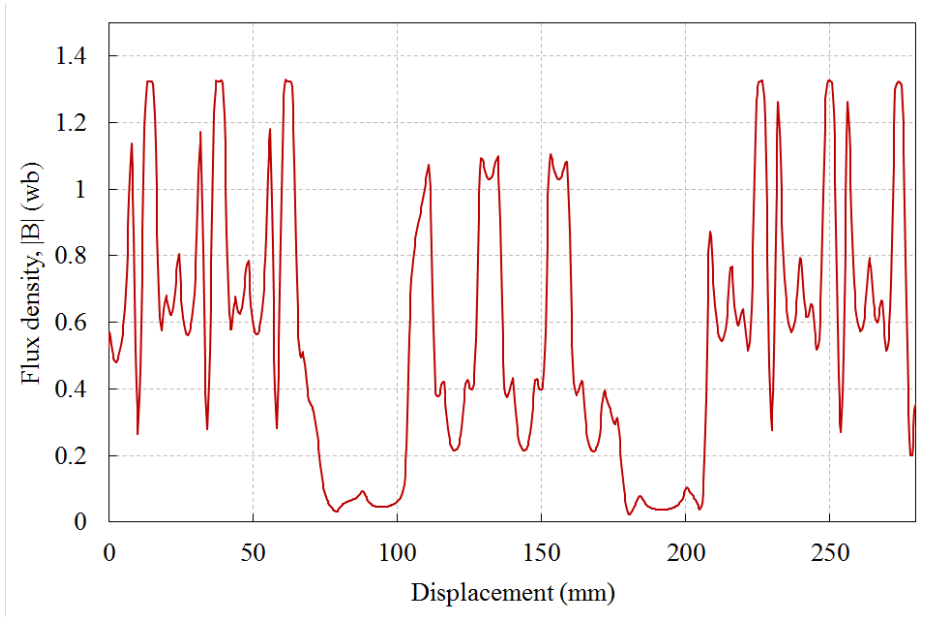


Figure 4.18: Active air gap flux density of the HCVHM model over the active machine length.

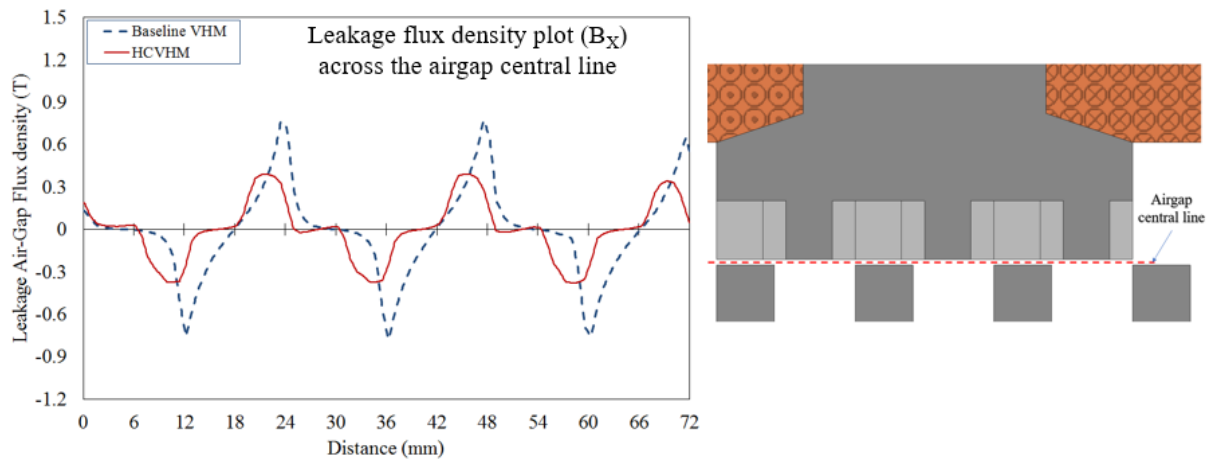


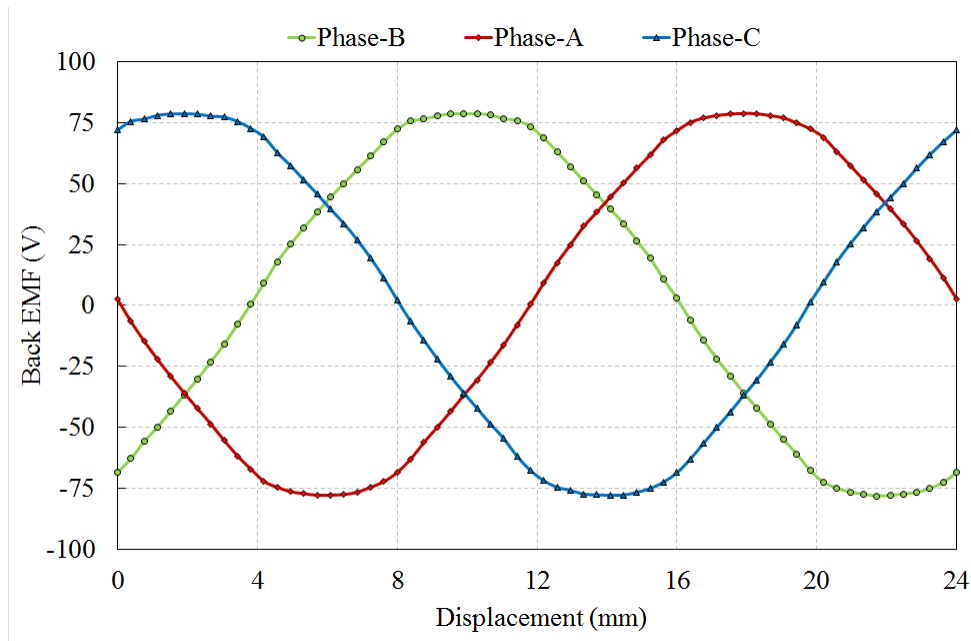
Figure 4.19: Leakage air gap flux density ( $B_x$ ) comparison

#### 4.4.2 Open Circuit Back EMF

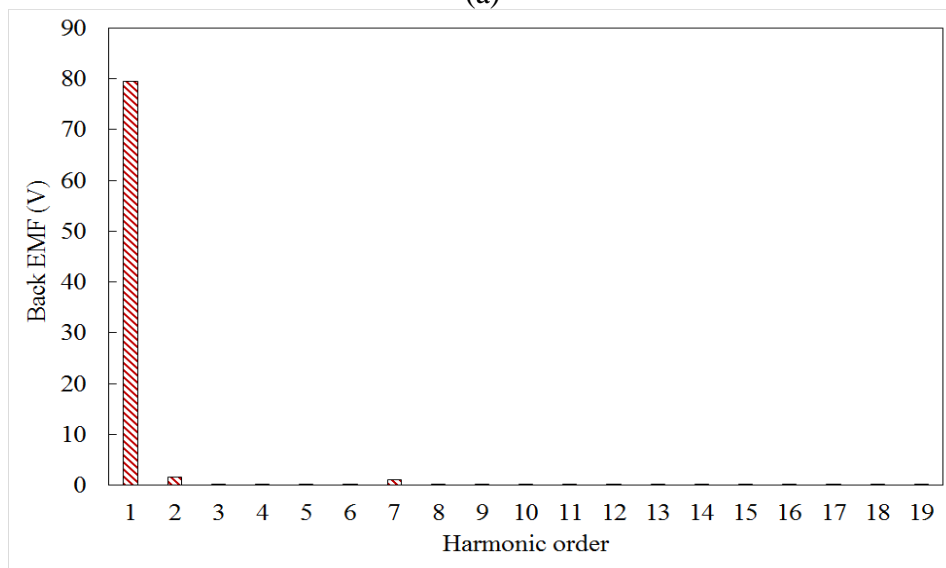
Open circuit back EMF or no-load EMF is the rate of change of induced flux linkage caused by the moving translator. The magnitude and direction of the EMF is given by the Faraday's law of electromagnetic induction expressed in,

$$E = -N \frac{d\phi}{dt} \quad (4-2)$$

The FEA simulation of three-phase back EMF for the final model is presented in Figure 4.20 (a). It can be seen that the three-phase back EMF are symmetrical and almost sinusoidal due to the low higher order harmonic contents. Figure 4.20 (b) represents the harmonic analysis of a single phase back EMF.



(a)



(b)

Figure 4. 20: a) Three phase back EMF for the proposed HCVHM. b) Harmonic analysis of phase back EMF.

### 4.4.3 Electromagnetic Excitation

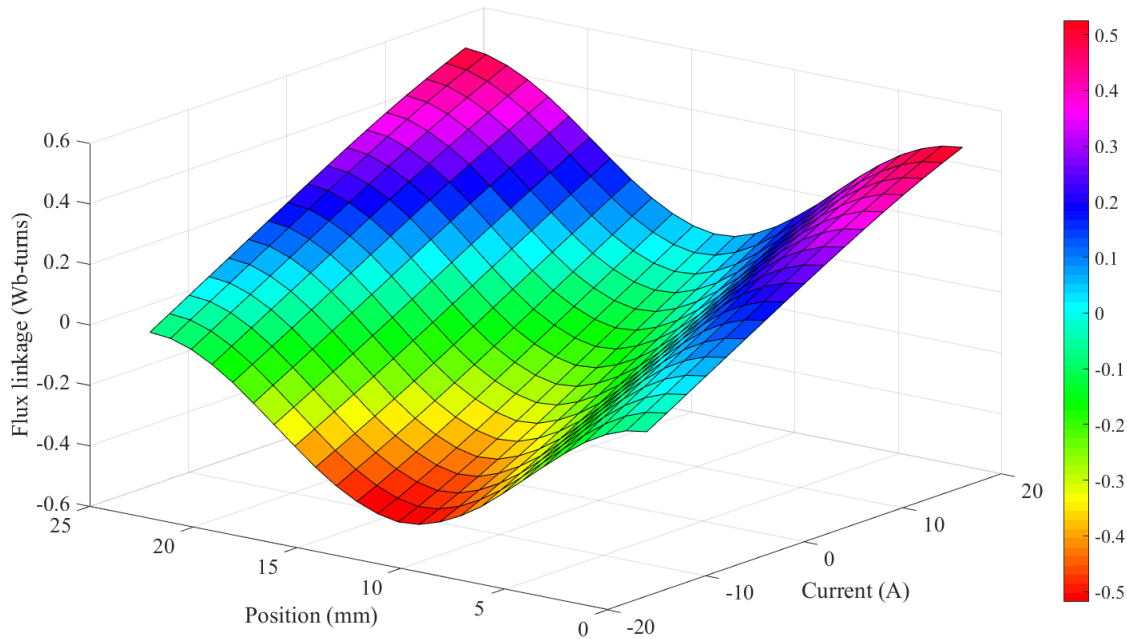


Figure 4. 21: Flux linkage map of an entire phase at the various position for different current levels.

One of the most effective ways to analyse the machine is by utilising the flux linkage map, which is shown in Figure 4.21. The flux linkage map is developed from the FEA model for various DC excitation currents including the magnets, at a different position over a full electrical cycle. Finally, all the flux data are accumulated and plotted in a 3D graph against position and excitation current.

The flux variation with the current is also symmetrical to the no-load (0A condition) flux linkage plot in Figure 4.5. But it can be clearly understood that, over the range of +16A to -16A current excitation, the flux linkage is not symmetrical and hence the entire flux vs position curve is shifted up or down depending on the excitation level. For example, flux at position = 0mm for +16A DC excitation is 0.52Wb-turns compared to -0.05Wb-turns at -16A. Again, the flux at position=12mm during +16A DC excitation is 0.07Wb-turns compared to -0.52Wb-turns at -16A. These unsymmetrical effects depend on the alignment and un-alignment of the DC excitation current with the magnet poles for different positions. As the magnetic excitation at a particular position is fixed, the excitation current actually guides the flux plot variation. Figure 4.22 illustrates the flux contour plots at two different positions for two different current excitation levels.

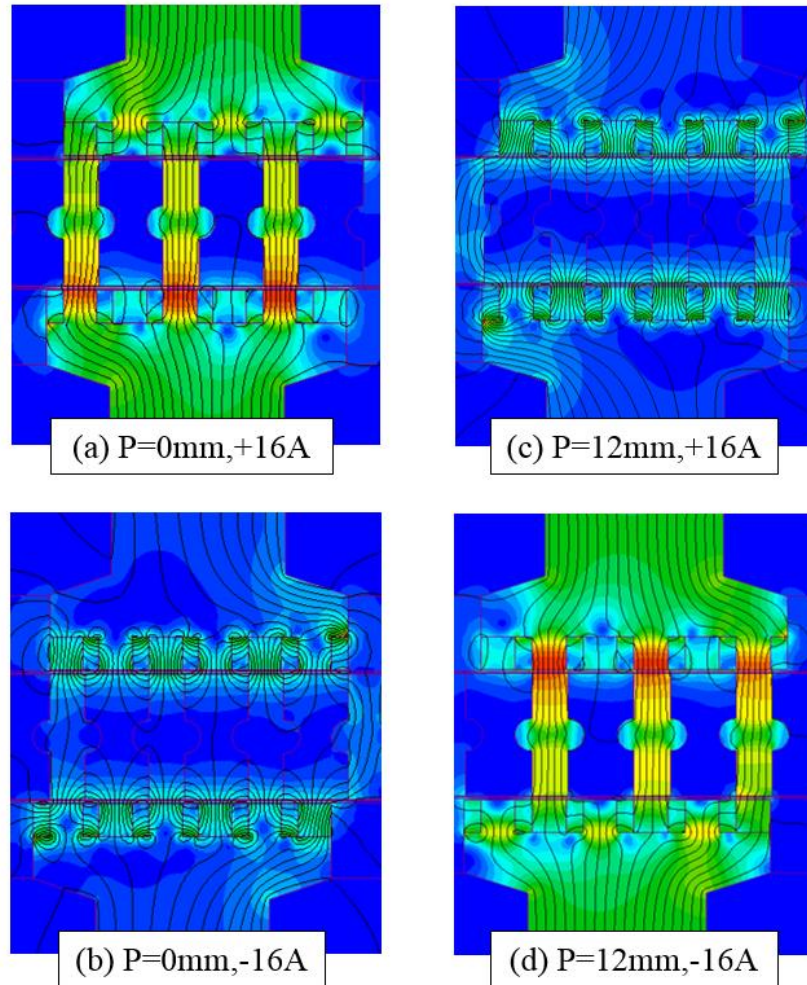
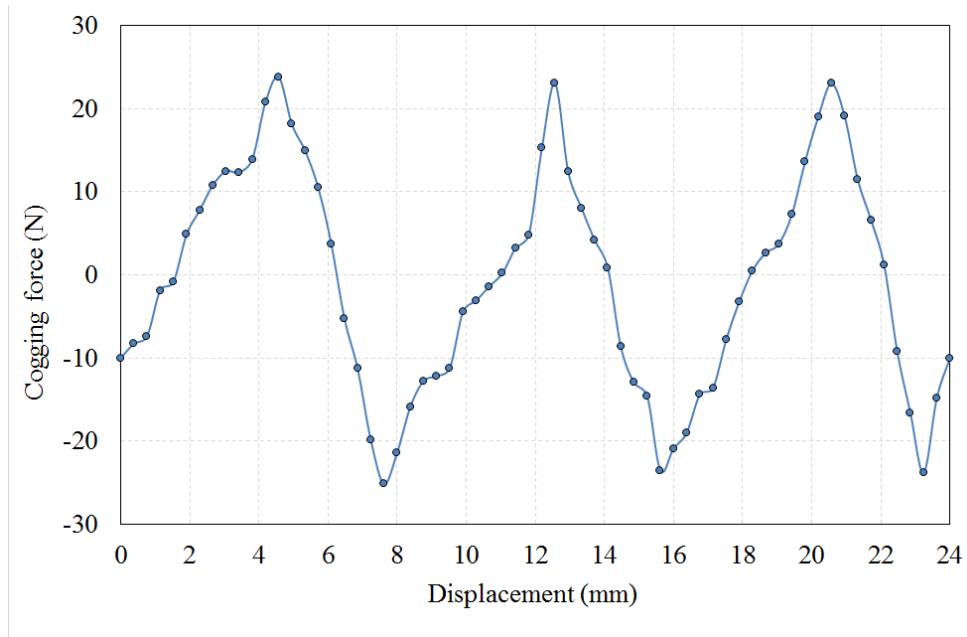


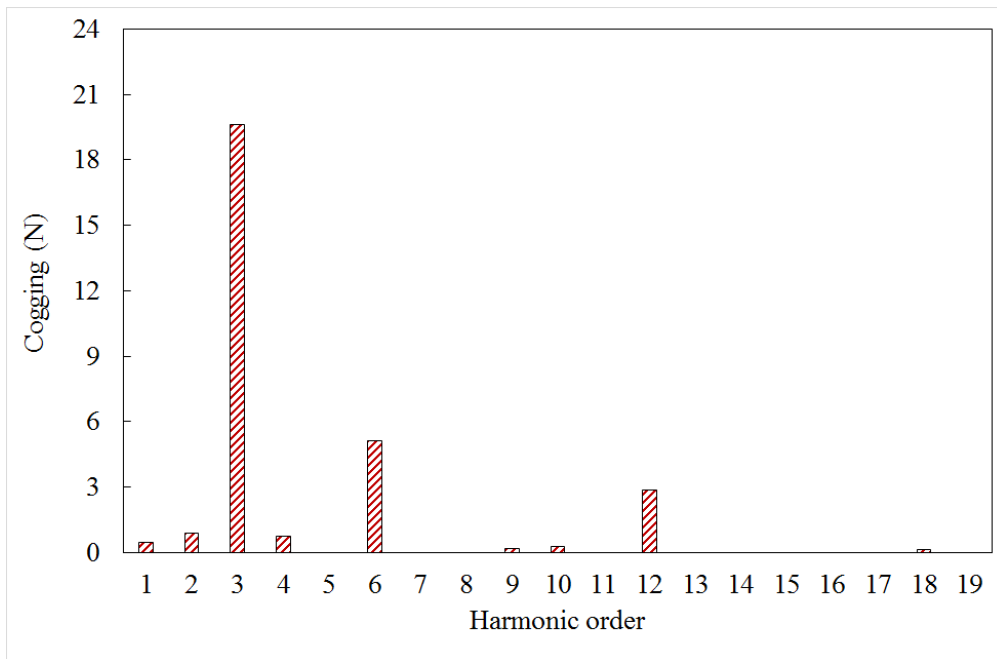
Figure 4. 22: Flux contour plot at different translator position at different DC excitation current.

#### 4.4.4 Cogging Force

Fig 4.23(a) represents the cogging force waveform over one full electrical cycle for the HCVHM model. The peak cogging force is 26N which is less than 3% of the rated force of the final machine model. It is also noticeable from Figure 4.23(b) that the proposed machine has the dominant 3<sup>rd</sup> harmonic, which is clear from the three cogging cycles over the displacement of one electrical cycle. Figure 4.23(b) also shows that the dominant higher order harmonics are 6<sup>th</sup> and 12<sup>th</sup> for the proposed machine.



(a)



(b)

Figure 4. 23: (a) Cogging force for the final design (b) harmonic analysis of the cogging force.

#### 4.4.5 Thrust Force

Figure 4.24 shows the variation in average thrust force variation of the HCVHM with different amplitudes of currents. The thrust force at various current is achieved by applying the current in phase with the back EMF. The thrust force increases linearly until the peak current of 16A which is chosen as the rated current of the HCVHM. Above this current, saturation effects cause the force response to be non-linear.

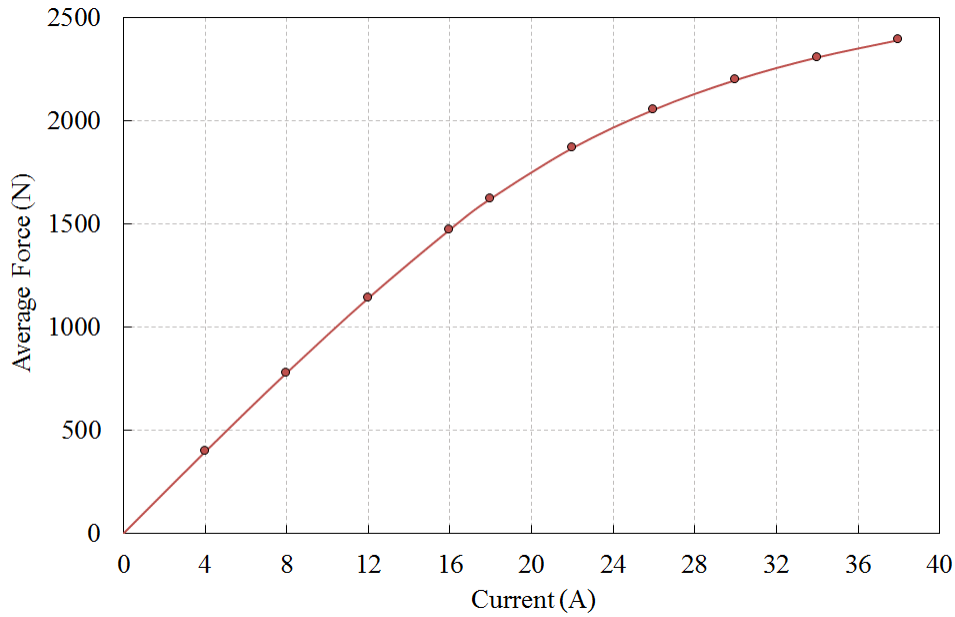


Figure 4. 24: Average force variation with peak current.

The thrust force ripple,  $f_r$  is calculated using equation (4-3) and is shown for rated current in Figure 4.25.

$$f_r = \frac{1}{F_{avg}} \sqrt{\sum_x F_x^2} \quad (4-3)$$

Where,

$F_{avg}$  = Average thrust force

$F_x$  = Instantaneous thrust at translator position  $x$

The thrust ripple of the machine mainly consists of three major components: Cogging force due to the interaction between electromagnetic flux and the variable permeance due to the translator teeth, distortion in the magnetic flux density distribution and the commutation phase current [95]. Figure 4.25 presents the thrust force variation over an electrical cycle with an average value of 1480N and a maximum force ripple of less than 6%.

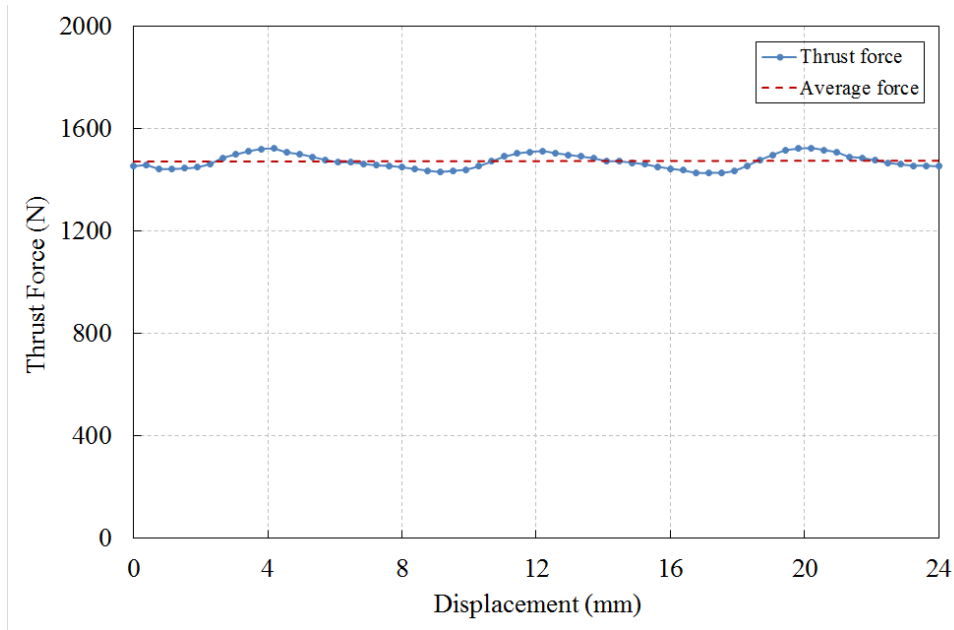


Figure 4. 25: Thrust force at various translator positions.

#### 4.4.6 Inductance Measurement

##### 4.4.6.1 Inductance equivalent circuit – Method A

The single-phase equivalent circuit of a permanent magnet synchronous machine consists of an EMF source with a series inductance and resistance as shown in Figure 4.26.

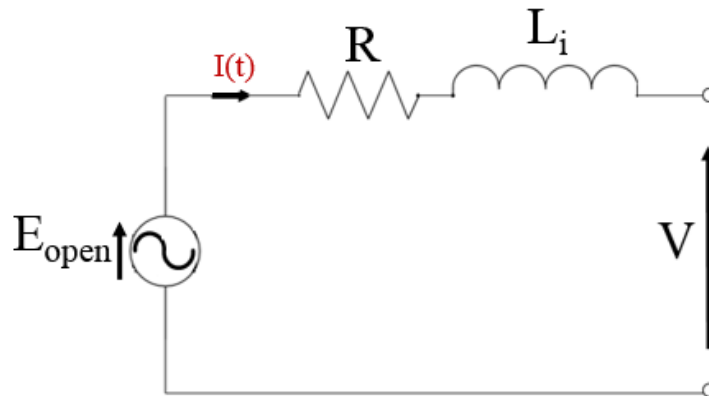


Figure 4. 26: Simple per phase equivalent circuit

Coil inductance is given by equation (4-4),

$$L_i = \frac{\psi_i}{I} \quad (4-4)$$

Where,

$\psi_i$  = Flux linkage due to the only electrical excitation (no PM).

$L_i$  = value of inductance at a position.

Applying Kirchhoff's Voltage Law (KVL) to the equivalent circuit gives a relationship between back EMF, inductance, terminal voltage, electrical excitation and resistance which can be deduced by the following equation.

$$V = E_{open} - L_i \frac{di}{dt} - IR \quad (4-5)$$

Where,

$E_{open}$  = the No load back EMF per phase

R= phase resistance

V= stator phase voltage

The inductance is the flux linkage per unit current without any PM excitation and can also be deduced from the gradient of the following figure, 19.8mH.

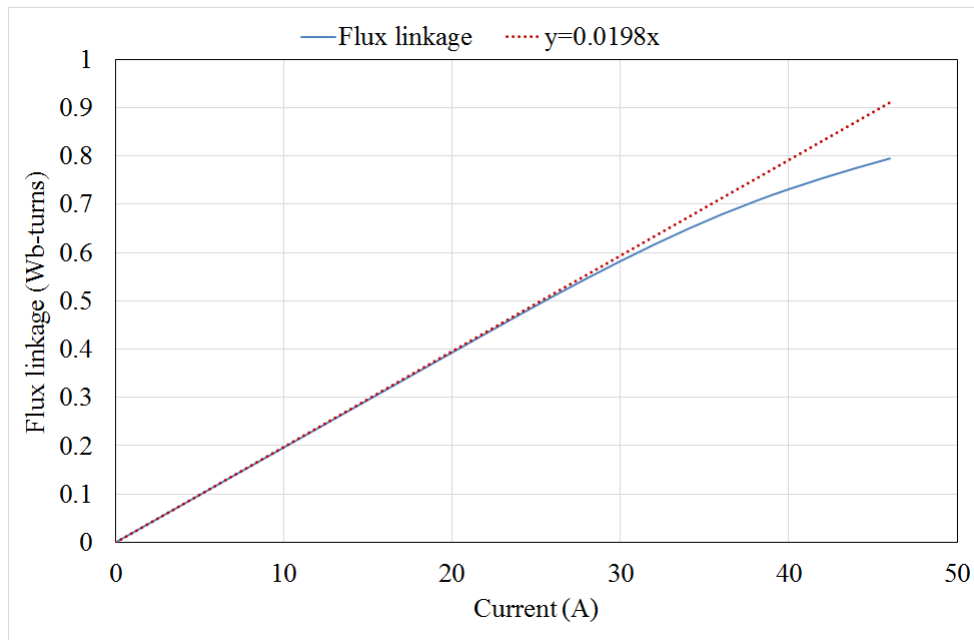


Figure 4. 27: Variation of phase flux linkage with only excitation current, without magnetic excitation.

#### 4.4.6.2 Electromagnetic excitation – Method B

To calculate inductance more accurately, the cross-coupling between magnetic excitation and armature excitation should be considered. Total flux linkage per phase is the sum of the flux from the PMs and the armature current, expressed by the following equation [96],

$$\psi_{total} = \psi_{PM} + L_i I \quad (4-6)$$

Phase inductance can be derived from the equation above,

$$L_{i,x} = \frac{\psi_{total} - \psi_{PM}}{I} \quad (4-7)$$

Where,

$L_{i,x}$  = Inductance due to the electromagnetic excitation for various position.

$\psi_{total}$  = Total flux linkage per phase

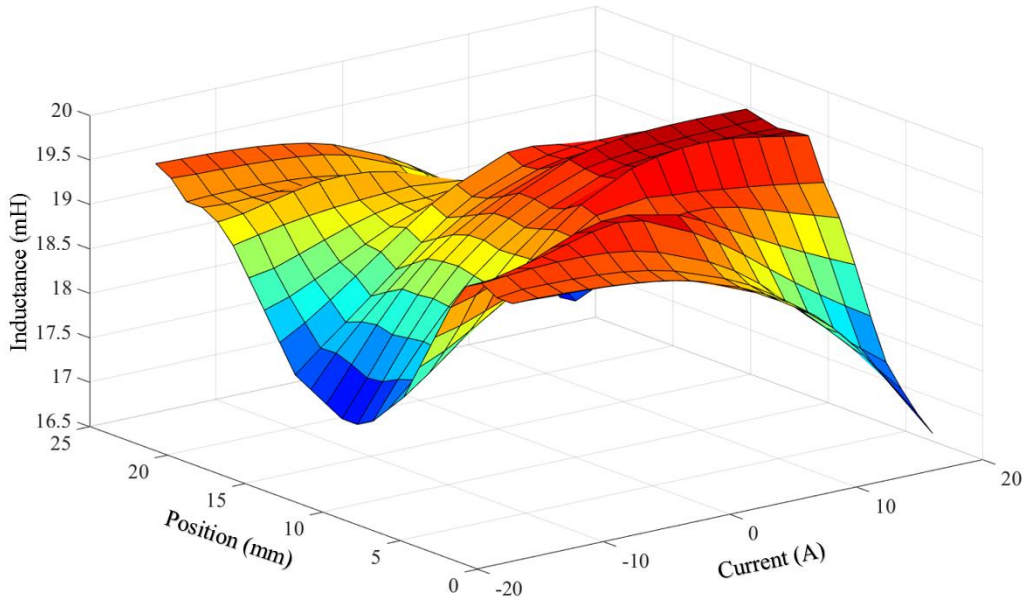


Figure 4. 28: Self-inductance at a different position for different current levels.

Figure 4.28 shows the FEA inductance results using equation (4-7). The 3D graph represents the distribution of inductance with varying current and position. The peak self-inductance found from the graphs is 19.3mH. The inductance varies greatly with a position at higher current, both in a positive or negative direction. There are inverse characteristics noticeable in the inductance versus position graphs across the zero armature current (PM excitation only) as the current moves between positive and negative values.

The step-variable inductance model can be described by the following equivalent circuit model, which is governed by equation (4-8).

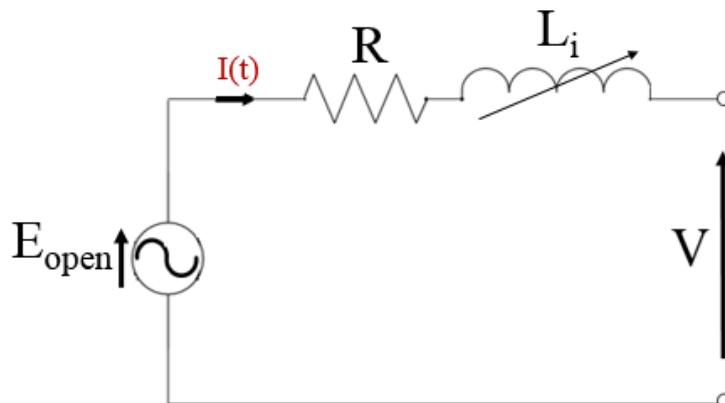


Figure 4. 29: Equivalent circuit model for step variable inductance

$$V = E_{open} - L_{i,x} \frac{di}{dt} - IR \tag{4-8}$$

Where,

$L_{i,x}$  = value of inductance at different translator position,  $x$ .

**4.4.6.3 Step function method – Method C**

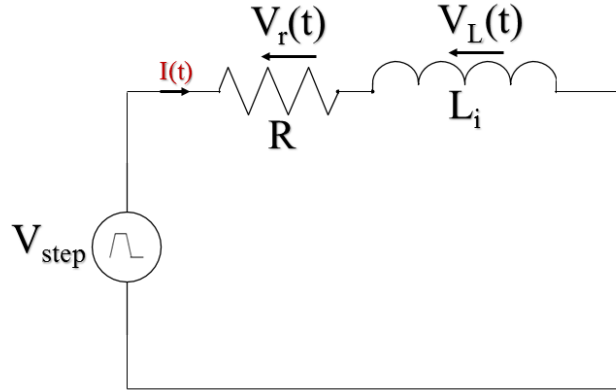


Figure 4. 30: Simple per phase equivalent circuit model with a trapezoidal DC voltage source

Another transient method to calculate the phase inductance is to calculate the phase flux linkage from the time-variant following equation using the circuit shown in Figure 4.30,

$$\psi(t) - \psi(0) = \int_0^t (V(t) - I(t)R) dt \tag{4-9}$$

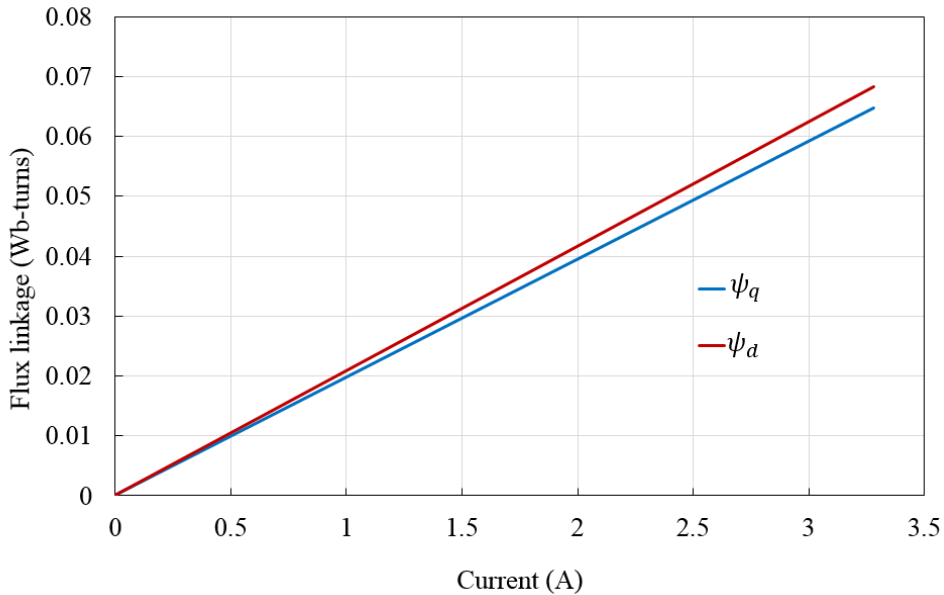


Figure 4. 31: Flux linkage variation with the current in one phase.

Where,

$V(t)$  = instantaneous value of voltage per phase.

$\psi(t)$  = instantaneous value of flux linkage per phase.

$I(t)$  = instantaneous value of current per phase.

$\psi(0)$  = flux linkage per phase due to magnetic excitation only at  $t=0$ .

Trapezoidal step voltage with a peak value of 0.9V has been applied to the phase winding to check the transient response of the current level at static positions. As mentioned in the previous section, due to the inductance effect, the current takes a slightly longer time to reach its maximum value compared to the voltage (current lags voltage). Again, it falls to zero later than the voltage becomes zero as the inductor takes time to discharge. During the fall or the rise time, equation (4-9) can be used to find the time-varying flux linkage response. Figure 4.31 illustrates the time-varying flux linkage against the current graph for aligned (maximum flux linkage) and unaligned (minimum flux linkage) position. It gives a maximum and a minimum self-inductance of 20.4mH and 19.7mH respectively.

#### 4.4.6.4 Synchronous inductance – Method D

Synchronous or phase inductance is the summation of self-inductance and mutual inductance. In this method, +DC current excitation is applied to the middle Phase-A and  $-DC/2$  current excitation level is applied to the other two phases. Then equation (4-7) can be used to calculate synchronous inductance for all three phases. Figure 4.32 plots the phase inductance of three phases for the final HCVHM.

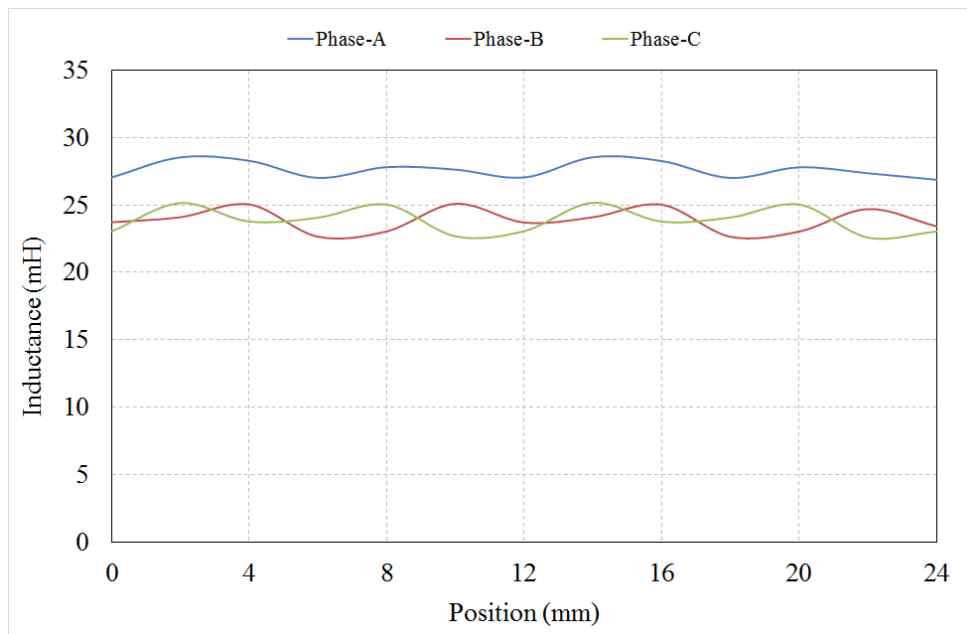


Figure 4. 32: Phase inductance between three phases.

#### 4.4.7 Power Factor Analysis

Power factor affects the cost of energy of a direct drive PTO in a wave energy converter [98]. The main disadvantage to the VHMs and all the Variable Reluctance Machines (VRMs) is that

they tend to operate at a low power factor, the typical range of 0.35-0.55 [7, 92]. This low power factor results from the large series inductance in the machine, significant leakage and inherent feature of the magnetic gearing, which hinders the useful power generation [7]. The proposed HCVHM can operate at a higher power factor compared to the range mentioned earlier due to the substantial reduction in the leakage flux and increase in the active flux. By increasing the magnetic loading (EMF) and reducing electric loading (MMF) for a fix rated force, the power factor can further be improved.

Increasing the axial length of a flat machine is one of the ways to increase the back EMF, which allows the electrical loading to be reduced whilst maintaining a fixed force. It can hence be used as a way of improving power factor but at the expense of machine and magnet mass.

The proposed HCVHM and the improved E-core VHM topologies are scaled in the axial direction from 60mm to 140mm to look at the effect of axial length on the power factor. The MMF was reduced with the increase of axial length to maintain a constant average force. For both topologies, the power factor is shown in Figure 4.33 to increase almost linearly with an increase in axial length. It is noticeable that the gradient of the HCVHM is higher than the VHM for the given range of axial length. This means the power factor to axial length ratio is higher in the HCVHM and provides more efficient power factor improvement.

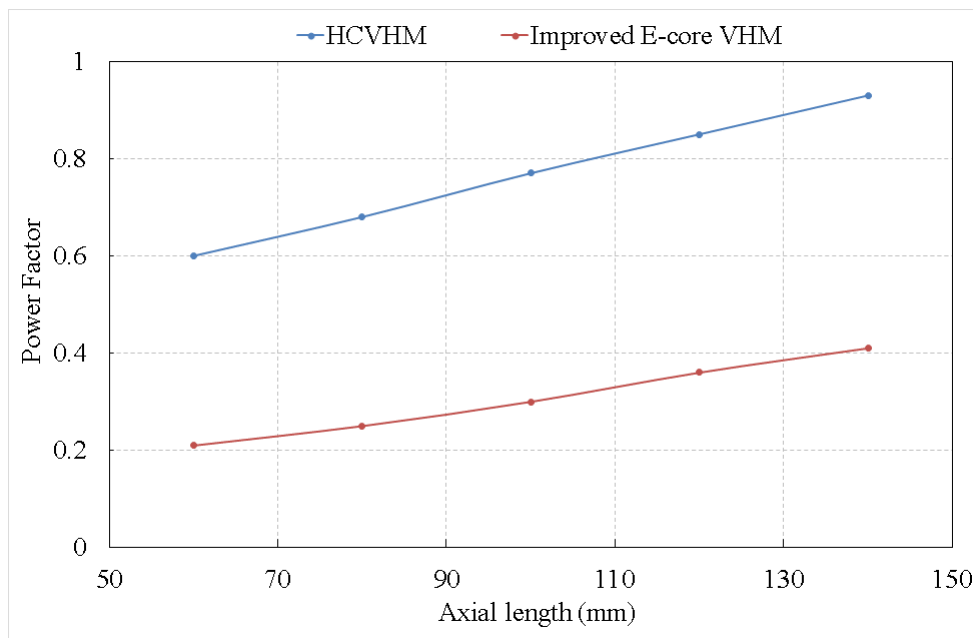


Figure 4. 33: Variation of the power factor with respect to the machine axial length

The no-load back EMF and cogging force of both machines will also increase with the axial length. Although the proposed HCVHM could operate with a much higher power factor of 0.93, when the axial length and thus magnet mass increases by 130% and its cogging force become

15% of the average force. This is due to the increase in THD of the no-load back EMF [98]. Therefore, very high power factor is achievable by the HCVHM, if the axial length, and hence magnet mass, were not a constraint.

#### 4.4.8 Concluding Remark

Table 4-3 summarises the main machine parameters and performance results of the two designs. It is shown that for the same average force and current loading, the improved E-core VHM uses almost double the amount of steel compared to the HCVHM and has a lower power factor. The HCVHM only utilise 20% more PM, while offering a much larger power factor and power density improvement with better efficiency, compared to the improved E-core VHM. Due to the outlined advantages, the flat version of the HCVHM is selected to be built and validated for the DD-WEC application.

*Table 4- 3: Specification of the final design parameters*

<b>Parameters</b>	<b>HCVHM</b>	<b>Improved E-core VHM</b>
Axial length (mm)	60	100
Translator total mass (kg)	2.31	4.55
Stator mass (kg)	12.42	20.7
PM mass (kg)	1.04	0.8
Back EMF (V)	80.60	77
Peak rated current (A)	16	16
Average Force (N)	1480	1490
Force ripple (%)	6	7
Shear stress (kN/m <sup>2</sup> )	43.84	26.3
Power density (kW/m <sup>3</sup> )	605	363
Power Factor	0.6	0.3
Efficiency (%)	89	80

## 4.5 Prototype Building and Construction

This section outlines the development and construction of the flat HCVHM including the linear test rig for laboratory testing. The main concept of the machine assembly is that the translator sits in the middle of two E-core stators. Both the flat E-core stators and twenty one segmented translator teeth are made of stacks of lamination sheets (Datasheet provided in the Appendix). An engineering solution has been developed to produce a rigid and flexible housing structure, which can carry all the machine's parts including translator and stators. Aluminium support caps that hold the E-core stators can be mechanically adjusted with the housing to control the air-gap of the machine. All the support structures including the housing are made of aluminium and TUFNOL material and the shaft is made of a cylindrical stainless-steel bar. The challenges encountered including machine construction, material manufacturing, test rig development, and assembly process will be explained in this chapter.

### 4.5.1 Stator Construction

#### 4.5.1.1 Laminated E-core stator

The stators were built from M270-35A graded electrical sheet of 0.35mm thickness. To avoid eddy current in the stator, laminations were bonded by specialist epoxy resin to make a stack using a special pressing structure showed in Figure 4.34(a). The stack thickness of the 600×300mm laminations was 60mm, to match the stator design criteria. The lamination stack was baked at 120°C for 2 hours to cure the epoxy resin and bond the lamination sheets. The wire eroding machine was used to cut the lamination stack into E-core stator shape. This method used DXF format file to automatically produce the selected component and is capable of cutting to a tolerance of  $\pm 0.1$ mm. Small hand file and liquid cleaning agents were used to remove any splatter, metal dust or rust in the stator piece. Figure 4.34(b) shows the finished laminated stator core.

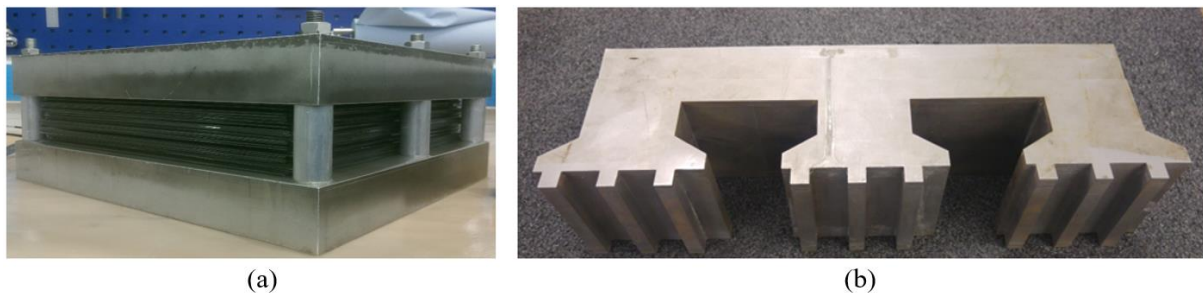


Figure 4. 34: (a) Lamination stack and bonding structure (b) wire eroded laminated stator

#### 4.5.1.2 Stator support

The prototype machine contains two aluminium support structures to accommodate two stators. Aluminium supports are machined from the solid aluminium block (Cast Tool Plate: ACP 5080R) of the dimension of  $420 \times 220 \times 40$  mm (Figure 4.35). Two windows have been made beside the stator pocket for handling and observation purposes. Six 8 mm holes have been made in front of the stator pocket for each aluminium cap to insert banana plugs in for coil terminals. Six more threaded holes each have been drilled across the length, on top and the bottom of the aluminium support. These twelve threaded holes allow the stator support to be attached to the main housing. There have been four flanged extrusion on four corners of the support to ensure proper positioning of the support structure into the window of the housing. The core back of each stator is buried inside the stator pocket of the aluminium support cap. Advanced Materials Epoxy resins & hardeners (ARADUR 5052CH & ARADLDITE LY5052) have been used to attach both the stators' core back inside the pockets. Figure 4.36(a) displays the machining process of the aluminium support and Figure 4.36(b) shows the attached E-core stator inside the aluminium support.

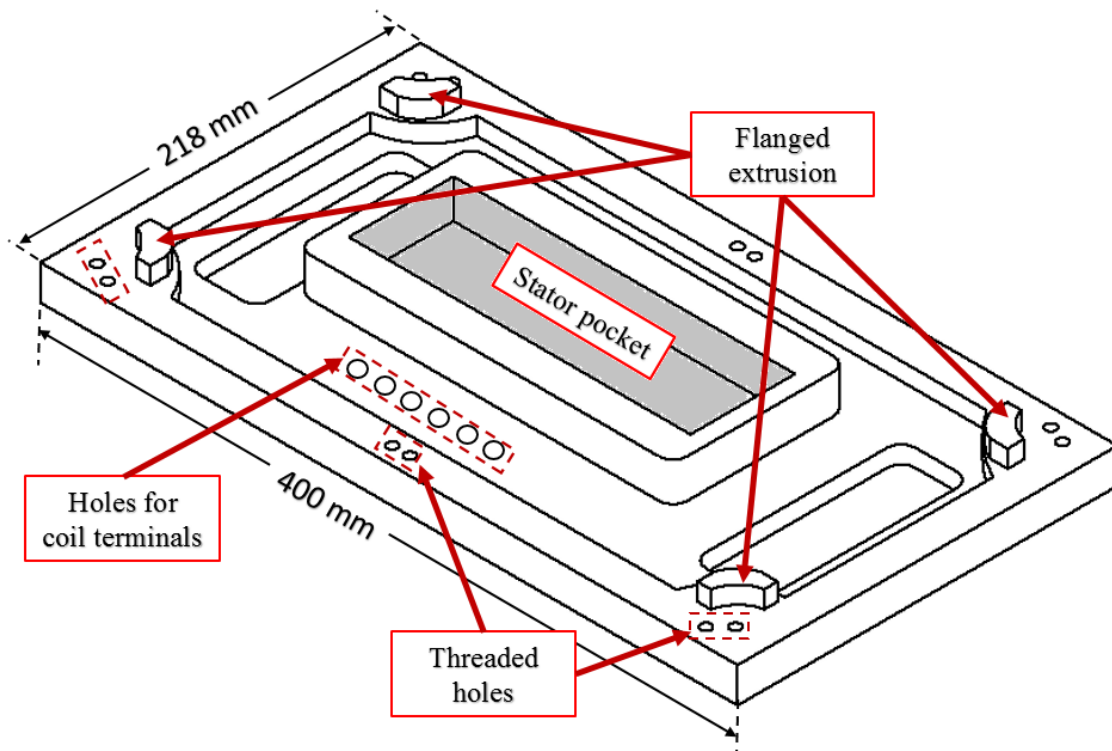


Figure 4. 35: Aluminium support structure for the stator assembly.



(a)



(b)

Figure 4. 36: (a) Machining of the aluminium support plate for the stator (b) Stator with aluminium cap support.

#### 4.5.2 Coils

Each stator consists of three teeth with a three-phase double layer concentrated winding. Top coils were marked by '1' and bottom phase windings were marked by '2' in Figure 4.37. Coil-1 and coil-2 of the respective phases are connected in series to give three phase windings. All the stator teeth have adopted a tooth shoe structure to reduce the stator mass and active length by accommodating the coils in the slots. It was decided to construct the coils from round enamel coated copper conductor with a diameter of 1.4mm.

Coils have been manually hand wound instead of using premanufactured bobbin winding. Slots were surrounded by 0.25mm thick Nomex thermal insulating sheets. All the sharp edges were covered with plastic tape prior to winding the teeth to protect the conductor insulation. Each coil has 100 turns.

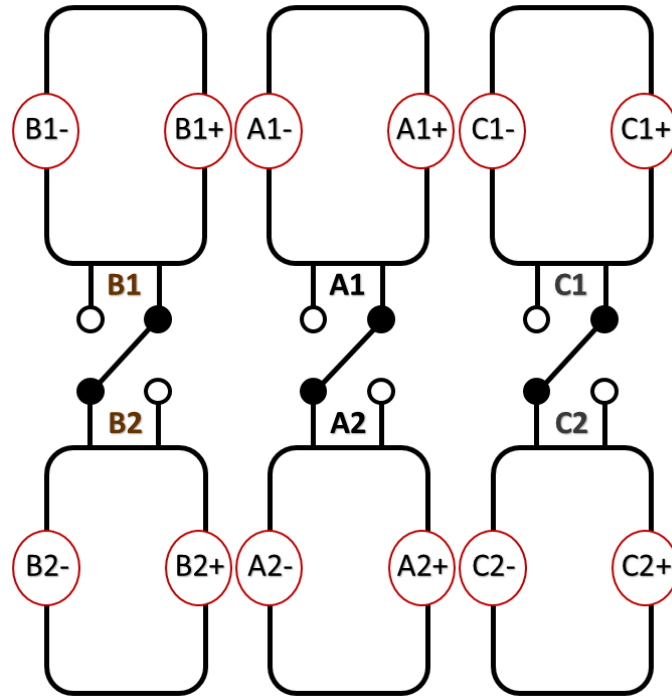


Figure 4. 37: Winding configuration for top and bottom stator

A small portable instrument, called ‘Megger’ was used to finally check the insulation between the coils and the stator structure. Each coil passed the test by showing very high resistance (mega-ohm range) between different coils and the stator structure. After successfully passing the insulation test, each coil was covered with varnish to ensure the bonding and improve their resistance to humidity. Finally, each coil was tightly wrapped with thermal insulating tapes as shown in Figure 4.38. Finally, all coils’ terminals were soldered to banana plug socket female connectors in the six designated holes on the stator support to provide a path for the coil terminals.

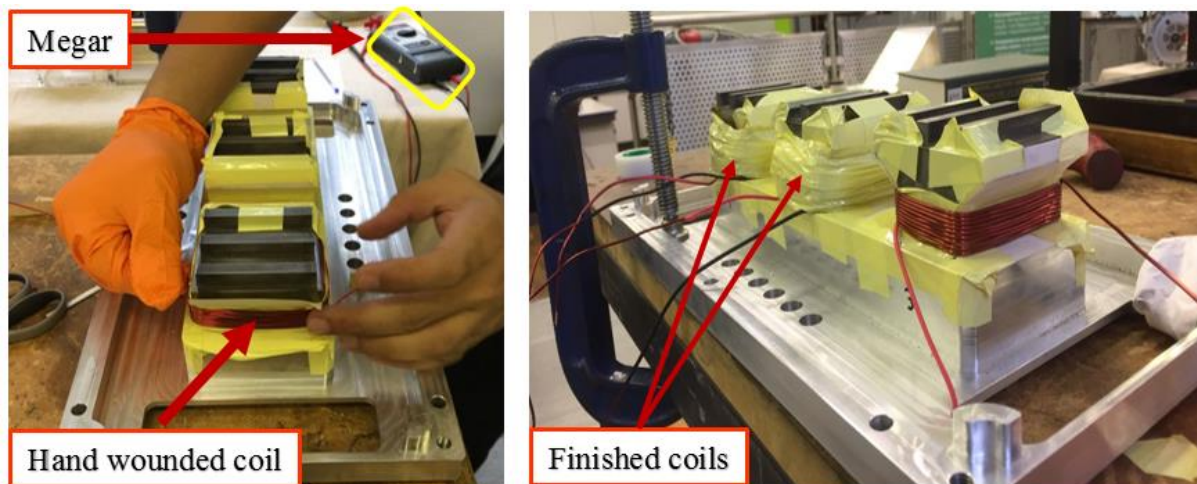


Figure 4. 38: Hand winding process and finished coils.

### 4.5.3 Permanent Magnets Assembly

The permanent magnets used in the prototype machine are shown in Figure 4.39. Rectangular nickel (Ni) plated Neodymium Iron Boron (NdFeB) grade N42H with a residual flux density ( $B_r$ ) of 1.26T at 20°C was used for the pole and translator magnets. Each stator uses 18 ‘*transition*’ magnets with a dimension of 60×8×4mm and 9 ‘*pole*’ magnets with a dimension of 60×8×8mm. The magnets were manufactured by Bunting Magnetics Europe Limited with a manufacturing tolerance of ±0.05mm.

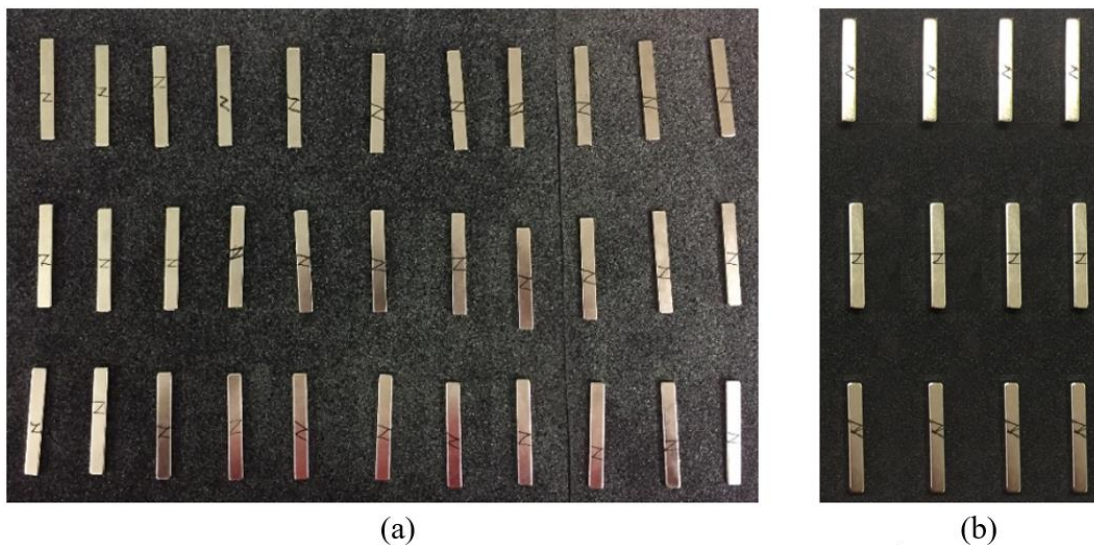


Figure 4. 39: Rectangular Neodymium Iron Boron (N42H) magnets (a) transition magnets (b) Pole magnets

After checking and marking the magnet polarities, advanced materials epoxy resins & hardeners (ARADUR 5052CH & ARADLDITE LY5052) have been used to bond the magnet in their designated positions inside the groves of the stator described before. The selected combination of the epoxy resin & hardener ones cured can withstand a tensile strength of up to 390MPa. To make sure about the placement and bonding between the magnets and the stator, a rectangular TUFNOL bar is used along with three steel clams to hold the magnets in their designated position until the glue gets hardened. It took almost 24 hours to completely cure the glue in room temperature. Figure 4.40 shows the curing stage of the magnets on one of the stators.

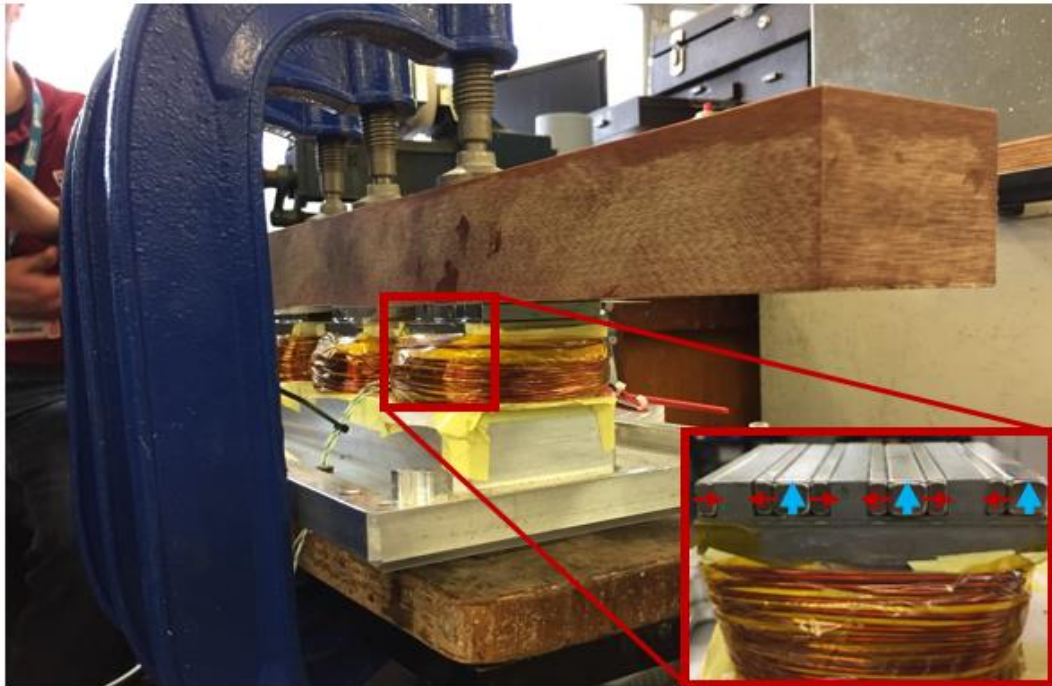


Figure 4. 40: Magnet assembly and curing stage in a stator.

#### 4.5.4 Translator Construction

The translator development and construction can be divided into two major parts: Translator segments and TUFNOL I-beam structure, which is the base for the translator segments.

##### 4.5.4.1 Translator segments

As one of the main purposes of this research is to reduce the mass of the translator, thick core back is removed from the traditional salient pole translator. Instead of the thick and heavy single laminated translator piece, all the identical translator teeth have been wire eroded individually from the 60mm thick lamination stack. Figure 4.41 shows the finished segments and the lamination direction for the prototype machine. Each segment has a length of 30mm and width of 8.5mm. Two semicircle extrusions (diameter of 6mm) were added in the design development to lock the teeth and stop them from being pulled out of the TUFNOL support by the attraction force of stator magnets. 21 segments were required for the machine, but 28 were produced in case of mechanical failures.

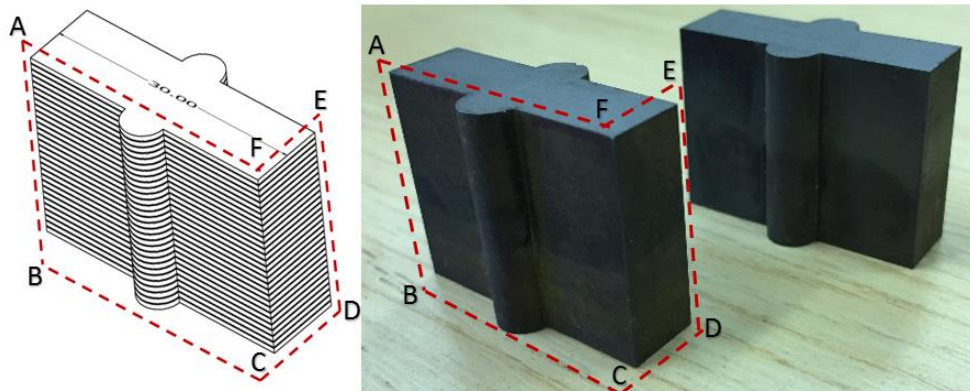


Figure 4. 41: Segmented translator teeth from laminated steel.

#### 4.5.4.2 TUFNOL I-beam structure

The segmented translator teeth are held in place by an I-beam made of solid TUFNOL block which is non-magnetic and can be machined by the milling machine to meet the design requirement. A rectangular TUFNOL Whale Sheet of 600×300×50mm dimension has been ordered from a leading UK supplier of cellular plastic building products named “Direct Plastic” (see appendix). The block was cut into 600×120×50mm block and 21 slots were machined across the width of the TUFNOL block by the technician for inserting the translator segments. Each slot has been machined to fit the translator segments accurately. Due to the use of a twisted drill bit, there remained half cylinder slots on top and bottom of the slots after inserting the segments (Figure 4.42).

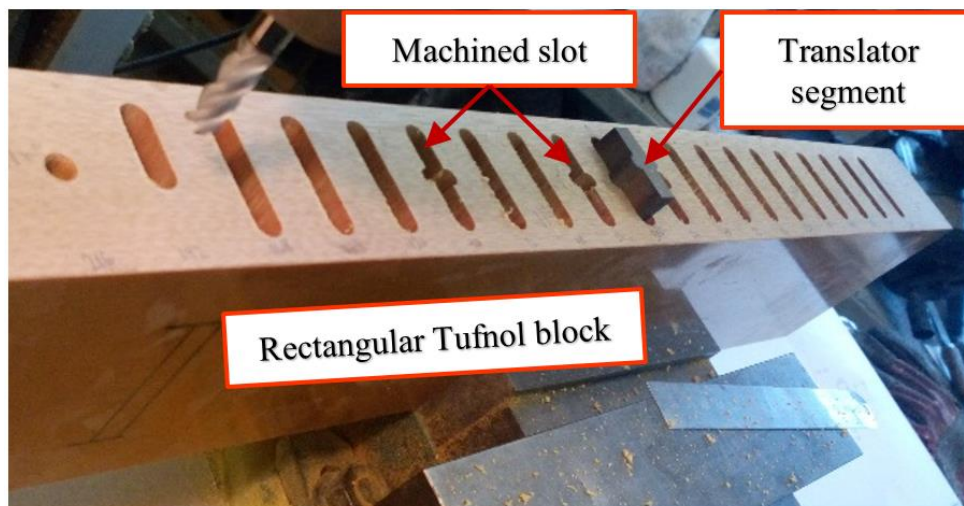


Figure 4. 42: Machining of TUFNOL I-beam structure.

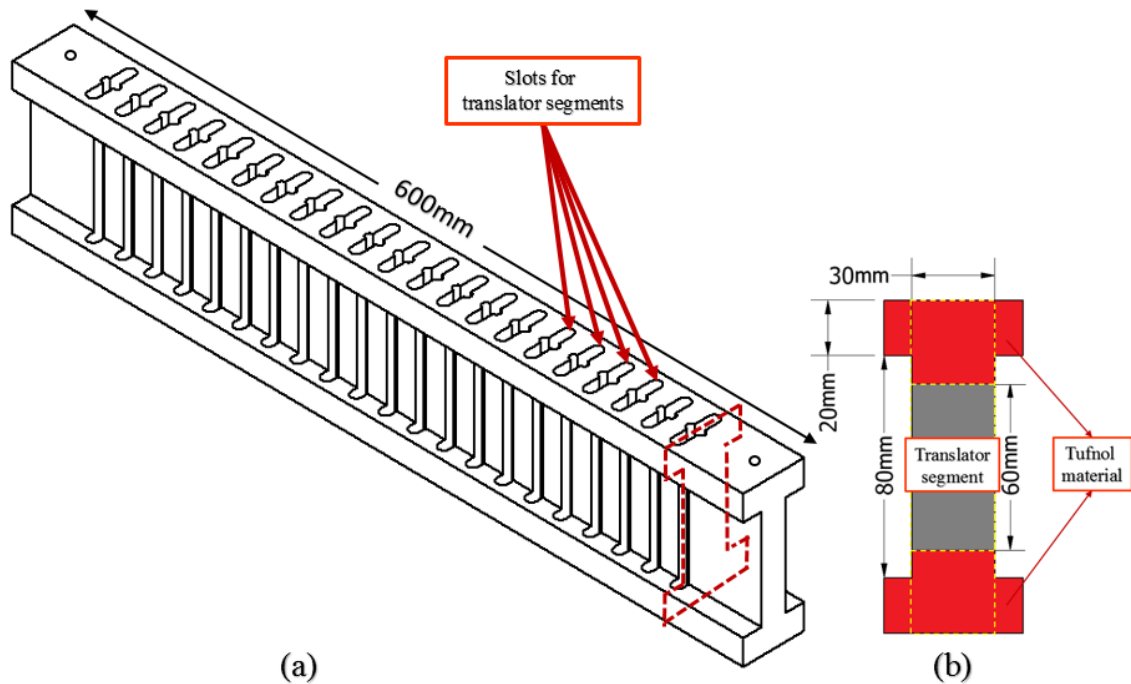


Figure 4. 43: (a) Machined TUFNOL I-beam structure with slots for translator segments (b) cross-section of the slot.

All the slots were 24mm apart from each other which is the translator tooth pitch. After machining the slots, two equal rectangular cuts were machined from both sides across the length of the TUFNOL block to give an I-beam shape shown in Figure 4.43(a). It shows the 3D drawing of the final TUFNOL I-beam structure with machined slots for translator segments. The thickness of the middle of the I-beam is 30mm to match the length of the translator teeth. There was 56mm un-slotted region on both ends of the TUFNOL structure to give strength and connect with the aluminium support structure with threaded bolts. Figure 4.43(b) shows all the dimensions of the cross-section of the TUFNOL I-beam across a slot.

#### 4.5.4.3 Translator segments assembly

After all the slots and I-beam TUFNOL structure was machined, 30mm thick wedges were inserted inside all the slots. Afterward, 21 translator teeth segments were inserted in a way that they sit exactly on top of the wedges so that they stay in the middle of the I-beam structure and there was 30mm clearance on top of the translator segments (Figure 4.44).

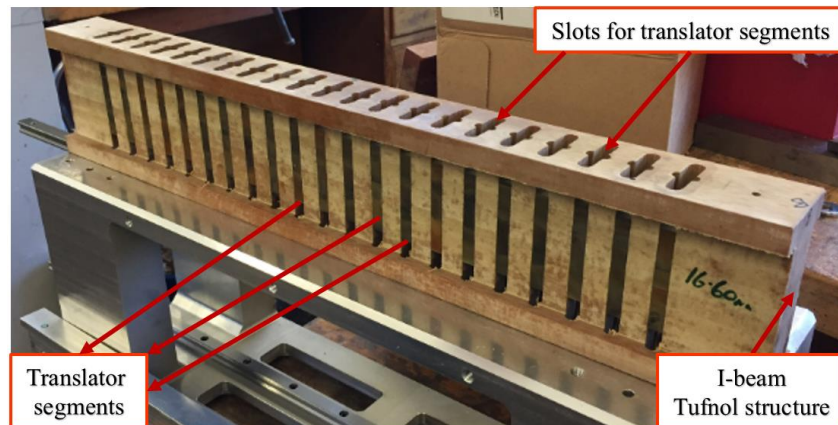


Figure 4. 44: Assembly of translator teeth segments inside the TUFNOL I-beam structure.

Then a 30mm clearance from the top of the translator teeth to the surface of the I-beam was filled with the potting component — hot melt glue. After the glue has cured, the I-beam is flipped so that the potted side is down, and the wedges are on top. The wedges were removed from the slots which revealed the slot on top of the segmented teeth. Then the previous method of filling those slots with the hot melt glue was repeated. Figure 4.45 illustrates the potted translator I-beam assembly.

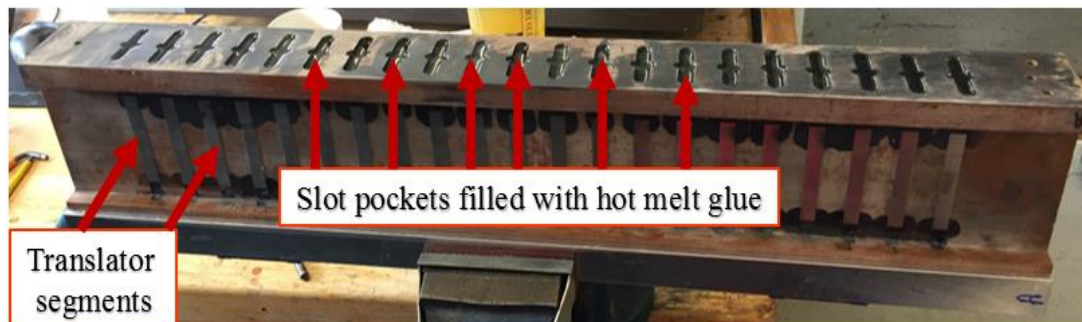


Figure 4. 45: Assembly of the translator teeth segments inside the TUFNOL I-beam structure.

#### 4.5.4.4 Aluminium I-beam caps

Two aluminium I-beam caps were fitted on top and bottom of the potted translator I-beam structure to accommodate the carriages. Two 600×200×20mm aluminium blocks were used to make the I-beam caps. Four bolts were used to attach those two caps with the TUFNOL I-beam (Figure 4.46).

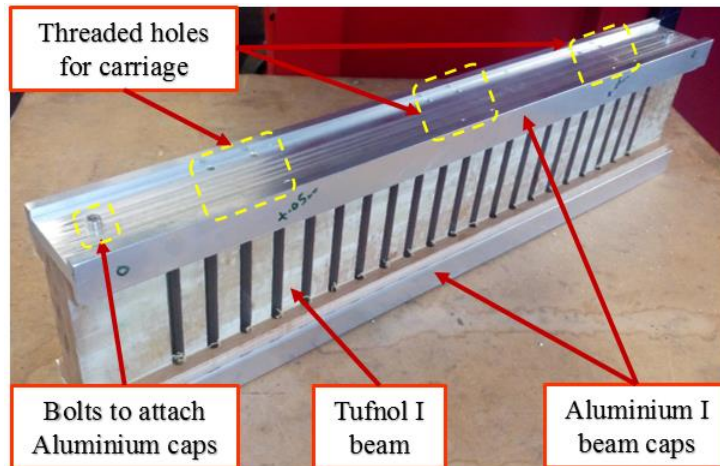


Figure 4. 46: Attaching the aluminium I-beam caps on the TUFNOL Structure.

#### 4.5.4.5 Shaft and carriage assembly on translator support

Three sets of four holes have been made on both aluminium caps to mount three carriages on each side shown in Figure 4.46. Four threaded bolts have been used for each of the six linear flanged carriages to attach with the aluminium I-beam caps. Apart from the threaded bolts, the flanged edge of the I-beam caps hold and support the carriages from being shifted and maintain the alignment of all the carriages (Figure 4.47). The shaft was made of non-magnetic graded stainless steel of 30mm diameter. It was connected to the translator structure by a U-shaped thick aluminium holder shown in Figure 4.47. The aluminium holder not only connects the shaft with the translator support but also holds the top and bottom aluminium parts with the TUFNOL structure. The other end of the shaft is threaded, to attach it with the actuator to move the whole translator structure backward and forward linearly.

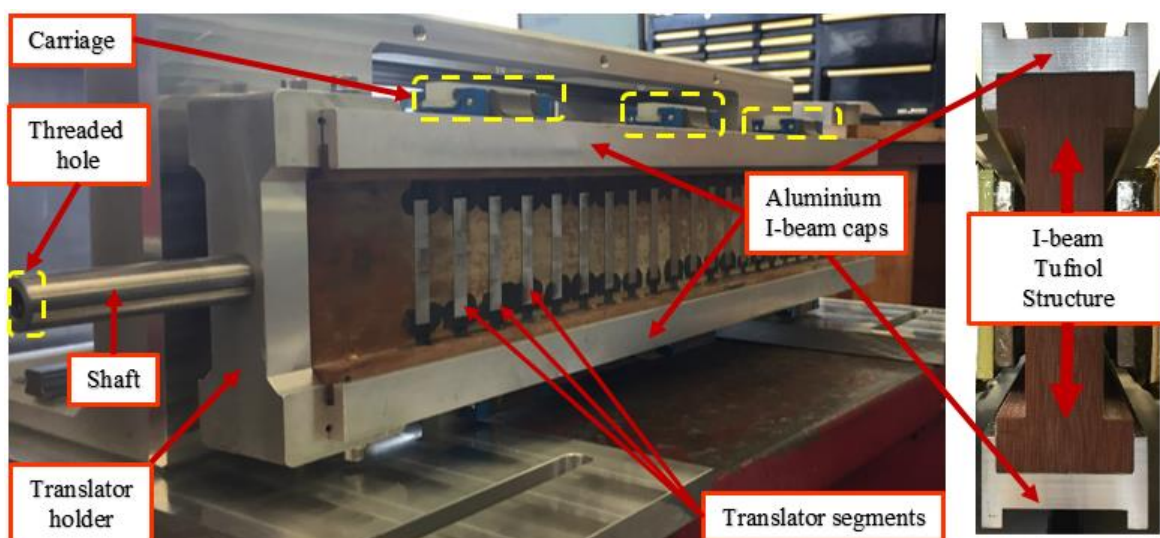


Figure 4. 47: Complete translator assembly.

#### 4.5.5 Machine Housing Development & Construction

The aluminium machine housing is one of the most important parts in the machine support and took almost three months to develop and build. It accommodates both the stators and the translator. Two 700mm long linear guide rails are supposed to be attached to the top and bottom surface of the housing structure. In the initial design, it was assumed that each rail will be connected to an individual base plate and then both the base plates would be mounted on four 'L' shape structural beams as shown in Figure 4.48. But this design would require a high number of component parts and assembly of all the parts accurately will be a real challenge. Again, the strength and loading capability were also important issues. It should have been required stainless steel structures to guarantee the strength, it would make the whole structure very heavy as well. So, after careful consideration and discussions, a new housing structure is developed and machined from a single solid block of aluminium-6082 with a dimension of 600×200×250mm.

Figure 4.49 shows a detailed 3D drawing of the final housing design with important dimensions. Translator window allows the translator to move linearly in and out of the housing. Both the stators along with their supports could be fitted through two sides and attached with the housing by the threaded bolts.

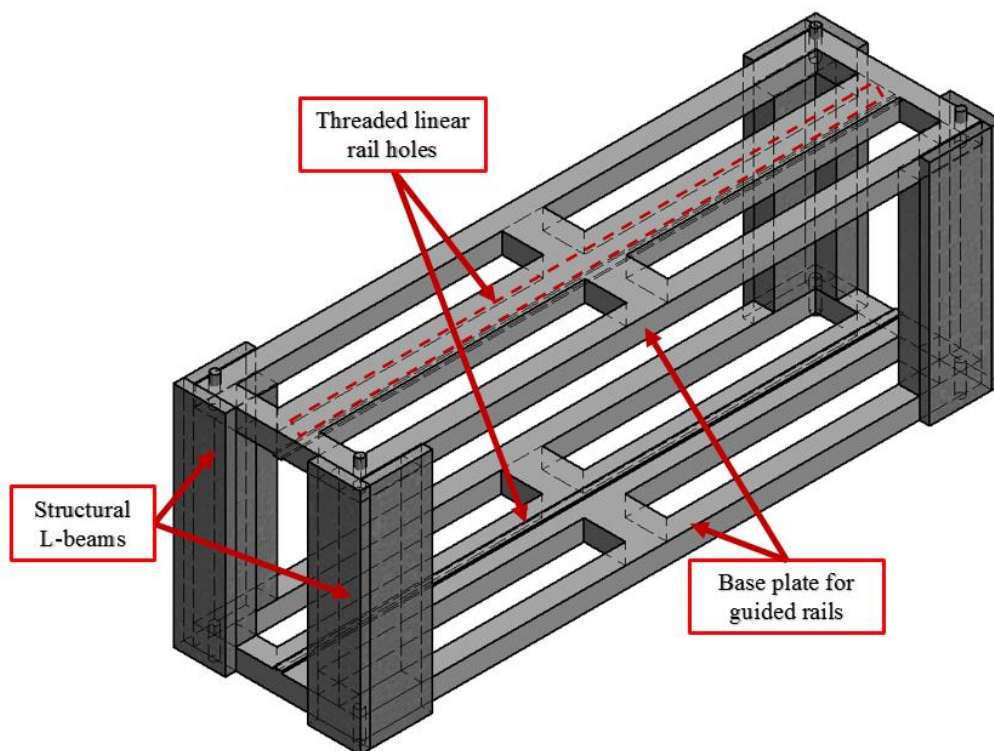


Figure 4. 48: Initial design for the steel housing structure

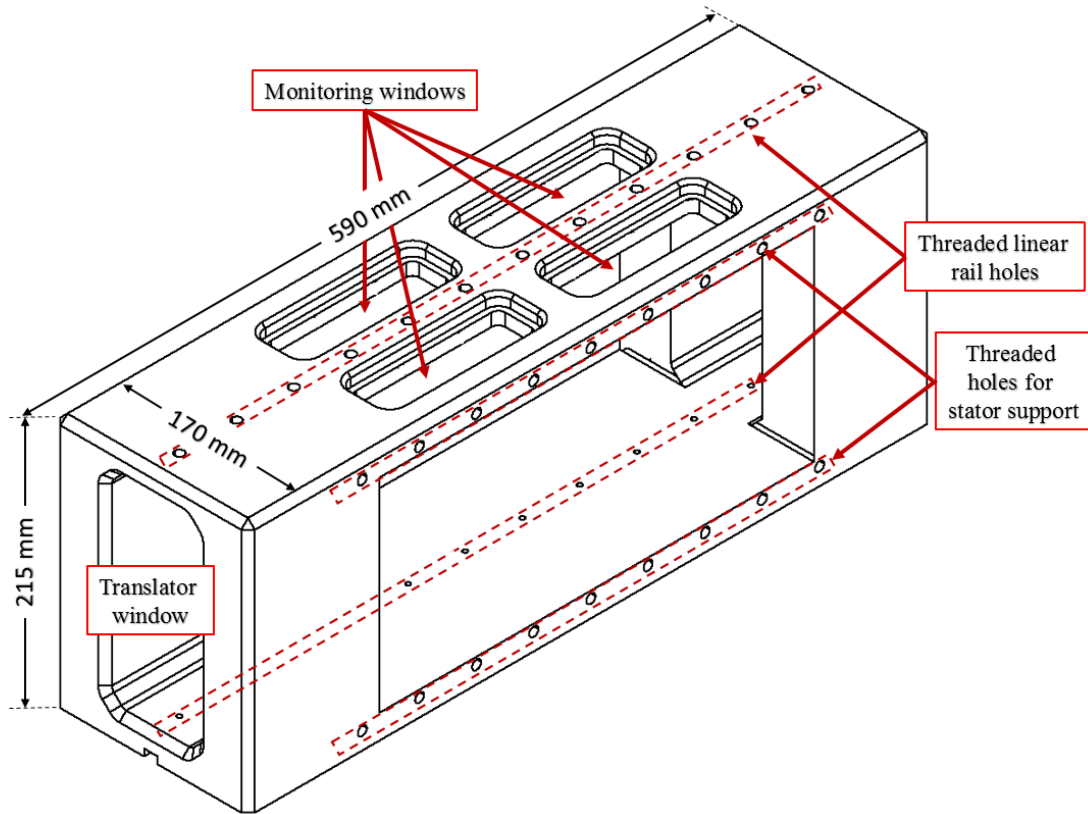


Figure 4. 49: Final design of the aluminium housing.

The housing allows the mechanical air gap to be adjusted from 7mm to 1mm by adjusting the bolt, which connects the stator aluminium supports (aluminium caps) to the housing. Four monitoring windows on top of the housing allow seeing inside the housing while under operating conditions. Figure 4.50(a) shows the solid aluminium block and Figure 4.50(b) is the finished single piece housing.

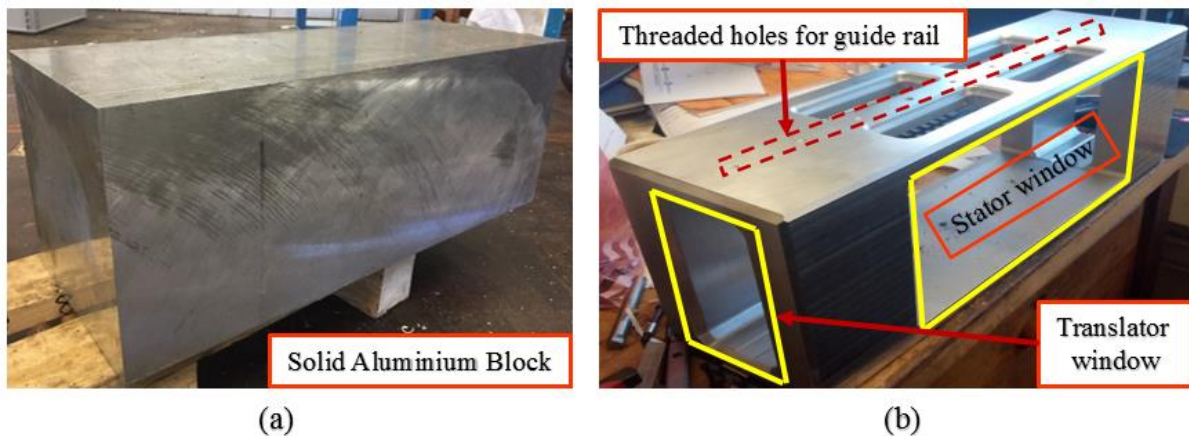


Figure 4. 50: Aluminium housing (a) solid Aluminium block (b) machined structure.

#### 4.5.6 Machine Assembly

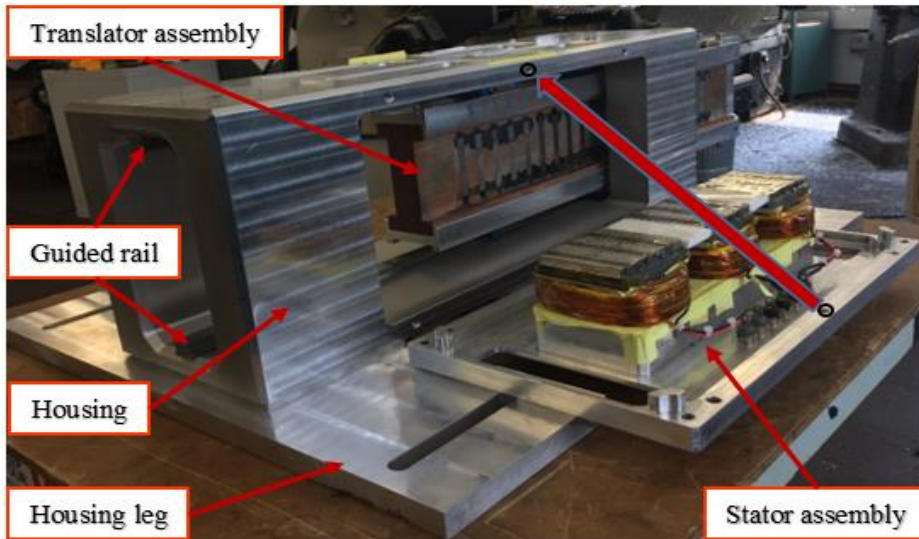


Figure 4. 51: Assembling the translator and the stators in the aluminium housing

Figure 4.51 illustrates the final assembling of the translator structure and the stator structure in the aluminium machine housing. First, the carriages of the segmented translator are aligned and inserted inside the housing using the extended linear guide rails (shown in Figure 4.51). Once all the carriages of the translator are coupled with the rail and the translator is set inside the housing, then stators with the caps were carefully inserted in the stator window. All the screws are bolted afterward to keep a big air-gap of 7mm at the beginning. As mentioned earlier, these screws can be easily controlled to adjust the air-gap manually later. Figure 4.52 illustrates the air-gap controlling mechanism clearly. Once, all the components were mounted and bolted safely, the whole structure was transferred into the flat testbed where the shaft of the translator would connect with the linear actuator via the small connector.

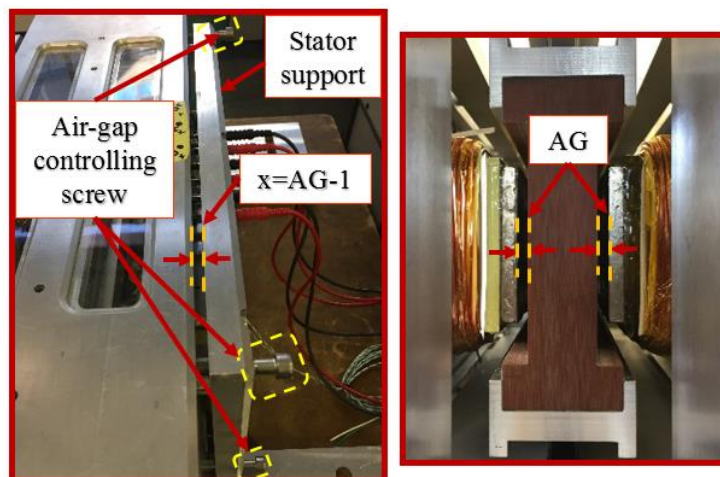


Figure 4. 52: Air-gap controlling by adjustment screws.

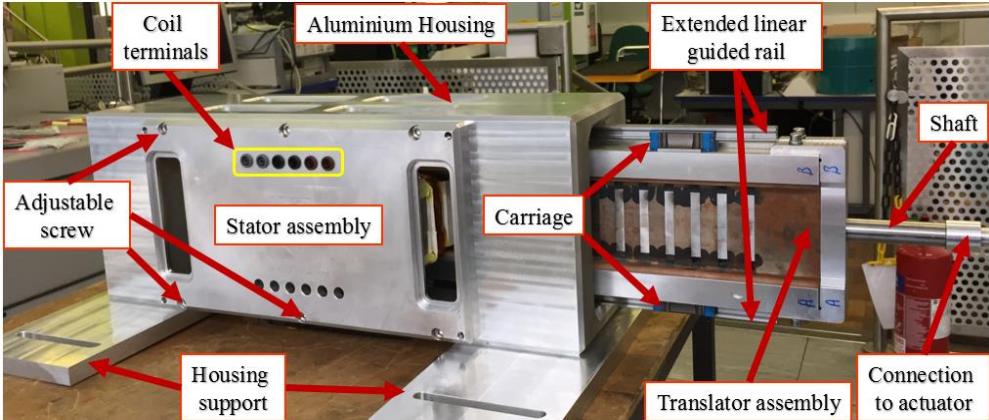


Figure 4. 53: Fully assembled linear HCVHM with segmented translator

Figure 4.53 shows the fully assembled final prototype machine on a wooden table. The whole structure will be attached over the base plate to form a test rig and will be illustrated in the next section.

## 4.6 Prototype Machine Testing

### 4.6.1 Thermal Testing

The thermal testing is done to determine the machine's capability to dissipate heat, which is a limiting factor for maximum force generation application. Magnetic saturation, magnet demagnetisation, insulation failure due to high temperature are some other limiting factors that can be caused by temperature rise in the machine. The major source of heat is the resistive power loss in the windings. A thermally limited current can be determined by knowing the dissipated resistive loss as heat in the winding.

Seven 'K-type' thermocouples have been attached in different parts of one of the two stators assembly, marked by yellow circles in the following figure. These thermocouples are used to monitor temperature rise at different parts of the stator assembly.

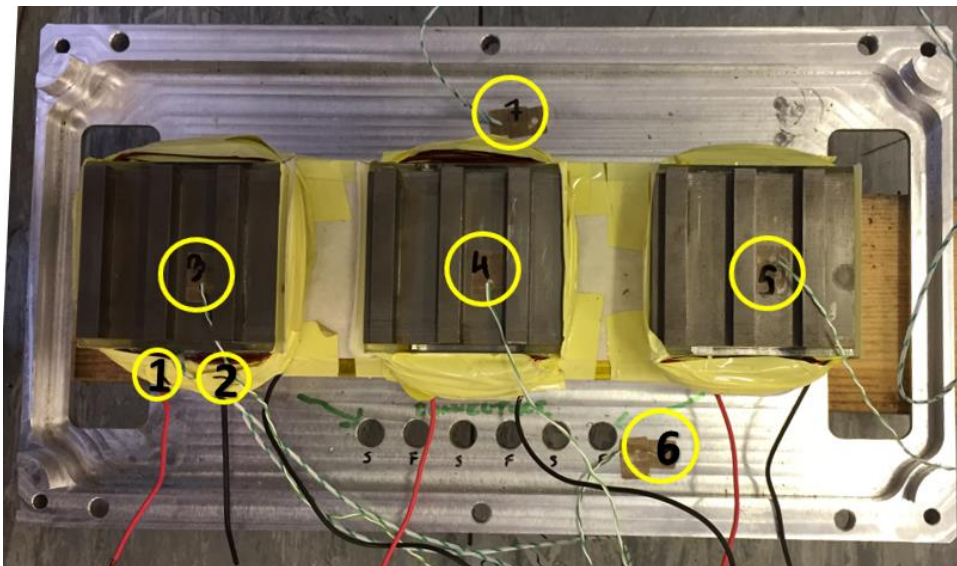


Figure 4.54: Position of thermocouples on the stator assembly.



Figure 4.55: Thermal testing of three-phase winding.

Thermocouples positions:

1. Coil centre
2. The surface of the coil
3. The surface of the stator tooth#1
4. The surface of the stator tooth#2
5. The surface of the stator tooth#3
6. The surface of the stator support
7. The surface of the stator support

For this test, three phase windings of the E-core stator are connected in series and fed with a constant direct current (DC) until the temperature of the thermocouples reached a steady state. The temperature from all the thermocouples was recorded every 5 seconds for the duration of the experiment. The cooling curve was also measured the maximum temperature monitored during the test is inside the coils. To monitor the maximum temperature points, Figure 4.56 shows the results of coil temperature for two different levels of current (7A and 8A), which both ran over a period of 4 hours. In the air, the peak coil temperature rises to 57°C and 75°C for 7A and 8A DC current respectively.

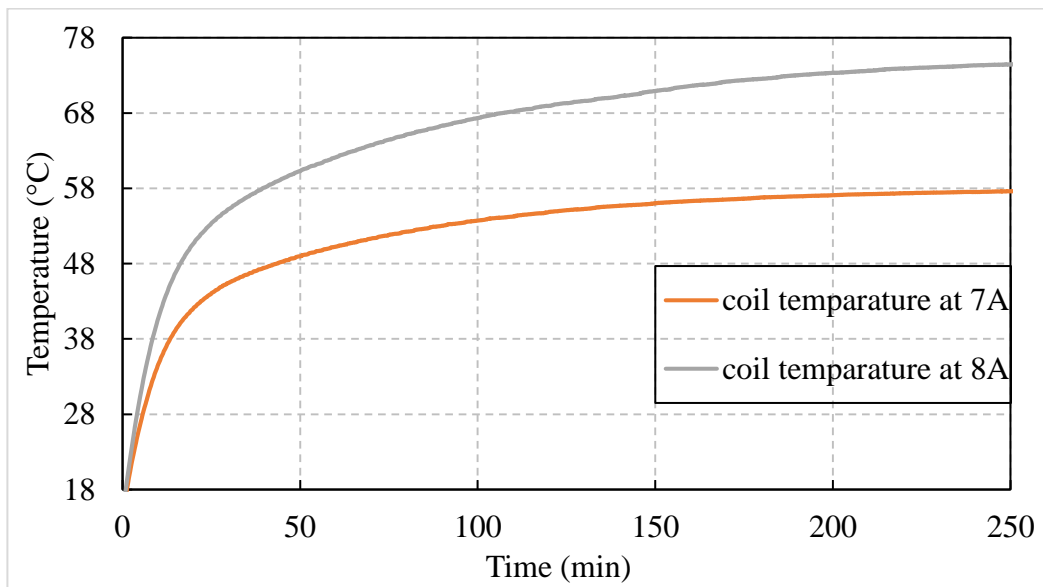


Figure 4. 56: Temperature rise of the coil center at different DC current level.

Thermal time constants are given in Table 4-4. The peak temperature rise in the coil is almost proportional to the increase in thermal time constant. A longer time constant means larger thermal inertia that depends on the surrounding environment. For water or oil cooling system, the time constant is even smaller.

Table 4- 4: Thermal test with various excitation current.

DC excitation	Peak temperature (°C)	The thermal time constant (min)
7A	57	11.5
8A	75	15.5

To ensure the proper insulation of the stator and stator casing, it was placed on top of a rectangular wooden structure (showed in the Figure 4.55) to ensure the heat dissipation is only due to the surrounding air.

The temperature of the machine components changes exponentially with time depending on their individual unique thermal time constants. To simplify the thermal modeling, it is assumed that there are only two thermal time constants- one for the armature windings/coils and the other which relates the stator core and the aluminium stator support. The time constant for the armature winding is much shorter than the time constant for the stator core and support. The average temperature rise can be expressed by the following equation,

$$T_{avg} = T_0 + T_c \left(1 - e^{-\frac{t}{\tau_c}}\right) + T_s \left(1 - e^{-\frac{t}{\tau_s}}\right) \quad (4-12)$$

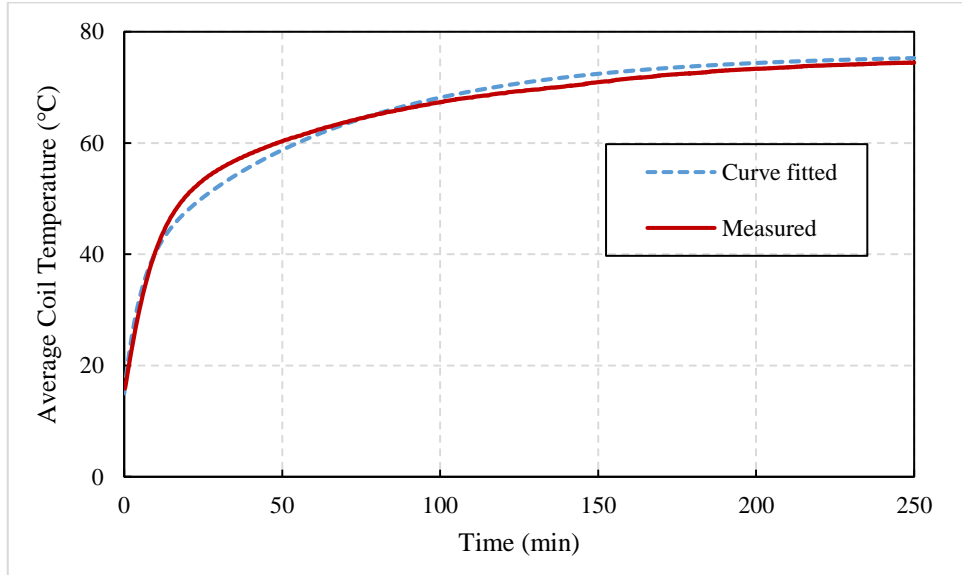


Figure 4. 57: The coil temperature rises for 250 minutes.

Where,  $T_0$  is the initial temperature which is assumed to be 15°C, the subscript ‘c’ refers to the “coil” and ‘s’ refers to the “stator and support” elements of the temperature rise.

Figure 4.57 shows the thermal test result which ran for 250minutes to reach thermal equilibrium. The red solid line is the measured temperature rise in the coil from the thermocouple and the blue

dashed line was predicted from the equation (4-12). The blue dashed line resembles the temperature rise in the combined stator core and the stator support structure where the  $T_s=23^\circ\text{C}$ ,  $T_c=38^\circ\text{C}$ ,  $\tau_s=300^\circ\text{C}$  and  $\tau_c=4000^\circ\text{C}$ . The temperature rises from the coil and the stator and support subsystem give the final steady state temperature of  $75^\circ\text{C}$  which very closely matched with the experimental results.

The thermal data can also be used to predict the rated operating current of the machine, assuming the thermal limit for the winding is  $T_2=150^\circ\text{C}$ . For the  $75^\circ\text{C}$  temperature rise, the current was 8A. Thermal power loss is proportional to the square of the average current. For the same heat transfer coefficient and machine surface area, the rated thermal current is found to be 11.3A (which is almost equivalent to a sinusoidal current with a peak amplitude of 16A) from the following equation,

$$\frac{I_{rated}}{I} = \sqrt{\frac{T_{rated}}{T}} \quad (4-13)$$

## 4.6.2 Force Measurement

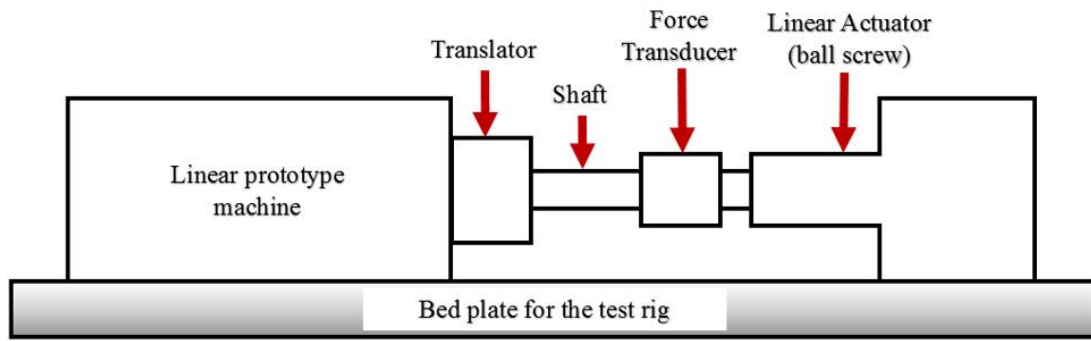
### 4.6.2.1 Description of Test rig set-up

To measure the static and transient forces, the linear prototype machine was mounted on a  $3000\text{mm}\times 900\text{mm}\times 50\text{mm}$  rectangular steel base plate. The cylindrical shaft was coupled with the translator and the force transducer. The other terminal of the force transducer was connected to the linear ball screw actuator. The translator movement was controlled by the in-built ball screw drive controller inside the actuator. Figure 4.58(a) illustrates the schematic of the test rig setup and Figure 4.58(b) shows the laboratory assembly set-up.

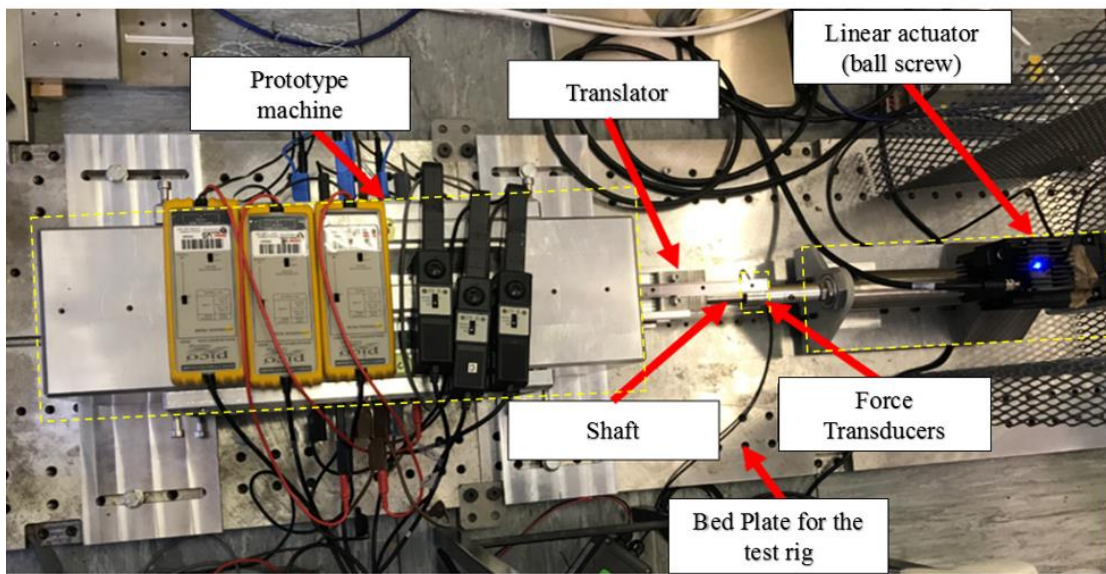
### 4.6.2.2 Cogging Force

Cogging force solely depends on the interaction between the stator and translator during magnetic excitation only; without any armature excitation. It introduces vibration and noise, which generates losses in the machine. It also introduces ripple in the electromagnetic thrust force produced by the machine.

A static test has been performed to measure the cogging force in the prototype. A 10kN force transducer is used to measure the static voltage at different translator position over 24mm distance (one electrical cycle). The voltage is then converted into the force by using the conversion ratio provided by the manufacturer (calibration certificate included in the appendix).



(a)



(b)

Figure 4. 58: Test rig setup for the prototype machine (a) schematic drawing (b) laboratory assembly

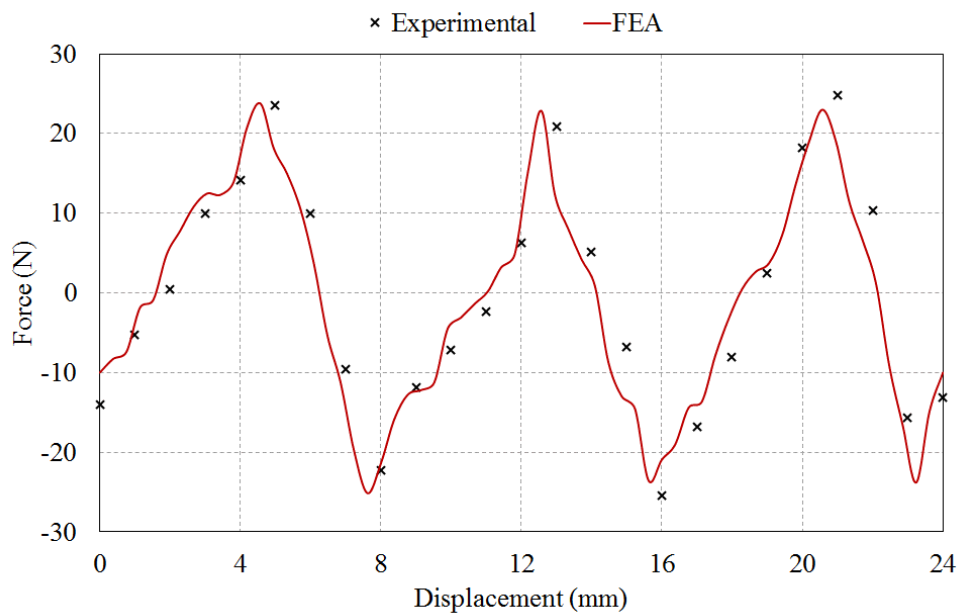


Figure 4. 59: Cogging force variation with the translator displacement after removing offset.

The measured cogging force is plotted in Figure 4.59, which correlates the FEA predicted cogging from the experimental result. It shows a good match between measured and predicted results with a maximum deviation of less than 10% that occurs at some measured points. These deviations are caused due to some unavoidable mechanical tolerance in the machining and assembly process of the segments in the translator e.g. gluing the PM by hand, friction in the sliding bearings, assembly of different machine components. There are also some displacement errors due to the tolerance of the linear actuator. However, friction and measurement errors also add up to this deviation.

#### 4.6.2.3 Thrust Force

DC static force testing method is used to measure the maximum force of the prototype for two different air-gaps. The variable air-gap is to validate the proposed model with the FEA design. Figure 4.60 shows the circuit connection for the test. This will emulate an instantaneous three-phase sinusoidal current. In this method, a fixed DC current is applied in one phase from the DC source and the other two phases experience half of the supplied current in the opposite direction. During this test, temperature rise inside the winding is monitored.

Figure 4.61 and Figure 4.62 compare the measured and simulated results during static force test for 8A DC current at two different air-gaps over one electrical cycle. During the experiment, both the forward and backward forces have been measured using the same 10kN force transducer. The measured forces are presented as the average of forwarding and backward forces. Though there are small differences in the peak values rather than between the phases of the waveforms, the correlation is considered acceptable. It is observed that the peak force variation between predicted and measured forces is around 8% in both the positive and negative direction. The divergence between simulation and measured results is due to the aforementioned explanation in the previous sub-section.

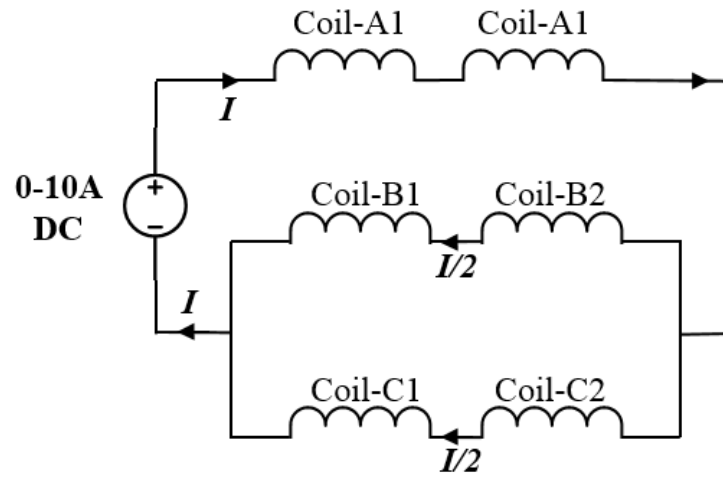


Figure 4. 60: Electrical circuit connection for the static force measurement.

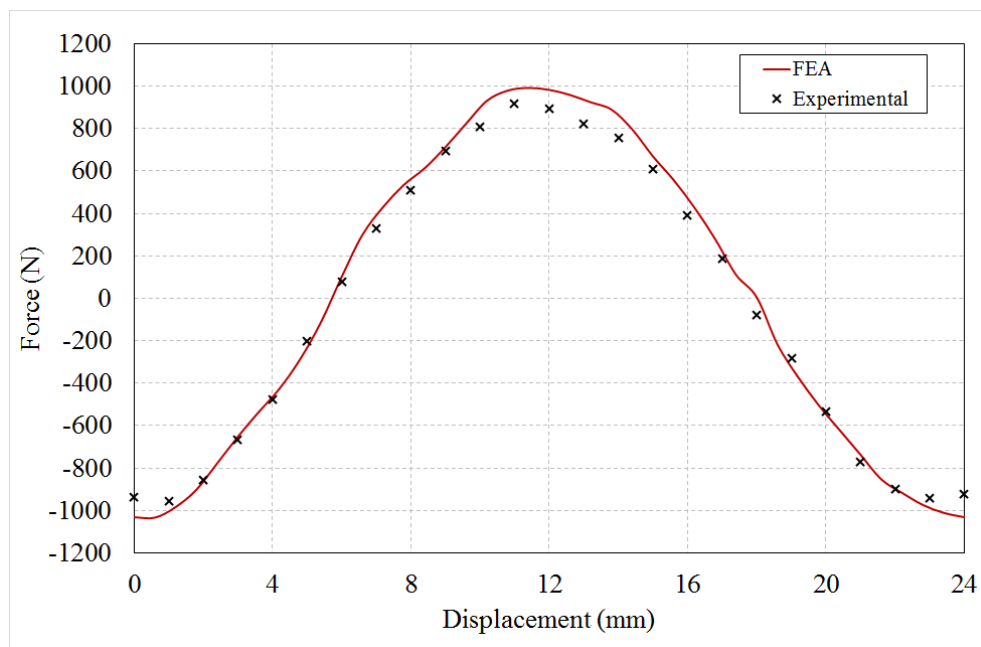


Figure 4. 61: Static force test at different translator position during 8A DC excitation (air-gap=1mm)

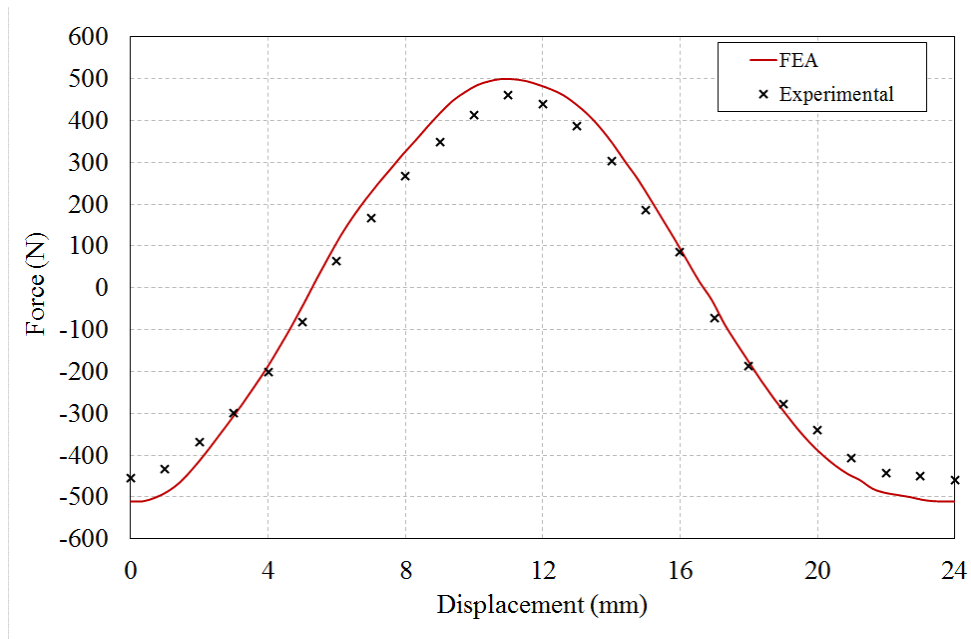


Figure 4. 62: Static force test at different translator position during 8A DC excitation (air-gap=2mm)

### 4.6.3 Electrical Performance

#### 4.6.3.1 Open circuit test

The open circuit test is performed by using the linear ball screw at various speeds, controlled via the manufacturer provided software. As mentioned before, two series connected windings made each phase for the prototype machine. Figure 4.63 shows the no-load EMF for two windings on opposite sides of the translator under the same phase. Both the EMF waveforms have almost zero phase difference between them with the same peak value. It also resembles that, number of turns in both windings under the same phase and air-gap setting on both sides are identical.

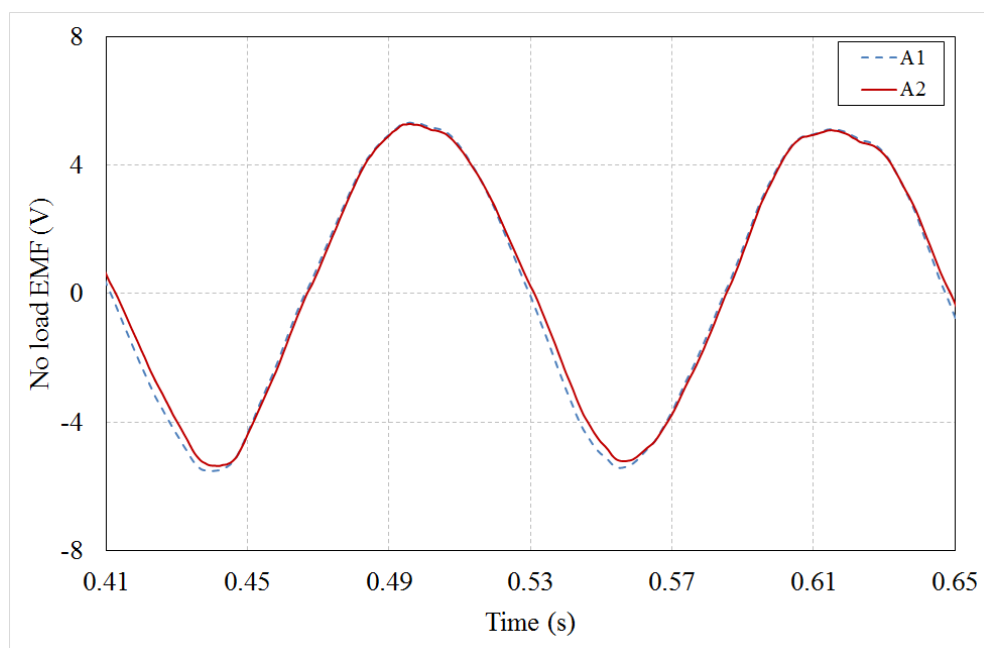
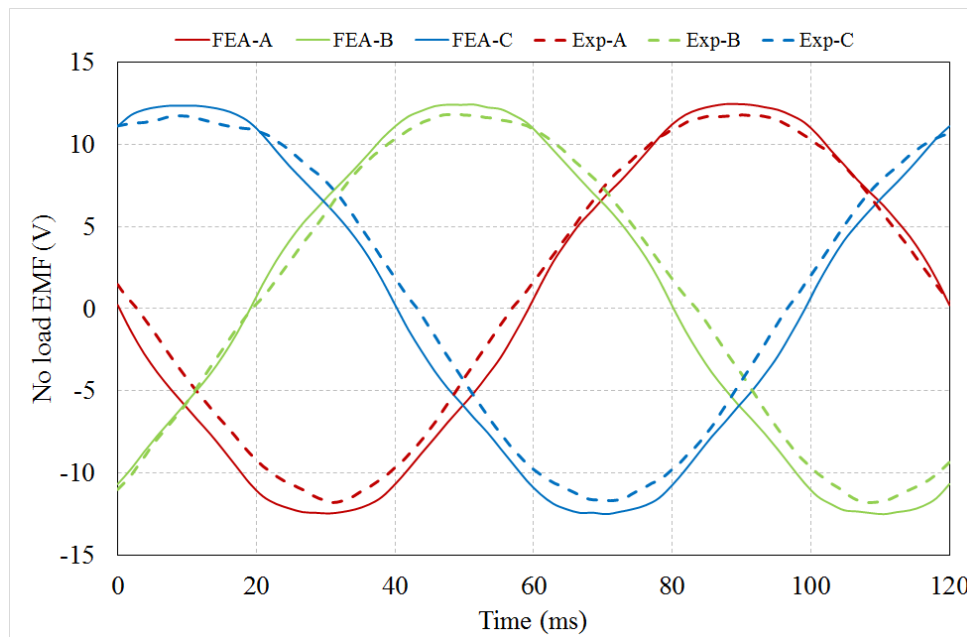
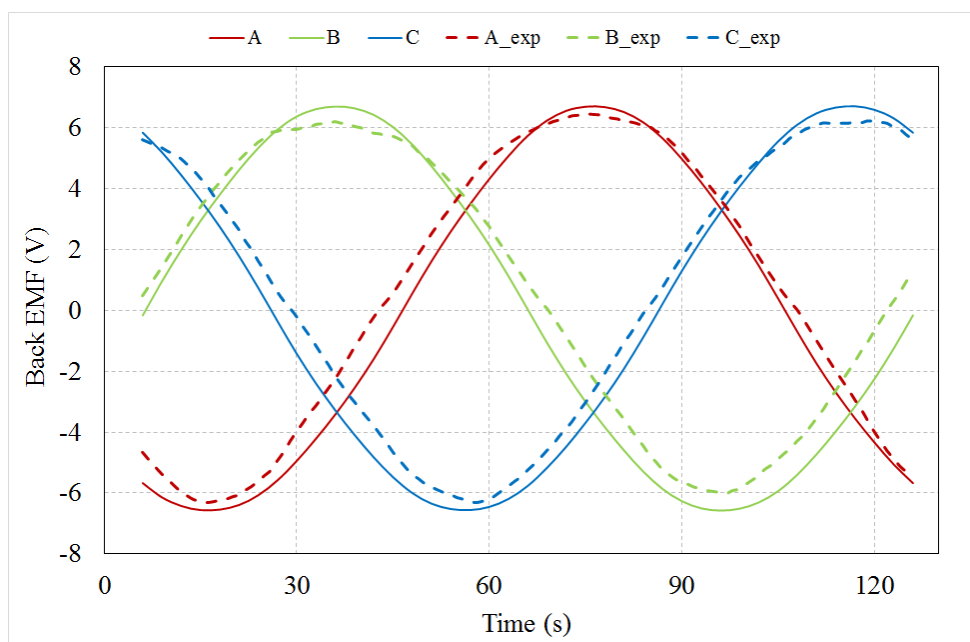


Figure 4. 63: Measured no-load EMF for two coils under the same phase at 0.2m/s

For further no-load tests, two windings under each phase are connected in series and the end terminals are connected to the oscilloscope to record the open circuit back EMF for all three phases. The two graphs in Figure 4.64 show the open circuit EMF comparison between predicted and measured results at a speed of 0.2m/s for two different air-gaps. Both graphs show a good correlation for both air-gaps. Experimental back EMFs show a maximum deviation of 6-7% at a constant speed of 0.2m/s. As experience in the previous sections, there might be some building and tolerance issue and also slight mechanical error might occur while setting air-gaps manually on both sides of the translator that results in lower back EMF compared to the simulation.



(a)



(b)

Figure 4. 64: Measured no-load EMF results (a) AG=1mm (b) AG=2mm.

Figure 4.65(a) shows the variation of no-load induced voltage with translator position at variable speed. The maximum speed reached during this variable speed operation is 1.3m/s. Figure 4.65(b) represents one electrical cycle from Figure 4.65(a) that resembles the three-phase EMF at 1.3m/s. The correlation between the simulated and measured voltage is very good with a deviation of less than 6% due to the aforementioned explanations.

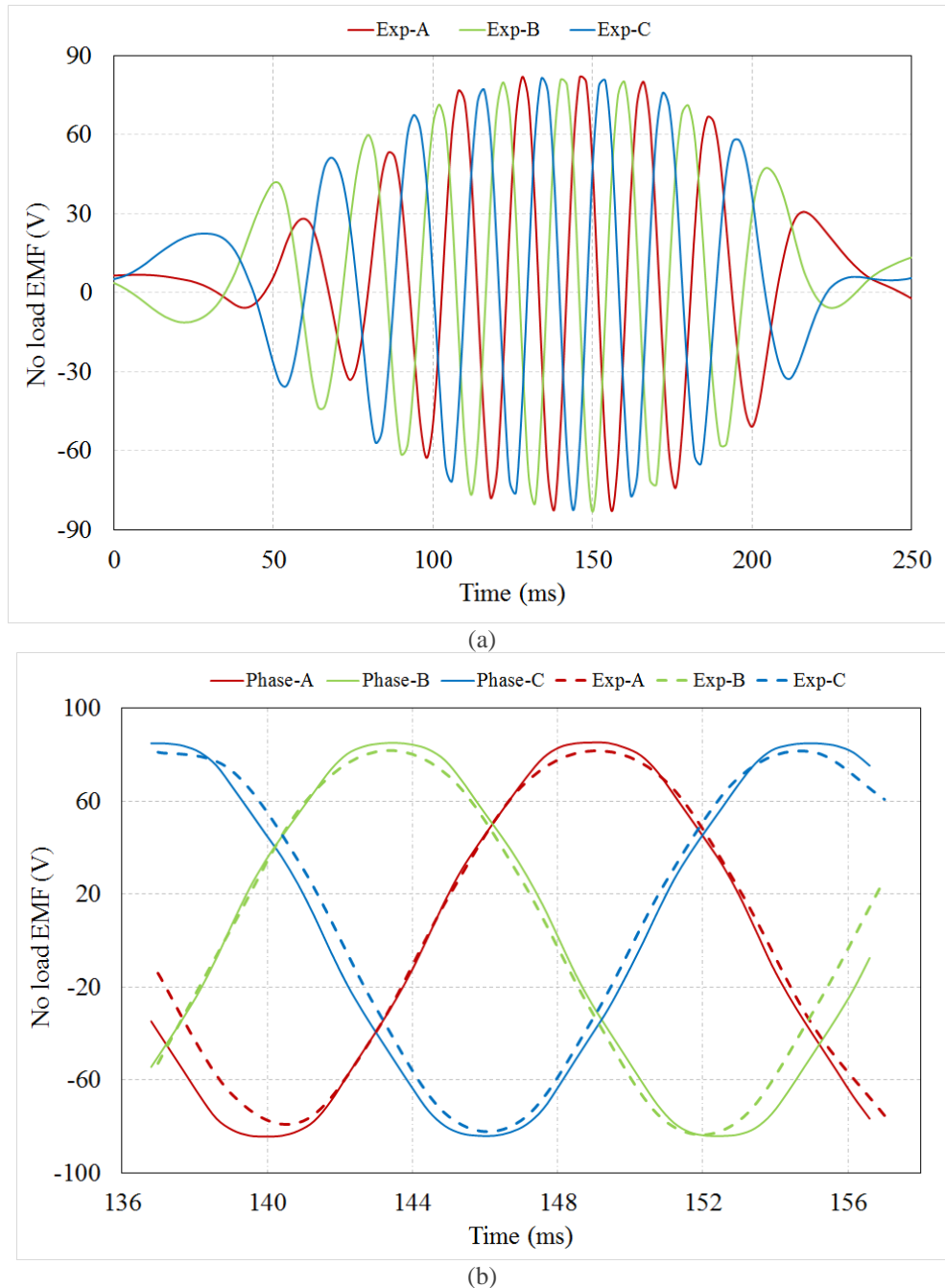
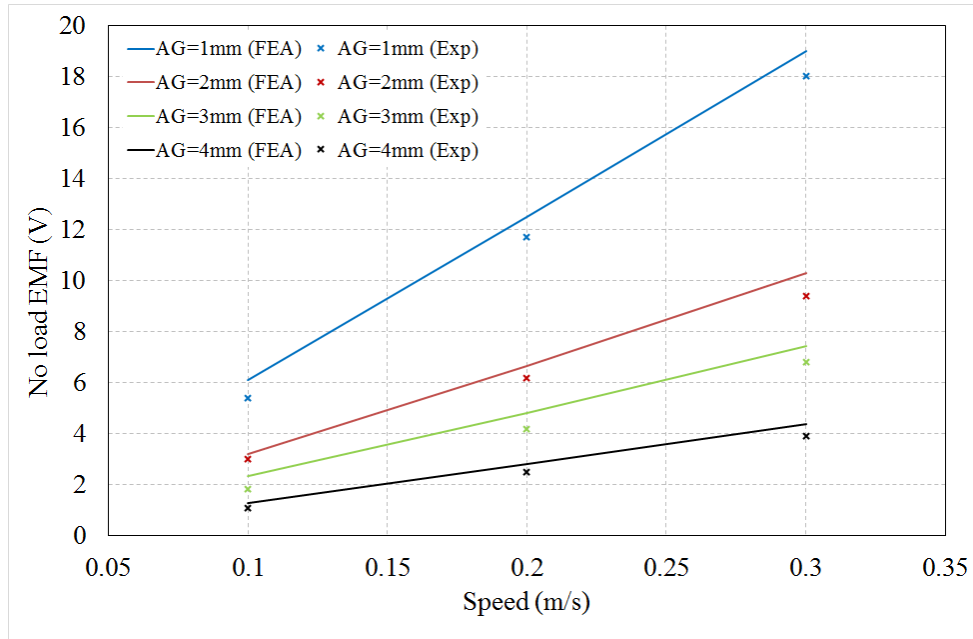


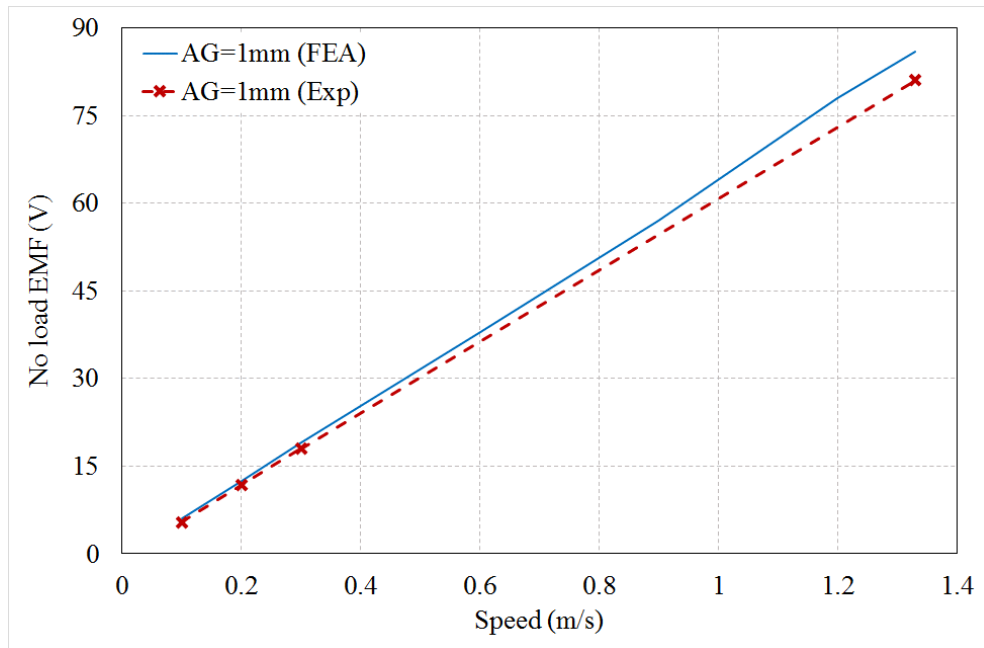
Figure 4. 65: Measured no-load EMF at variable speed (a) for single mechanical stroke (b) compared with simulation over one electrical cycle.

Finally, Figure 4.69(a) summarise the peak open circuit EMF for various speed from 0.1m/s to 0.3m/s for four different air-gaps. Except for some minor deviation in the measured voltage, the measured induced back EMF is directly proportional to the speed and inversely proportional to

the air-gap. These no-load induced voltages at different operating points matched well with the theory and simulation. Confidence can hence be placed in the experimental results, as the linear trend of the measured back EMF results closely matched with the FEA predictions of the simulated results. There are some small deviations. Figure 4.66(b) illustrates the comparison of no load back EMF between simulated and experimental results upto a peak speed of 1.3m/s. The deviation between measured and predicted results is found to be around 6% at maximum speed.



(a)



(b)

Figure 4. 66: Measured no-load EMF variation with speed (a) different air-gap (b) at 1mm air-gap.

4.6.3.2 Short circuit test

Short circuit tests have been performed to predict the current during a short circuit fault condition. Three terminals from three phases were connected in star connection and the other terminals were shorted. The translator was moved at 0.2m/s speed. Figure 4.67 compares the experimental and simulated results of three phase short circuit current. The maximum simulated current is 9.2A compared to 8.7A measured, which gives a deviation of only 5.6%.

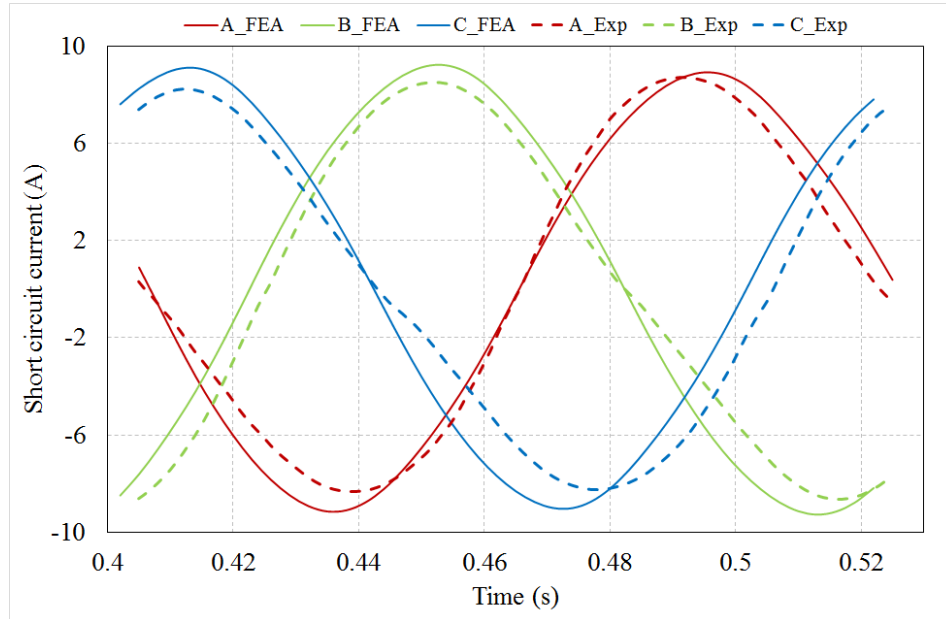


Figure 4. 67: Short circuit current test

#### 4.6.4 Resistance Measurement

The winding resistance is measured individually for every coil. A DC current is applied on individual winding and the corresponding voltage across the winding is measured. The voltage is divided by the supplied current to get the winding resistance. The measurement from two coils of the same phase is simply added together to get the phase resistance. The measurement is performed on all three phases and is found to be  $0.65\Omega$ ,  $0.64\Omega$  and  $0.635\Omega$  for phase-A, phase-B and phase-C respectively. It should be mentioned that, as the resistance depends on the temperature, all the measurements are performed at an ambient temperature of around  $20^\circ\text{C}$ .

#### 4.6.5 Single Coil Inductance Measurement

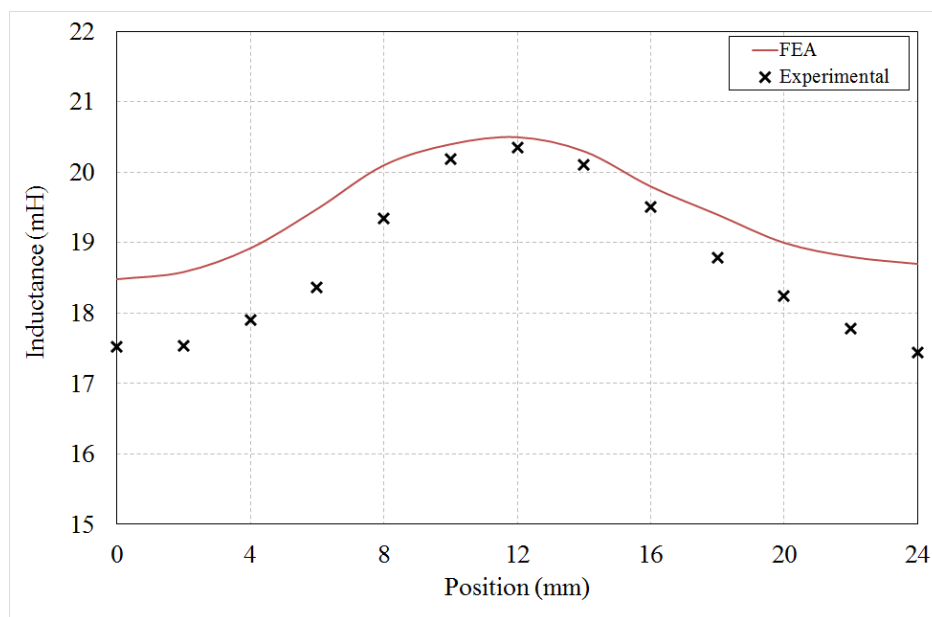


Figure 4. 68: Comparison of experimental and simulation predicted self-inductance of an entire phase.

Replacing the magnetic regions of the simulation with air allows the inductances of the phases to be investigated. The single coil inductance of the prototype machine is measured without the PM attached to the stator. The inductance has been measured in the prototype by applying a 50Hz voltage from a Fluke RCL meter to the phase winding, with the translator being stationary. This procedure is repeated for varying translator positions over a complete electrical cycle. The result is presented in Figure 4.68 which compares the measured self-inductance with the simulated result found from section 4.4.6.2 (method B).

#### 4.6.6 Phase Inductance Measurement

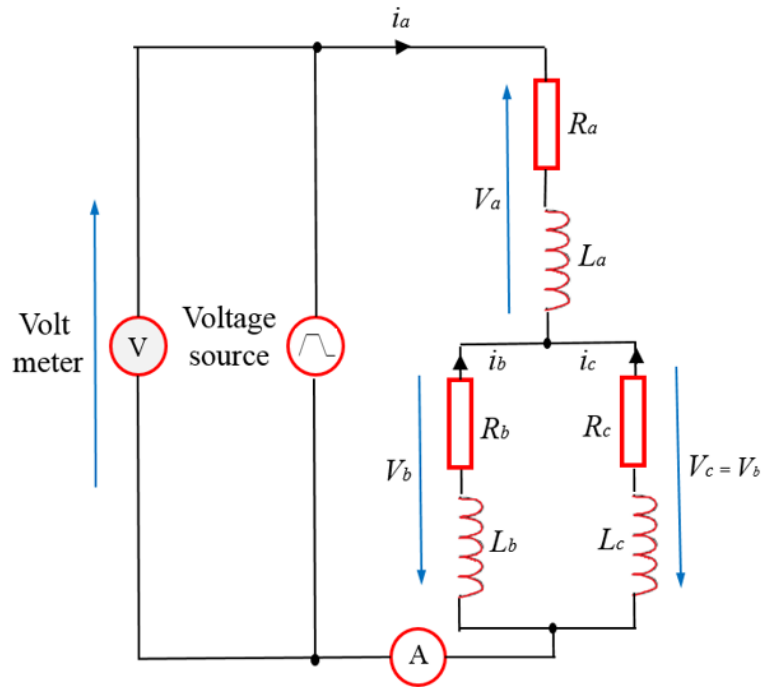


Figure 4. 69: Inductance measurement setup for transient trapezoidal voltage input.

In this method, the measurements were performed with the translator fixed in alternative positions. The machine windings were connected based on the diagram shown in Figure 4.69, in which two phases were connected in parallel and afterward in series with the third phase. As can be seen in the figure, the machine was supplied with a controllable voltage source and the line current was measured through a clamp meter. The controllable voltage source can deliver a trapezoidal voltage. The voltage is used to give rise to the current in the circuit. As it is clear from the circuit, phase-A will experience positive current while the other two parallel phases will experience negative current which is half the magnitude. When the translator was fixed on the desired position, the circuit was supplied with the controlled trapezoidal voltage and the transient current and voltage measurements were conducted under each phase. The same procedure was performed for different translator positions for a complete electrical cycle length. The instantaneous value of flux linkage can be easily calculated from equation (4-11). Furthermore, the phase inductance ( $L_{hase}$ ) can be given by,

$$L_{phase} = \frac{\psi(t) - \psi(0)}{I(t)} \quad (4-14)$$

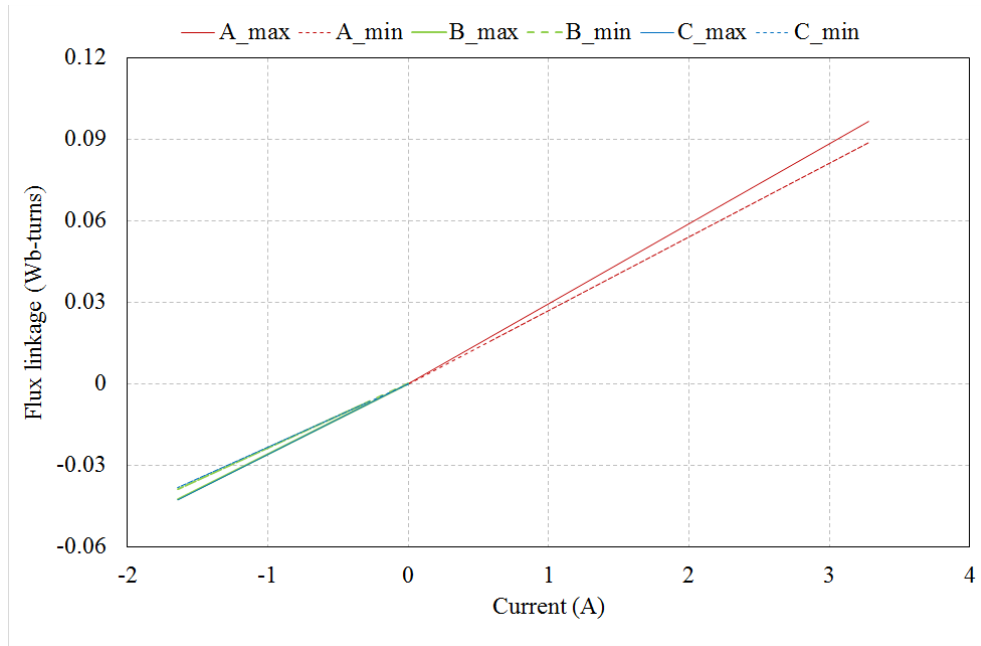


Figure 4.70: Flux linkage plots against the current for three phases.

Phase inductance can be calculated from equation (4-14) and plotted in Figure 4.70. Table 4-5 summarise maximum and minimum of three-phase synchronous inductance for both measured and predicted results. Clearly, phase-A inductance is higher compared to the other two phases, as it experiences mutual fluxes from both phase-B and phase-C. The following results also show a very good match between measured and predicted FEA results with a maximum deviation of 4%.

Table 4- 5: Synchronous phase inductance for three phases

Parameters	FEA-Inductance (mH)	Measured-Inductance (mH)
Phase A_max	28.5	29.4
Phase A_min	26.9	27.1
Phase-B_max	25	25.9
Phase-B_min	22.7	23.7
Phase-C_max	25.2	26.1
Phase-C_min	22.5	23.3

#### 4.7 Conclusion

Details of the development, construction, and verification of the lab-scale prototype HCVHM have been described in this chapter. A double-sided E-core HCVHM with a new PM array has been developed and optimised. The presented HCVHM offers a substantial saving of translator mass by employing a segmented translator structure. Therefore, the machine has the potential to achieve higher force density per machine volume compared to its variant with coreback with a similar amount of PM material. It should be acknowledged that the number of active materials

including volume and mass of PM and translator are very important specially for long translator linear generators. It also offers an almost 85% reduction in translator mass compared to the baseline machine presented in the previous chapter, which is vital in terms of long stroke applications like wave energy power take-off. To summarise, the proposed machine is optimised for minimum active material mass and improved performance results.

The concept development and construction procedures of the novel machine housing and the test rig have been explained step by step. It is also expected that further reduction of mass can be possible through mechanical design optimisation of the rig. Unique segmented translator teeth structure allows them to be attached firmly inside the slots of the non-magnetic TUFNOL structure, letting them withstand the strong electromagnetic attraction force during operation. Construction of the translator structure proved to be the trickiest part, although the assembly process of the stators and translator into the main housing were easy, as the initial air-gap could be controlled to be big enough to avoid any big force acting between them.

The electromagnetic model gave a good agreement to predict the performance of the lab prototype. 3D effects are also considered in the finalised FEA model, which allows comparing the performance of the lab prototype to be more accurate. Various sets of tests are successfully performed and compared with the 3D FEA results with a good match. These results confirm the validity of the performance of the chosen design modeling. Although there are some unavoidable mechanical constraints, limitations in the testing instruments and minor data handling errors, the results are a good foundation, suggesting that the proposed HCVHM is a viable solution for a force dense machine for DD-WEC and further research in this area should be continued.

## Chapter 5: The Cylindrical Vernier Hybrid Machine-I

### 5.1 Introduction

In this chapter, a cylindrical Vernier Hybrid Machine (VHM-I) is proposed as an evolution from a flat single sided variant of the E-core linear Vernier Hybrid Machine presented in chapter 3. Three dimensional (3D) FEA has been used for both the flat and cylindrical models to perform a comparison study. A basic geometric study demonstrates that active mass saving is possible by moving to the cylindrical topology and it can provide a higher force to weight ratio for a fixed PM mass and current density to the flat variant [17]. A laboratory prototype is built and tested to validate the simulation results.

To perform a better comparison of the two machines, both a flat and cylindrical model has been designed and analysed using 3D FEA. The key model parameters held constant between the topologies. The initial design specifications are summarized in Table 5-1.

*Table 5- 1: Initial design specification and model parameters*

<b>Parameters</b>	<b>Values</b>
Average mechanical power (W)	220
No. of PM pole per stator tooth	6
Air gap length (mm)	1
PM width (mm)	12
PM thickness (mm)	2.5
Stator pole pair pitch (PPP) (mm)	24
Translator pitch (mm)	24
Translator teeth width (mm)	10
Translator pitch (mm)	24
Rated speed (m/s)	1.2
Current density (A/mm <sup>2</sup> )	3.5

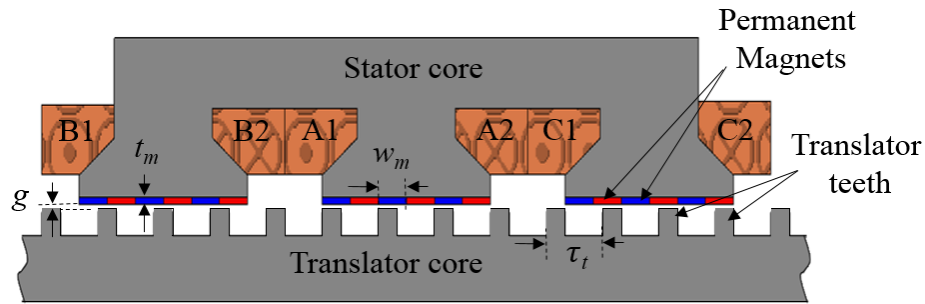


Figure 5. 1: Flat E-core VHM-I topology

## 5.2 Single Sided Flat VHM-I Topology

A single-sided flat E-core linear VHM-I is shown in Figure 5.1. As mentioned in chapter 3, the coils and magnets are both mounted on the stator, leaving the translator to be a purely iron salient structure with a thick core-back. Alignment and un-alignment between magnet poles and translator teeth produce maximum and minimum flux linkage respectively. The principle of operation of the single sided VHM-I is similar to the double sided VHM described in chapter 3. The only difference with the double-sided topology is all the flux linking the translator teeth now pass through the translator core back. Thus the translator core back needs to be as thick as the stator core back. The topology is hence suited to low speed, high force direct drive applications. The non-contact method of magnetic gearing enables this machine to reach higher force density without a conventional mechanical gearbox [1, 2, 3].

## 5.3 Cylindrical VHM-I Topology

In this section, a cylindrical version of the VHM-I, shown in Figure 5.2, is introduced as a logical development from the flat version presented in Figure 5.1.

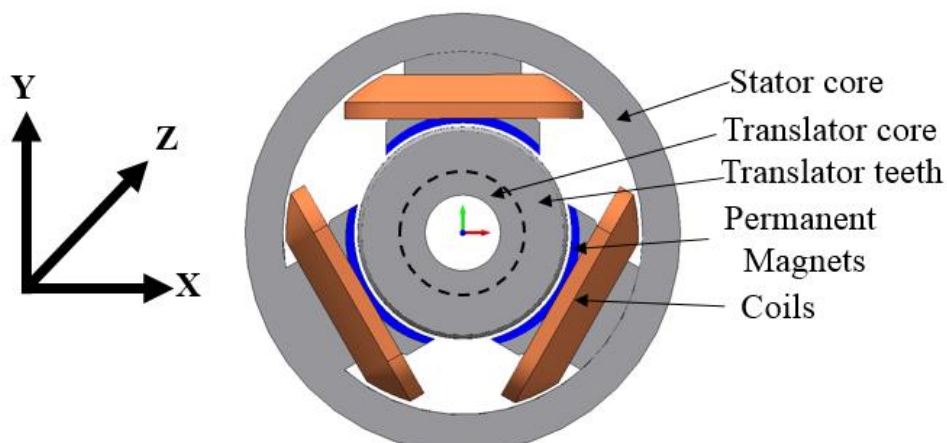


Figure 5. 2: Cylindrical VHM-I topology

### 5.3.1 Motivation

Cylindrical topologies may have advantages in Direct Drive – Wave Energy Converters (DD-WECs) simply by merit of the smooth cross section offering a better surface for sealing than

the flat (square) counterpart. In addition, the increased surface area to volume ratio makes for shorter stators. It also provides very low net electromagnetic attraction forces between the stator and the translator due to the 3D symmetrical structure (three stator teeth distributed by 120° around the translator) compared to the single-sided flat structure. Finally, the structure is axisymmetric, and so should be able to withstand parasitic forces/torques equally well from all directions. The flux path of the cylindrical topology is in the axial, radial and circumferential direction in both the translator and the stator. Therefore, a simple laminated structure, which is well suited to the flat topology, is not appropriate in the cylinder version. It is here assumed that the entire stator and translator are made from soft magnetic composite (SMC).

### ***5.3.2 Soft Magnetic Composite (SMC)***

Soft Magnetic Composites (SMCs) are compact ferromagnetic powder particles surrounded by an electrically insulating layer that can be formed into complex geometric shapes by means of powder metallurgy. These SMC materials offer several advantages over laminated steel cores in most applications which include 3D isotropic ferromagnetic behavior, relatively low total core loss at medium and high frequencies, low eddy current loss, possibilities for improved thermal characteristics, flexible machine design and assembly, and a prospect for compact design which can greatly reduce weight and provide excellent cost efficiency. The major drawback is the high cost due to the complex manufacturing process which combines conventional Permanent Magnet (PM) compaction with multistep compaction followed by low-temperature heat treatment [99, 100]. However, the isotropic property of SMC makes it prone to easy breakdown during the compression process if there are micro-cracks between adjacent particles, which is another mechanical challenge. Although the permeability of the SMC is lower than that of the laminated steel due to the insulation layers, the 3D magnetic flux path makes it superior for the complex mechanical geometry which is very complicated to make with laminated steel [101].

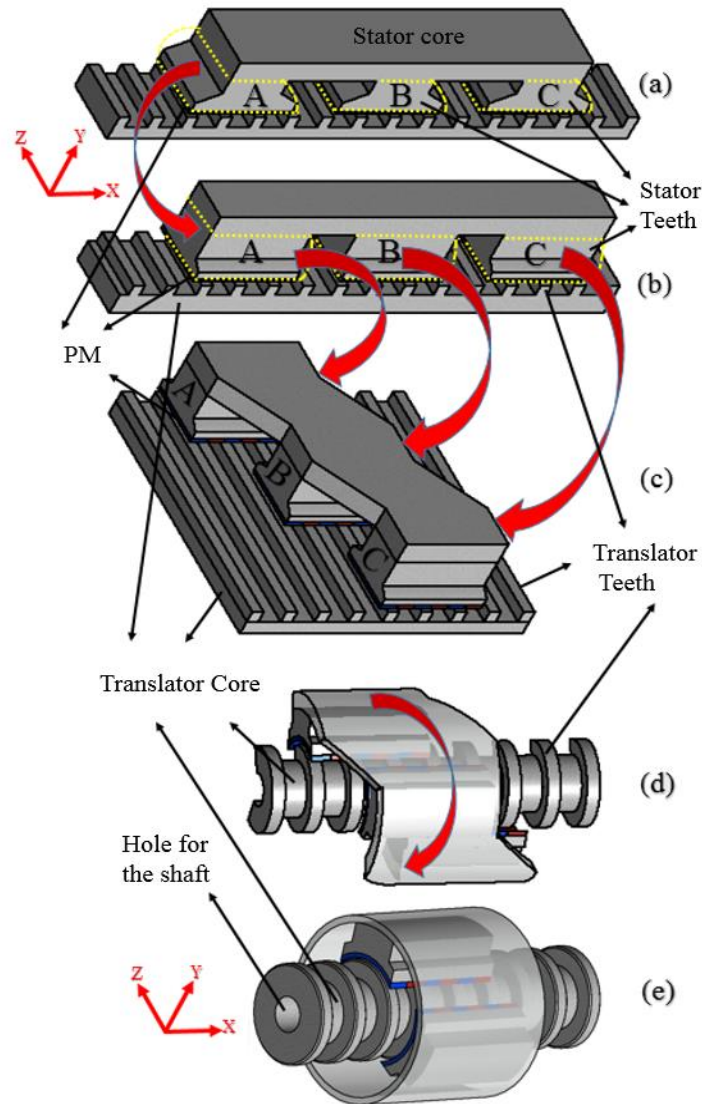


Figure 5. 3: Cylindrical VHM-I model development from flat VHM-I

### 5.3.3 Design Development

The flat VHM-I can be specified by its PMs, stator teeth, stator core, coils, translator teeth, and translator core. Conceptually, the cylindrical version can be developed from its linear counterpart shown in Figure 5.3(a) by the following steps:

1. Rotating the stator teeth by  $90^\circ$  around the axis of PM's magnetisation (Y-axis), Figure 5.3(b).
2. Extruding the translator teeth along the axial length (Z-axis) and moving the stator tooth-B and stator tooth-C to be almost aligned with tooth A. To achieve a 120 electrical degree phase difference between stator teeth, they must be offset in the X direction ( $W_{st}$ ), Figure 5.3(c), by a function of the translator tooth pitch,  $\tau_t$  in the equation (5-1).

$$W_{st} = \tau_t \left( k - \frac{1}{3} \right); k=1, 2, 3, \dots \quad (5-1)$$

3. The entire machine is now wrapped around the axis of motion (X-axis) – with a centre through the translator core, Figure 5.3(d).
4. The translator core can be hollowed out and the stator core forms a cylindrical shell enclosing all three stator teeth as shown in Figure 5.3(e).

#### 5.3.4 Principle of Operation

The basic operation of the cylindrical design is identical to that of the flat counterpart. The alignment and un-alignment of PMs and translator teeth drive flux around the stator and translator. In the cylindrical model, however, all three phases link through the same translator teeth, as the translator flux path is now circumferential and parallel to the teeth (rather than perpendicular to the teeth in the original flat version). The translator core carries just a small amount of flux related to the shift between stator teeth,  $W_{st}$  in equation (5-1), thus the volume of the translator core material can, therefore, be minimised for the cylindrical model.

### 5.4 Simplified Geometrical Analysis

This section presents a general geometric representation of the flat and cylindrical VHM-I. The translator tooth-width is set to  $a$ , which is assumed to be equal to the PM width ( $w_m$ ) and is used to scale the other dimensions based on a simplified flux flow. The active air-gap area, coil conductor area, and magnet mass are set as equal in the flat and cylindrical versions.

#### 5.4.1 Flat Topology

Figure 5.4 shows the flat version of the VHM-I. The left-hand stator tooth is in the aligned position and, ignoring leakage flux, must have a thickness of  $3a$  to carry flux from the three translator teeth it encompasses. For simplicity, the stator slot depth is also set to  $3a$ . In reality, significant leakage occurs between the magnets [90]. In recognition of this, in order to present a low mass design, the stator core back and translator core-back are set to half this value,  $3a/2$ . Using equation (5-1), the gap between stator teeth is set to  $4a/3$ . It is easily shown that the length of the stator core-back is  $53a/3$  and the stator slot width would be  $13a/3$ .  $l_a$  is the active length into the plane of the figure.

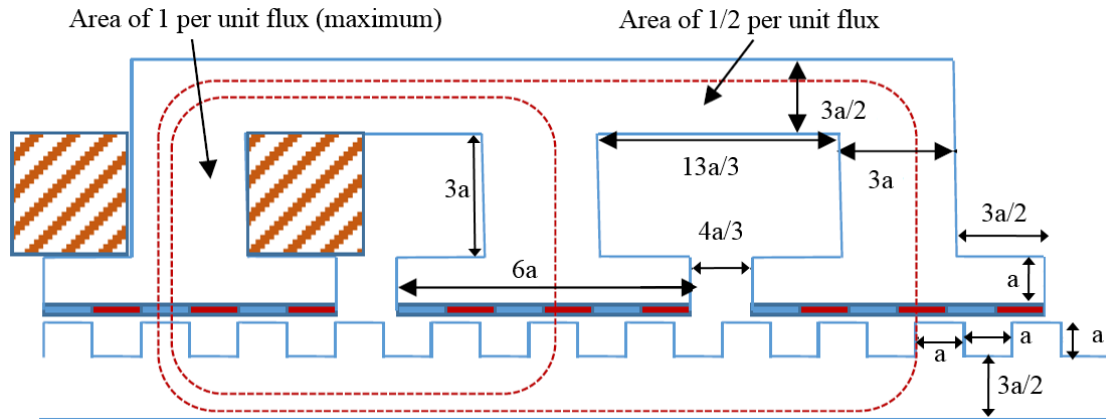


Figure 5. 4: Simple geometry of flat VHM used to build a simple mass model

### 5.4.2 Cylindrical Topology

The cross-sectional areas of the stator teeth of the two machines are shown to be equal in Figure 5.5. The stator teeth in the cylindrical machine are seen to have a width of  $l_a/2$ .

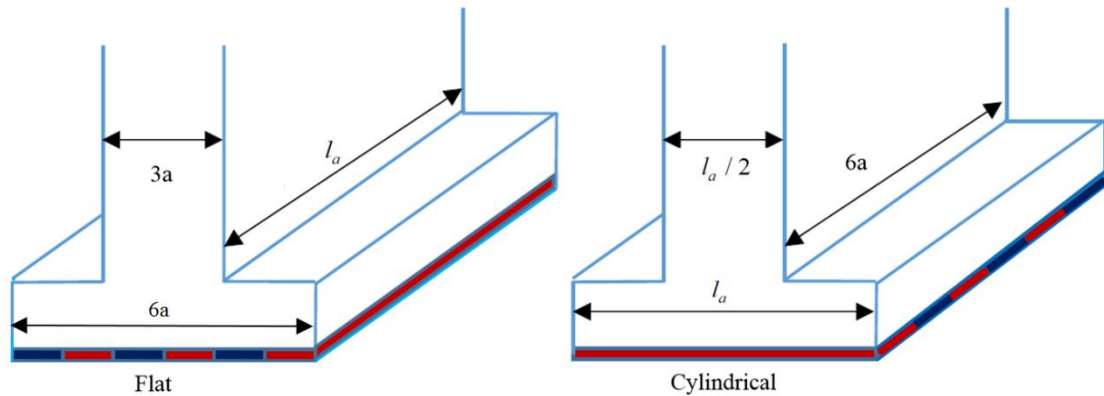


Figure 5. 5: Simple geometry of flat VHM used to build a simple mass model.

In Figure 5.6(a), the assumed flux path is shown for full alignment in the upper stator tooth. In the cylindrical machine, the stator core-back and translator core-back take half the flux in each direction as the flux path splits at the stator tooth root – implying a required stator core-back of half the stator tooth width,  $l_a/4$ . To be consistent with the assumptions used in the flat geometry, the stator core-back depth is halved to account for leakage, i.e.  $l_a/8$ . Similarly, the depth of the combined translator tooth and core-back is set to  $(l_a/8)$ . The translator slot depth is assumed to be  $a$ , as for the flat machine.

Each of the three stator teeth in Figure 5.6 is allocated  $120^\circ$  (mechanical), assumed to be  $90^\circ$  active and a  $30^\circ$  space between teeth. Equation (5-2) thus fixes the radius of the air-gap,  $r_{ag}$ , such that the magnet mass between the two versions is constant.

$$r_{ag} = \frac{l_a}{\frac{\pi}{2}} = \frac{2l_a}{\pi} \tag{5-2}$$

Table 5- 2: Basic machine dimensions for flat and cylindrical geometry.

Parameter	Flat VHM-I	Cylindrical VHM-I
Stator tooth width	$3a$	$la/2$
Stator tooth span	$6a$	$90^\circ$
Stator tooth length	$la$	$6a$
Translator tooth-width	$a$	$a$
PM width	$a$	$a$
space between stator teeth	$4a/3$	$30^\circ$

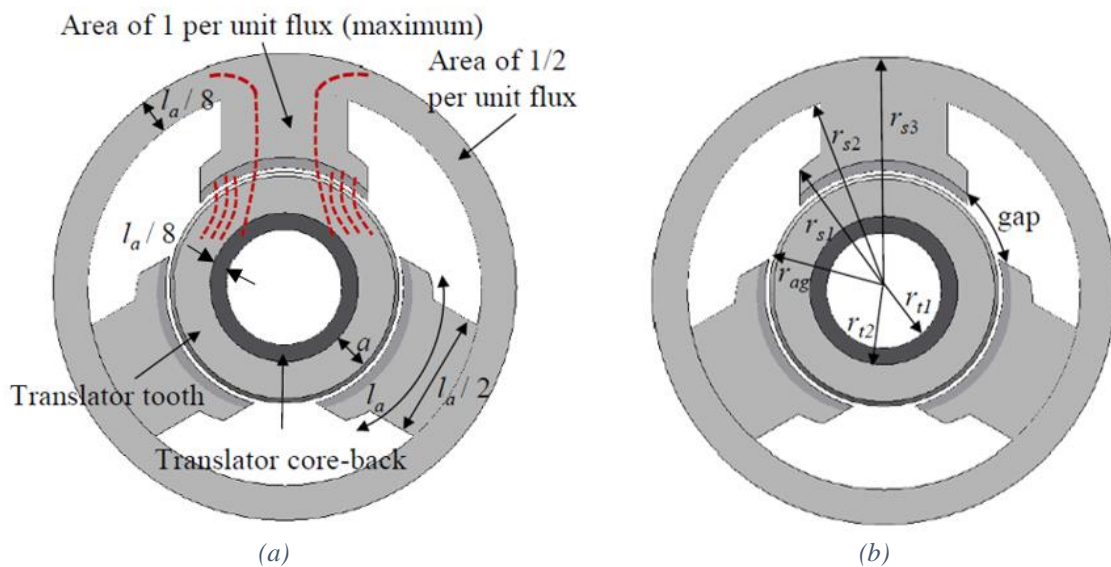


Figure 5. 6: Simple geometry of cylindrical VHM used to build a simple mass model

Ignoring the air gap length, which is assumed small compared to  $r_{ag}$ , the other radii labeled in Figure 5.6(b) are defined in Table 5.2.

Table 5- 3: Definition of radii in cylindrical VHM-I

Symbol	Definition
$r_{s1}$	$r_{ag} + a$
$r_{s2}$	$r_{s1} + 3a$
$r_{s3}$	$r_{s2} + l_a/4$
$r_{t1}$	$r_{ag} - l_a/2$
$r_{t2}$	$r_{ag} - a$

Initial 3D FEA can be used to validate the assumed flux path and assumptions about flux density. For example, Figure 5.7 shows no-load flux density in the stator core back for the two versions is equal.

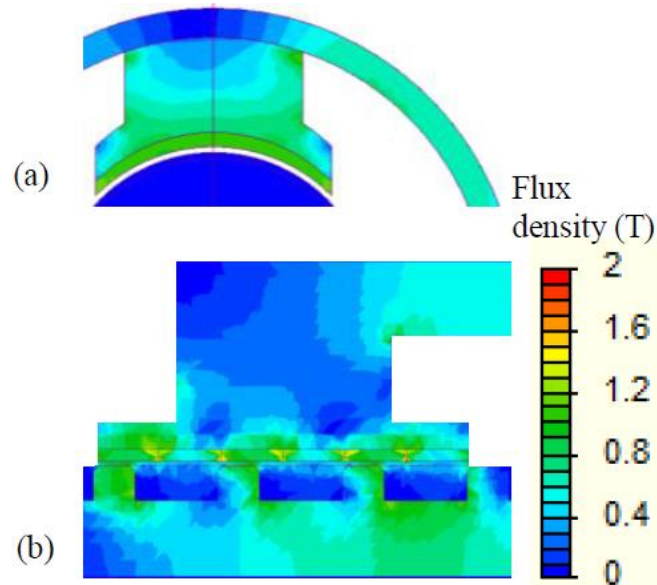


Figure 5. 7: Equivalence of flux density in the stator core back for (a) Cylindrical VHM-I (b) Flat VHM-I

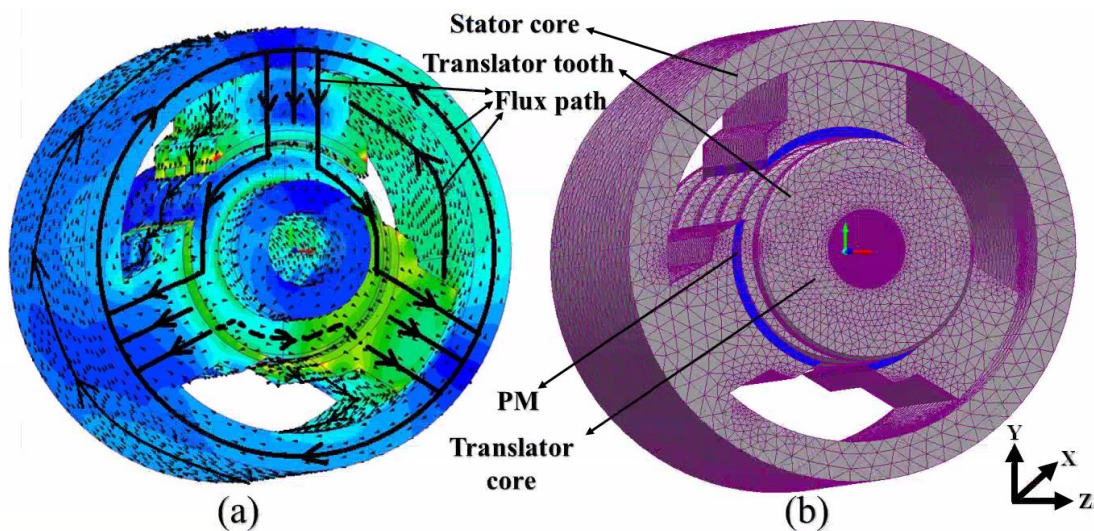


Figure 5. 8: The cylindrical prototype design in 3D FEA, a) magnetic flux distribution and b) 3D mesh

Figure 5.8 shows the FEA model of the cylindrical machine, including the no-load magnetic flux distribution. Each stator tooth consists of a single-phase fractional slot winding with six radially magnetized arc shaped PMs interacting with three translator teeth.

### 5.5 Electromagnetic Performance

Both machines have undergone a design study to minimise active material and maximise force production. The final designs deviate slightly from the simple geometry described in section 5.4. The two machines were shown in Figure 5.1 and 5.2, and have, for example, thinner core-backs and shaped stator teeth for performance improvement and mass reduction. Some of the

key machine variables are shown in Table 5-4. The ratio of the active area to machine volume is higher in the cylindrical machine.

*Table 5- 4: Model parameters for both machines does*

<b>Parameters</b>	<b>Flat VHM-I</b>	<b>Cylindrical VHM-I</b>
PM mass (kg)	0.18	0.18
Stator core thickness (mm)	16	8
Active number of translator teeth	9	4
Translator core thickness (mm)	15	5
Active air gap area (mm <sup>2</sup> )	12600	15758
Active machine volume (mm <sup>3</sup> )	836010	776578
Active machine length (mm)	280	88
Stator mass (kg)	2.84	3
Translator mass (kg)	2.9	1.12
Coil mass (kg)	1	0.9

### **5.5.1 Flux Density**

Figure 5.9 shows a plot of the flux density under the teeth for both machines. Magnetically, the machines are very similar, with the cylindrical version having a slightly higher flux density due to the decreasing area as the flux travels radially towards the centre of the translator – a ‘flux focusing’ type effect. Figure 5.10 shows the flux density harmonics spectra. It can be clearly seen that the higher order harmonics are similar due to the similar nature of the interaction of flux between stator PM and translator. The fundamental harmonic, which contributes to the force production, is higher in the cylindrical VHM.

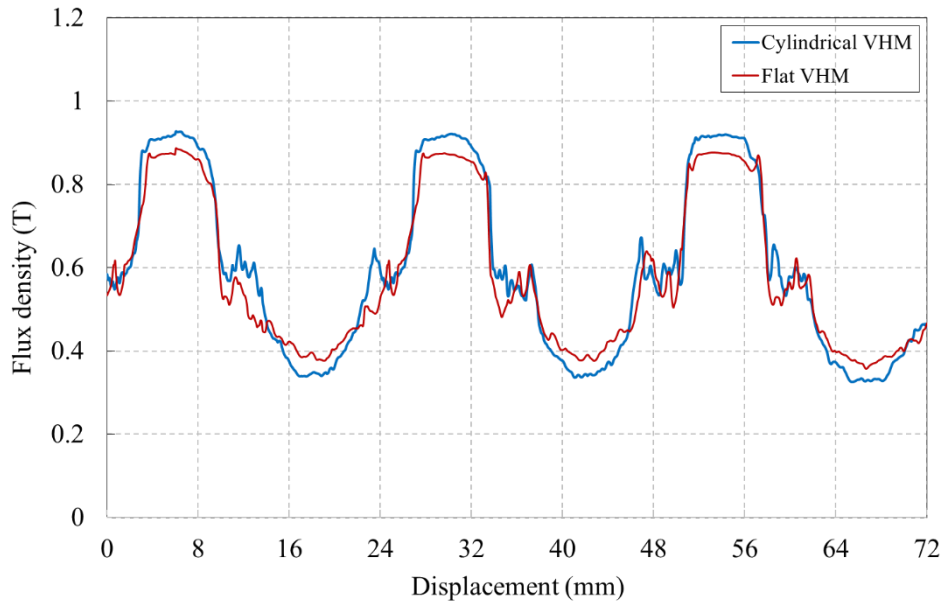


Figure 5.9: Flux density comparison under full stator tooth length during maximum flux linkage

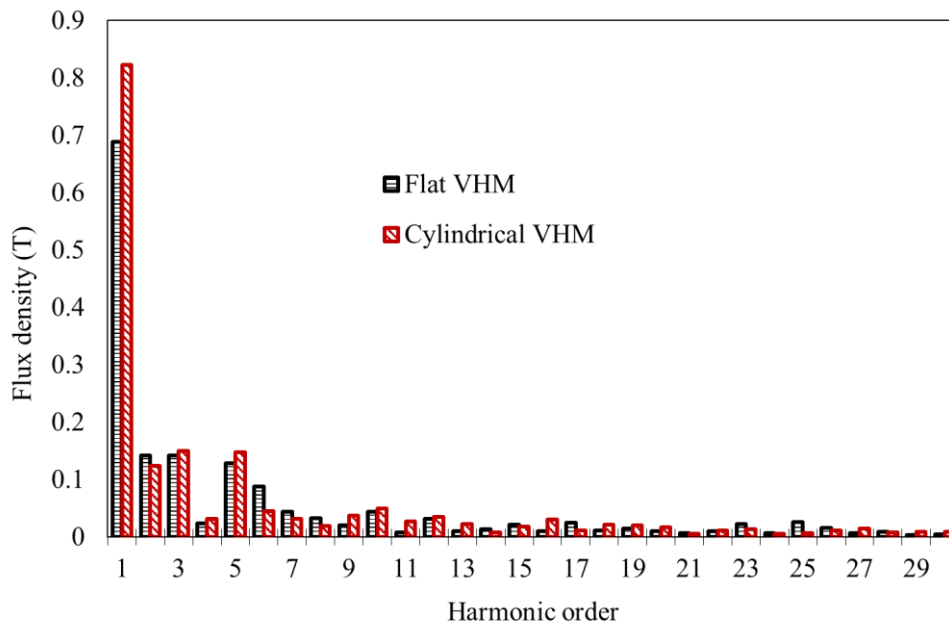


Figure 5.10: Flux density harmonics comparison for one translator pitch.

### 5.5.2 Flux Linkage

Figure 5.11 shows the comparison of three-phase flux linkage between the flat and the cylindrical VHM. The higher flux linkage for the cylindrical model is predicted from the previous sub-section, as the cylindrical version has a higher flux density in the air-gap, it links more flux in the phase windings.

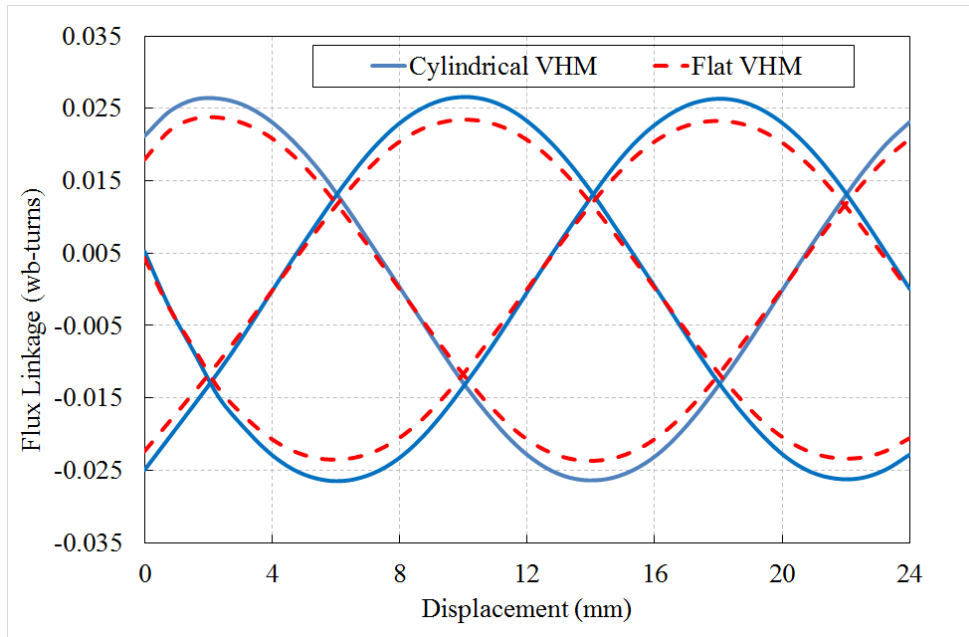


Figure 5. 11: Three flux linkage comparison between flat and cylindrical VHM-I

### 5.5.3 No-load Back EMF

Figure 5.12 presents the three phase no-load back EMF waveform of the cylindrical and flat VHM-I at the nominal speed of 1.2 m/s. The cylindrical machine has 11.5% higher amplitude of back EMF, clarified by the higher first order harmonic shown in Figure 5.13. This is a direct result of the higher flux density resulting from the flux focusing effect of the cylindrical machine.

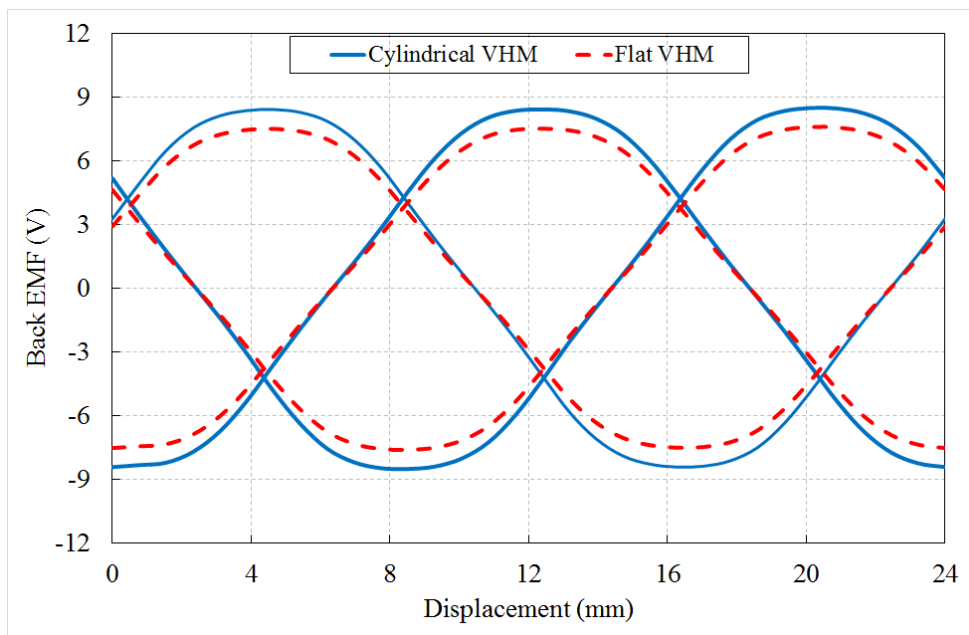


Figure 5. 12: Three back EMF comparison between flat and cylindrical VHM-I

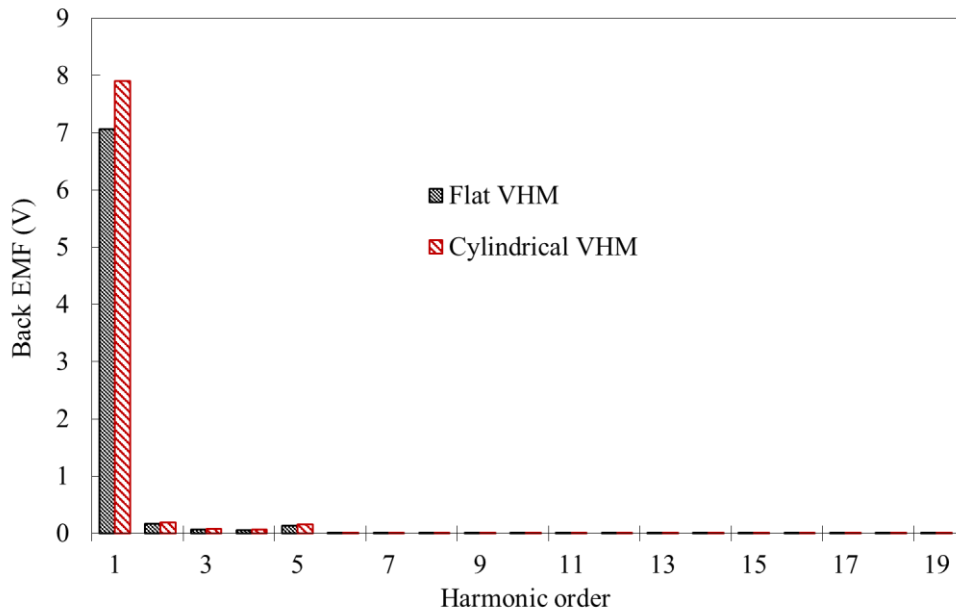


Figure 5.13: Back EMF harmonics of flat and cylindrical VHM-I

#### 5.5.4 Electromagnetic Forces

The cogging force at zero current is illustrated in Figure 5.14 which shows there are three similar cogging cycles per electrical cycle for cylindrical and flat VHM-I, while the cylindrical VHM-I produces lower peak to peak cogging compared to the flat version.

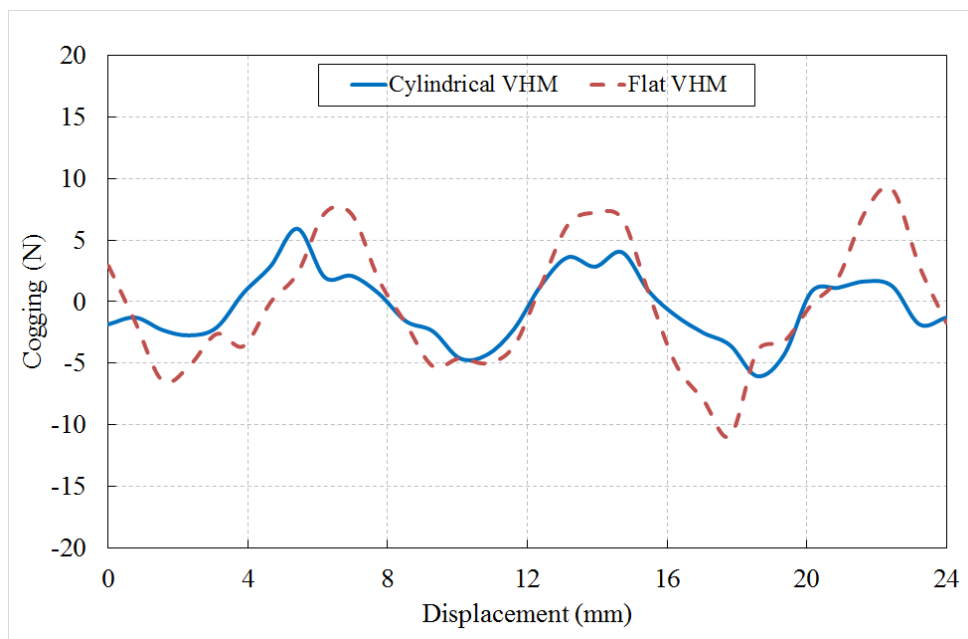


Figure 5.14: Cogging force comparison between flat and cylindrical VHM-I

Fig 5.15 shows the force produced by a sinusoidal current injected into the q axis. The average thrust force of the cylindrical model is 180 N compared to 162 N for the flat model at a rated current density of  $3.5\text{A}/\text{mm}^2$ . The percentage increase in the force of the cylindrical version is almost 11%, which is equal to the percentage increase in back EMF.

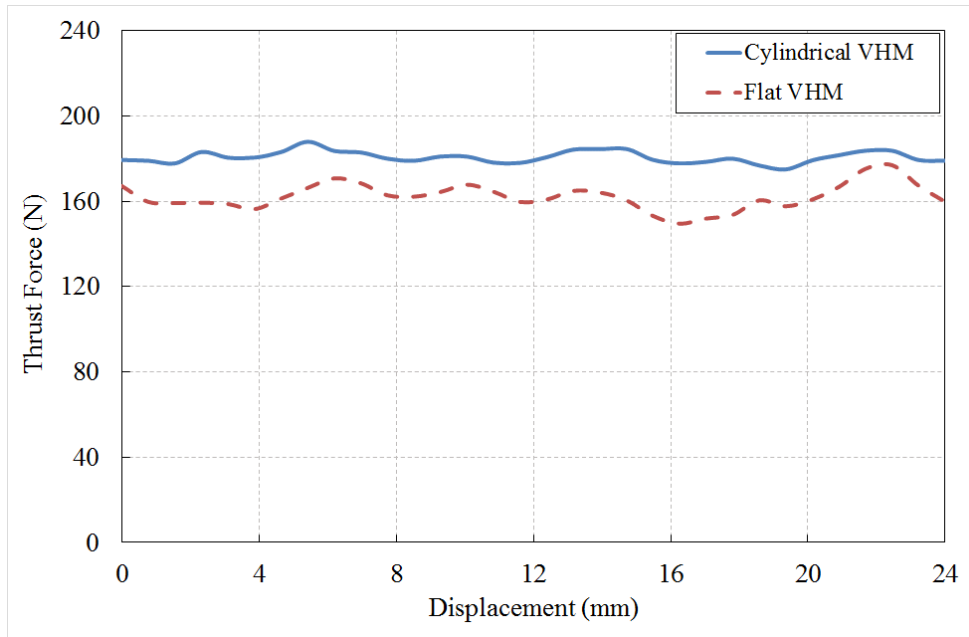


Figure 5. 15: Thrust force comparison between flat and cylindrical VHM-I

### 5.5.5 Phase Inductance

Three phase inductances are calculated based on the method in [96], which is also been used in section 4.4.6.4 (Synchronous inductance – Method D). The three-phase inductance is shown in Figure 5.16. It can be seen from Table 5.5 that all three-phase inductance are very similar and all of them have a very small variation (maximum of 2%). It shows the symmetrical flux distribution during electrical excitation. As all three teeth are wrapped around to form a cylinder, so all of them use the same core back which links the flux between them. As the ripple is very small, it can be said that the effect of saliency is very little.

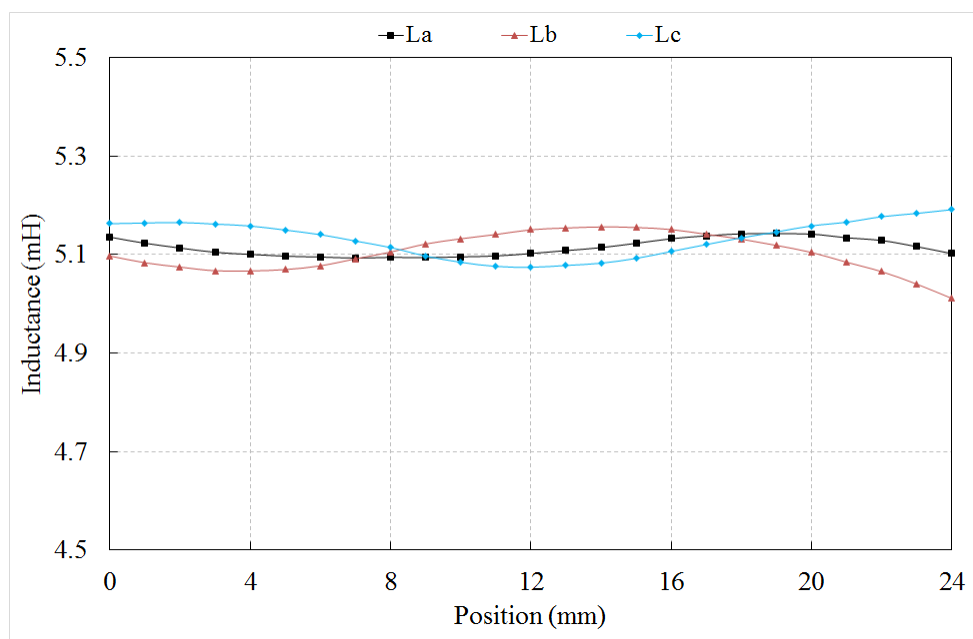


Figure 5. 16: Three phase inductance of the cylindrical machine.

Table 5- 5: Three phase inductance for the cylindrical machine

<b>Inductance</b>	<b>L<sub>avg</sub> (mH)</b>	<b>L<sub>pk-pk</sub> (mH)</b>	<b>% ripple</b>
La	5.11	0.05	1.0
Lb	5.1	0.1	2.0
Lc	5.13	0.1	1.9

### 5.5.6 Comparison

Machine power density ( $K$ ), as defined in equation (5-9), can be used to compare electrical machines running at the same speed and current density.

$$K = \frac{P}{V} \propto \frac{F}{V} \quad (5-9)$$

Where,  $P$  is the power, and  $V$  is the active volume of the machine.

For both flat and cylindrical machines, the rated speed and current density are constant. Machine power density is therefore proportional to the output force and inversely proportional to the active volume of the machine, equation (5-9). Table 5-6 compares the predicted machine performance for the two topologies. The cylindrical model gives a higher power density due to its lower active volume and increased force capability.

The power factor is a known issue with this family of machines, and it will likely be affected by the move from a flat to a cylindrical cross-section. The analysis here has assumed the machine is operated at a constant speed, and when loaded, the current is controlled to be in phase with the back EMF. Ignoring any saturation effects, the operating power factor is equal to the ratio of open circuit back EMF to loaded terminal voltage. At the rated speed of 1.2 m/s, it was shown earlier that the cylindrical machine had a higher back EMF, with the open circuit RMS voltage being 12% greater. Terminal voltage, as calculated by FEA, differs by less than 2% and so the increase in back EMF translates directly into an increase in the power factor. The flat E-core VHM-I has a power factor of 0.39, whereas the cylindrical machine operates at a power factor of 0.44. Whilst the author accepts this is still a low value, the adoption of a cylindrical topology for linear variants represents a meaningful improvement in power factor which could equally be applied to other variants of the Vernier Hybrid Machine that exhibit a better power factor such as [79].

Table 5-6 summarises the predicted performance of flat and cylindrical VHM-I under loaded and no-load conditions.

*Table 5- 6: FEA performance comparison between flat and cylindrical VHM-I*

<b>Parameter</b>	<b>Flat VHM-I</b>	<b>Cylindrical VHM-I</b>
Open circuit voltage (V)	7.6	8.4
No-load Flux linkage (mWb-turns)	26.3	23
Thrust force (N)	162	180
% Thrust force ripple	16%	7%
Cogging force(N)	20	12
Power Factor	0.39	0.44
Shear stress (kN/m <sup>2</sup> )	13.7	12.3
Machine Power density (kW/m <sup>3</sup> )	194	386
Force density (kN/m <sup>3</sup> )	162	321

## 5.6 Prototype Construction

This section outlines the construction and assembly process of the cylindrical VHM-I and experimental test rig setup for pursuing experiments. The stator is constructed from Soft Magnetic Composites (SMC) materials and comes out to be a single component piece. Special arc-shaped neodymium magnets poles were attached with the stator teeth shoe surface. The longer translator has almost 3.5 times the length compared to the short stator. The translator also made out of SMC with 13 salient teeth. The challenges encountered during the construction and assembly process will be discussed in the following subsections.

### 5.6.1 SMC Stator Design

Construction steps for the stator are shown in Figure 5.17. The stator is constructed from five cylindrical blocks of ‘Somaloy 5P’ Soft Magnetic Composite (SMC) material manufactured by ‘Hoganas’. The datasheet of ‘Somaloy 5P’ can be found in appendix I. This SMC is one kind of pressed powder material, which is suitable for low iron loss and can carry 3D flux in a different direction. Each 200mm diameter pre-pressed block is manufactured in 20mm thickness, shown in Figure 5.17(a). Therefore, five disc blocks were needed to construct the 88mm long stator. First, five blocks were attached by strong industrial glue to form a 100mm long cylinder. Then, 12mm of the cylinder length were machined cut to get the 88mm long structure. Figure 5.17 (b) shows the 88mm long stacked cylindrical structure.

As three stator teeth are in different positions across the length of the stator, grooves of 8mm and 16mm were machined on each side of the cylinder using a milling machine. Figure 5.17(c) clearly represents two grooves and their position on both sides of the cylinder. Figure 5.17(d) shows the machined cylinder with grooves (two on top visible and two on the bottom surface). Then the grooved cylinder was set inside the CNC wire cut machine to machine out the stator teeth structure. Figure 5.17(e) represents the wire eroded single stator piece with three 72mm long stator teeth, each separated by 8mm, across the length.

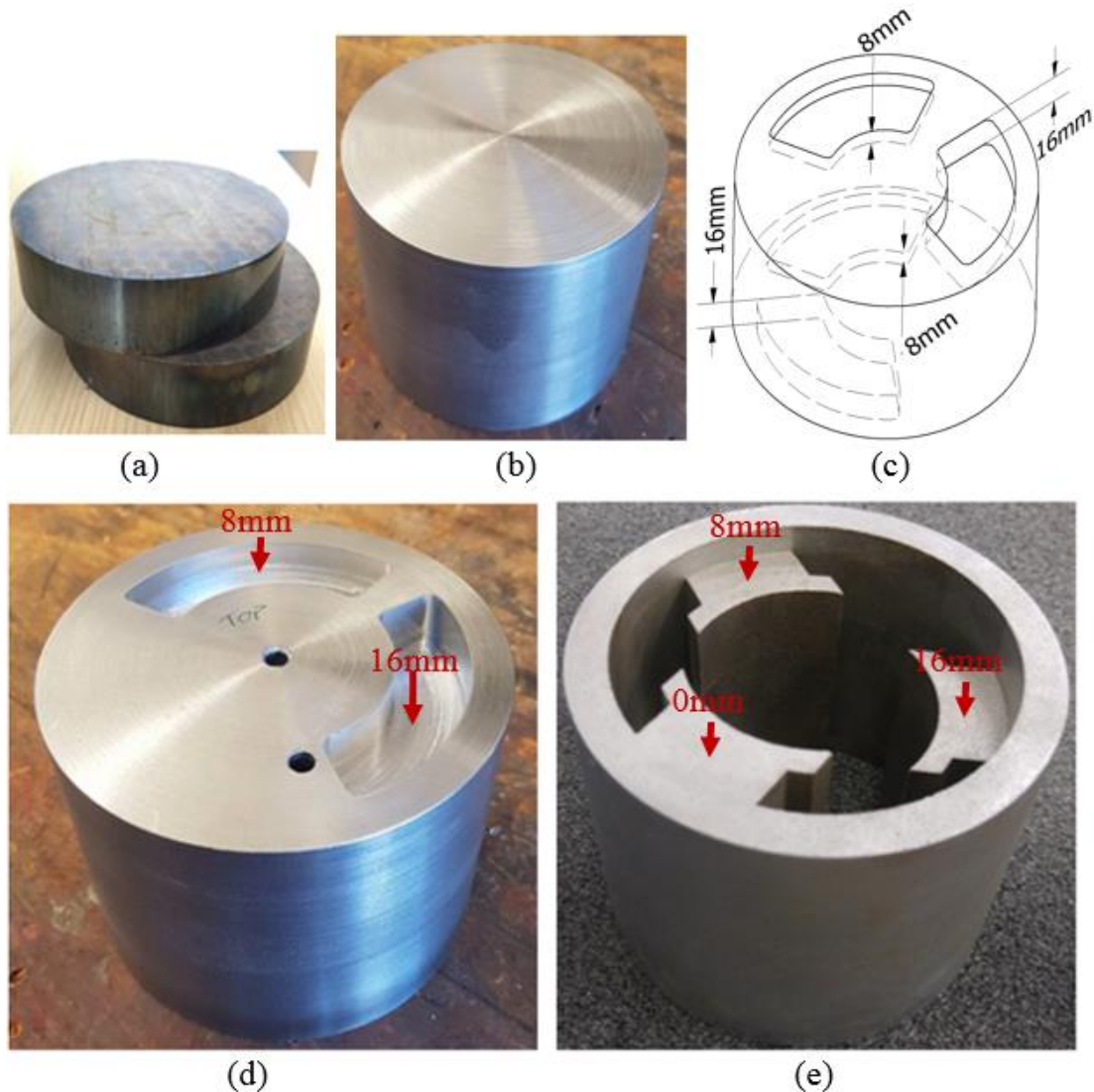


Figure 5. 17: Cylindrical SMC stator construction processes

### 5.6.2 Arc Magnets

Neodymium-Iron-Boron and Samarium Cobalt magnets are the most commonly used rare earth magnets used for high force dense electrical machines. Neodymium-Iron-Boron has a very high energy density with a high residual flux density of up to 1.4T, while they can be easily demagnetised in lower temperatures than Samarium Cobalt magnets. However, Samarium Cobalt magnets have a relatively lower residual flux density of around 1.1T range. Therefore, for the low speed and high-power application, Neodymium-Iron-Boron (N42) is selected for the respective wave energy generator for high force density while having a reasonable demagnetizing temperature of around 120°C.

Nickel (Ni) plated sintered Neodymium-Iron-Boron of grade N42H (datasheet in Appendix G) is used for their high residual flux density of 1.33T and a high operating temperature of maximum 120°C. For the shape of the stator teeth, special arc-shaped N42H magnets were

ordered from “Bunting Magnetics Co.” with an arc angle  $90^\circ$ , the inner radius of 29mm, PM thickness of 2.5mm and a 12mm magnet width (axial length). Half of the arc magnets are inward magnetised, and the remaining magnets are outward magnetised to match the design. The top two pictures of Figure 5.18 represent the two different orientations of arc magnets ordered from the manufacturer.

The magnets are then glued one by one using PERMABOND® ES562 single-part, heat-cure Epoxy, which has a maximum shear strength of 35MPa and tensile strength of  $40\text{N/mm}^2$ . After gluing all the magnets, the PM assembled stator was heat cured for 60 minutes at a  $100^\circ\text{C}$  oven. The final PM assembled SMC stator can be seen in Figure 5.18.

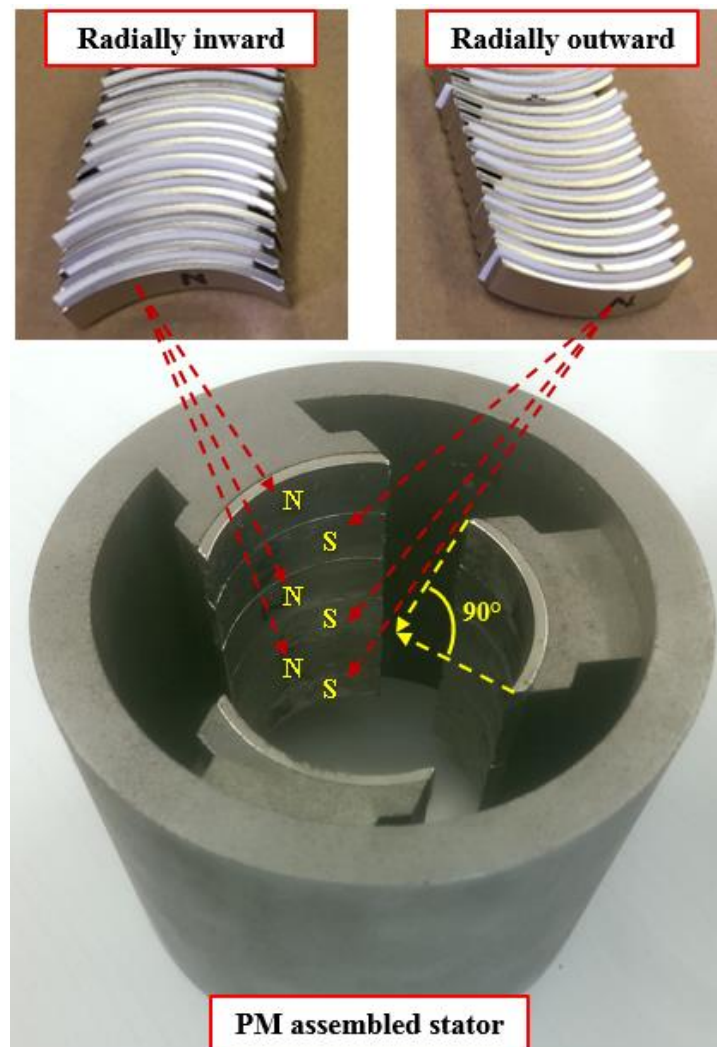


Figure 5. 18: Arc-shaped PMs and magnet assembled stator

### 5.6.3 Coils

Round enamel coated copper conductor was used to constructing the coils. As the geometry of the stator makes winding of the coils difficult, a preformed bobbin wound coil with ordered and structured layers and turns were used. Each coil was premade using a manual hand winding

machine one at a time. Copper wire with a standard wire gauge of 19 (diameter 1.02mm) was used for the coils. The aluminium bobbin winding jig consists of three sections: Central rectangular disc with smoothening edges is 20mm thick (coil width) and 100mm long that formed the central diameter of the bobbin, and two end cap discs matching the outer diameter of the winding that can be clamped with the central disc by two bolts. The clamped bobbin jig was too big to mount it onto the available winding machine. So, the bobbin jig structure was mounted on a 'Milling Bench Drill Vice Clamp' for holding it steady during manual winding. Prior to starting the winding process, two nylon threads were attached to the jig to tie the finish coils, so that the coil windings stay together even after disassembling from the jig. One thermocouple was placed in the middle of a phase winding to monitor the coil temperature. Two bolts were unscrewed to detach the outer disc of the bobbin jig and the coil can be carefully dissembled from the jig. Each stator tooth is surrounded by pre-bent slot liner Nomax paper (temperature resistance up to 205°C) of 1mm thickness to ensure insulation between coils and stator teeth. It also prevents the stator teeth from damaging the coil enamel covering any sharp edges. Then the coil can be inserted inside each stator tooth. To protect and hold the windings together, each coil was coated with varnish and then with epoxy resin to stick them with the stator core back. Six heat shrink tubes were used to mark the three phases with different colors. Figure 5.19 displays the front and back side of the stator with assembled three-phase coils.

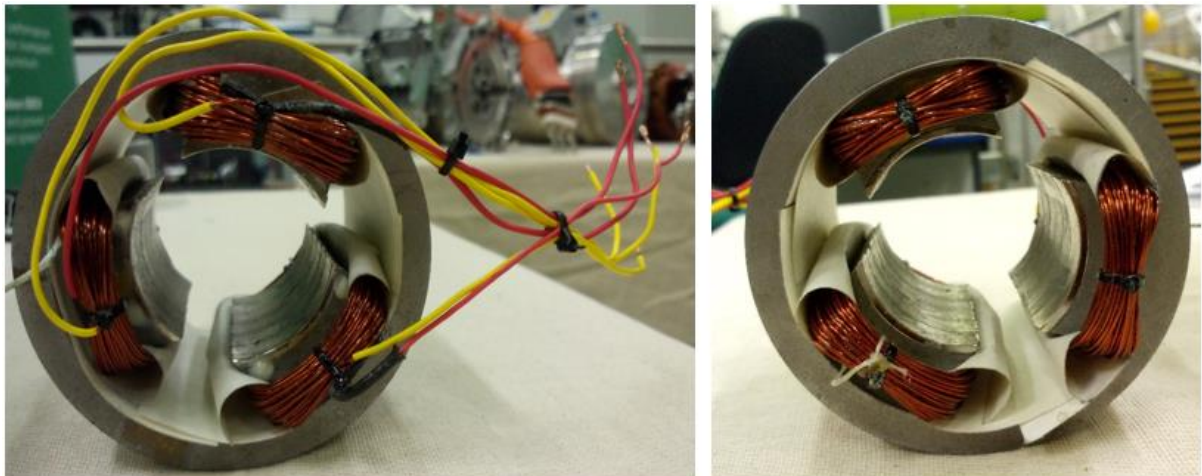


Figure 5. 19: Completed three phase windings in the stator

#### 5.6.4 Stator Housing

Housing components parts for the stator were constructed from aluminium. The stator assembly including the housing consist of the following components:

1. Half cylindrical housing base with an arc diameter equal to the stator outer diameter.
2. Half cylindrical housing shell cap with an arc diameter of 200mm.

3. Front end cap ring.
4. Back end cap ring.
5. 5mm stainless steel socket cap Screw, M5.
6. Bolts for the end caps.
7. 8mm stainless steel socket cap Screw, M8.
8. Panel mount barrier terminal block, 2 rows, 6 ways.

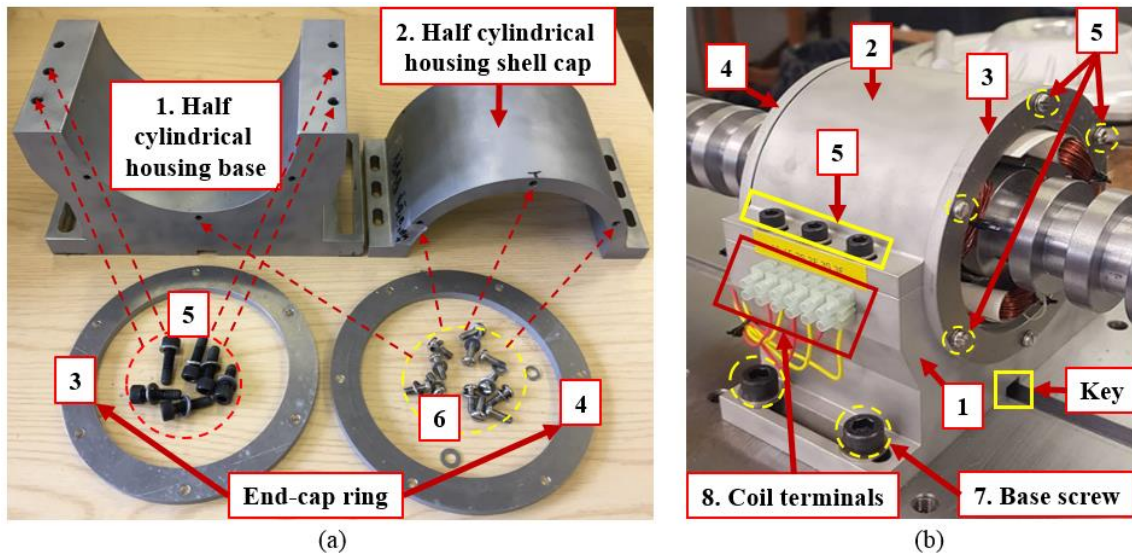


Figure 5. 20: (a) Stator housing components (b) stator assembly.

Figure 5.20(a) represents the component parts and Figure 5.20(b) shows the assembled stator. The stator structure sits in between the housing base and the housing shell. Then the M5 screws were used to fix the top housing cap to fix on the base. The stator was axially locked and sealed by the two end caps. Then the coil terminals were connected to the 6-way terminal block. The whole structure then mounted on the base plate of the test rig by the guided key and the M8 screws.

## 5.6.5 SMC Translator Construction

### 5.6.5.1 Translator design

40mm long SMC cylindrical blocks of a diameter of 80mm were used to construct the translator. Figure 5.21 (a) shows the 40mm long single block of SMC manufactured by the ‘Hoganas’. Each block was machined to form ring shape with an inner diameter of 20mm and an outer diameter of 56mm to match the design criteria. As the manufacturing company does not produce longer blocks of SMC, multiple blocks were stacked together by using strong industrial glue to form a 320mm long cylindrical structure. A 1m long stainless-steel rod of 20mm diameter was inserted across the hole of the integrated cylinder structure to be used as the central shaft. The cylindrical structure was then locked with two end screws (Figure 5.21 (b)).

Two ends of the SMC cylinder were locked with the shaft by connecting end screws. The whole cylindrical structure with the shaft was mounted on the milling machine to machine the salient translator structure. Figure 5.21(b) shows the translator structure and shaft are mounted on the milling machine with a portion of the machined SMC translator.

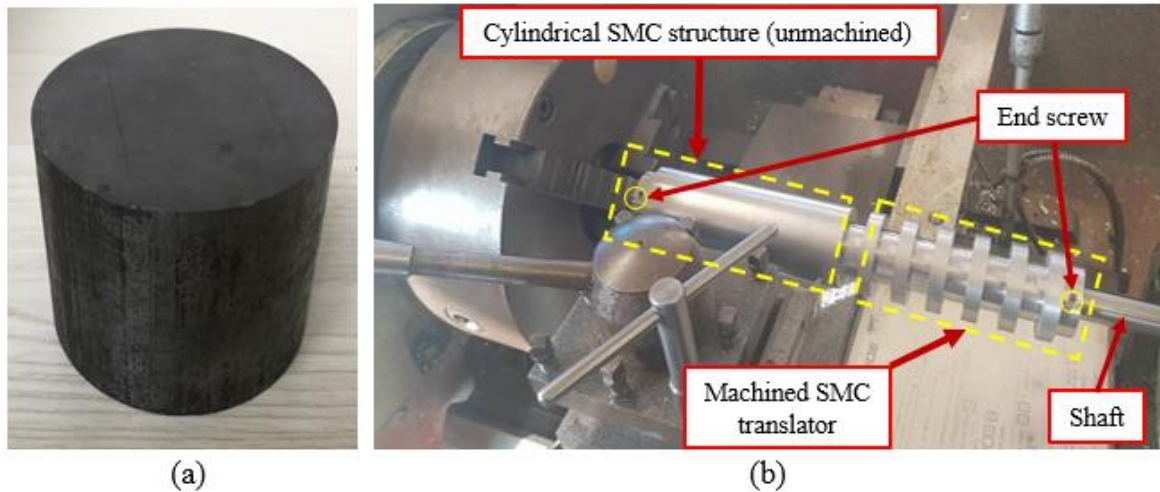


Figure 5. 21: (a) 40mm long SMC block (b) translator construction in the milling machine.

#### 5.6.5.2 Bearing and translator support

Two 20mm linear flanged ball bushings were mounted on the two translator support stands. Both the shaft and the linear ball bushings were supplied by Automation Components UK Company. Each translator support stand was machined from 100mm×300mm×40mm blocks of aluminium. Two linear bushings were inserted inside the predrilled slots of the aluminium stands. Figure 5.22 shows the translator shaft mounted on the two translator support structures and can translate across the bushings.

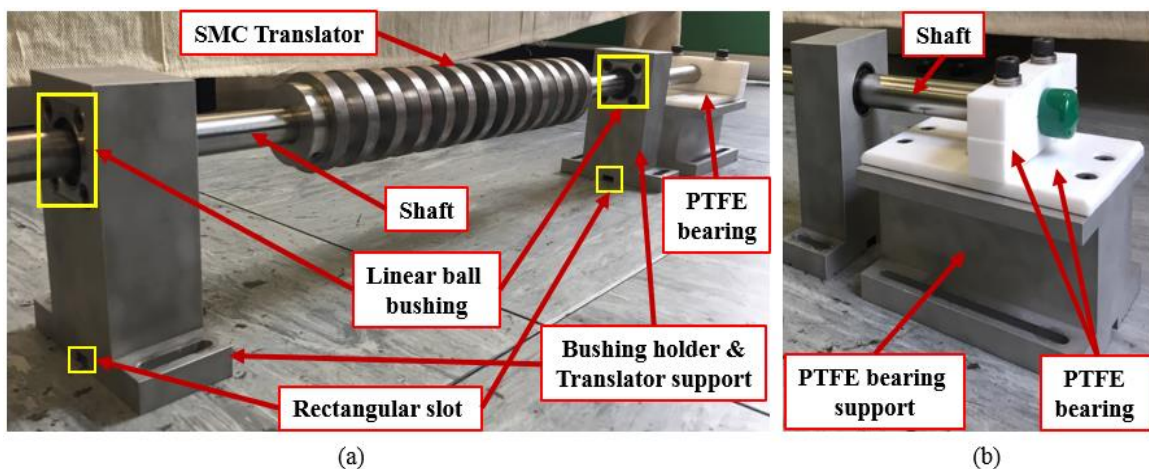


Figure 5. 22: (a) Translator assembly components (b) PTFE bearing support and end cap bearings.

Due to a slight bend in the shaft, free rotation would cause the air-gap to be varied always while the translator is moving. To avoid any free rotation of the cylindrical translator across the

moving axis, a PTFE bearing structure was included in the translator support structure. Figure 5.22(b) illustrates the PTFE bearing support base and the bearing end caps sitting at the end of the translator support. The end bar also serves another job by restricting the shaft from completely getting out of the bushing and being disassembled.

### 5.6.6 Final Assembly

The Stator assembly was first mounted rigidly on the 1m testbed with a sliding and keying capability to ensure accurate positioning. Then two translator and bushing support structures were mounted on the same central axis of the bedplate. First, the translator shaft was inserted in one of the bushings and then carefully slid through the centre of the stator to the other bushing. Once, the shaft was inserted into both of the bushings, the translator was carefully slid inside the stator to check the alignment and air-gap. The sliding capabilities of the bedplate were useful to fix the bushing supports in their specific position. Figure 5.23 shows a full assembly of the Cylindrical VHM-I prototype on the bedplate rig.

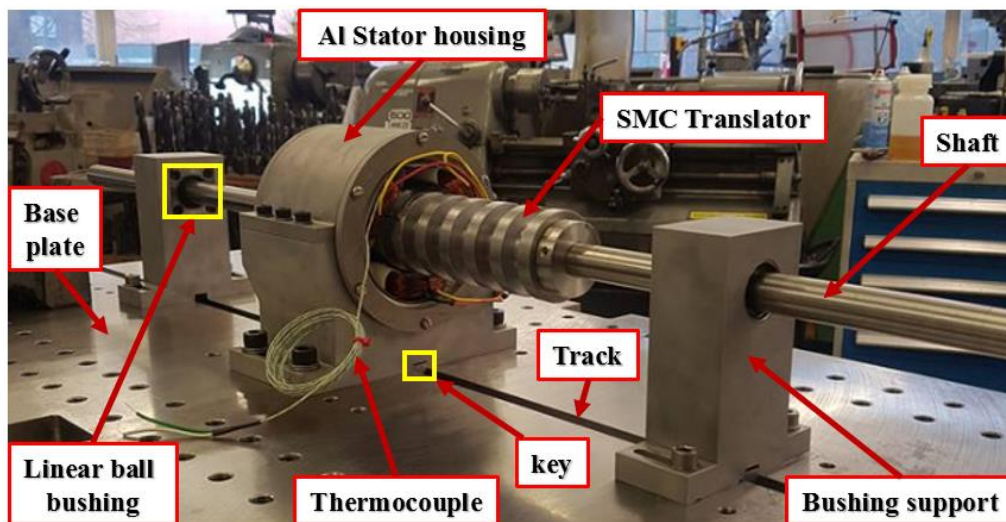


Figure 5. 23: Final Machine assembly on the bed plate.

There was some problem after mounting the translator on the rig, it was found that the shaft was slightly bent and magnetic, as mentioned in the previous section. So there was some non-linearity in the air-gap, which is considered during the testing and validation of results.

### 5.7 Prototype Testing

The test results will be obtained to validate the prototype performance in this section. The experimental results from the prototype built in the previous section will be compared against the FEA results presented earlier in this chapter. All the tests were carried out in the Newcastle University electrical power laboratory. The prototype testing includes the following tests:

1. Resistance measurement

2. Inductance measurement
3. Open circuit test
4. Static Force measurement
  - a. Cogging force
  - b. Thrust Force

### 5.7.1 Test Rig

The cylindrical prototype was mounted horizontally on a 1m long thick base plate and powered by an electric linear actuator with a maximum of 300mm stroke length. The linear actuator allows the prototype machine to be tested under variable and constant speed operation. It also allows the translator to perform the static test at various displacements. Figure 5.24 shows a fully assembled cylindrical prototype mounted on the bedplate and ready for testing.

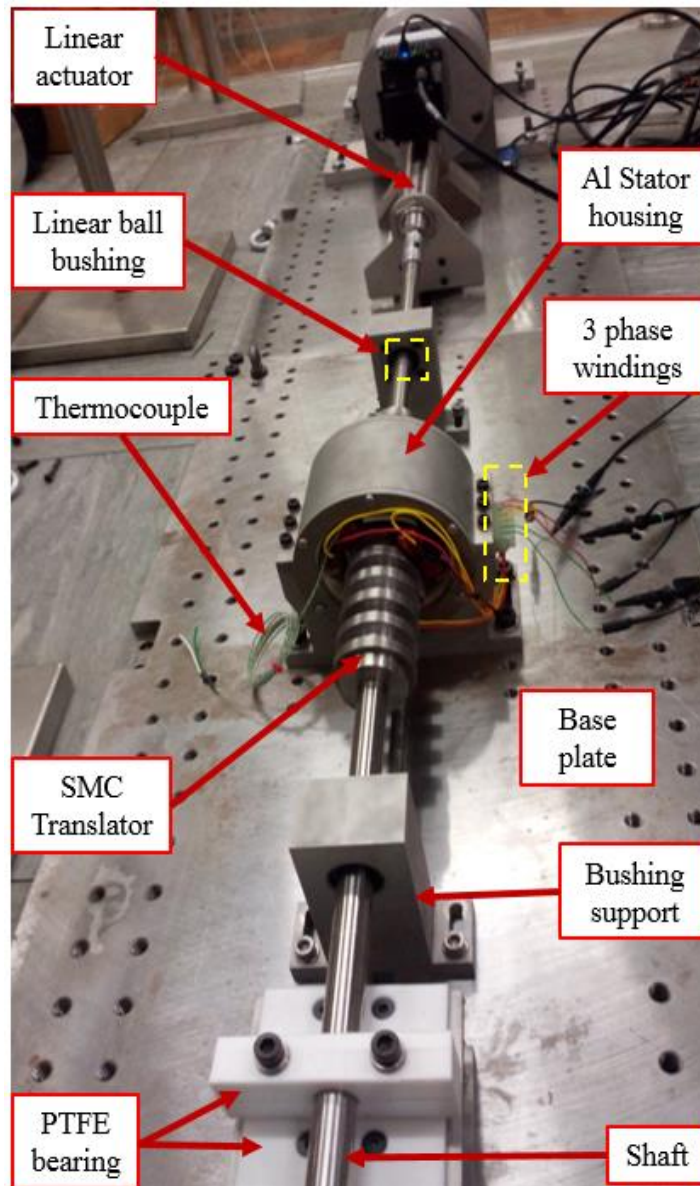


Figure 5. 24: Fully assembled cylindrical VHM-I mounted on the test rig.

### 5.7.2 Resistance Measurement

DC voltage of known magnitude is applied in each of the phase windings and the corresponding current is recorded by the multimeter. Then the phase resistance can be easily calculated by using Ohm's law. Another method is to directly measure each coil resistance by a digital multimeter. Table 5-7 presents phase resistances by both methods mentioned.

Table 5- 7: Phase resistance measurement

Phases	Ohm's law ( $R=V/I$ )	Digital multimeter
Phase-A resistance ( $\Omega$ )	0.540	0.542
Phase-B resistance ( $\Omega$ )	0.535	0.538
Phase-C resistance ( $\Omega$ )	0.539	0.54

### 5.7.3 Inductance Measurement

The static test was performed to measure the inductance in each phase. The transient AC current of 1A was applied from a 50Hz power supply in each phase individually. Corresponding phase voltages were measured at the machine terminals. From the measured voltage and applied current, the impedance can be calculated. Using the measured resistance in each phase, phase inductance can be calculated from the impedance. Table 5-8 shows the measured and FEA simulated inductance for three phases.

Table 5- 8: Comparison between measured and simulated inductance results

Inductance	Measured	Phase inductance (FEA)	% error
Phase-A	6.2mH	5.11mH	21%
Phase-B	5.8mH	5.1mH	14%
Phase-C	5.5mH	5.13mH	7%

Measured inductance is 21% higher than the FEA predicted results. The main reason behind the difference is most likely to be due to the non-uniform air-gap under each stator tooth (Figure 5.27), which will be discussed in the coming sub-section. Non-uniform nature of hand wound coils and tolerance in the material properties are some of the other reasons which might add to the difference in the results.

### 5.7.4 Open Circuit Test

The machine has been tested by being driven open circuit by the ball screw over a 100 mm displacement with a peak speed of just over 1 m/s. Three voltage probes were used to monitor the three phase no load voltages induced in the windings. Figure 5.25 shows the three phase no load EMF for variable speed during one mechanical cycle.

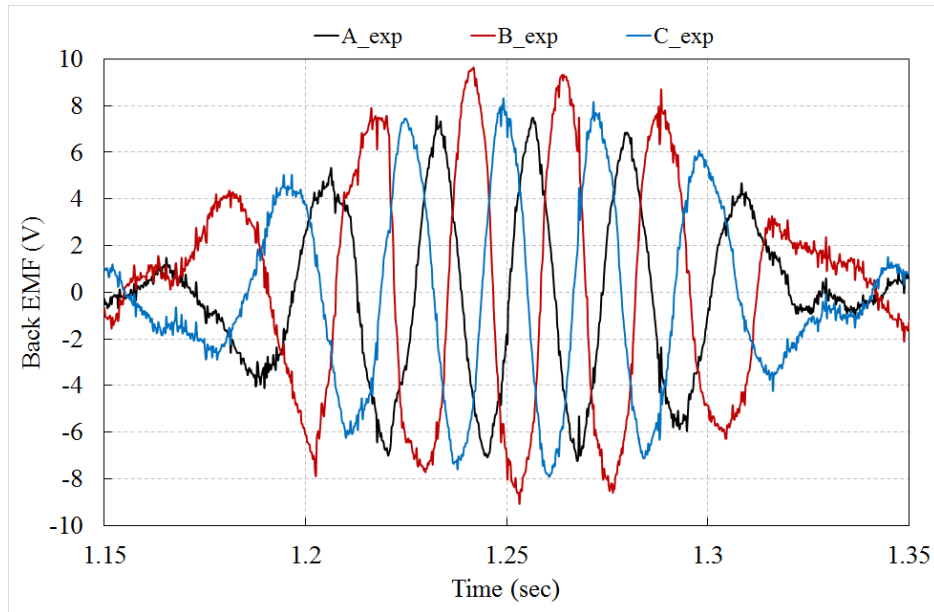


Figure 5. 25: Measured EMF for single mechanical stroke.

Figure 5.26 shows the comparison between the simulation and measured results over 2 electrical cycles. In the simulation, the variation in RMS EMF across the three phases is less than 2%. In the measured values, there is a maximum variation of 26%, with RMS values of 1, 0.73 and 0.83 per unit. This is because the translator is eccentric in the stator - meaning each phase of the prototype has a different magnetic air-gap, and the value of that air-gap is not constant with the angular position. This resulted from the bent shaft. Air gap size across the three teeth of the prototype was measured at various points in the air-gap and throughout the oscillation cycle and found to vary between 0.6 mm and 1.1 mm. The variation is clearly visible in Figure 5.27.

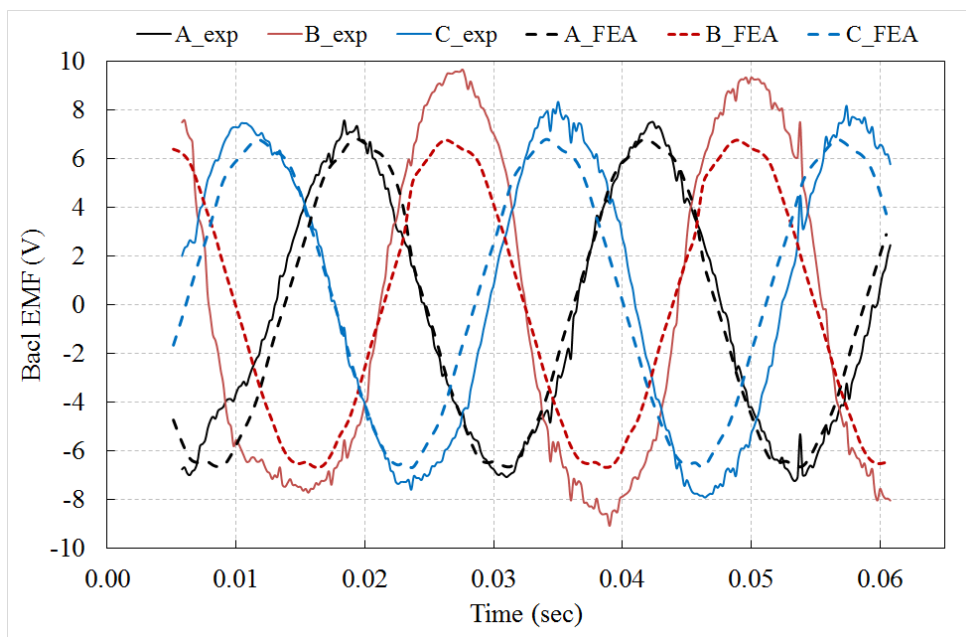


Figure 5. 26: Back EMF comparison between experimental and simulation results over two electrical cycles

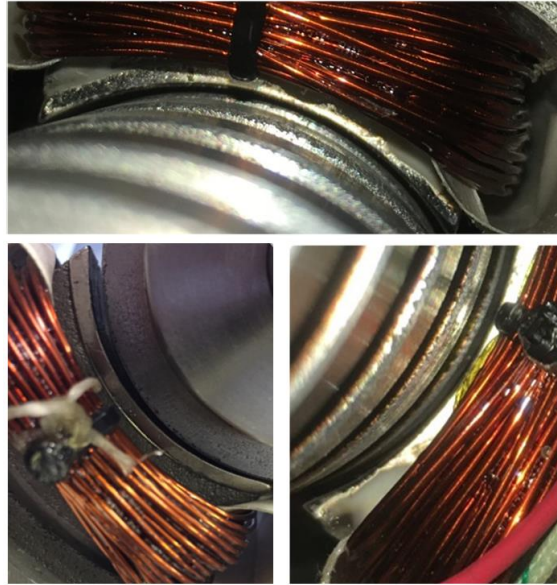


Figure 5.27: The three air-gap regions of the prototype under three stator teeth.

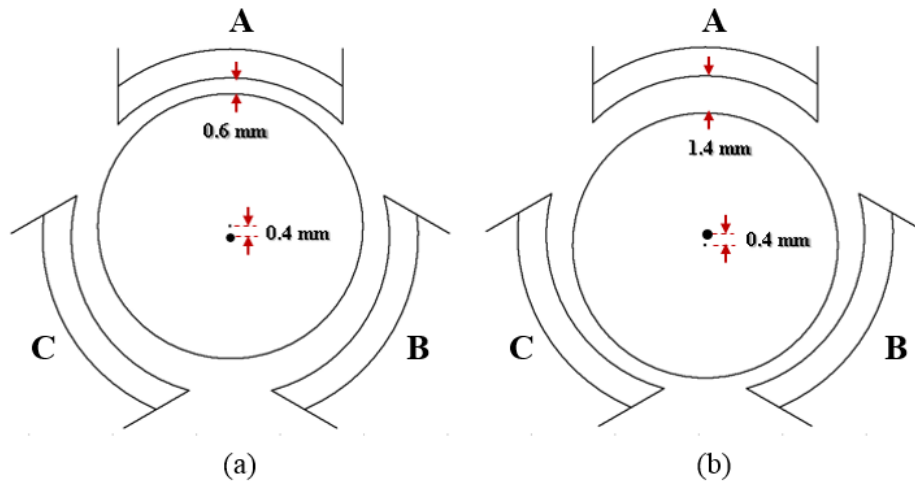


Figure 5.28: Air-gap imbalance (a) translator shifted up by 0.4mm (b) translator shifted down by 0.4mm

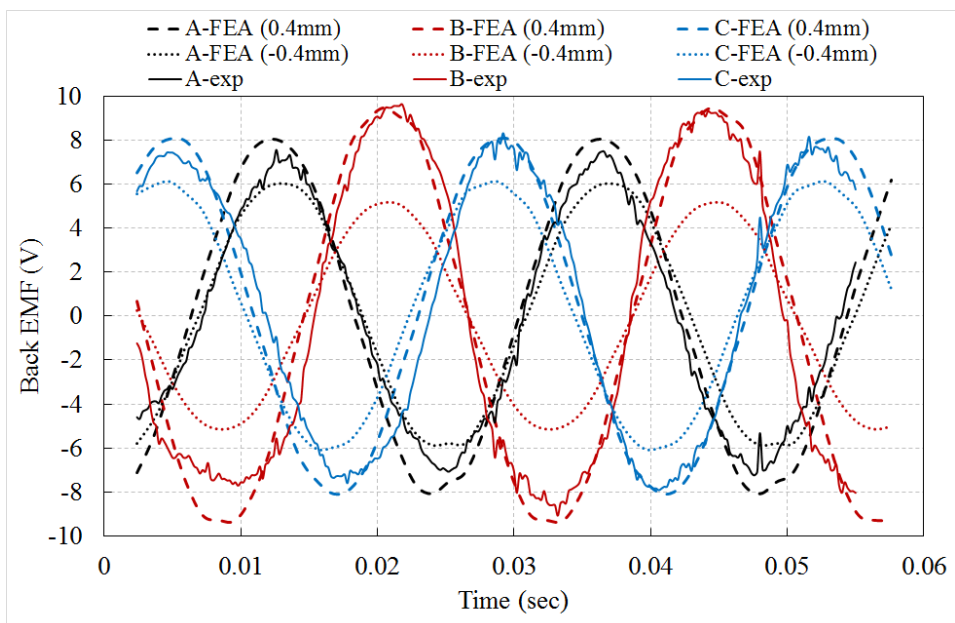


Figure 5.29: Measured (exp) and simulated (FEA) results for two values of offset translator.

To validate the fact that eccentricity was causing the imbalance, two FEA models were adapted to allow for a non-concentric stator. It was offset with respect to the centre line of phase A by +/- 0.4 mm giving a variation in the average air-gap across the three teeth of 0.7 -1.3 mm, as shown in Figure 5.28. A direct comparison of the offset simulations and the experimental results is shown in Figure 5.29.

Table 5-9 shows a summary of the simulation and experimental results. The offset of the prototype translator is likely not along the centre line of a tooth, and so none of the simulations in Table 5-8 is fully representative of the real prototype testing situation. The +0.4 mm offset result gives the closest result to the measured EMF value (maximum of 8% error) and also represents the closest approximation to the measured air-gap.

*Table 5- 9: Simulated and measured performance of the cylindrical VHM-I*

<b>Parameters</b>	<b>Simulation</b>			<b>Measured</b>
Offset (mm)	0.4	0.0	-0.4	---
Phase-A air-gap (mm)	0.7	1	1.3	0.6-1.1
Phase-B air-gap (mm)	1.2	1	0.9	0.6-1.1
Phase-C air-gap (mm)	1.2	1	0.9	0.6-1.1
RMS back EMF—B/A (p.u)	0.86	1.02	1.21	0.73
RMS back EMF—C/A (p.u)	0.83	0.99	1.17	0.83
Phase-A peak EMF (V)	9.63	7.05	6.31	9.64
Phase-B peak EMF (V)	8.17	6.97	7.34	8.32
Phase-C peak EMF (V)	8.18	7.01	7.45	7.56
Error in peak EMF—phase-A	0%	27%	35%	-
Error in peak EMF—phase-B	2%	16%	12%	-
Error in peak EMF—phase-C	-8%	7%	1%	-

## **5.7.5 Static Force Measurement**

### **5.7.5.1 Cogging force**

Figure 5.30 shows the comparison between experimental and FEA predicted results (uniform air-gap) for the cogging force of the machine. The linear actuator was used to move the translator by static position in 1mm steps and the respective cogging force was measured by the force transducer. The trend (moving average) of the experimental results follow the predicted results and is reasonable. However, comparing the peak cogging points, it shows a maximum of over 100% variation in the experimental results.

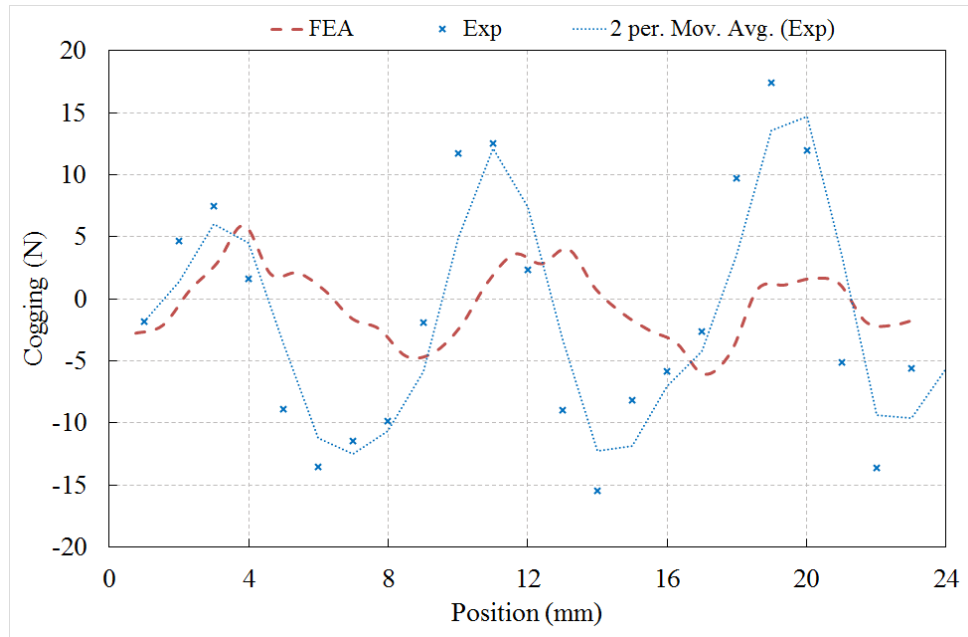


Figure 5. 30: Comparison between experimental and predicted results.

This discrepancy in the cogging force is most likely due to the imbalance in the air-gaps under three phases, which is already described in the previous sub-section. The second important factor is the mechanical tolerance/accuracy of the linear actuator. Although the movement of the translator was commanded to be 1mm by the associated software, there might be variation in the range of fractions of mm. Other factors might include mechanical tolerance in magnet assembly, manufactured PMs characteristics compared to the FEA provided characteristics and also the accuracy of the load cells (force transducer). However, the amplitude of the experimental results is only reasonable, the model clearly predicts the shape of the cogging force characteristic.

#### 5.7.5.2 Thrust force

A similar static force measurement technique was performed as mentioned in the previous sub-section. The only difference is the applied current in all three phases. Force was measured at every 1mm of displacement of the translator by the linear ball screw. Phase-A was energised with 0-4A DC in 1A intervals, while the other two phases were supplied by half of the phase-A current in the opposite direction to mimic the nature of three phase instantaneous current. Figure 5.31 shows the measured static force curves for varying current. The peak applied current was limited to 4A due to the limitation of the DC power supply available during the experiment.

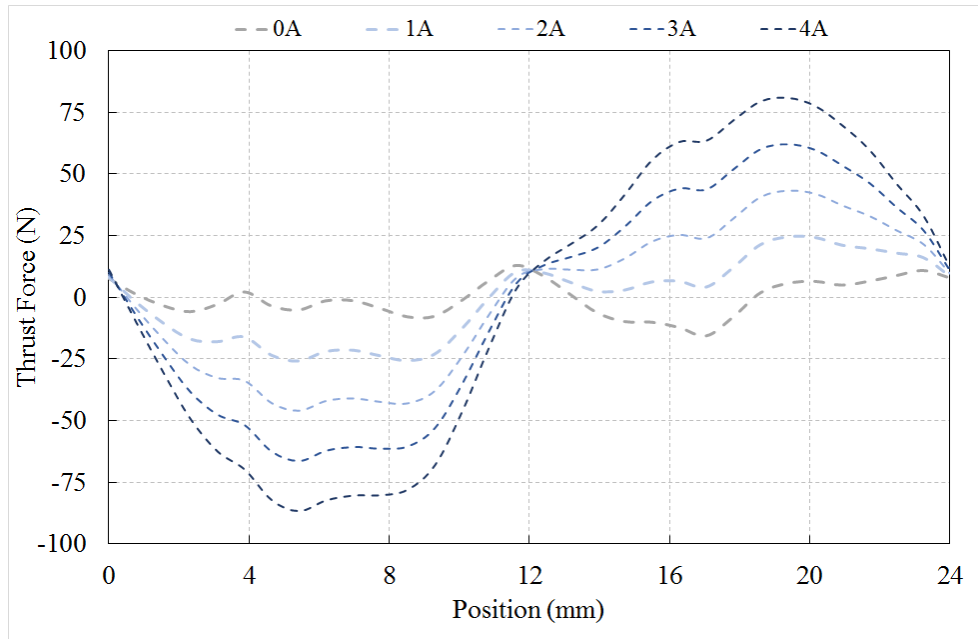


Figure 5. 31: Experimental results for the static force test.

Figure 5.32 shows the peak thrust force at different DC current level. It compares the experimental results with the simulated model for two different offset levels for the translator as mentioned earlier in the no-load test. It can be clearly understood that the experimental result falls in between the two offset limits and the variation minimises as the current level increases. However, peak thrust forces are still proportional to the applied current. Therefore, it can be agreed that the correlation between the simulated and the experimental results can be considered as a reasonable match.

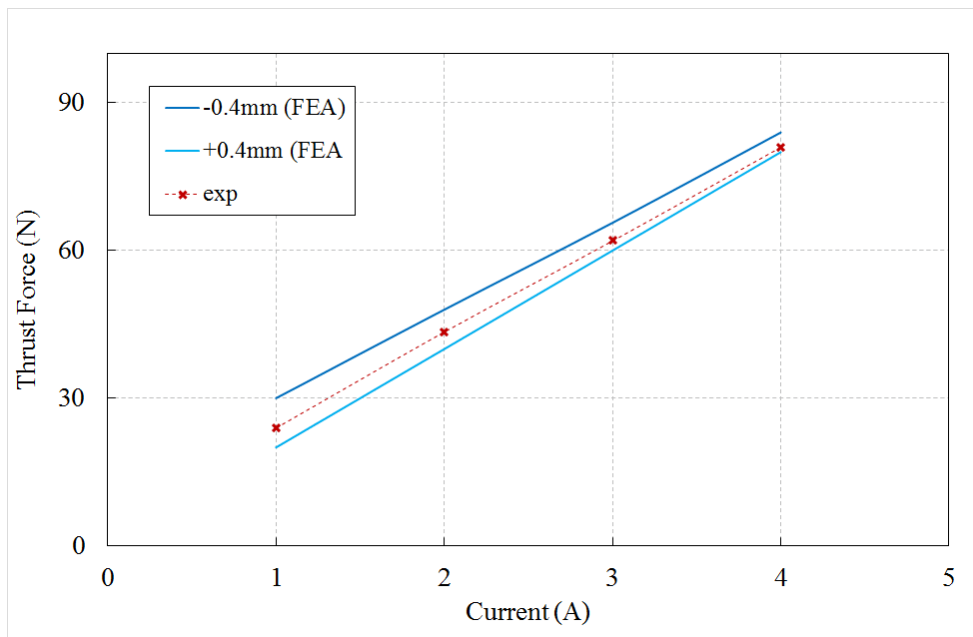


Figure 5. 32: Peak force comparison between simulation and experimental results for varying current.

### 5.8 Power Factor

The power factor for both machines has been calculated and compared using transient FEA simulation. The power factor is estimated based on the amplitudes of the terminal voltage and the phase current. Assuming the machines are connected to the fully rated converter, the three phase sinusoidal currents are applied in phase with the back EMF to achieve the maximum thrust force. The power factor is then obtained by the cosine of the phase angle between the voltage and the current. It was found that the phase angle between current and voltage are  $67^\circ$  and  $64^\circ$  for flat and cylindrical machine respectively. The cylindrical machine can achieve a power factor of 0.44 compared to 0.39 for the flat variant. Therefore, the flux concentration effect from the cylindrical machine improves the performance and the power factor compared to the flat VHM.

### 5.9 Conclusion

A cylindrical variant of the linear single sided Vernier Hybrid Machine (VHM-I) has been introduced. A basic geometrical study has been used to show that it can offer a mass saving in some scenarios compared to the single-sided flat topology. A more thorough design study based on FEA has indicated that the cylindrical version can offer an 11% improvement in the average force, and reduce cogging on the translator to a minimal compared to the flat VHM-I topology with no change in the magnet mass and current density. The improved performance is primarily due to the flux focusing effect of the cylindrical version increasing the flux density in the air-gap combined with an improved air-gap area to volume ratio. Finally, the cylindrical topology has been built using SMC billets and demonstrated in a laboratory, where a measured imbalance in the back EMF across the three phases of 14-17% is believed to be due to an offset translator. Simulations could replicate experimental results to within 8%.

## Chapter 6: Cylindrical Vernier Hybrid Machine-II

### 6.1 Introduction

In this chapter, another cylindrical Vernier Hybrid Machine (VHM-II) with a three dimensional (3D) flux path has been developed from the flat double-sided E-core Vernier Hybrid Machine (VHM-II). Both machines have an equal amount of PM material mounted on the surface of the stator teeth (Figure 6.1). 3D FEA is performed in order to predict the flux flow and compare the performance of the flat and cylindrical versions. Comparative FEA performance between them shows that the cylindrical VHM-II provides higher force density for a fixed Permanent Magnet (PM) mass and current density. The Pole shifting method has also been applied for the cylindrical VHM-II prototype. Finally, the cylindrical topology with pole shifted stators has been constructed in the laboratory and tested to evaluate and validate the predicted machine performance.

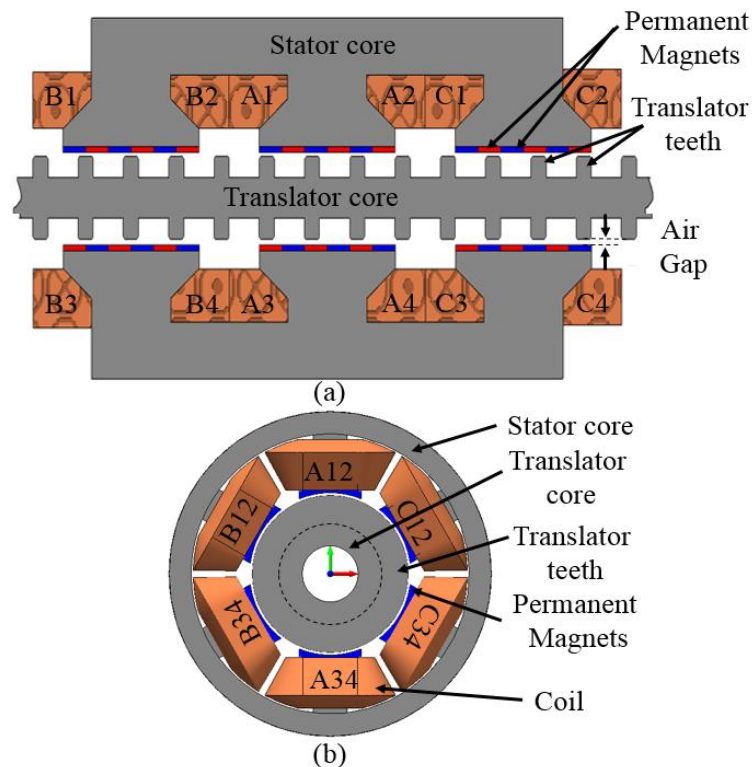


Figure 6. 1: (a) Flat double sided E-core VHM-II (b) cylindrical VHM-II

The main difference between the VHM-II and the VHM-I of chapter 5 is the number of stator teeth. The VHM-II has double the number of PM poles and the coils per phase compared to the VHM-I, while the overall PM mass is the same between them. The flat version of the VHM-II is double sided and has double the axial length compared to the flat VHM-I, which gives an

equal stator and PM mass between them. The VHM-II has the advantage to be skewed (pole shift) in the direction of motion to reduce the cogging and the force ripple.

## 6.2 Machine Specification

A double-sided flat E-core VHM-II machine and a cylindrical VHM-II are shown in Figure 6.1. The flat machine presented in chapter 3 is scaled down and a translator with core back is used instead of the segmented translator — to allow the same translator to be used in the experimental work to match the specification of the lab-scale cylindrical VHM-II. Table 6-1 presents an outline specification of the lab-scale machine.

*Table 6- 1: Main machine parameters for the cylindrical VHM-II*

<b>Parameters</b>	<b>Values</b>
The maximum outer diameter (mm)	200
Shaft diameter (mm)	20
Stator teeth per phase	2
Pole pairs per stator tooth	3
Air gap length (mm)	1
Stator pole pair pitch (PPP) (mm)	24
Translator pitch (mm)	24
Rated current density (A/mm <sup>2</sup> )	3.5

## 6.3 Development of the Cylindrical Topology

Cylindrical linear machines have the merit of a smooth cross-section, potentially offering a better surface for sealing than the flat (rectangular) counterpart. The increased surface area to volume ratio makes for shorter stators and a reduction in the number of component parts compared to flat versions. Finally, as mentioned in the previous chapter, the cylindrical structure enables the generator to withstand parasitic forces/torques equally well from all directions above or under the water. Hence, a cylindrical version of the VHM-II is developed from the previously reported double-sided flat version as shown in Figure 6.2(a) by the following steps:

1. Rotating the stators 90° around the axis of PM's magnetisation (Y-axis), shown in Figure 6.2(b).
2. Extending the translator teeth along the axial length (Z-axis). Shifting the stator teeth pairs under phase A and phase C to be almost aligned with the teeth under phase B. For a 120 electrical degree phase shift between three phases A, B and C must be offset relative to each

other in the X direction, Figure 6.2(c). If  $\tau_t$  is the translator tooth pitch, then the shift is defined in equation (6-1)

$$X_{shift} = \tau_t \left( n - \frac{2}{3} \right); n=0, 1, 2, 3, \dots \quad (6-1)$$

3. The two stators and the translator are now wrapped around the axis of motion (X-axis) to form a tubular structure—Figure 6.2(d) and Figure 6.2(e). Magnets and stator teeth are hence formed into arc shapes. The stator cores are joined and now form a cylindrical shell covering all six stator teeth showing in Figure 6.2(e).

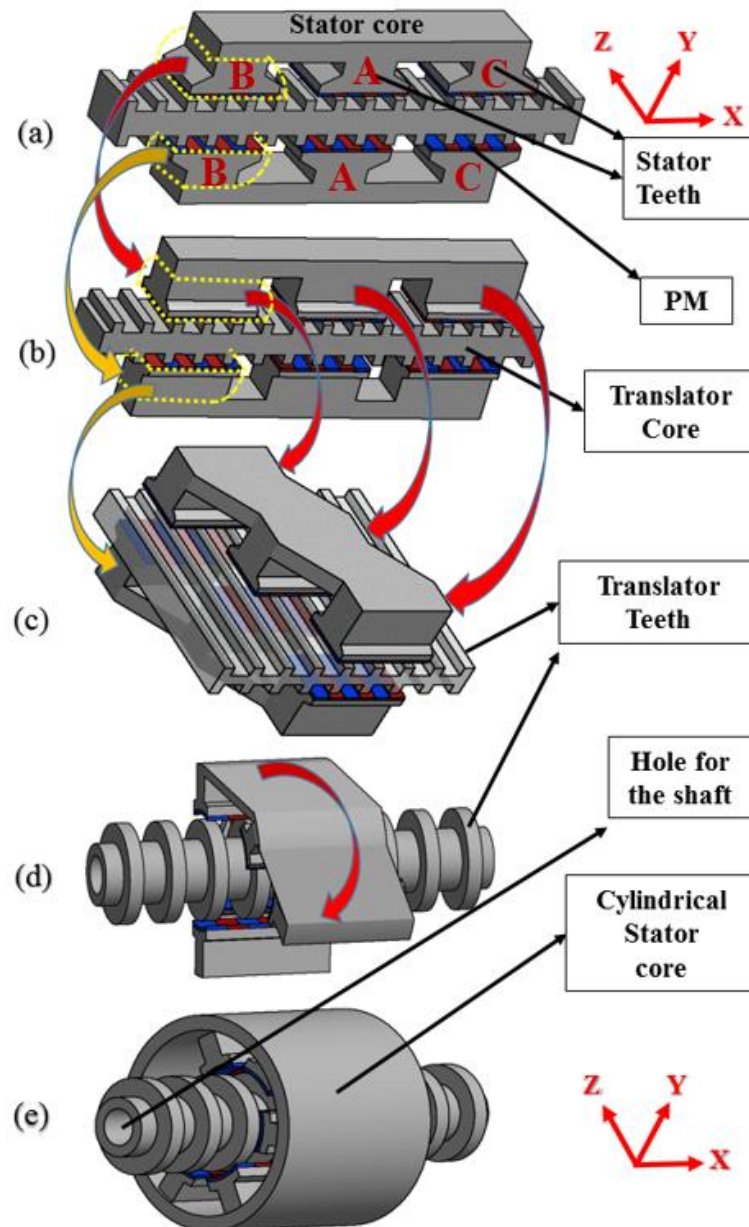


Figure 6. 2: Cylindrical Vernier machine topology development.

#### 6.4 Principle of Operation

The principle of operation of the cylindrical VHM-II is almost identical to the flat version, with the alignment and un-alignment of PM and translator teeth directing the magnetic flux around the stator and translator as mentioned in chapter 3. However, in the cylindrical model, all stator teeth sit on a combined core back. The flux path can be understood from Figure 6.3 that shows the three independent flux paths for three phases in the alignment position. During the un-alignment position, most of the flux leaks due to the opposite polarities of the adjacent magnets and the resultant flux linkage in those coils under the same phase is almost zero. However, all three phases link through the same translator teeth and core back, as the translator flux path is now circumferential and parallel to the stator teeth, rather than perpendicular to the teeth in the double-sided flat version. As there is a mechanical shift,  $X_{shift}$  between stator teeth, the stator teeth end (in Z- direction) of different phases do not always share the same translator tooth. Therefore, the translator core carries only a small amount of flux in the transverse direction (Z-axis) between stator teeth due to the shift. For this reason, the volume of the translator core back can be downsized for the cylindrical model compared to the flat version.

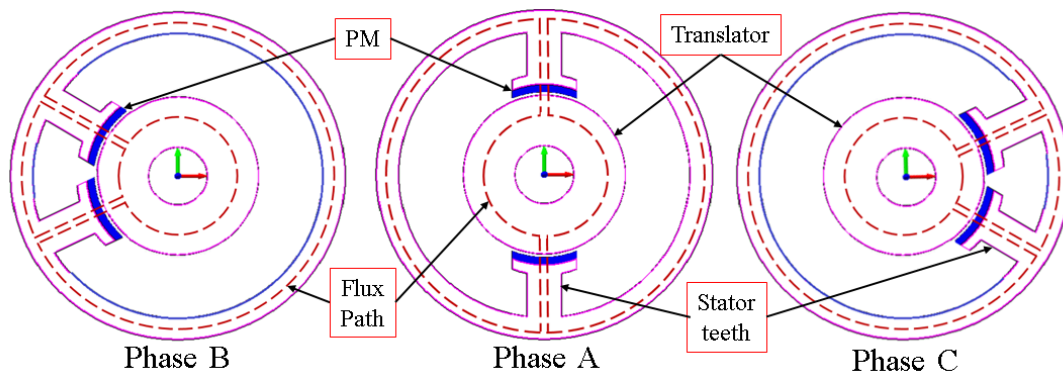


Figure 6. 3: 2D flux path representation of the separated three phases of the cylindrical machine

#### 6.5 Finite Element Analysis & Machine Performance

In order to analyse and compare the flat and cylindrical versions, both topologies have been built and investigated by FEA. The important parameters including PM volume and current density are fixed between both the topologies and presented in Table 6-2.

Table 6- 2: Model Parameters for both Machines

Parameter	Flat VHM-II	Cylindrical VHM-II
PM thickness (mm)	2.5	2.5
PM length / PM arc length (mm)	22.5	22.5 (45°)
Axial length / outer diameter (mm)	22.5	116

Active length (mm)	280	90
PM mass (kg)	0.18	0.18

Figure 6.4 shows the refined 3D mesh setup of the FEA model and the no-load flux distribution of the cylindrical topology. The black arrows show the direction of the flux flow in Figure 6.4(a).

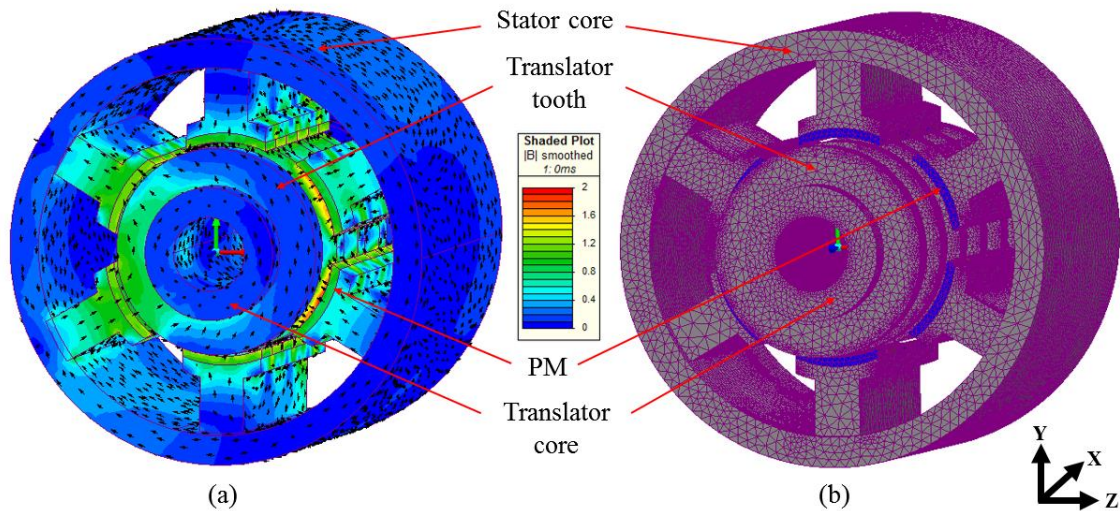


Figure 6. 4: 3D model of cylindrical VHM-II, a) Magnetic flux density distribution b) 3D mesh

### 6.5.1 Reduction of Cogging by Pole Shifting

Pole shifting is equivalent to skewing or short pitching in linear machines, which is commonly used to eliminate or minimise the parasitic effects of the higher order harmonics in the cogging force. It was demonstrated in chapter 3 that the most dominant 6<sup>th</sup> order harmonic can be minimised by implementing the pole shifting method in the flat double-sided VHM. The cylindrical variant of the double-sided topology is also analysed for the minimum cogging and force ripple by implementing the pole sifting method [86].

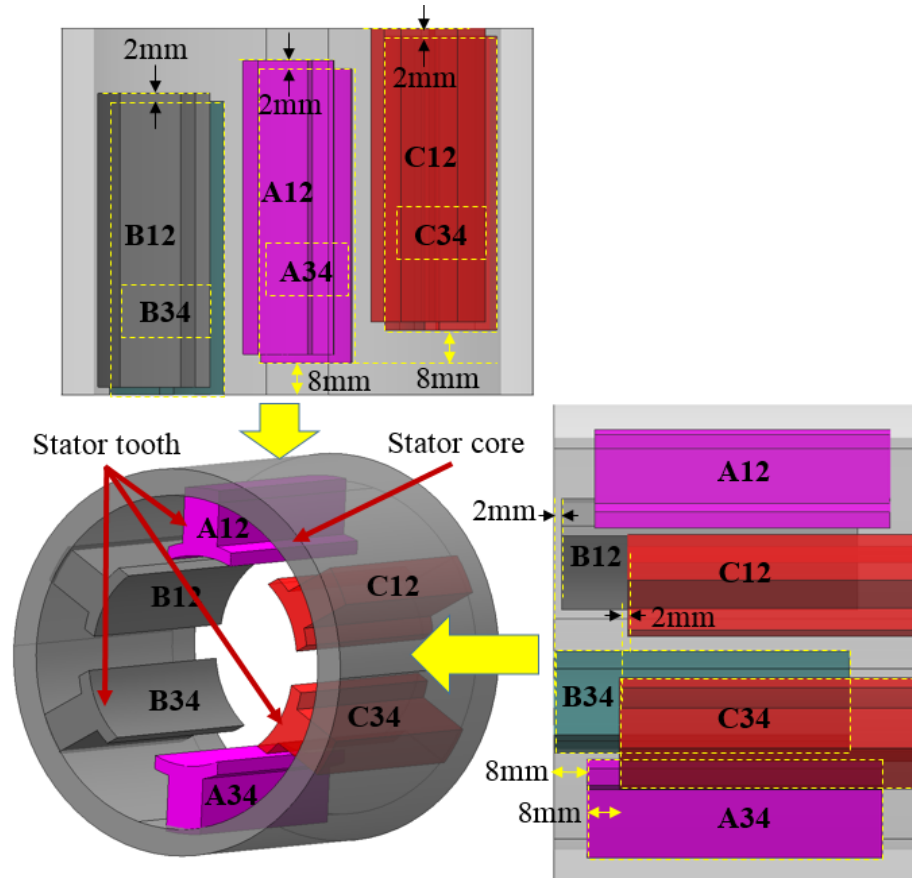


Figure 6. 5: Stator teeth geometry of the cylindrical topology for cogging reduction

Figure 6.5 illustrates the stator teeth and pole shifting method for the cylindrical topology. All six stator teeth are labeled as A12, A34, B12, B34, C12 and C34 under three phases – A, B and C. Each phase is physically shifted in the direction of motion by 8mm ( $1/3^{\text{rd}}$  of the translator tooth pitch) with respect to each other, which is equivalent to  $120^\circ$  electrical. To illustrate the pole shifting method for the cylindrical machine, three teeth under three phases (A12, B12, and C12) stay in their fix positions, while the other teeth (A34, B34, and C34) shift by certain amounts to see the effect on cogging. Figure 6.5 shows that A34, B34, and C34 are shifted by 2mm in the direction of motion from A12, B12, and C12 respectively, which is equivalent to  $30^\circ$  electrical shift.

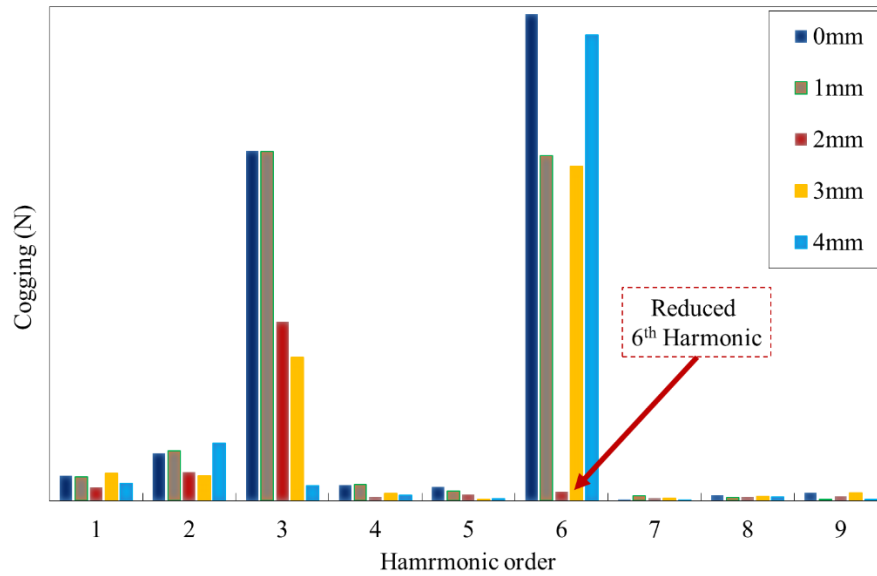


Figure 6. 6: Harmonic distribution for different pole shifted models.

In each position and for each relative displacement of stator teeth, the cogging force is simulated. Figure 6.6 shows the harmonic analysis for relatively shifted stator teeth and poles under the same phases. 0mm to 4mm shifts between stator teeth under the same phases have been analyzed to demonstrate the cogging performance variation. It can be clearly seen that the dominant 6<sup>th</sup> order harmonics reduced to a great extent for the 2mm shift, which has also been proved in chapter 3 for the double-sided flat variant. The displacement between stator poles under the same phase has the disadvantage of reducing the fundamental harmonic in the phase armature coils of the magnetic flux when the displacement is further increased.

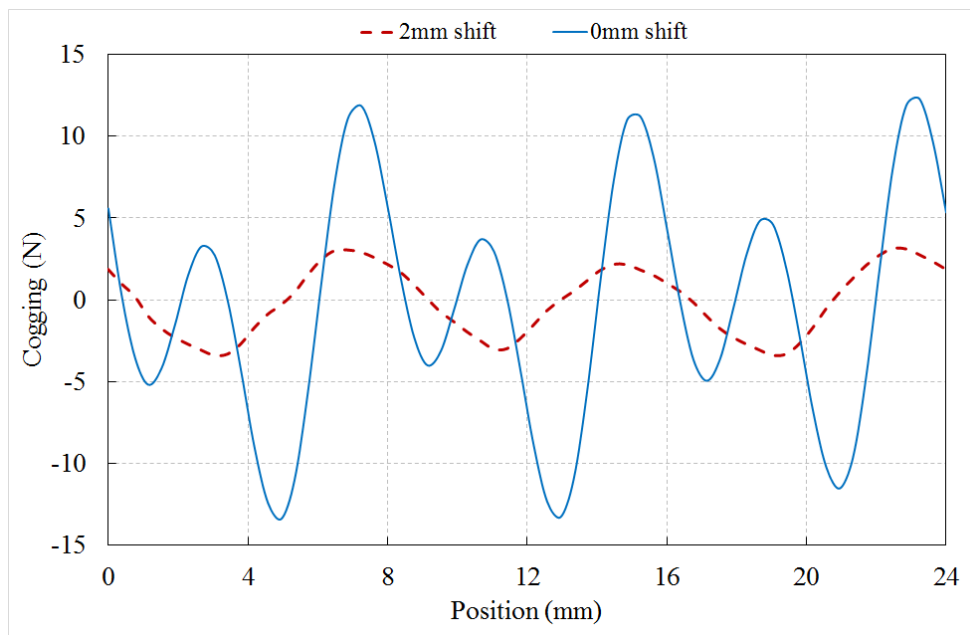


Figure 6. 7: Cogging force variation by pole shifting.

Figure 6.7 shows the cogging for a complete electrical cycle for 0mm and 2mm pole shifts. It is noticeable that the 2mm shift provides the lowest cogging — consists of 3 cycles with three peaks and three troughs while reducing the average force by only 3%.

Table 6- 3: Cogging and average force variation for various stator teeth and pole shift

Pole shift (mm)	Cogging (N)	% cogging reduction	Average force (N)	% force reduction
0	24	0%	197	0%
1	19	20%	193	2%
<b>2</b>	<b>6.5</b>	<b>73%</b>	<b>190</b>	<b>3%</b>
3	13	46%	181	9%
4	16	33%	173	12%

### 6.5.2 Flux linkage

Figure 6.8 shows the flux linkage plot for all six coils in the cylindrical VHM-II. A most noticeable feature is the shift in flux linkage between coils under the same phase. This shift is caused by the 2mm axial shift between two stator teeth and poles under the same phases, which is demonstrated in the previous section to reduce cogging. Therefore, the coil flux is shifted by 2mm in the direction of motion giving a reduction in phase flux linkage. However, the direction of flux is reversed every half electrical cycle over the translator pitch, as mentioned in the operation principle. It also represents that the flux linkage is a smooth function of relative translator teeth and magnet position.

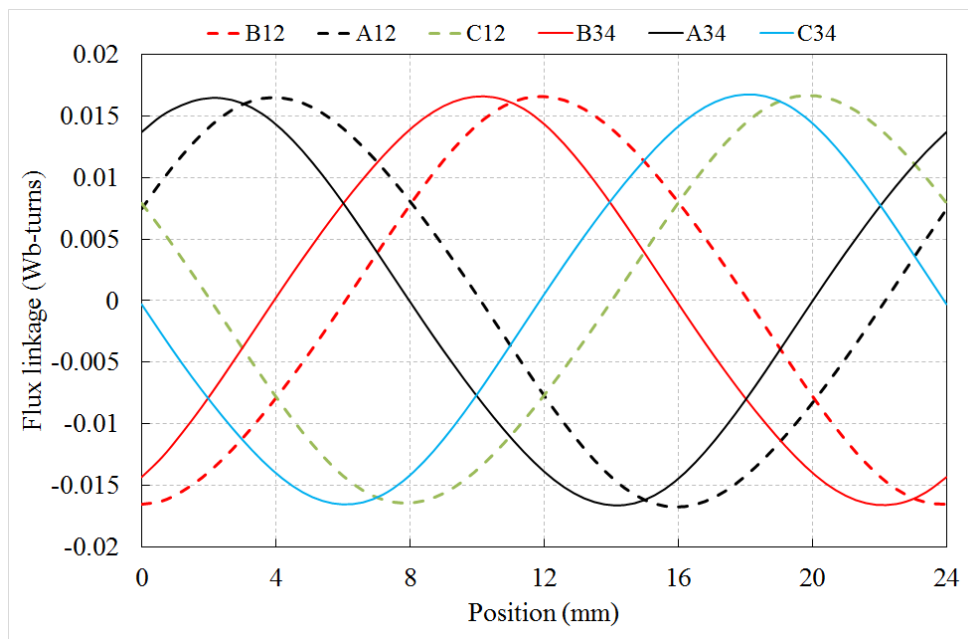


Figure 6. 8: No load armature coil flux linkage

**6.5.3 Back EMF**

No load back EMF plot for all six coils for the VHM-II is plotted in Figure 6.9. As discussed earlier in the flux linkage section, the back EMF of two coils under the same phase are also shifted by 2mm in the axial direction due to the physical displacement between the stator teeth. However, three phases can be clearly distinguished and symmetrical with a 120° electrical shift between them.

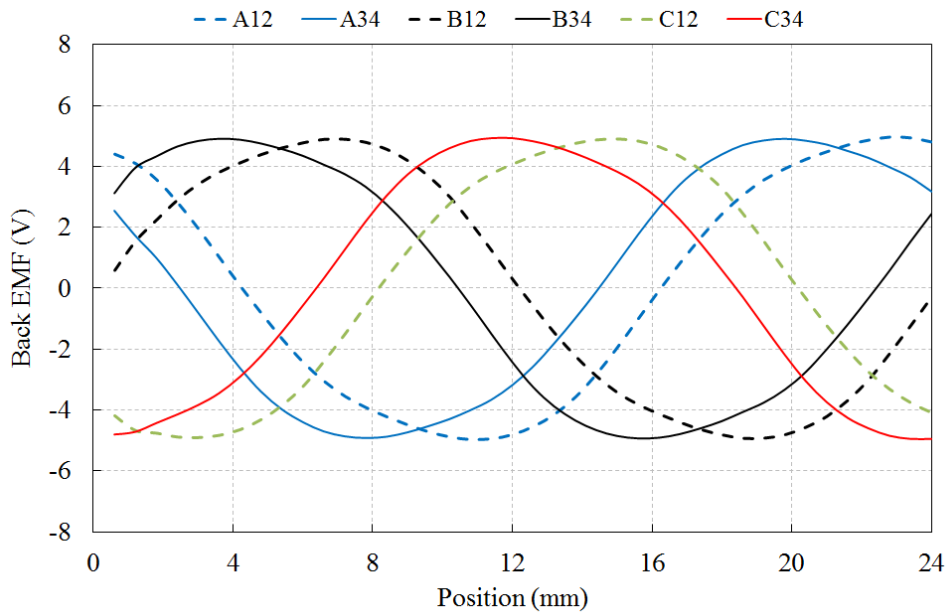


Figure 6. 9: No load armature coil back EMF

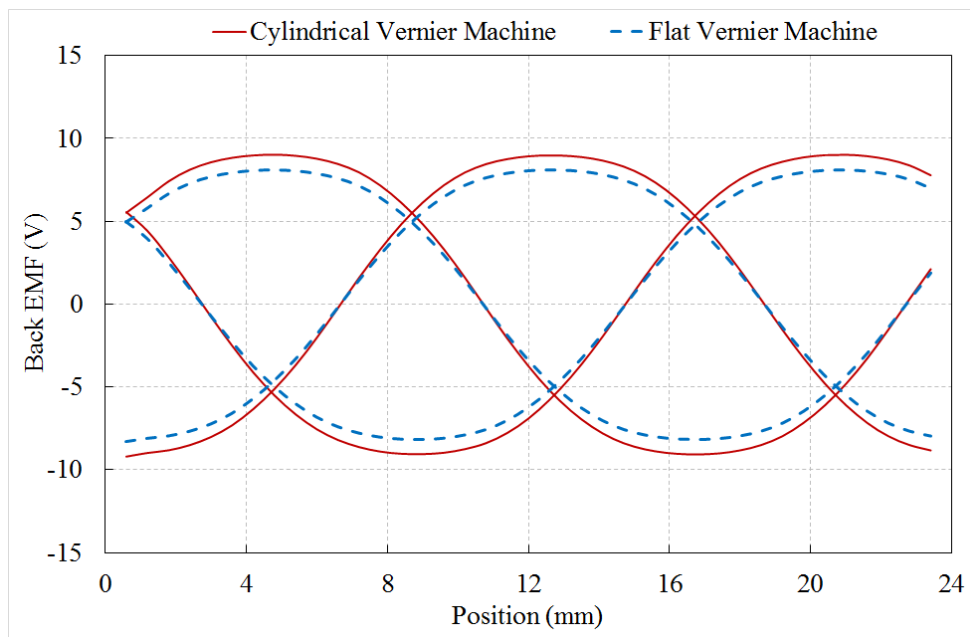


Figure 6. 10: Three-phase back EMF comparison between flat and cylindrical topology

Figure 6.10 demonstrates the comparison of three-phase back EMF between cylindrical and flat machines at the nominal speed of 1.2m/s. The back EMF from two coils under the same phase, displayed in Figure 6.9 are summed together to get the phase voltages. The shift between coil EMF causes a slight reduction in the phase back EMF of less than 5%. Again, as mentioned above, a  $120^\circ$  electrical shift between phases can be observed with an identical peak voltage level for both topologies.

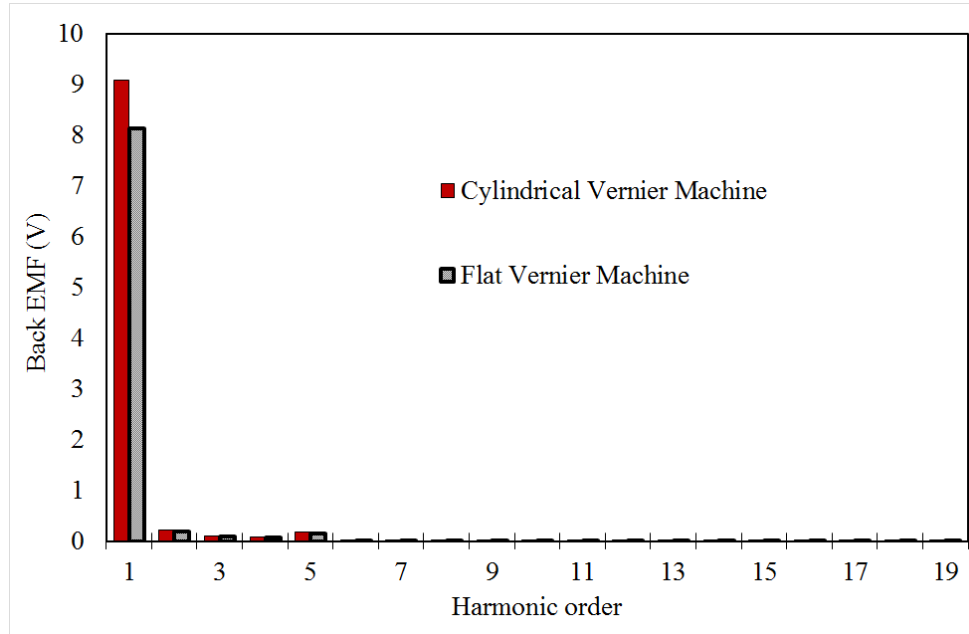


Figure 6. 11: EMF harmonics comparison between flat and cylindrical

The cylindrical machine including stator and translator are constituted of SMCs, while the flat machine is constituted of laminated iron sheets as it is possible in this case to reduce the induced eddy current and thus the iron loss. The cylindrical VHM-II provides almost 10% higher back EMF than the flat version. Figure 6.11 confirms that the cylindrical machine has a higher fundamental first order EMF harmonic compared to the flat VHM-II. This is because the arc-shaped magnets in the cylindrical model concentrate the flux into the slotted translator unlike the flat model, which creates a higher flux density in the air gap region. This flux concentration phenomenon has been demonstrated earlier in the previous chapter with the flux density plot.

### 6.5.4 Thrust Force

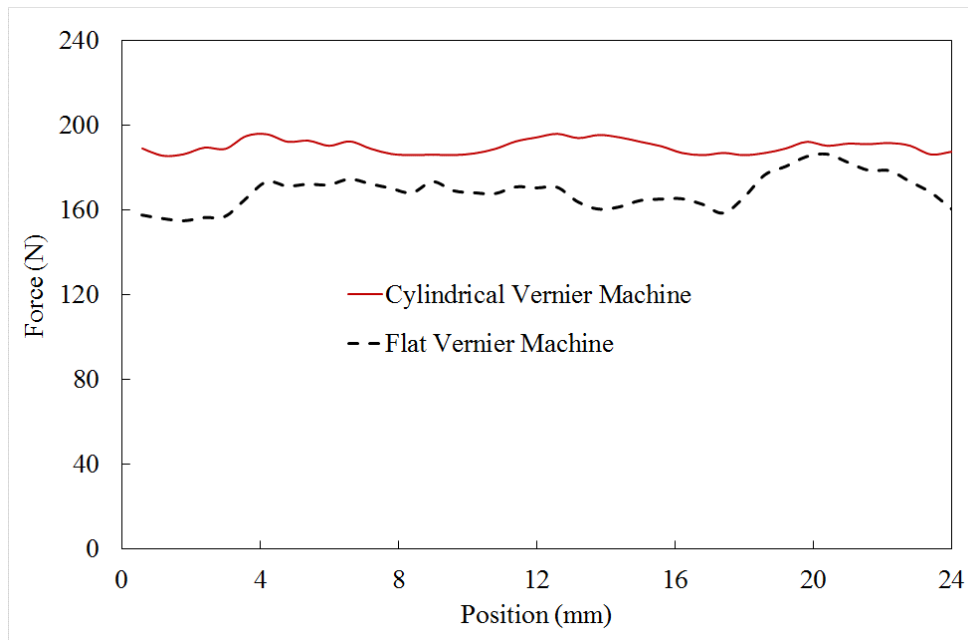


Figure 6.12: Thrust force comparison between flat and cylindrical VHM-II at rated current

Thrust force produced by both the machines at the same rated current density and speed is presented in Figure 6.12. A sinusoidal current was injected into the q axis of the machine and the average thrust force of the cylindrical model was found to be 190N compared to 170N for the flat model. This higher thrust force is due to the higher fundamental EMF component in the cylindrical model. The force ripple is 10N compared to 26N for the flat version. Force ripple in the cylindrical VHM-II is only 5.5% of the average force due to the reduction of cogging by the pole shifting method analysed previously in this chapter.

### 6.5.5 Inductance

The inductance calculation is based on the method mentioned in section 4.4.6.4 (Synchronous inductance – Method D). Static 3D FEA has been performed to find the three-phase flux linkage with and without armature current over a displacement of one full electrical cycle. Figure 6.13 presents three-phase inductances. It is important to notice that, inductances in phase-B and phase-C are slightly higher than phase-A. This is because the self-inductance of phase B and C are higher than phase A.

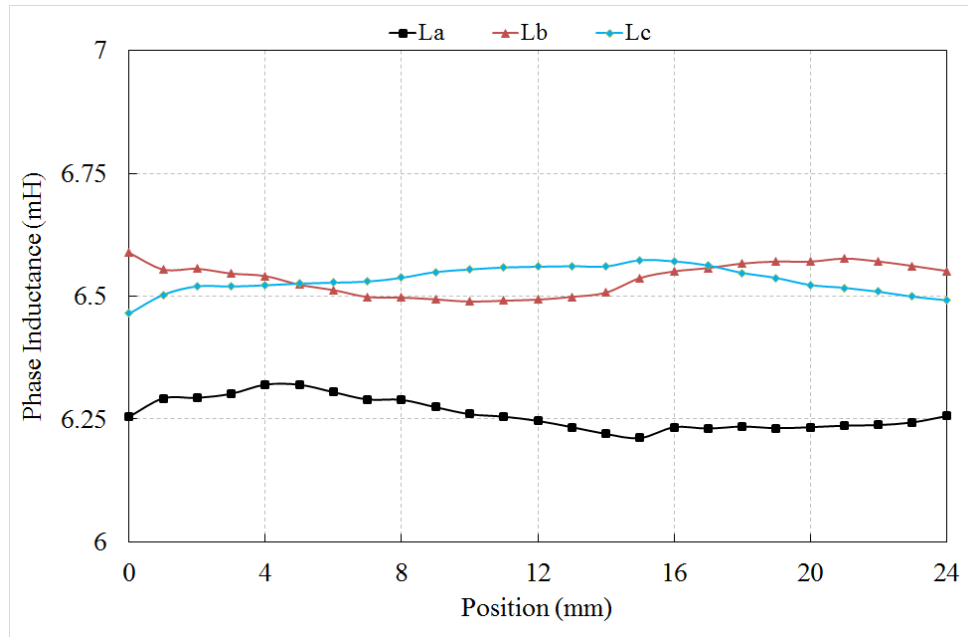


Figure 6.13: Phase inductance for 3D FEA

This inductance consists of two components – a self-induced flux component and mutually induced flux component from another coil under the same phase. As phase-B and phase-C both consist of two adjacent coils, these coils have higher self-inductance due to mutually induced flux component within coils under the same phase compared to almost no mutually induced flux between coils under phase A, where two coils faced opposite to each other separated by the translator (Figure 6.1).

Table 6- 3: three phase inductances for the cylindrical machine

	$L_{avg}$ (mH)	$L_{pk-pk}$ (mH)	% ripple
La	6.26	0.11	1.8
Lb	6.54	0.1	1.5
Lc	6.53	0.11	1.7

It can be observed that the variation of inductance between the d and q axis is less than 2% for all three phases. This basically states that these machines have almost no salient torque, which justifies why in this research, it has been assumed that current is controlled to be in the q axis in order to achieve maximum force as for all the machines in this thesis.

FEA performance of the flat and the cylindrical VHM-II are compared and presented in Table 6-4.

*Table 6- 4: FEA performance comparison between flat and cylindrical VHM-II*

<b>Performance</b>	<b>Flat VHM-II</b>	<b>Cylindrical VHM-II</b>
Open circuit voltage (V)	8.1	9
No load flux linkage (mWb-turns)	29	32
Average Thrust force (N)	170	190
% Thrust force ripple	15	5.5
Cogging force (N)	20	6.5
Shear stress (kN/m <sup>2</sup> )	13	12
Machine power density (kW/m <sup>3</sup> )	255	400
Force density (kN/m <sup>3</sup> )	213	333

## 6.6 Prototype Machine Building & Testing

A small-scale laboratory prototype cylindrical machine has been designed and built to prove the concept and validate the FEA. Both the translator and the stator structure were made of Soft Magnetic Composite (SMC) materials in order to accommodate the 3D flux path (radial, axial and circumferential). Component pressing was not practical for a one-off prototype and so the entire machine is made from multiple 20mm prototype cylindrical billets. Therefore, the prototype material was magnetically poorer than the pressing component directly. The translator is made from a series of blocks mounted on a common shaft. The entire stator including six stator teeth was made from a stack of SMC blocks.

### 6.6.1 SMC Stator Design

The stator for the cylindrical VHM-II has been constructed from the SMC blocks of the same dimensions as mentioned in the previous chapter for the cylindrical VHM-I. Adjacent phases are shifted by 8mm which is equivalent to  $120^\circ$  electrical and two stator teeth in the same phase are relatively shifted by 2mm from each other. Therefore, the stator length needs to be 2mm higher than the VHM-I, 90mm. The inner and outer diameter of the stator remained the same as for the VHM-I in the previous chapter. The VHM-II has six stator teeth, each having a length of 72mm and an inner arc of  $45^\circ$ . The milling and wire eroding process remain the same as mentioned in the previous chapter. Figure 6.14(a) shows the 90mm machined cylinder block, which is stacked from five SMC blocks. Figure 6.14(b) presents the completed stator structure with the relative shift of stator teeth across the length.

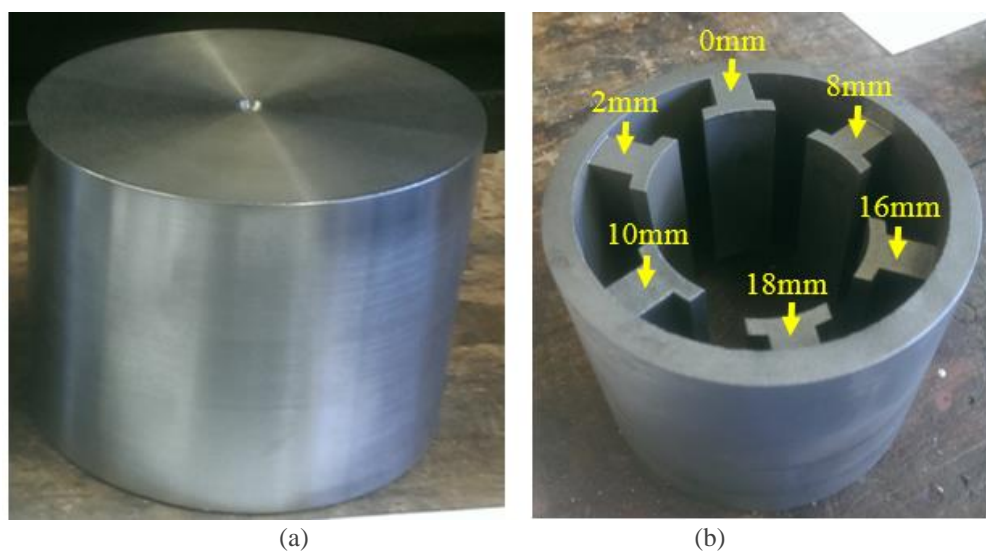


Figure 6. 14: (a) Cylindrical SMC block (b) single piece stator structure

### 6.6.2 Permanent Magnets

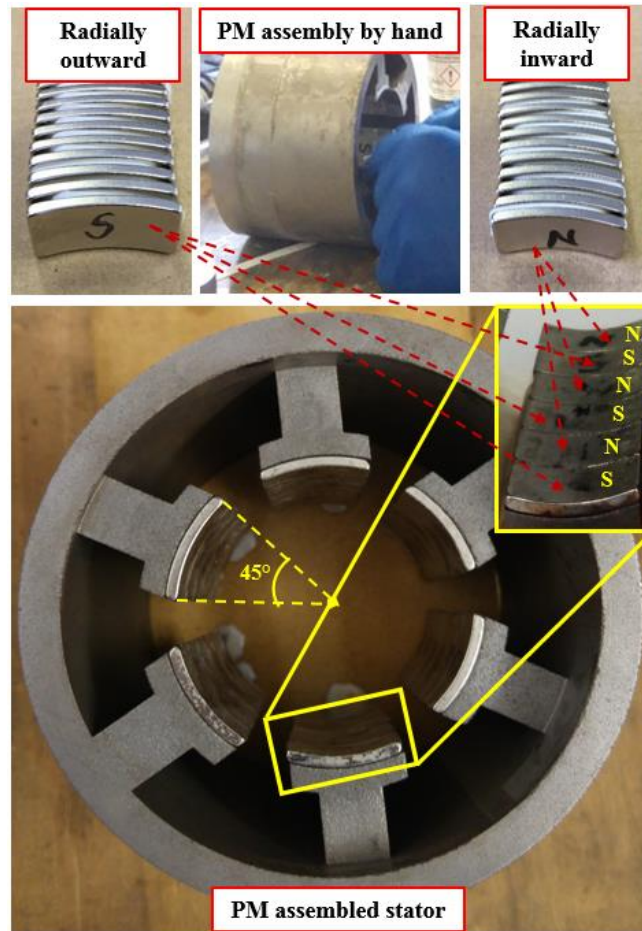


Figure 6.15: PM assembly and the stator.

Neodymium magnets of grade N42H are used, which have the same properties mentioned in the previous chapter. However, Cylindrical VHM-II has double the number of magnets compared to the VHM-I as the number of stator teeth is doubled. It has a smaller magnet arc angle of  $45^\circ$  (half than that of the cylindrical VHM-I) while the PM thickness, width and arc radius remain the same as 2.5mm, 12mm, and 29mm respectively, as mentioned for the cylindrical VHM-I. The number and orientation of the magnets in each stator tooth are also the same as alternating adjacent polarities. All the magnets are glued using the same PERMABOND® ES562 single-part, heat-cure Epoxy. The PM assembled stator is shown in Figure 6.15.

### 6.6.3 Coils

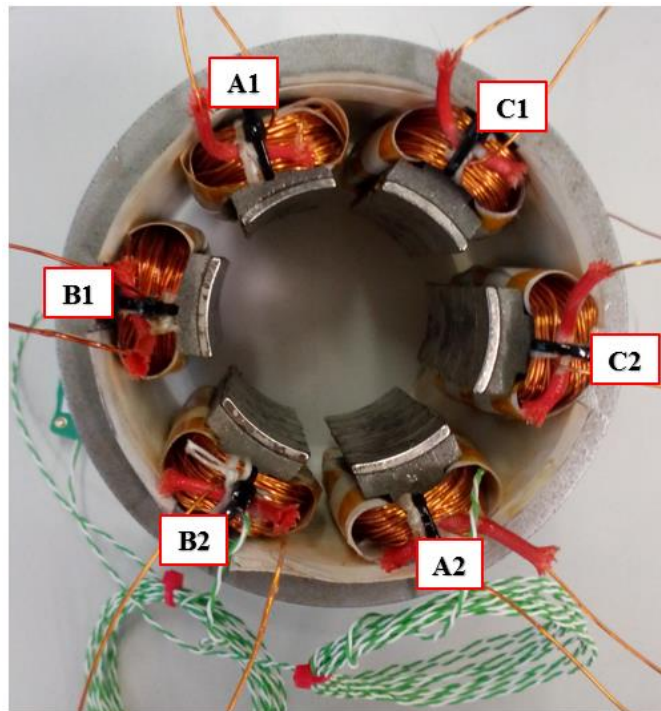


Figure 6. 16: coils assembled stator

The construction of the coils is identical to the VHM-I explained in the previous chapter. An aluminum bobbin jig was built to match the geometry of the stator tooth structure. Each coil consisted of 65 turns to match the coils from the VHM-I. Again, each stator tooth was insulated by Nomax slot liners prior to putting on the pre-constructed bobbin coils onto the stator teeth. Two thermocouples were placed- one inside a coil layer and the other one on the surface of one of the coils. Twelve heat shrink tubes- 4 for each phase were used to mark three phases with three different colors. Figure 6.16 shows the stator with six identical coils assembled for three phases.

### 6.6.4 Stator Housing and Final Machine Assembly

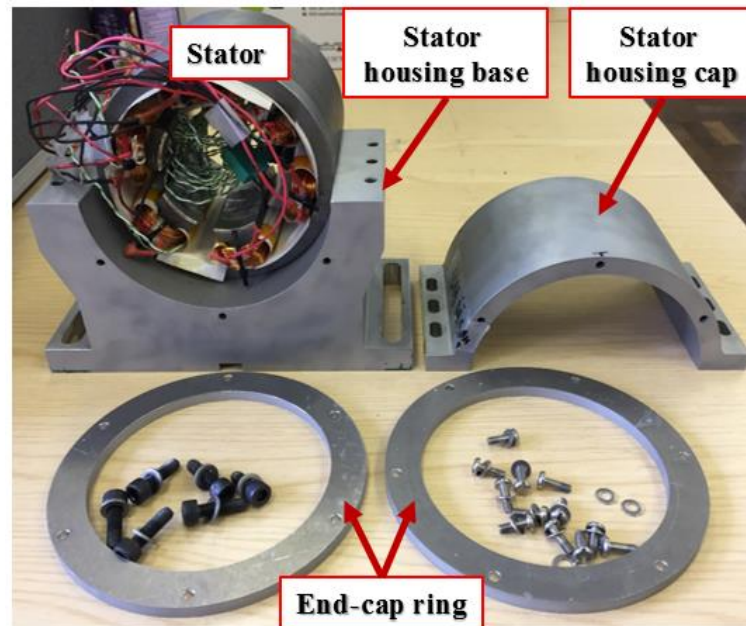


Figure 6.17: components of the stator housing.

The same stator housing components were used for the cylindrical VHM-II, which were described in the previous chapter. As the outer diameter was the same for both the cylindrical machines, the same housing base, and the caps were reused. Figure 6.17 shows the stator sitting on the stator housing base and the other components which were already described in the previous chapter. The left picture of Figure 6.18 shows the stator assembly mounted on the 2m long and 30mm thick bedplate with keying for aligning positions. The same translator, linear ball bushing and support structure mentioned in the previous chapter were used for this cylindrical VHM-II prototype as well. The assembly process was identical to the cylindrical VHM-I mentioned in the previous chapter. A fully assembled cylindrical VHM-II is displayed on the right-hand side of Figure 6.18.

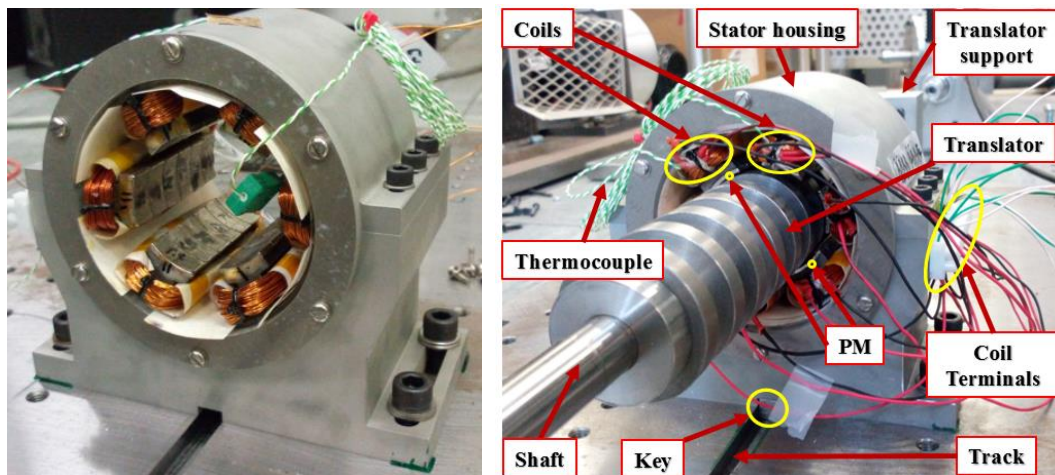


Figure 6.18: Assembled stator on the bed plate and the full machine assembly.

## 6.7 Prototype Testing

Figure 6.19 represents the fully assembled machine connected with a linear ball screw actuator, which provides reciprocating motion and is used to test the prototype machine. The maximum length of each mechanical stroke is 200mm which was restricted by the length of the translator. Similar individual tests were carried out in the same laboratory as mentioned in the previous chapter.

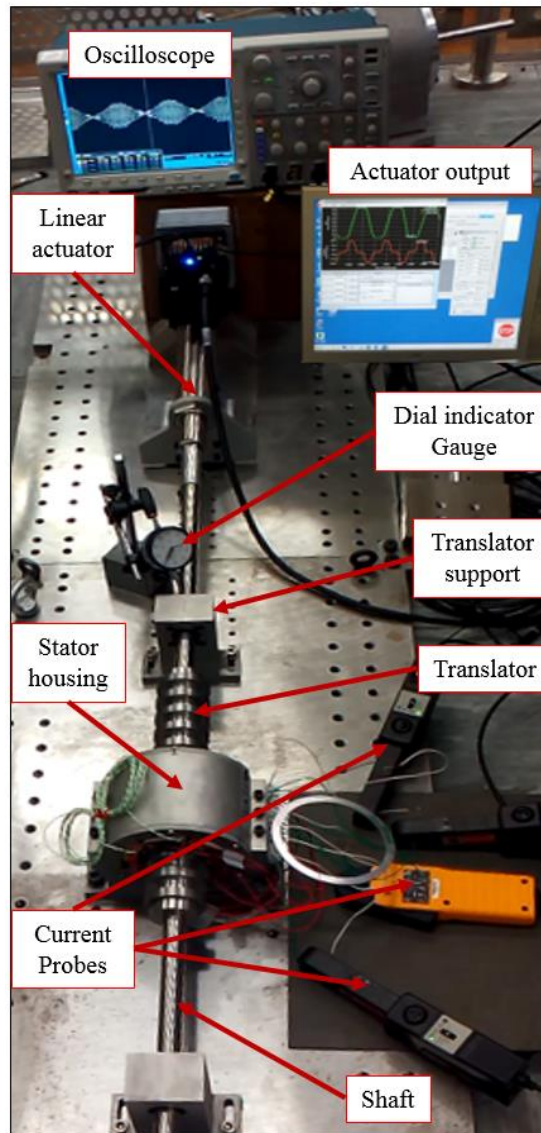


Figure 6. 19: Prototype cylindrical VHM-II is driven by a ball screw actuator and being tested.

### 6.7.1 Resistance Measurement

The resistance of all six coils has been measured and phase resistances were calculated by simply adding resistances of two coils under the same phase together. Resistances of phase-A, phase-B and phase-C were found to be  $1.03\Omega$ ,  $1.02\Omega$ , and  $1.03\Omega$  respectively.

### 6.7.2 Inductance Measurement

Using the method presented in chapter 5, a maximum value of inductance was measured to be 6.2mH. Table 6-5 presents the three-phase inductance comparison between simulated and experimental results. There is a maximum of 8% error in the measurement, which shows a good agreement between FEA and experimental results. The most likely reasons behind these differences in measured and simulated results are the non-uniform nature of air-gap due to the bent shaft and hand winding tolerances.

Table 6- 5: comparison between measured and simulated inductances.

Inductance	Measured (peak)	3D FEA predicted (peak)	% error
Phase-A	5.8mH	6.3mH	8%
Phase-B	6.2mH	6.6mH	6%
Phase-C	6.1mH	6.6mH	7.5

### 6.7.3 No Load Test

#### 6.7.3.1 Open circuit test – per coil

Figure 6.20, Figure 6.21 and Figure 6.22 represent the no-load back EMF for the set of two coils under phase-A, phase-B, and phase-C respectively. It is important to notice that the back EMF for two coils in each phase is shifted by 30° electrical, which is equivalent to 2mm linear displacement. This displacement is caused by the shift between two stator teeth under the same phases as mentioned in the construction part. Again, a big variation of peak EMF between two coils under the same phases was also noticeable. This variation is most likely to be caused by the non-uniform air-gap under each stator teeth. It will be explained later clearly in this chapter.

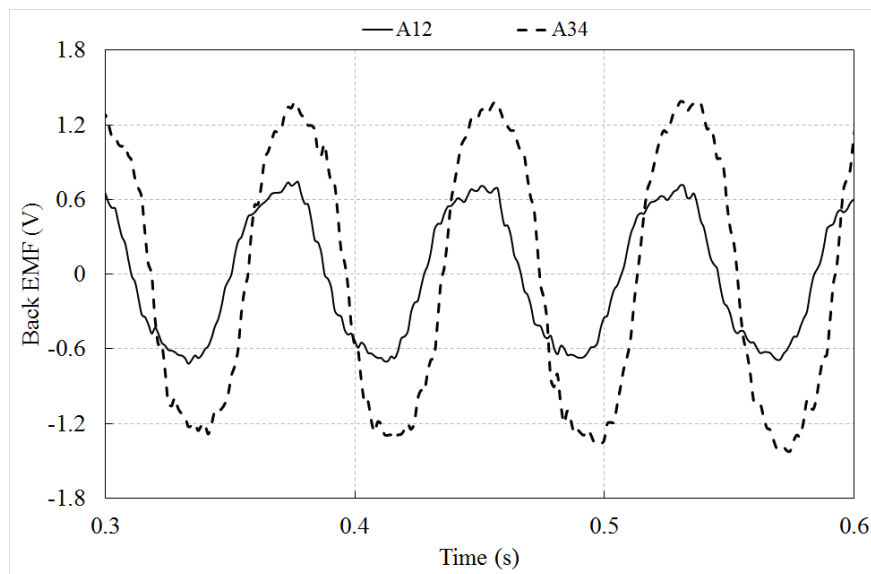


Figure 6. 20: No-load EMF for coil A12 and A34 under phase-A

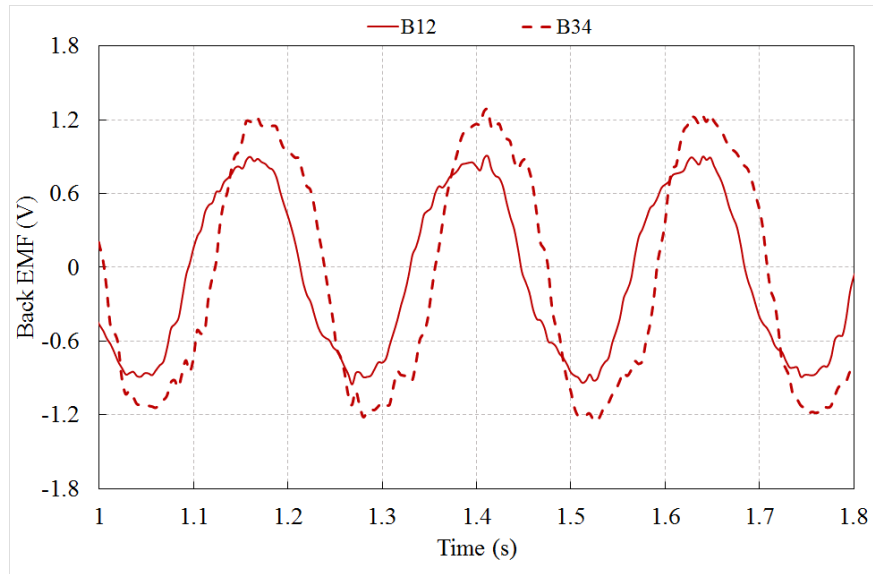


Figure 6. 21: No-load EMF for coil B12 and B34 under phase-B

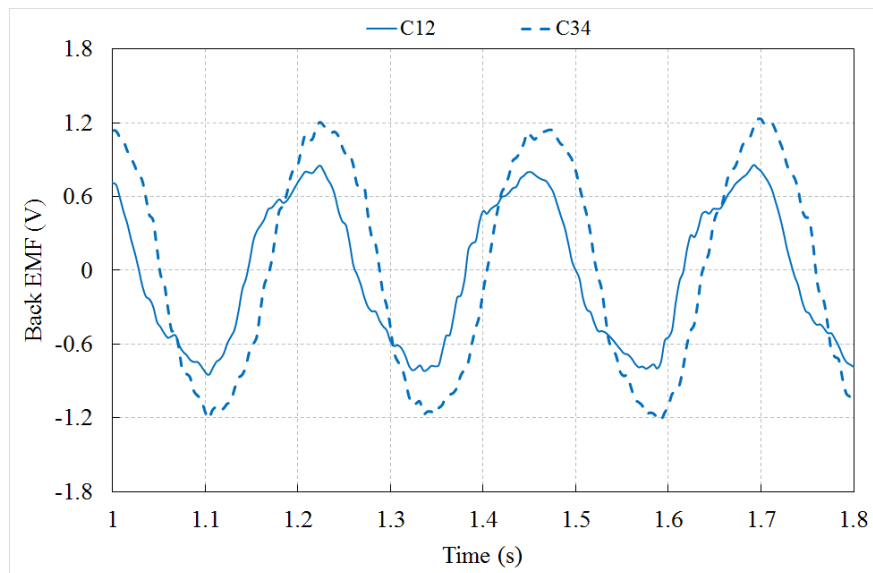


Figure 6. 22: No-load EMF for coil C12 and C34 under phase-C

### 6.7.3.2 Open circuit test – per phase

Figure 6.23 presents the comparison between the simulation and measured results of the no-load back EMF over an electrical cycle at a constant velocity of 0.3m/s. For the measured EMF values, there is a maximum variation of 11% between phases. The RMS values of phase-A, phase-B and phase-C are measured to be 1.49V, 1.55V, and 1.38V respectively. The unequal EMF distribution in the experimental result was due to the translator not being exactly concentric in the middle of the stator, resulting in each phase of the prototype having a different mechanical air-gap. It is clearly visible in Figure 6.24. Nevertheless, there was a maximum of 12% variation between the simulation and the experimental result in phase C. The simulated results give a balanced three-phase back EMF.

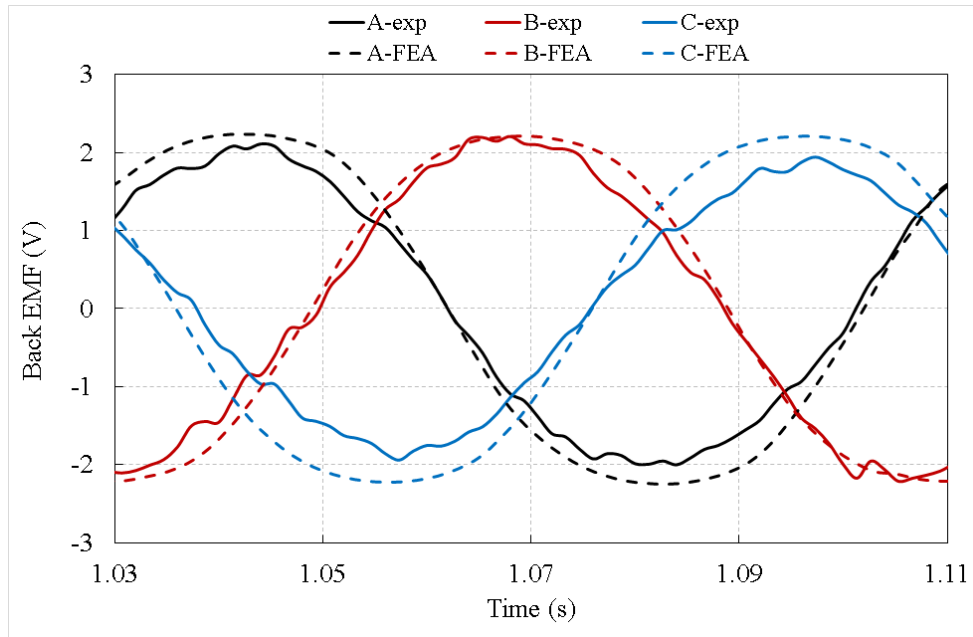


Figure 6. 23: Three-phase EMF comparison between measured and predicted results

### 6.7.3.3 Non-uniform air-gap distribution

Initially, the approximate air-gap under each stator tooth was measured by brass feeler gauges. As the structure is cylindrical, accurate measurement of the air-gap was not possible by using the available rectangular feeler gauge. To validate the prototype, an FEA model with approximate air-gaps was adapted to allow for a non-concentric stator. It was offset with respect to Y-axis (the centre line of phase-A) by  $-0.4\text{mm}$  and  $-1\text{mm}$  with respect to the X-axis (perpendicular to the centre line of phase-A), giving a variation in the average air-gap across the three phases (A, B, C) of  $1\text{mm}$ ,  $0.95\text{mm}$ , and  $1.1\text{mm}$  respectively.

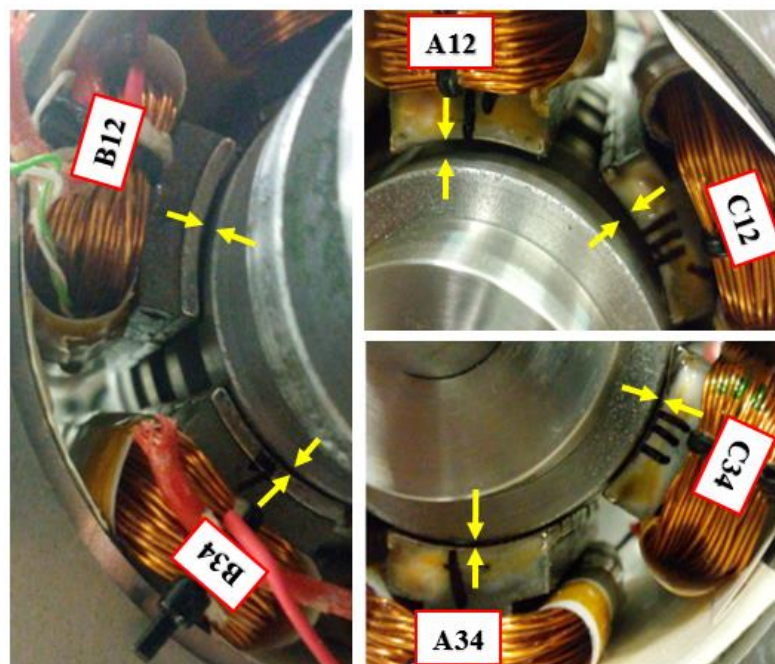


Figure 6. 24: Uneven mechanical air-gap regions of the prototype.

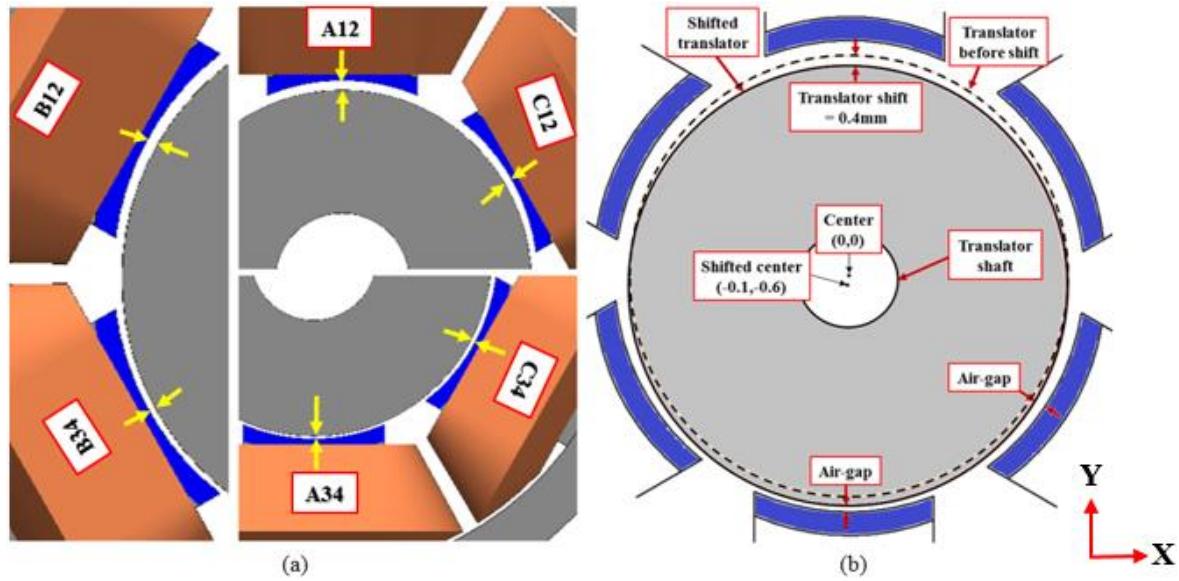


Figure 6. 25: Uneven mechanical air-gap regions (a) simulation (b) geometry.

The offset in the air-gap of the FEA model is clearly demonstrated in Figure 6.25. Direct comparison and summary of the offset simulations and the experimental results are presented in Table 6-6. The offset is likely not to be along the centre line of the translator teeth, and the simulation results in Table 6-6 are therefore not fully representative of the real prototype testing situation. However, the offset simulation results give a close match to the measured EMF value (maximum of 7.4% error) and also represents the fairly close approximation to the measured air-gap.

Table 6- 6: Simulated and measured no-load performance at 0.3m/s velocity

Stator tooth	FEA		Approximate Air-gap (mm)	FEA back EMF (V)	Exp. back EMF (V)	% Error in back EMF
	Air-gap (mm)	Back EMF (V)				
Coil-A12	1	1.2	1.6	0.8	0.75	6.3
Coil-A34	1	1.17	0.4	1.55	1.46	5.8
Phase-A	1	2.2	2	2.2	2.1	4.5
Coil-B12	1	1.17	1.2	1.07	1	6.3
Coil-B34	1	1.2	0.7	1.38	1.29	6.5
Phase-B	1	2.2	1.9	2.3	2.19	4.8
Coil-C12	1	1.17	1.4	0.96	0.89	7.4
Coil-C34	1	1.2	0.8	1.28	1.2	6.3
Phase-C	1	2.2	2.2	2.05	1.94	5.3

### 6.7.3.4 Open Circuit Test at varying speed

The machine has been tested by being driven open circuit over a 200mm displacement, with a peak speed of 1.4 m/s. Figure 6.26 shows the no-load EMF results of two mechanical strokes under variable speed operation. The translator was reciprocating with an approximate sinusoidal displacement profile. It can be seen that the peak back EMF of all three phases are around 10V, which is considered fair in comparison with the simulation.

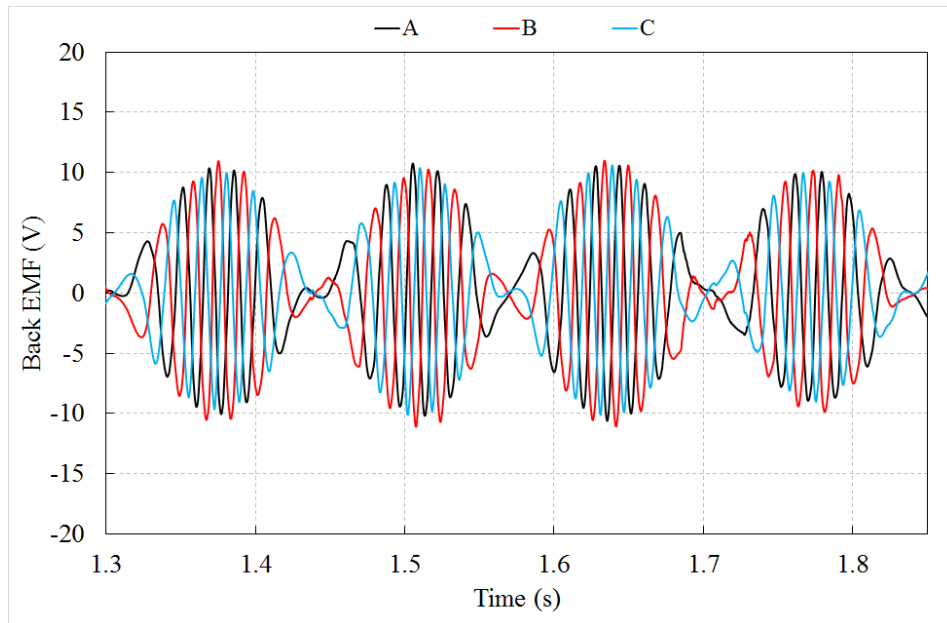


Figure 6. 26: Measured three phase no load back EMF for three mechanical strokes for linear reciprocating motion, peak linear speed of 1.4m/s.

## 6.7.4 Static Tests

### 6.7.4.1 Cogging force

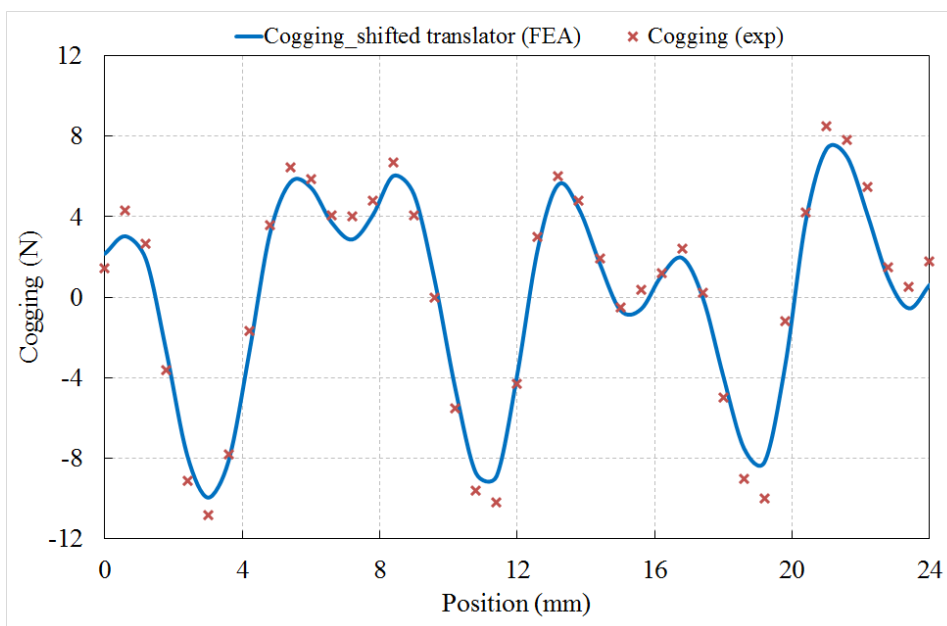


Figure 6. 27: Cogging comparison between experimental and predicted results.

The open circuit static test was performed to measure the cogging force in the prototype machine. The translator was moved by one electrical cycle (24mm) in steps of 1mm. The nature of a non-repeating pattern can be explained by the non-uniform air-gaps, which is described in the previous subsection. Although the simulation was performed under the close approximation of the measured non-uniform air-gaps, the experimental result of the cogging force shows good agreement between the predicted and measured results with a maximum cogging variation of around 5%. The likely reasons behind these deviations are the same as mentioned in the previous chapter namely, tolerance of linear actuator, the accuracy of the load cell (force transducer), and an imbalance in mechanical air-gap, etc.

#### 6.7.4.2 Thrust force

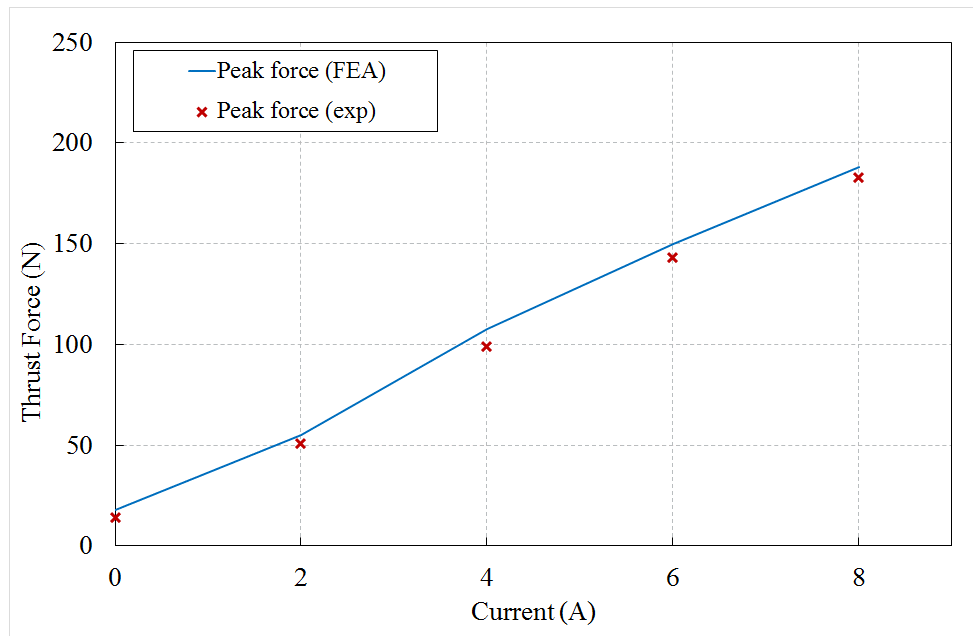


Figure 6. 28: Peak force comparison between simulation and experimental results for varying current.

Static force measurement was performed for four different DC current level. The steps and the electrical circuit connection were mentioned in the previous chapter. The maximum level of DC current applied was 8A and the peak force achieved was around 170N. Figure 6.28 shows the peak force comparison between FEA and experimental result represents a reasonable match with a maximum deviation of around 8%.

## 6.8 Conclusion

A cylindrical version of the linear VHM-II with a 3D flux path has been developed from the improved double-sided E-core flat topology. Basic mechanical design development and FEA have been performed to show that the cylindrical machine can offer better performance including 10% higher force compared to the double-sided flat topology with the same magnet

mass and current density. Pole shifting method was also utilised to reduce the cogging and the force ripple of the machine down to 6% of the rated force.

The cylindrical machine has been made from identical SMC blocks. The stator and the translator come out to be a single piece component, which reduces the overall number of components of the machine. The result is a topology that is easy to assemble because of the low number of mechanical components and very simple mechanical structure. Prototype build, assembly and generation of experimental results of the cylindrical VHM-II have been performed to validate the concept of the cylindrical topology in the laboratory. It can be concluded that all the simulations and experiments were successfully matched, although the physical imbalance of the active air-gap in the prototype construction and assembly resulted in a maximum of 18 % imbalance between phase voltages.

As mentioned in chapter 3, the cylindrical topology could be made out of the segmented translator to improve its performance and translator mass. However, due to the limitation of time and resources, the same translator with core back was used to validate both the cylindrical prototypes presented in chapter 5 and chapter 6.

## Chapter 7: Generalised Linear Machine and Comparison

### 7.1 Introduction

In this chapter, the electromagnetic performance of a cylindrical version of the Halbach Consequent Pole Vernier Hybrid Machine (HCVHM) is analysed and compared with a scaled down version of the flat topology presented in chapter 4. The important dimensions like the air-gap radius, stator outer diameter and stator tooth shape of the cylindrical model are identical to the cylindrical VHM-II presented in chapter 6. As this is a simulation study, the cylindrical version of the HCVHM has not been physically built in the laboratory. Furthermore, a detailed comparative study between all six topologies presented in the last four chapters including three flat topologies and three cylindrical versions of those flat VHMs has been made in terms of the electromagnetic performance and machine volume, for a fixed air-gap radius, PM mass, and an equivalent axial length.

### 7.2 Cylindrical Halbach Consequent Pole Vernier Hybrid Machine

Similar to cylindrical VHM-I and cylindrical VHM-II, the flat HCVHM presented in chapter 4 can also be converted into a cylindrical model with a segmented translator structure, which can provide better performance compared to the equivalent flat version. For a fair comparison, the flat version presented in chapter 4 is scaled down to match the magnet mass and the current density of the cylindrical topology. The outer stator diameter of the cylindrical machine is limited to 120mm as per the manufactured SMC block dimension. Figure 7.1 shows the detail design, magnet orientation and other parameters of the cylindrical Halbach Consequent Pole machine (HCVHM). This cylindrical model also consists of the same stator and translator outer diameter, six identical stator tooth concentrated windings and six teeth stator structure, as the VHM-II presented in chapter 6. However, the most noticeable feature is the segmented cylindrical translator teeth sandwiched between light non-magnetic blocks, as derived in chapter 4 for the flat version. Therefore, translator mass is reduced to a great extent compared to the cored translator used in chapter 5 and chapter 6. The operation principle of the machine is the same as the flat version explained in chapter 4.

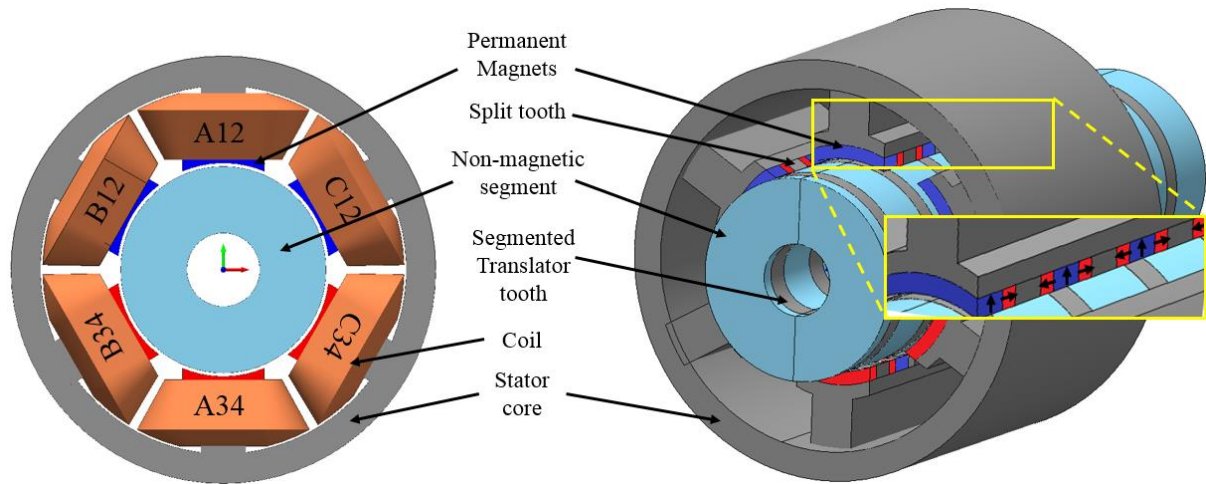


Figure 7. 1: Cylindrical Halbach Consequent Pole VHM

### 7.2.1 Flux Linkage

It is verified in chapter 4 that the novel Halbach Consequent Pole magnet orientation improves the machine performance by reducing the leakage flux and increasing the active flux yield that links the phase windings. Figure 7.2 represents a 3D flux contour plot for the cylindrical HCVHM. It is also discussed that the converted cylindrical topology offers higher flux linkage and thus flux density compared to the flat topology, due to the flux concentration effect of the arc magnets [82]. A comparison between the three-phase no load flux linkage of the flat HCVHM and the cylindrical HCVHM is plotted in Figure 7.3. The cylindrical machine provides a peak flux linkage of 36mWb-turns compared to 32mWb-turns for the flat topology, meaning that a 12.5% higher flux linkage can be achieved by the cylindrical HCVHM. Furthermore, all three phase flux linkage is very much symmetrical and shifted by  $120^\circ$ .

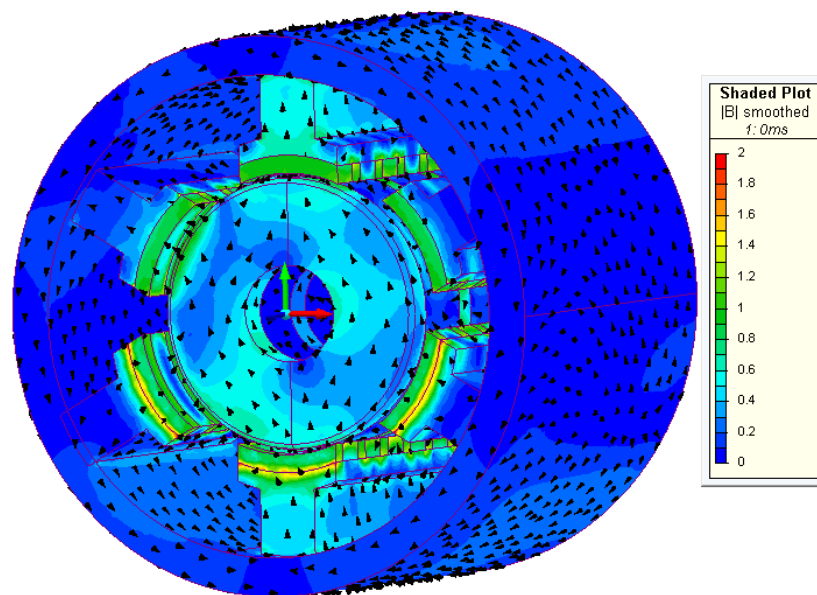


Figure 7. 2: No load magnetic flux distribution plot of the cylindrical HCVHM

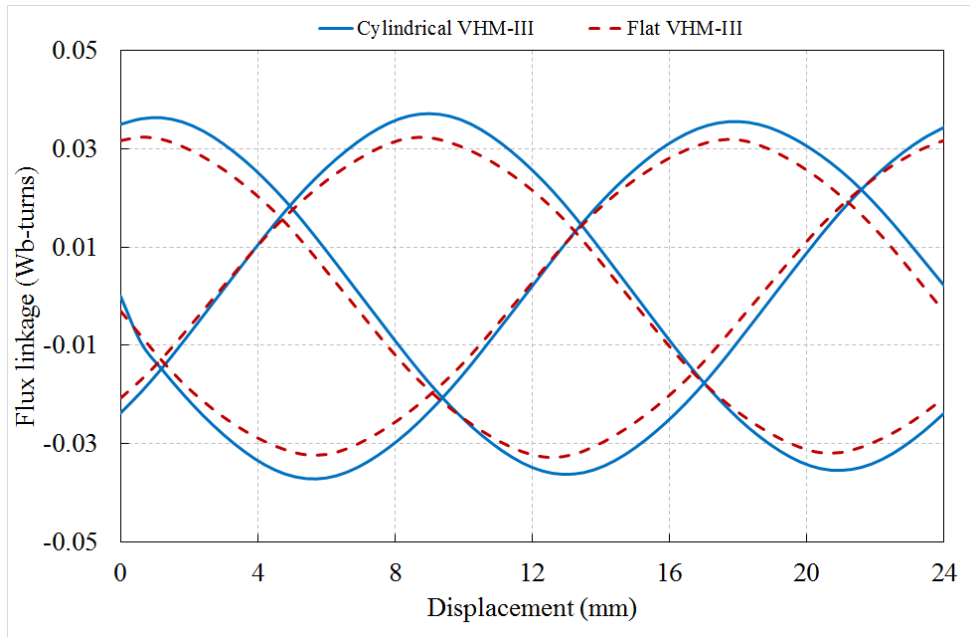


Figure 7. 3: No load magnetic flux linkage comparison between flat and cylindrical model

### 7.2.2 Back EMF

Figure 7.4 shows the induced open-circuit back EMF comparison between the flat HCVHM and the cylindrical HCVHM. As shown in chapter 4, the back EMF waveform is slightly distorted due to some higher order harmonic contents, while all the three phases are symmetrical and shifted by one-third of the translator pitch. It can also be noticed that the cylindrical HCVHM contributes to almost 11.5% higher back EMF compared to the flat version due to the flux concentration by the arc-shaped magnets which are described for the other cylindrical models as well.

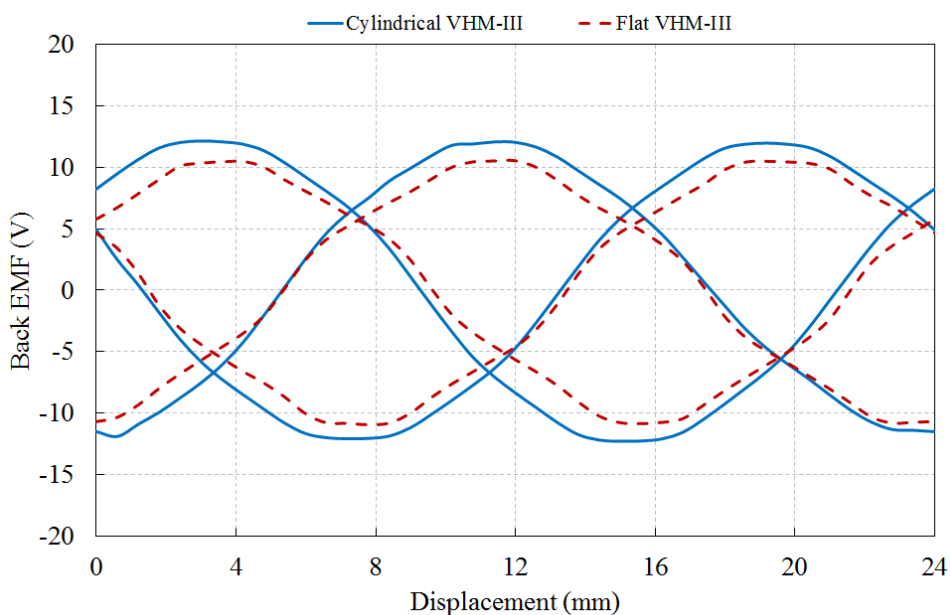


Figure 7. 4: No load three phase back EMF comparison between flat and cylindrical model

### 7.2.3 Thrust Force

Figure 7.5 presents a comparison of thrust force for the two machines for a constant current density of  $3.5\text{A/mm}^2$ . As expected, the Cylindrical HCVHM produces 11.3% higher force compared to the flat HCVHM owing mainly to the improvement in the active flux linkage and back EMF. It also produces lower force ripple. Hence, the cylindrical HCVHM has also the highest thrust force compared to all the six small scaled machines, which is presented in Table 7-1.

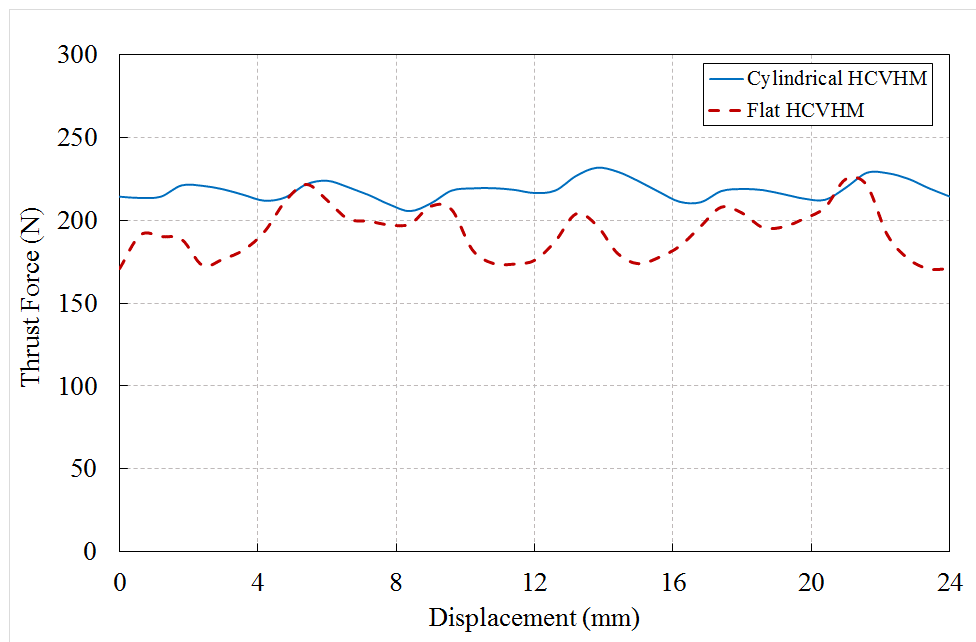


Figure 7. 5: Electromagnetic thrust force comparison between flat and cylindrical model

### 7.3 Machine Performance Comparison

This section discusses the performance comparison between all six VHM models presented in this thesis with a conventional linear PM machine (Figure 7. 6) with the similar overall dimensions and current density. The comparison is carried out based on the FEA performed for a fixed axial length, air-gap radius, PM pole pair pitch, stator outer diameter, current density, copper mass, and magnet mass. The comparison focuses on the following:

1. Back EMF
2. Thrust force
3. Cogging force
4. Active machine volume
5. Translator mass
6. Force density
7. Force per magnet mass

Table 7- 1: Machines' performance and parameters comparison

Parameter	Conventional PM Machine	VHM-I		VHM-II		HCVHM	
		Flat	Cylindrical	Flat	Cylindrical	Flat	Cylindrical
Thrust force (N)	140	162	180	170	190	195	217
% Thrust ripple	5	16	7	11	3	18	10
Cogging (N)	8	20	12	20	6.5	32	23
Back EMF (V)	6	7.6	8.4	8.1	9	10.5	12
Machine volume ( $\times 10^{-3} \text{ m}^3$ )	0.56	1.0	0.56	0.8	0.57	0.80	0.58
Axial length / air-gap radius (mm)	29	45	29	22.5	29	22.5	29
Active length (mm)	88	280	88	282	90	284	92
Machine mass (kg)	5.5	6.92	5.2	5.37	4.45	5.43	4.57
Magnet mass (kg)	0.18	0.18	0.18	0.18	0.18	0.18	0.18
Translator mass (kg)	1	2.9	1.12	1.3	1.12	1.3	0.94
Stator mass (kg)	2.3	2.84	3	2.84	2.7	2.9	2.7
Coil mass (kg)	1.5	1	0.9	1.05	1.57	1.05	1.57
Power density ( $\text{kW/m}^3$ )	300	194	386	255	400	293	449
Force density ( $\text{kN/m}^3$ )	250	162	321	213	333	244	374
Force/magnet mass ( $\text{kN/kg}$ )	0.78	0.90	1.00	0.94	1.06	1.08	1.20
Power Factor	0.55	0.39	0.44	0.42	0.48	0.65	0.73

Table 7-1 shows a direct comparison between a conventional tubular linear PM machine and the presented flat and cylindrical topologies of fixed axial length and equivalent diameter. Figure 7. 6 shows the cross-section of the conventional three phase linear tubular PM machine with similar dimensions and the same pole pair pitch as the VHMs. It consists of six stator teeth, six coils, and the same PM mass as the other VHMs. The cylindrical VHM-I provides more than 20% higher force than the conventional linear tubular PM machine for the same active machine volume and current density. For both flat and cylindrical versions, the VHM-II provides 5% higher force than the VHM-I due to the higher magnet utilisation. The VHM-I has longer magnet poles, which lead to higher leakage flux. As the VHM-II topologies have double the number of magnet poles compared to the VHM-I the same translator reacts with higher number of smaller magnet poles surrounding the translator teeth for VHM-II and the reaction

force between them are more stable due to the flux spreading evenly through the pole piece giving a better distribution of magnet pole flux in the air-gap. Furthermore, pole shifting also allows the cylindrical VHM-II to achieve around 50% less cogging and force ripple compared to the cylindrical VHM-I. Again, it is also possible to reduce the mass of the translator further by employing the segmented translator.

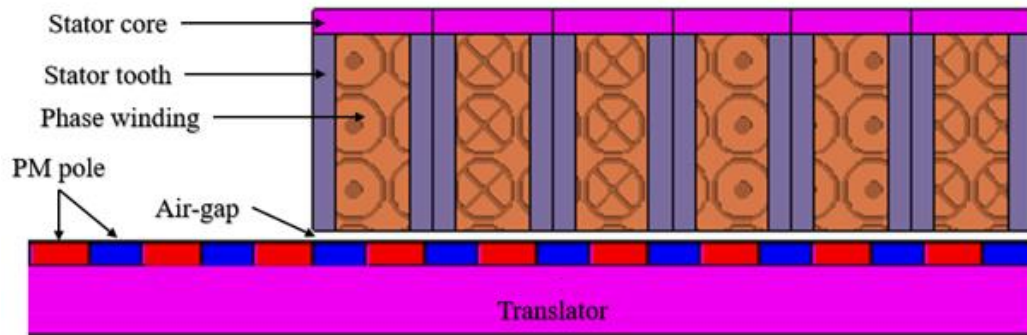


Figure 7. 6: Cross-section of a conventional linear tubular PM machine

The cylindrical HCVHM provides the maximum force per magnet mass and power density of  $449\text{kW/m}^3$  for a similar number of magnets and current density compared to the other topologies. It is also noticeable that all the cylindrical topologies provide almost 50% higher force density and higher power factor compared to their flat variant for the presented model dimension. The coil mass of the double-sided cylindrical VHM-II and HCVHM models are higher compared to the other models due to the double the number of end windings. However, their translators can be made out of segmented teeth which can reduce the active translator mass of up to 16%, and for longer stroke applications, it can be saved further to provide a substantial net reduction in the total machine mass. Figure 7.7 shows the comparison of the dimensions of the flat and the cylindrical machine topologies.

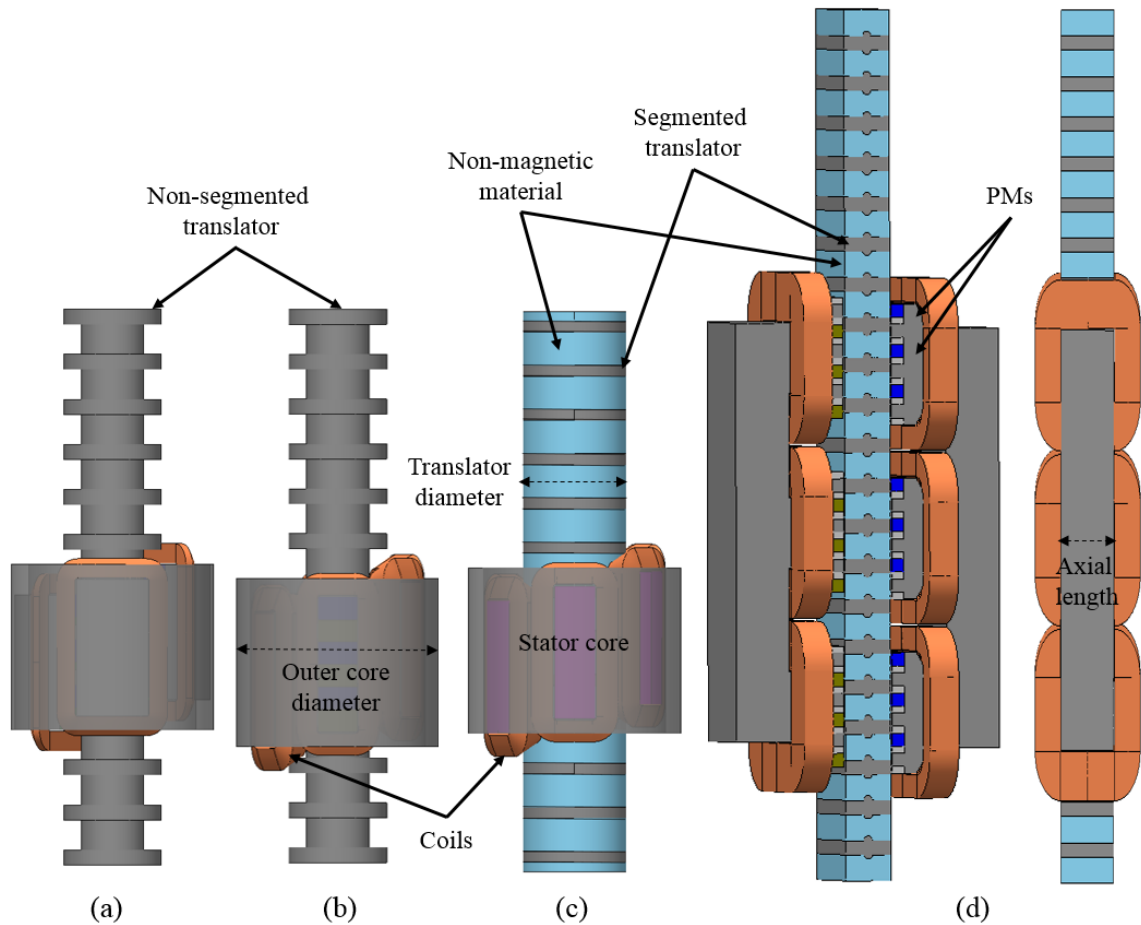


Figure 7. 7: 3D view (a) cylindrical VHM-I with a non-segmented translator (b) Cylindrical VHM-II with a non-segmented translator (c) Cylindrical HCVHM with a segmented translator (d) flat HCVHM

#### 7.4 Generalised Linear Machines

To design a linear machine with a constant active area over a stroke length, the stator or translator must be oversized. Ordinarily, this would be the translator, and in the VHM this is a pure iron teeth structure.

Considering the flat topology, the mass of the translator is a function of the axial length,  $l_a$ , the stator length,  $L$ , and the peak to peak amplitude of oscillation or stroke length,  $x$  – all defined in Figure 7.8.

Equation (7-1) defines the amplitude ratio  $X$  as the ratio of stroke length to the stator length.

$$X = \frac{x}{L} \quad (7-1)$$

For a flat translator, ignoring the slots, the volume is related to its three dimensions by equation (7-2). Similarly, for the stator, it is defined in equation (7-3).

$$v_{translator} = h_t (L + X)l_a \quad (7-2)$$

$$v_{stator} = h_s L l_a \quad (7-3)$$

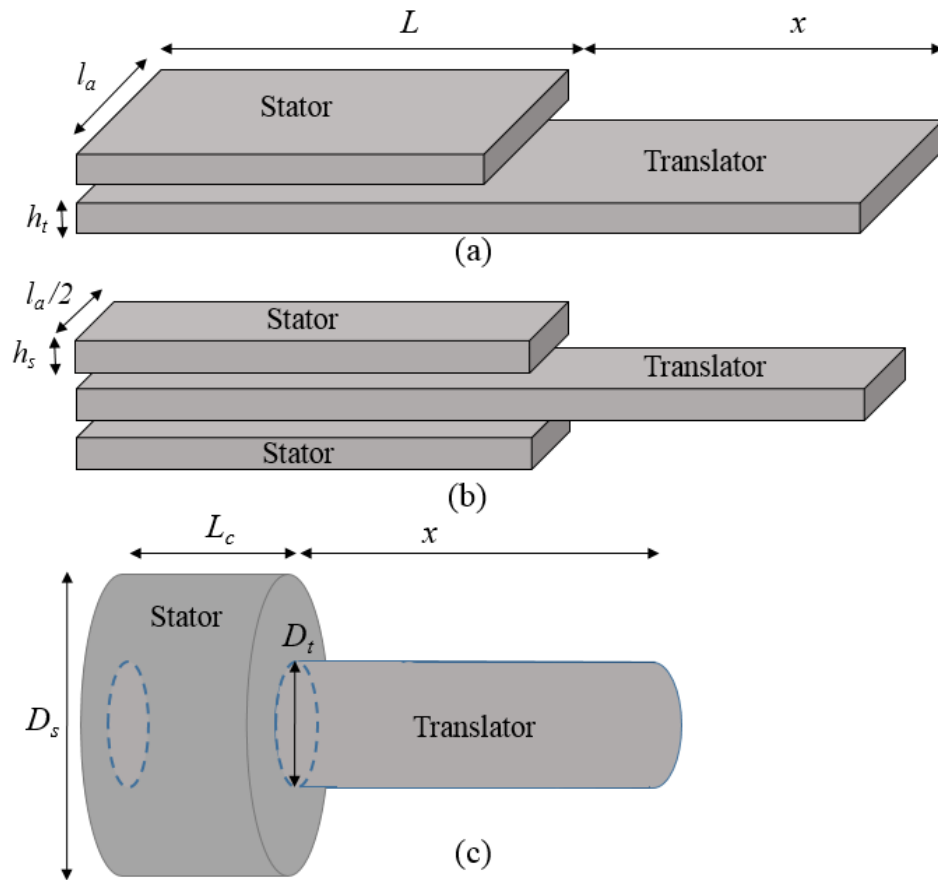


Figure 7. 8: General linear machine dimensions, including stroke length,  $x$  (a) Single sided flat topology (b) double-sided flat topology with a shorter axial length (c) Cylindrical topology.

To react a fixed force in any given topology of the linear electrical machine requires a fixed active area and hence equation (7-4) can be used to relate the active and axial lengths required for a given specification.

$$l_a = \frac{F}{\sigma L} \tag{7-4}$$

Where  $\sigma$  is the shear stress capability and  $F$  is the specified force requirement. The machine volumes may now be given by equation (7-5) and equation (7-6).

$$v_{translator} = \frac{F}{\sigma} h_t \left(1 + \frac{x}{L}\right) \tag{7-5}$$

$$v_{stator} = h_s \frac{F}{\sigma} \tag{7-6}$$

For a specific force requirement, the stator volume is hence independent of the amplitude ratio, whereas the translator volume is not. For a minimum use of active material, equation (7-5) implies  $X$  should be minimised, which for a fixed stroke length means  $L$  should be maximised -

equation (7-1). Therefore from equation (7-4),  $l_a$  should be minimised. In summary, for linear machines delivering a fixed force with a fixed stroke length, machines with a longer active length  $L$  and a shorter axial length  $l_a$  are likely to have a lighter translator.

However, considering only active part of the single-sided and double-sided flat machines, active machine volume can be expressed by the following equations,

$$v_{Single\ sided} = L l_a (h_t + h_s) \quad (7.7)$$

$$v_{double\ sided} = L \left( \frac{l_a}{2} h_t + l_a h_s \right) \quad (7.8)$$

It is clear that the double-sided flat topology doesn't save any stator volume, but does save half of the translator volume, which is the heaviest part, especially for the long stroke application. For example, the translator of Figure 7.7(b) is lighter than that of Figure 7.7(a) even though the active air-gap area and stroke length are the same.

Similarly, from Figure 7.7(c), the active volume of the cylindrical topology can be given by,

$$v_{Cylinder} = \pi \left( \frac{D_s}{2} \right)^2 L_c \quad (7.9)$$

$$v_{cylinder-translation} = \pi \left( \frac{D_t}{2} \right)^2 L_c \quad (7-10)$$

Where  $D_s$  is the outer diameter of the cylindrical stator,  $D_t$  is the translator outer diameter which is a function of the axial length ( $l_a$ ) of the relevant flat topology presented in chapter 5 and  $L_c$  is the active length of the machine.

## 7.5 Comparison of Machine Volume

Figure 7.9 represents a plot of the machine active volume against air-gap area for the flat (single-sided and double-sided) and the cylindrical topologies, derived from the simplified geometry assumptions above. The volume of the copper and magnet in all the topologies are assumed equal for the individual air-gap area.

For the flat machines, mass varies linearly with axial length,  $l_a$  and thus with the active air-gap area. For the cylindrical machine, where the air-gap radius is a function of  $l_a$ , the mass varies with  $l_a^2$  and thus with the square of the active air-gap area. Hence, Figure 7.8 shows that for the machines with a low active air-gap area, the equivalent cylindrical machine can offer a lower mass than the flat version, whereas, for 0.02m<sup>2</sup> active air-gap area (60mm or larger axial lengths), the cylindrical machine volume becomes comparatively large. It can be clearly seen that the double-sided flat machine also provides higher mass savings as the axial length and

thus the active air-gap area increases, which are discussed in the previous section. The plot also shows a very little difference in active machine volume between cylindrical VHM-I, VHM-II, and HCVHM, as VHM-II and HCVHM have 2mm and 4mm longer machine length than the VHM-I respectively.

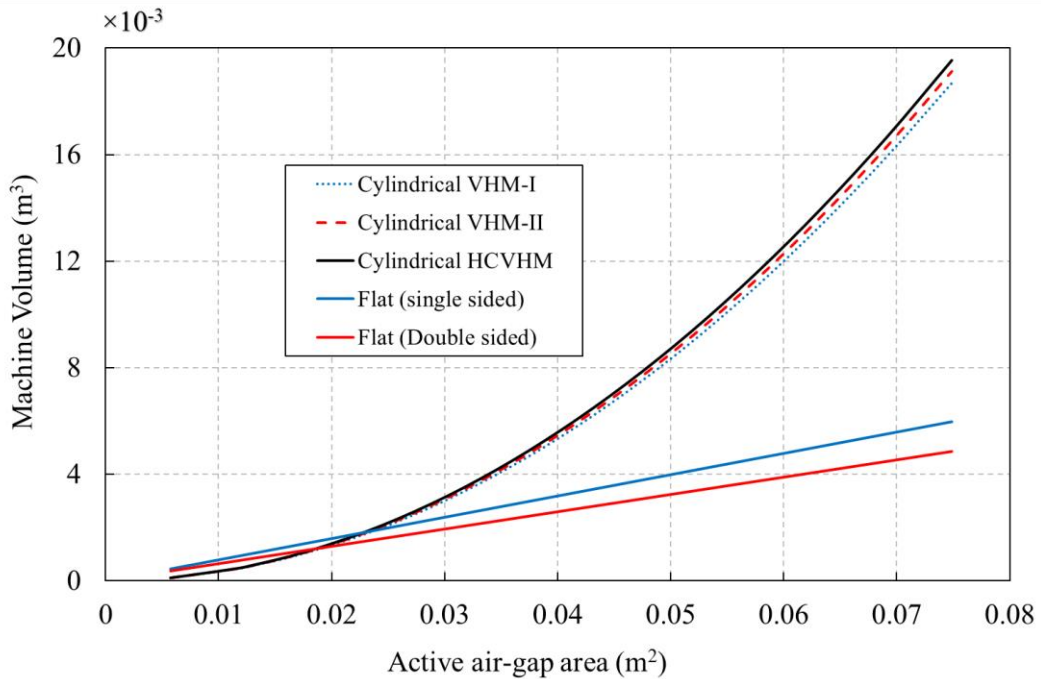


Figure 7. 9: Comparison of active machine volume with different topologies of cylindrical and flat machines for fixed axial length, copper mass, and magnet mass

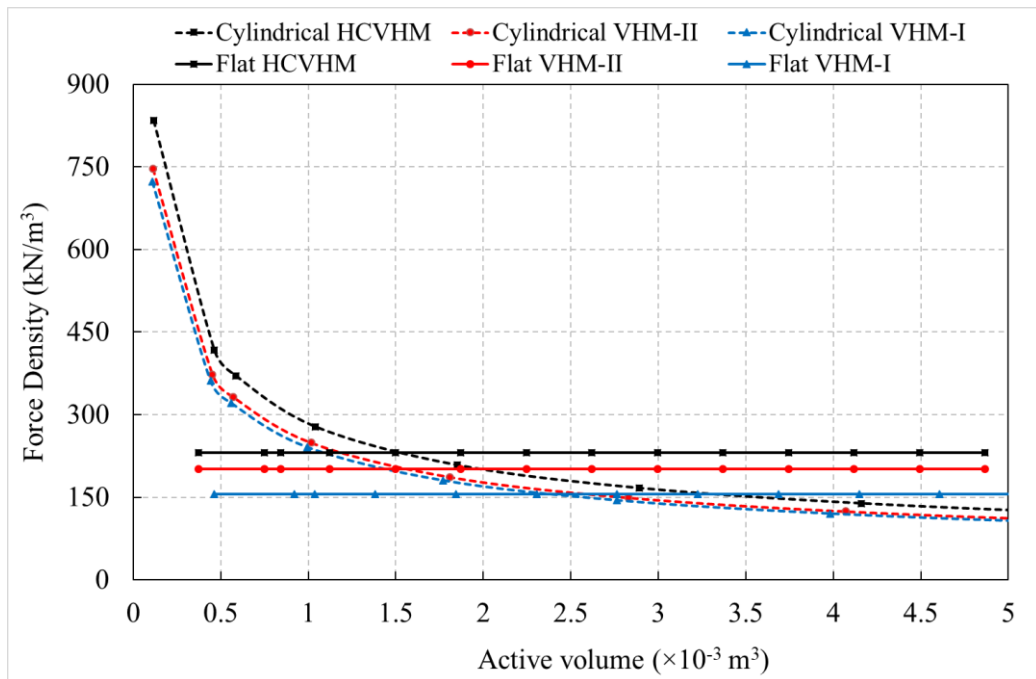


Figure 7. 10: Force density against equivalent axial length plot for all six machine topologies.

Figure 7.10 presents a comparison of force density against equivalent active machine volume for all six machines. Individual axial length defines a fixed magnet mass for all six machine topologies and a specific air-gap diameter, which can be calculated from equation (5-2). It shows that as the equivalent axial length and thus the active volume of the machines is further increased from  $1.5 \times 10^{-3} \text{ m}^3$ , the force density of the cylindrical machines becomes lower compared to the constant force densities of the flat topologies. As the volume and the rated thrust force both are linearly proportional to the axial length, all flat machines provide constant force density across the range of various axial lengths. The volume of the cylindrical machines varies with the square of the equivalent air-gap radius, while the force varies linearly. This is the reason that the cylindrical models show a very high force density for lower axial length and then exponentially reduces with the axial length.

Furthermore, considering the stroke length, lower values of  $X$  and axial length give a lower translator volume, thus lower mass for the double-sided topologies.

To summarise, all the flat versions are superior to their cylindrical counterparts at higher axial length over 80mm, a smaller number of active components are required for manufacturing the cylindrical ones. Furthermore, the cylindrical topologies are easy to assemble because of a low number of mechanical components and a very simple mechanical structure. Again, the cylindrical cross-section is also believed to have the potential to be more suitable for integration into wave energy converters as there is no requirement for the translator to resist torsional forces. Dynamic sealing is also likely to be less challenging. It can be concluded from the study and discussion that there is clearly some merit in pursuing a cylindrical VHM in terms of volume and mass saving and higher force density compared to the flat design at lower axial lengths.

## 7.6 Conclusion

This chapter shows convincing remark that any flat topology of VHM can be transformed into cylindrical topology with better performance, but only up to a small range  $\sim 0.1\text{m}$  of axial length. The key criteria of the selection of an electrical machine for the WEC applications are the performance per  $\text{kg} / \text{m}^3$ . Although the cylindrical versions of the flat VHMs provide better electromagnetic performance including high force density of  $373\text{kN}/\text{m}^3$  and power density of  $449\text{kW}/\text{m}^3$ , as they need to scale up against larger axial lengths for higher power rating, the manufacturing and assembly of the arc magnet material being used are likely to become an issue. Furthermore, manufacturing SMC bocks with a larger diameter will be very complicated as the diameter increases with a square of the active power. To reduce the total requirement of the material, the central hole needs to be big, which further causes mechanical problems.

Therefore, these discussions can clearly draw a decisive conclusion about selecting a machine topology based on the required power level. The flat versions are more suitable for standalone larger power generators for WEC applications, while the small-scale cylindrical models also show useful promises for multiple lower power devices working together for the bulk of energy generation.

## Chapter 8: Conclusion and Future Work

### 8.1 Introduction

The key technical achievements are summarised and further research to complete the work presented in the thesis is suggested in this chapter. The main purpose of this thesis was to inspect and analyse different permanent magnet linear electrical machine topologies for improved performance in Direct Drive Wave Energy Converters (DD-WECs). There have been specific efforts on the improvement of force and power density with better PM utilisation, and reduction of the translator mass. Improving the machine power factor was also an important matter of concern. One full-scale flat machine and two small-scale cylindrical machines were designed, analysed, built and validated by experimental tests in the University laboratory. The main objectives including high force density, reduction in machine mass and improvement of power factor were achieved for all the developed designs.

### 8.2 Contribution to Knowledge & Technical Achievements

The principal contribution of this research is the development of three high force dense linear VHMs for the Direct Drive Power Take-Off system. It includes development, modeling, optimisation, building, and testing of the machines for high thrust force and power at reduced magnet and translator mass.

The contributions of the author's Ph.D. have been discussed in detail in the previous chapters and can be summarised as follow:

- Optimisation of the existing C-core VHM-II [7] into E-core VHM-II to reduce Permanent Magnet (PM) material usage and improve mechanical structure. As a result, the new topology provides a rigid structure and is able to produce a higher force density with a 37% PM mass reduction and a further reduction in active component parts compared to the existing baseline design.
- The development of a new segmented translator along with an integrated assembly structure eliminates the thick and heavy translator core back — offering a significant reduction in the material usage and translator mass.
- Implementation of pole shifting methods in the E-core VHM-II design to reduce the force ripple up to 82%, while managing to produce 14% higher rated force.
- A novel Halbach Consequent Pole PM array has been developed, built and experimentally validated in the University laboratory. It utilises the same E-core stator and segmented translator structure while providing higher PF, almost 40% improvement in power density,

67% higher shear stress, and increased force per magnet mass at the same rated current density compared to the developed flat E-core VHM-II mentioned earlier. There is also a significant reduction of 72% in the active translator mass compared to the existing topology.

- Two Novel cylindrical variants of the flat VHMs have also been designed and developed to offer around 12% increase in the average force and significant improvement in the machine power density all with a lower cogging force compared to the flat versions.
- After design analysis, small scale 220W cylindrical VHM-I and VHM-II prototypes have been built in the laboratory, where both stators and the common translator were constructed from the prototyping Soft Magnetic Composite (SMC). The prototypes have been successfully tested and demonstrated that there was an imbalance in the mechanical air-gap due to the offset translator caused by the non-linear shaft. It caused a maximum of 26% and 18% imbalance in the three-phase back EMF for the cylindrical VHM-I and VHM-II respectively. Eccentric translator models have been successfully simulated to mimic this practical imbalance in the mechanical air-gap which could replicate the experimental results to within 8%.
- Three small scale cylindrical versions of the flat VHMs are designed and analysed to compare the improved performance but were limited by the force per active volume at a high rated power compared to the flat topologies.
- Finally, a detailed performance comparison between all the presented linear VHMs and a conventional linear PM machine has been performed for a specific axial length, equivalent air-gap diameter, and constant PM mass.
- The developed cylindrical VHM models proved to provide superior performance compared to their flat variants, while the flat versions, especially double-sided HCVHM topology provides the best force to volume ratio at a higher axial length (larger generators).

### 8.3 Suggestions for Future Work

The research presents different opinions for future works. The following recommendations are:

- Structural analysis of the flat Halbach Consequent Pole Vernier Hybrid Machine (HCVHM) needs to be carried out to have a good prediction of the translator deflection, which may be caused by the magnetic attraction force between stator and translator.
- Research on scaling-up the flat HCVHM to deliver the required power demanded by a real wave energy converter can be considered, in which the overall size and mass of the large-scale machine can be determined.

- Building and testing the cylindrical topology of the Halbach Consequent Pole Vernier Hybrid Machine (HCVHM) with a segmented translator to validate the novel PM array for the cylindrical version. Further work on mass and volume reduction of the presented cylindrical machines for a higher power rating can give the cylindrical topologies strong advantages over the flat counterpart. Integrating the associated drive and power electronic components inside the machine might reduce the overall volume of the system and make the overall system more compact and efficient.
- Implementing some neutrally buoyant non-magnetic material to assemble the segmented translator teeth might improve the mechanical and thus overall system efficiency and smoothen the motion of the translator to react the ocean waves.
- The designed flat HCVHM still has more than 5% force ripple due to the end effect which is a very common phenomenon for linear machines. As low force ripple is required for the Wave Energy Converters, mitigating the end effect by utilising the tapered stator ends might further improve the overall force ripple.
- Further investigation of the PMs may lead to an improvement in the operating power factor.
- Further development and mechanical analysis of the support structures and the linear test rig can be made to evaluate the possible mass saving and testing of the full-scale machine in the real wave condition with associated power electronic drives and controller.

#### **8.4 Conclusion**

The conclusion of this research has been the successful design, development, construction, testing, and validation of multiple linear permanent magnet machines for Direct-Drive Wave Energy Converters (DD-WECs). A flat Halbach Consequent Pole Vernier Hybrid Machine (HCVHM) capable of delivering 1.8kW and two smaller scale cylindrical topologies capable of delivering 220W at 1.2m/s have been built and tested. Despite there were some differences to the expected performance, validation of the design methodology and concept designs have been successfully performed.

## References

- [1] I. López, J. Andreu, S. Ceballos, I. M. de Alegría, and I. Kortabarria, "Review of wave energy technologies and the necessary power-equipment," *Renewable and sustainable energy reviews*, vol. 27, pp. 413-434, 2013.
- [2] J. Falnes, *Ocean waves and oscillating systems: linear interactions including wave-energy extraction*: Cambridge university press, 2002.
- [3] R. Yemm, *Pelamis WEC: Full-scale Joint System Test* vol. 24: DTI, 2003.
- [4] K.-S. Choi, D.-S. Yang, S.-Y. Park, and B.-H. Cho, "Design and performance test of hydraulic PTO for wave energy converter," *International Journal of Precision Engineering and Manufacturing*, vol. 13, pp. 795-801, May 01 2012.
- [5] M. A. Mueller and N. J. Baker, "Modelling the performance of the vernier hybrid machine," *IEE Proceedings-Electric Power Applications*, vol. 150, pp. 647-654, 2003.
- [6] M. A. H. Raihan, N. J. Baker, K. J. Smith, and A. A. Almoraya, "Investigation of a doubly salient Halbach array linear permanent magnet machine for wave energy converters," in *2017 20th International Conference on Electrical Machines and Systems (ICEMS)*, 2017, pp. 1-5.
- [7] N. J. Baker "Linear Generators for Direct Drive marine Renewable Energy Converters" Ph.D. thesis. .
- [8] Capturing the Ocean's Energy, Yale School of Forestry & Environmental Studies. Available online: [https://e360.yale.edu/features/capturing\\_the\\_oceans\\_energy](https://e360.yale.edu/features/capturing_the_oceans_energy). (Accessed on 19 December 2018).
- [9] J. M. Leishman and G. Scobie, *The development of wave power: a techno-economic study*: Economic Assessment Unit, National Engineering Laboratory, Department of Industry, 1978.
- [10] C. Miller, "Wave and tidal energy experiments in san francisco and santa cruz," ed: August, 2004.
- [11] Y. Masuda, "Wave-Activated Generator, Int," in *Colloq Exposition Oceans, France, Bordeaux*, 1971.
- [12] Y. Masuda, "An experience of wave power generator through tests and improvement," in *Hydrodynamics of ocean wave-energy utilization*, ed: Springer, 1986, pp. 445-452.
- [13] Y. Masuda and M. E. McCormick, "Experiences in pneumatic wave energy conversion in Japan," in *Utilization of ocean waves—Wave to energy conversion*, 1986, pp. 1-33.
- [14] A. F. O. Falcão and J. C. C. Henriques, "Oscillating-water-column wave energy converters and air turbines: A review," *Renewable Energy*, vol. 85, pp. 1391-1424, 2016.
- [15] T. Setoguchi and M. Takao, "Current status of self rectifying air turbines for wave energy conversion," *Energy conversion and management*, vol. 47, pp. 2382-2396, 2006.
- [16] The tidal power plant of La Rance, Available online: <https://www.edf.fr/groupe-edf/producteur-industriel/energies-renouvelables/hydraulique/edf-hydraulique-bretagne-normandie/l-usine-maremotrice-de-la-rance/decouvrir-et-comprendre> (Accessed on 20 January 2019).
- [17] F. d. O. Antonio, "Wave energy utilization: A review of the technologies," *Renewable and sustainable energy reviews*, vol. 14, pp. 899-918, 2010.
- [18] Edinburgh Wave Power Group. Available online: <http://www.homepages.ed.ac.uk/v1ewave/>. (Accessed on 20 December 2016)
- [19] The Aguçadoura Wave Farm – The World's First Wave Farm. Available online: <https://www.marineinsight.com/offshore/the-agucadoura-wave-farm-the-worlds-first-wave-farm/> (Accessed on: 12 September 2018).
- [20] Making waves: UK firm harnesses power of the sea ... in Portugal. Available online: <https://www.theguardian.com/technology/2008/sep/25/greentech.alternativeenergy> (Accessed on 26 December 2017).

- [21] Pelamis Wave Power. Available online: <http://www.pelamiswave.com>. (Accessed on 5 December 2016)”
- [22] B. Drew, A. R. Plummer, and M. N. Sahinkaya, "A review of wave energy converter technology," ed: Sage Publications Sage UK: London, England, 2009.
- [23] Coppe UFRJ. Available online: <http://www.coppenario20.coppe.ufrj.br>. (Accessed on 10 October 2015)”
- [24] Department of business, energy and industrial strategy, “UK Energy in Brief 2018”, Available online: [https://assets.publishing.service.gov.uk/government/uploads/system/uploads/attachment\\_data/file/728374/UK\\_Energy\\_in\\_Brief\\_2018.pdf](https://assets.publishing.service.gov.uk/government/uploads/system/uploads/attachment_data/file/728374/UK_Energy_in_Brief_2018.pdf). (Accessed on 5 January 2019)
- [25] H. Polinder, B. C. Mecrow, A. G. Jack, P. G. Dickinson, and M. A. Mueller, "Conventional and TFPM linear generators for direct-drive wave energy conversion," *IEEE Transactions on Energy Conversion*, vol. 20, pp. 260-267, 2005.
- [26] L. Huang, H. Yu, M. Hu, J. Zhao, and Z. Cheng, "A novel flux-switching permanent-magnet linear generator for wave energy extraction application," *IEEE Transactions on Magnetics*, vol. 47, pp. 1034-1037, 2011.
- [27] H. Polinder, M. E. C. Damen, and F. Gardner, "Linear PM generator system for wave energy conversion in the AWS," *IEEE transactions on energy conversion*, vol. 19, pp. 583-589, 2004.
- [28] Ocean News, “Cornwall Attracts New Wave of Investment”, 9 November 2016. Available online: <https://www.oceannews.com/news/energy/cornwall-attracts-new-wave-of-investment>. (Accessed on 2 July 2014)
- [29] Joseph, D.M., 2010. A double-sided tubular linear synchronous generator for wave-energy conversion (PhD dissertation). .
- [30] Report to Congress on the Potential Environmental Effects of Marine and Hydrokinetic Energy Technologies - U.S Department of Energy – 2009. Available online: <https://www.energy.gov/eere/water/downloads/report-congress-potential-environmental-effects-marine-and-hydrokinetic-energy>. (Accessed on 1 July 2017)”
- [31] Future trends in the Baltic Sea, available at: [http://wwf.panda.org/wwf\\_news/?194764/Future-trends-in-the-Baltic-Sea](http://wwf.panda.org/wwf_news/?194764/Future-trends-in-the-Baltic-Sea). (Accessed on 17 October 2018).
- [32] Ocean Wave Energy. Available online: <https://www.boem.gov/Ocean-Wave-Energy/> (Accessed on 20 February 2018).
- [33] H. Polinder, M. A. Mueller, M. Scutto, and M. Goden de Sousa Prado, "Linear generator systems for wave energy conversion," in *Proceedings of the 7th European Wave and Tidal Energy Conference, Porto, Sept., 2007*.
- [34] T. W. Thorpe, *A brief review of wave energy*: Harwell Laboratory, Energy Technology Support Unit London, 1999.
- [35] Ocean Energy Systems: Annual report 2016. Available online: <https://www.ocean-energy-systems.org/publications/annual-reports/document/oes-annual-report-2016/>. (Accessed on 2 March 2016)
- [36] A. Clément, P. McCullen, A. Falcão, A. Fiorentino, F. Gardner, K. Hammarlund, *et al.*, "Wave energy in Europe: current status and perspectives," *Renewable and sustainable energy reviews*, vol. 6, pp. 405-431, 2002.
- [37] L. Duckers, "Wave power," *Engineering Science & Education Journal*, vol. 9, pp. 113-122, 2000.
- [38] M. Mueller and N. J. Baker, "A low speed reciprocating permanent magnet generator for direct drive wave energy converters," *International Conference on Power Electronics, Machines and Drives (Conf. Publ. No. 487)*, pp. 468-473, 2002.

- [39] J. Callaghan and R. Boud, "Future Marine Energy. Results of the Marine Energy Challenge: Cost competitiveness and growth of wave and tidal stream energy," *Carbon trust*, 2006.
- [40] J. Falnes, "A review of wave-energy extraction," *Marine structures*, vol. 20, pp. 185-201, 2007.
- [41] U. A. Korde, "Control system applications in wave energy conversion," in *OCEANS 2000 MTS/IEEE Conference and Exhibition. Conference Proceedings (Cat. No. 00CH37158)*, 2000, pp. 1817-1824.
- [42] K. Bønke and N. Ambli, "Prototype wave power stations in Norway," in *Utilization of Ocean Waves—Wave to Energy Conversion*, 1986, pp. 34-45.
- [43] A. Ilyas, S. A. R. Kashif, M. A. Saqib, and M. M. Asad, "Wave electrical energy systems: Implementation, challenges and environmental issues," *Renewable and Sustainable Energy Reviews*, vol. 40, pp. 260-268, 2014.
- [44] T. Aderinto and H. Li, "Ocean wave energy converters: Status and challenges," *Energies*, vol. 11, p. 1250, 2018.
- [45] G. Bevilacqua and B. Zanuttigh, "Overtopping Wave Energy Converters: general aspects and stage of development," 2011.
- [46] Aquamarine Power – Available online: [www.aquamarinepower.com](http://www.aquamarinepower.com). (Accessed on 6 January 2018)
- [47] M. A. Mueller, H. Polinder, and N. Baker, "Current and novel electrical generator technology for wave energy converters," in *2007 IEEE International Electric Machines & Drives Conference*, 2007, pp. 1401-1406.
- [48] A. F. d. O. Falcão, "The shoreline OWC wave power plant at the Azores," in *Fourth European Wave Energy Conference, Aalborg, Denmark, Dec, 2000*, pp. 4-6.
- [49] A. Energy, "Oscillating water column wave energy converter evaluation report," *The Carbon Trust, Marine Energy Challenge*, 2005.
- [50] H. Polinder, B. C. Mecrow, A. G. Jack, P. Dickinson, and M. A. Mueller, "Linear generators for direct-drive wave energy conversion," in *IEEE International Electric Machines and Drives Conference, 2003. IEMDC'03.*, 2003, pp. 798-804.
- [51] N. W. Bellamy, "The circular sea clam wave energy converter," in *Hydrodynamics of Ocean Wave-Energy Utilization*, ed: Springer, 1986, pp. 69-79.
- [52] AWS Ocean Power – Available online: [www.awsocan.com](http://www.awsocan.com) (Accessed on 15 June 2018).
- [53] E. Spooner and J. Grimwade, "Snapper™: an efficient and compact direct electric power take-off device for wave energy converters," in *Proceedings of the World Maritime Technology Conference, London, UK, 2006*, pp. 6-10.
- [54] Seventh Framework Programme – Available online: [www.snapperfp7.eu](http://www.snapperfp7.eu). (Accessed on 22 January 2016).
- [55] P. McKeever, C. Ng, B. Caffrey, R. Crozier, and E. Spooner, "'Snapper'wec device development—the grid interface system'," in *Proc. Ninth European Wave and Tidal Energy Conf*, 2011.
- [56] M. Leijon, C. Boström, O. Danielsson, S. Gustafsson, K. Haikonen, O. Langhamer, *et al.*, "Wave energy from the North Sea: Experiences from the Lysekil research site," *Surveys in geophysics*, vol. 29, pp. 221-240, 2008.
- [57] M. Chatzigiannakou, I. Dolguntseva, and M. Leijon, "Offshore deployments of wave energy converters by seabased industry AB," *Journal of Marine Science and Engineering*, vol. 5, p. 15, 2017.
- [58] O. Danielsson, "Wave energy conversion: Linear synchronous permanent magnet generator," *Acta Universitatis Upsaliensis*, 2006.

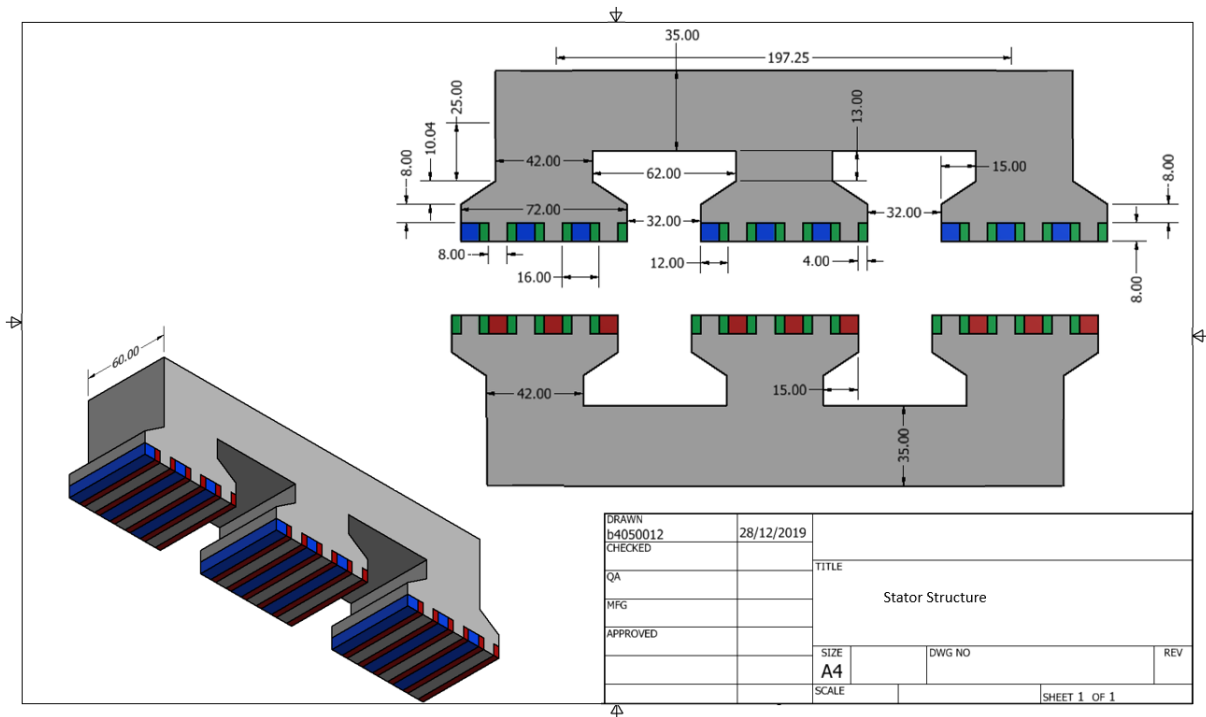
- [59] Strategic Initiative for Ocean Energy (SI OCEAN), Available online: <https://ec.europa.eu/energy/intelligent/projects/en/projects/si-ocean#results> Accessed on 15 January 2019.
- [60] NyTeknik, Waves - Sweden's new big industry. Available online: <https://www.nyteknik.se/energi/vagor-sveriges-nya-storindustri-6417696>. (Accessed on 10 August 2018)
- [61] J. H. Prudell "Novel Design and Implementation of a Permanent Magnet Linear Tubular Generator for Ocean Wave Energy Conversion", M.Sc. thesis. .
- [62] Columbia Power Technologies – Available online: [www.columbiapwr.com](http://www.columbiapwr.com). (Accessed on 10 December 2018).
- [63] J. Prudell, M. Stoddard, E. Amon, T. K. A. Brekken, and A. Von Jouanne, "A permanent-magnet tubular linear generator for ocean wave energy conversion," *IEEE Transactions on Industry Applications*, vol. 46, pp. 2392-2400, 2010.
- [64] R. Vermaak "Novel Air-Cored Permanent Magnet for Direct Drive Ocean Wave Energy Converters", Doctor of Philosophy in the Faculty of Engineering at Stellenbosch University, March, 2013. .
- [65] Trident Energy – Available online: [www.tridentenergy.co.uk](http://www.tridentenergy.co.uk). (Accessed on 20 December 2018)
- [66] P. C. J. Clifton, R. A. McMahon, and H. P. Kelly, "Design and commissioning of a 30 kW direct drive wave generator," in *5th IET International Conference on Power Electronics, Machines and Drives (PEMD 2010)*, 2010, pp. 1-6.
- [67] N. Hodgins, O. Keysan, A. S. McDonald, and M. A. Mueller, "Design and testing of a linear generator for wave-energy applications," *IEEE Transactions on Industrial Electronics*, vol. 59, pp. 2094-2103, 2012.
- [68] N. Hodgins, A. McDonald, J. Shek, O. Keysan, and M. Mueller, "Current and future developments of the C-GEN lightweight direct drive generator for wave & tidal energy," in *European Wave and Tidal Energy Conference*, 2009, pp. 352-359.
- [69] J. L. N. J. R. Joubert, J. Reinecke, I. Meyer, "Wave Energy Converters (WECs)," Centre for Renewable and Sustainable Energy Studies, Faculty of Engineering, North-West University, South Africa, October 2013.
- [70] Wedge Global – Available online: [www.wedgeglobal.com](http://www.wedgeglobal.com). (Accessed on 13 February 2018)
- [71] I. Ivanova, O. Ågren, H. Bernhoff, and M. Leijon, "Simulation of a 100 kW permanent magnet octagonal linear generator for ocean wave conversion," in *Fifth European wave energy conference, Cork, Ireland*, 2003, pp. 17-19.
- [72] Seabased AB, available at: [www.seabased.com](http://www.seabased.com), (Accessed on 1 January 2019).
- [73] C. Boström, O. Svensson, M. Rahm, E. Lejerskog, A. Savin, E. Strömstedt, *et al.*, "Design proposal of electrical system for linear generator wave power plants," in *2009 35th Annual Conference of IEEE Industrial Electronics*, 2009, pp. 4393-4398.
- [74] L. Ran, M. A. Mueller, C. Ng, P. J. Tavner, H. Zhao, N. J. Baker, *et al.*, "Power conversion and control for a linear direct drive permanent magnet generator for wave energy," *IET renewable power generation*, vol. 5, pp. 1-9, 2011.
- [75] O. Keysan, M. Mueller, A. McDonald, N. Hodgins, and J. Shek, "Designing the C-GEN lightweight direct drive generator for wave and tidal energy," *IET Renewable Power Generation*, vol. 6, pp. 161-170, 2012.
- [76] J. Wang and N. J. Baker, "Comparison of flux switching and modulated pole linear machines for use with a free piston," in *2015 IEEE International Electric Machines & Drives Conference (IEMDC)*, 2015, pp. 642-648.
- [77] D. Li, R. Qu, and T. A. Lipo, "High-power-factor vernier permanent-magnet machines," *IEEE Transactions on Industry Applications*, vol. 50, pp. 3664-3674, 2014.

- [78] F. Zhao, T. A. Lipo, and B.-i. Kwon, "Dual-stator interior permanent magnet vernier machine having torque density and power factor improvement," *Electric Power Components and Systems*, vol. 42, pp. 1717-1726, 2014.
- [79] T. W. Ching, K. T. Chau, and W. Li, "Power factor improvement of a linear vernier permanent-magnet machine using auxiliary DC field excitation," *IEEE Transactions on Magnetics*, vol. 52, pp. 1-4, 2016.
- [80] K. Nilsson, O. Danielsson, and M. Leijon, "Electromagnetic forces in the air gap of a permanent magnet linear generator at no load," *Journal of Applied Physics*, vol. 99, p. 034505, 2006.
- [81] A. W. van Zyl, C. G. Jeans, R. J. Cruise, and C. F. Landy, "Comparison of force to weight ratios between a single-sided linear synchronous motor and a tubular linear synchronous motor," in *IEEE International Electric Machines and Drives Conference. IEMDC'99. Proceedings (Cat. No. 99EX272)*, 1999, pp. 571-573.
- [82] N. J. Baker, M. A. H. Raihan, and A. Almoraya, "A Cylindrical Linear Permanent Magnet Vernier Hybrid Machine for Wave Energy," *IEEE Transactions on Energy Conversion*, 2018.
- [83] N. J. Baker, M. A. Mueller, and M. A. H. Raihan, "All electric drive train for wave energy power take off," in *5th IET International Conference on Renewable Power Generation (RPG) 2016*, 2016, pp. 1-6.
- [84] E. Spooner and L. Haydock, "Vernier hybrid machines," in *IEE Proceedings - Electric Power Applications*, vol. 150, no. 6, pp. 655-662, 7 Nov. 2003. doi: 10.1049/ip-epa:20030909.
- [85] M. A. H. Raihan, N. J. Baker, K. J. Smith, and A. A. Almoraya, "An E-core linear vernier hybrid permanent magnet machine with segmented translator for direct drive wave energy converter," in *2017 IEEE International Electric Machines and Drives Conference (IEMDC)*, 2017, pp. 1-6.
- [86] L. Huang, M. Hu, J. Liu, C. Liu, and W. Zhong, "Design and analysis of a linear hybrid excitation flux-switching generator for direct drive wave energy converters," *Advances in Mechanical Engineering*, vol. 5, p. 963093, 2013.
- [87] W. Zhao, J. Zheng, J. Wang, G. Liu, J. Zhao, and Z. Fang, "Design and analysis of a linear permanent-magnet vernier machine with improved force density," *IEEE Transactions on Industrial Electronics*, vol. 63, pp. 2072-2082, 2016.
- [88] K. Xie, D. Li, R. Qu, and Y. Gao, "A novel permanent magnet vernier machine with Halbach array magnets in stator slot opening," *IEEE Transactions on Magnetics*, vol. 53, pp. 1-5, 2017.
- [89] Y. Huo, R. Qu, Y. Gao, S. Jia, and X. Fan, "Design of a linear vernier permanent magnet machine with high thrust force density and low thrust force ripple," in *2017 IEEE International Electric Machines and Drives Conference (IEMDC)*, 2017, pp. 1-6.
- [90] A. A. Almoraya, N. J. Baker, K. J. Smith, and M. A. H. Raihan, "Development of a double-sided consequent pole linear vernier hybrid permanent-magnet machine for wave energy converters," in *2017 IEEE International Electric Machines and Drives Conference (IEMDC)*, 2017, pp. 1-7.
- [91] D. Li, R. Qu, J. Li, and W. Xu, "Consequent-pole toroidal-winding outer-rotor Vernier permanent-magnet machines," *IEEE Transactions on Industry Applications*, vol. 51, pp. 4470-4481, 2015.
- [92] S.-U. Chung, J.-W. Kim, B.-C. Woo, D.-K. Hong, J.-Y. Lee, and D.-H. Koo, "A novel design of modular three-phase permanent magnet vernier machine with consequent pole rotor," *IEEE transactions on magnetics*, vol. 47, pp. 4215-4218, 2011.
- [93] Y. Liu, H. Y. Li, and Z. Q. Zhu, "A High-Power Factor Vernier Machine With Coil Pitch of Two Slot Pitches," *IEEE Transactions on Magnetics*, pp. 1-5, 2018.

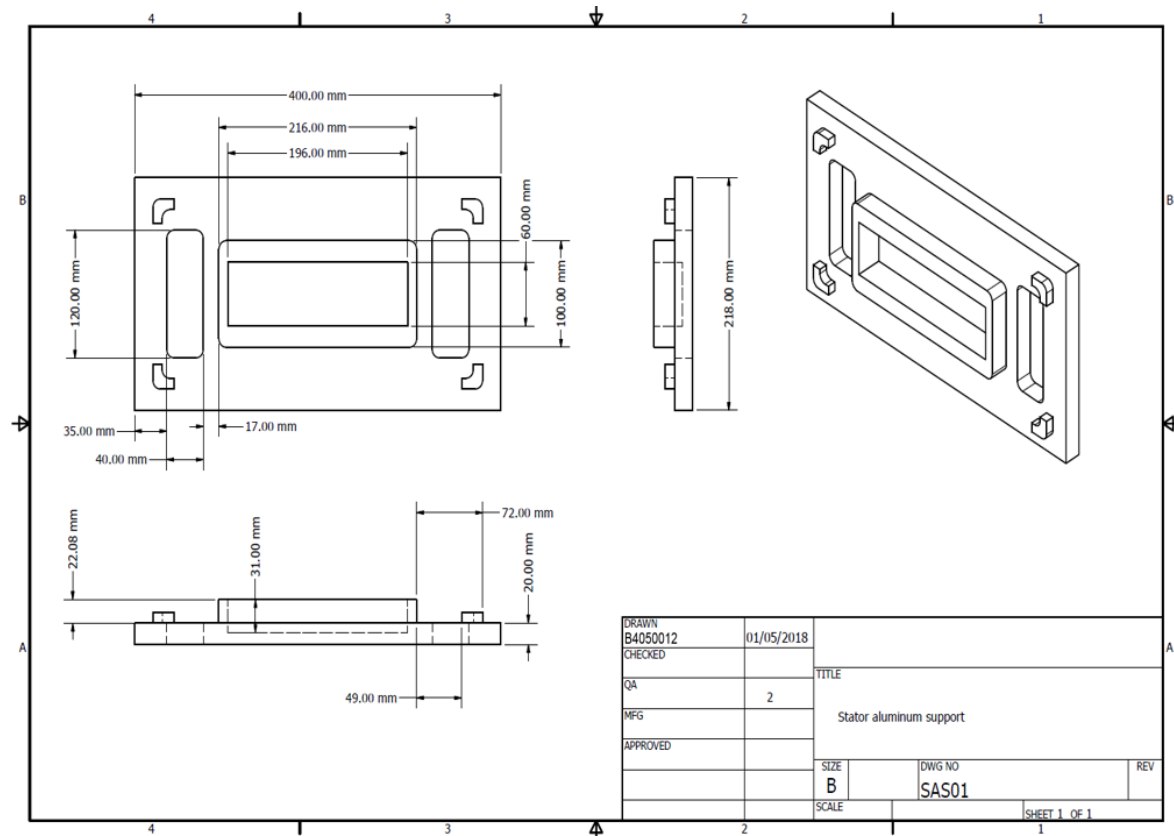
- [94] J. Ji, W. Zhao, Z. Fang, J. Zhao, and J. Zhu, "A novel linear permanent-magnet vernier machine with improved force performance," *IEEE Transactions on Magnetics*, vol. 51, pp. 1-10, 2015.
- [95] J. F. Gieras, Z. J. Piech, and B. Tomczuk, *Linear synchronous motors: transportation and automation systems*: CRC press, 2016.
- [96] M. Cheng, K. T. Chau, and C. C. Chan, "Static characteristics of a new doubly salient permanent magnet motor," *IEEE Transactions on Energy Conversion*, vol. 16, pp. 20-25, 2001.
- [97] Electronics Tutorials: LR Series Circuit. Available online: <https://www.electronics-tutorials.ws/inductor/lr-circuits.html> (Accessed on 15 august 2016)
- [98] N. J. Baker, M. A. H. Raihan, A. A. Almoraya, J. W. Burchell, and M. A. Mueller, "Evaluating Alternative Linear Vernier Hybrid Machine Topologies for Integration Into Wave Energy Converters," *IEEE Transactions on Energy Conversion*, vol. 33, pp. 2007-2017, 2018.
- [99] H. Shokrollahi and K. Janghorban, "Soft magnetic composite materials (SMCs)," *Journal of Materials Processing Technology*, vol. 189, pp. 1-12, 2007.
- [100] Hogan: metal powders. Available online: <https://www.hoganas.com/en/> (Accessed on 20 august 2018)
- [101] R. Qu, G. B. Kliman, and R. Carl, "Split-phase claw-pole induction machines with soft magnetic composite cores," in *Conference Record of the 2004 IEEE Industry Applications Conference, 2004. 39th IAS Annual Meeting.*, 2004, pp. 2514-2519.
- [102] Global Energy Statistical Yearbook 2019. Available online: <https://yearbook.enerdata.net/electricity/electricity-domestic-consumption-data.html> / (Accessed on 10 august 2019)

## Appendix A: Flat Stator and Support Structure

### 1. Flat Stator Structure

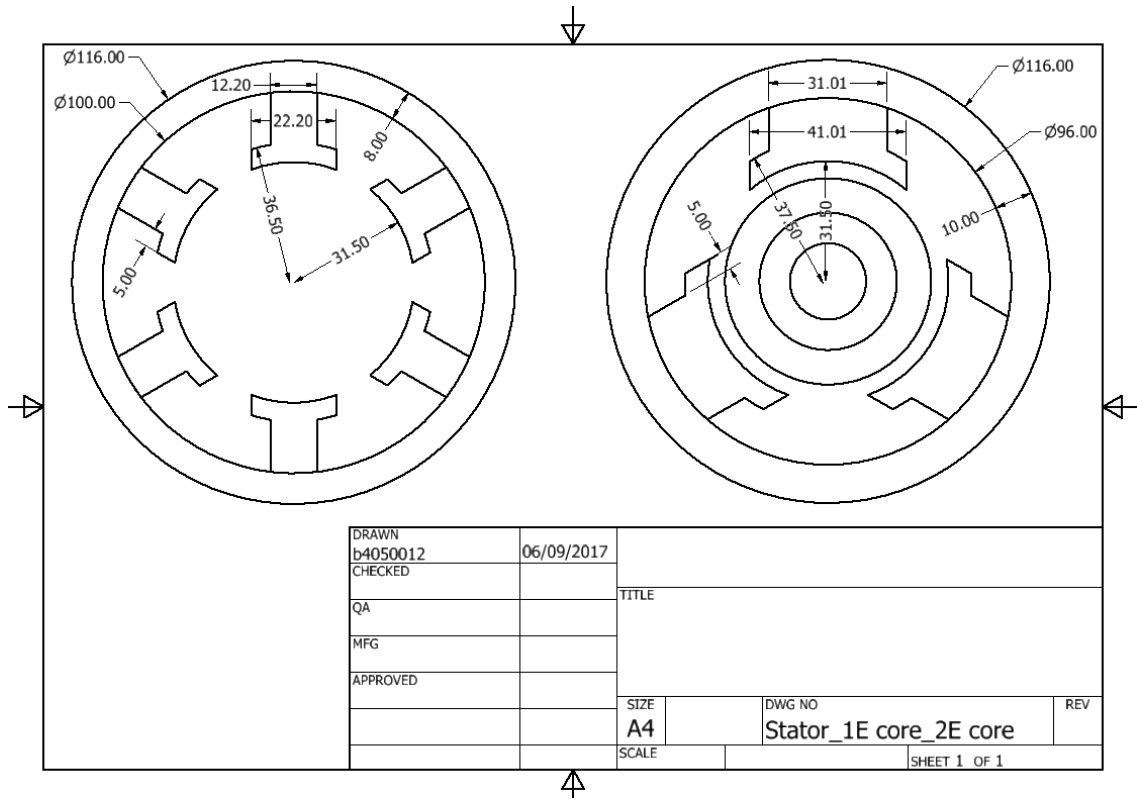


### 2. Stator Support Structure

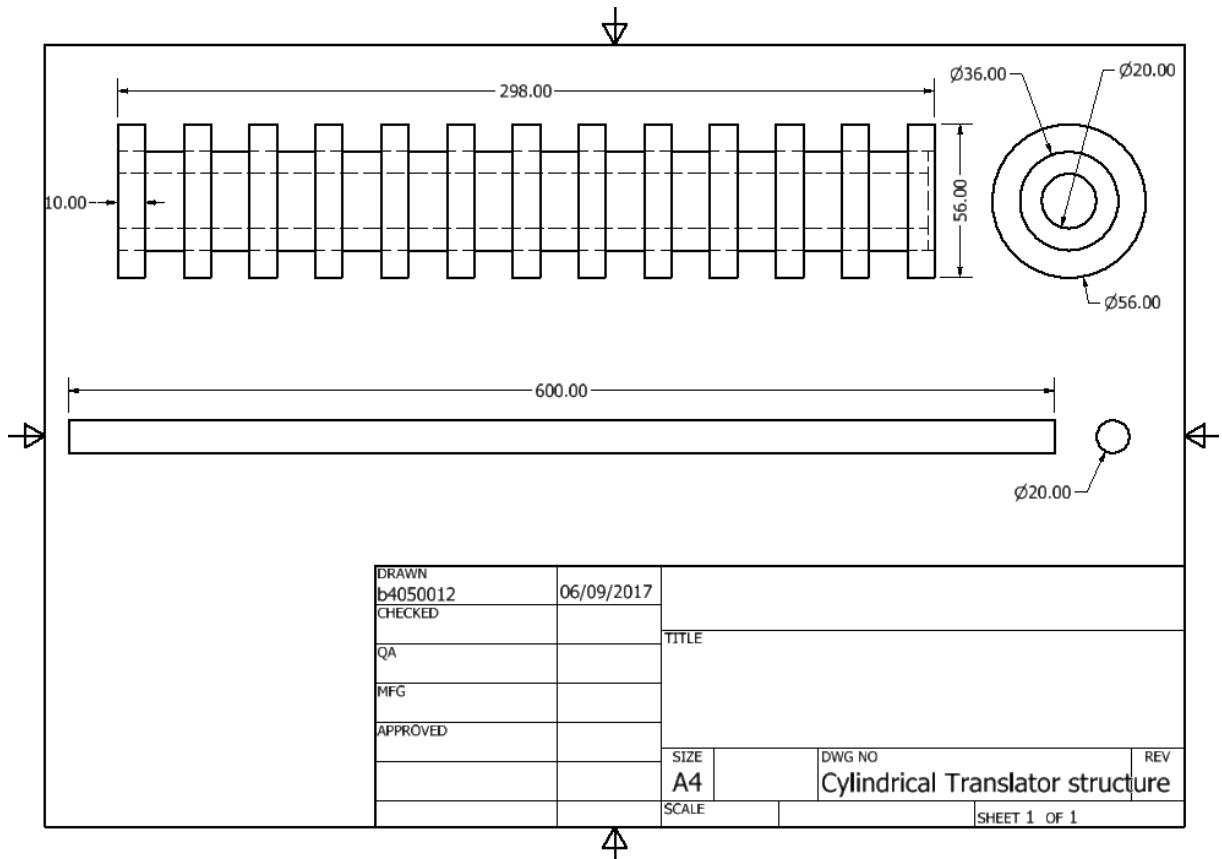


## Appendix B: Cylindrical Machines and Structural Support

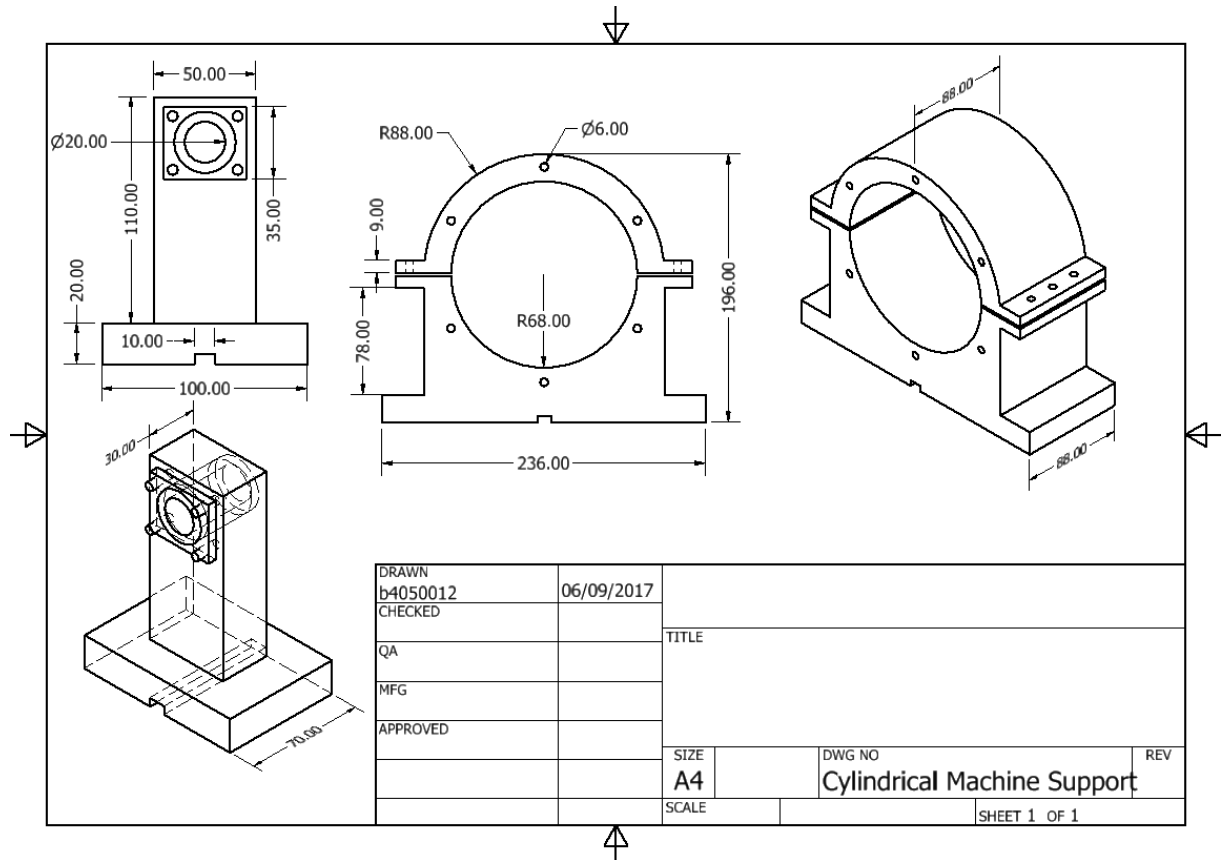
### 1. Cylindrical Stator Structure



### 2. Cylindrical Translator Structure



3. Cylindrical Machine Support Structure

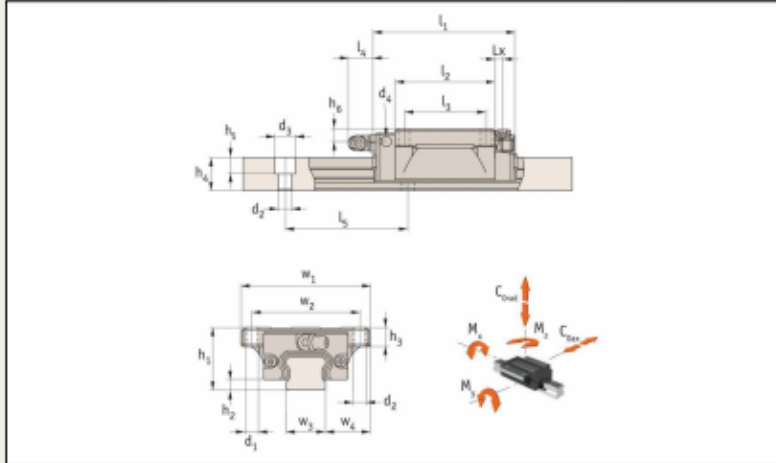


## Appendix C: Flanged Carriage (L1016.F)

### Flanged Carriages - Standard

with retained ball cage

### Linear Guideways



**L1016.F**

**Material**  
Hardened and ground steel.

**Technical notes**  
Select the size and number of carriages to suit the required load

then select the required rail length, (see part nos. L1016.15 through to L1016.55).  
Standard preload carriages are  $K_0$  (no preload) or  $K_1$  ( $0,02 \times$  dynamic load capacity). Other preloads available on request.

**Tips**  
Improved version with ball cages allowing the carriages to be removed from the rail without the balls falling out.

Order No.	Rail size	$h_1$	$w_1$	$l_1$	$h_2$	$h_3$	$h_4$	$h_5$	$h_6$	$w_2$	$w_3$	$w_4$	$l_2$	$l_3$	$l_4$	$l_5$	$d_1$	$\sigma_{\text{max}}$ Kg
L1016.F15	15	24	47	58,6	3,4	7,5	13,0	5,5	5,5	38	15	16,0	40,2	30	5,7	60	M5	0,21
L1016.F15-L	15	24	47	66,1	3,4	7,5	13,0	5,5	5,5	38	15	16,0	47,7	30	5,7	60	M5	0,23
L1016.F20	20	30	63	70,1	4,5	9,0	16,3	8,5	7,1	53	20	21,5	48,5	40	12,3	60	M6	0,40
L1016.F20-L	20	30	63	82,9	4,5	9,0	16,3	8,5	7,1	53	20	21,5	61,3	40	12,3	60	M6	0,46
L1016.F25	25	36	70	79,2	5,8	10,0	19,2	9,0	10,2	57	23	23,5	57,5	45	12,2	60	M8	0,57
L1016.F25-L	25	36	70	93,9	5,8	10,0	19,2	9,0	10,2	57	23	23,5	72,2	45	12,2	60	M8	0,72
L1016.F25-XL	25	36	70	108,6	5,8	10,0	19,2	9,0	10,2	57	23	23,5	86,9	45	12,2	60	M8	0,89
L1016.F30	30	42	90	94,8	7,0	12,0	22,8	12,0	10,0	72	28	31,0	67,8	52	11,7	80	M10	1,10
L1016.F30-L	30	42	90	105,0	7,0	12,0	22,8	12,0	10,0	72	28	31,0	78,0	52	11,7	80	M10	1,34
L1016.F30-XL	30	42	90	130,5	7,0	12,0	22,8	12,0	10,0	72	28	31,0	103,5	52	11,7	80	M10	1,66
L1016.F35	35	48	100	111,5	7,5	12,0	26,0	14,0	11,5	82	34	33,0	80,5	62	11,5	80	M10	1,50
L1016.F35-L	35	48	100	123,5	7,5	12,0	26,0	14,0	11,5	82	34	33,0	92,5	62	11,5	80	M10	1,90
L1016.F35-XL	35	48	100	153,5	7,5	12,0	26,0	14,0	11,5	82	34	33,0	122,5	62	11,5	80	M10	2,54
L1016.F45	45	60	120	129,0	8,9	15,5	31,1	16,0	14,4	100	45	37,5	94,0	80	10,8	105	M12	2,27
L1016.F45-L	45	60	120	145,0	8,9	15,5	31,1	16,0	14,4	100	45	37,5	110,0	80	10,8	105	M12	2,68
L1016.F45-XL	45	60	120	174,0	8,9	15,5	31,1	16,0	14,4	100	45	37,5	139,0	80	10,8	105	M12	3,42
L1016.F55	55	70	140	155,0	12,7	18,5	38,0	19,0	14,0	116	53	43,5	116,0	95	10,8	120	M14	3,44
L1016.F55-L	55	70	140	193,0	12,7	18,5	38,0	19,0	14,0	116	53	43,5	154,0	95	10,8	120	M14	4,63
L1016.F55-XL	55	70	140	210,0	12,7	18,5	38,0	19,0	14,0	116	53	43,5	171,0	95	10,8	120	M14	5,16

Order No.	$d_2$	$d_3$	$d_4$	Dynamic load C kN	Static load $C_{\text{load} \pm \text{ax}}$ kN	$M_x$ Nm	$M_y$ Nm	$M_z$ Nm
L1016.F15	4,5	7,5	M3 x 0,5	11,67	19,90	137	120	120
L1016.F15-L	4,5	7,5	M3 x 0,5	14,12	24,05	166	171	171
L1016.F20	6,0	9,5	M6 x 1,0	17,98	30,96	289	224	224
L1016.F20-L	6,0	9,5	M6 x 1,0	23,30	40,11	376	366	366
L1016.F25	7,0	11,0	M6 x 1,0	25,25	41,73	447	358	358
L1016.F25-L	7,0	11,0	M6 x 1,0	32,44	53,63	576	577	577
L1016.F25-XL	7,0	11,0	M6 x 1,0	36,58	64,30	691	833	833
L1016.F30	9,0	14,0	M6 x 1,0	37,33	55,50	719	560	560

Tel: 0333 207 4498 Email: sales@automotioncomponents.co.uk  
Fax: 01483 26 67 75 Web: automotioncomponents.co.uk

**AUTOMOTION<sup>®</sup>**  
**COMPONENTS**

## Flanged Carriages - Standard

with retained ball cage

### Linear Guideways

Order No.	d <sub>2</sub>	d <sub>3</sub>	d <sub>4</sub>	Dynamic load C kN	Static load C <sub>0rad + ax</sub> kN	M <sub>x</sub> Nm	M <sub>y</sub> Nm	M <sub>z</sub> Nm
L1016.F30-L	9,0	14,0	M6 x 1,0	48,35	71,88	931	836	836
L1016.F30-XL	9,0	14,0	M6 x 1,0	53,83	88,18	1142	1361	1361
L1016.F35	9,0	14,0	M6 x 1,0	53,31	82,66	1307	991	991
L1016.F35-L	9,0	14,0	M6 x 1,0	66,61	103,29	1633	1424	1424
L1016.F35-XL	9,0	14,0	M6 x 1,0	73,29	127,68	2020	2330	2330
L1016.F45	14,0	20,0	M8 x 1,25	73,14	111,30	2353	1559	1559
L1016.F45-L	14,0	20,0	M8 x 1,25	86,99	132,39	2798	2170	2170
L1016.F45-XL	14,0	20,0	M8 x 1,25	100,52	166,87	3527	3455	3455
L1016.F55	16,0	23,0	M8 x 1,25	88,26	136,62	3385	2361	2361
L1016.F55-L	16,0	23,0	M8 x 1,25	119,10	183,14	4538	4202	4202
L1016.F55-XL	16,0	23,0	M8 x 1,25	161,43	259,71	6430	6617	6617

Tel: 0333 207 4498 Email: [sales@automotioncomponents.co.uk](mailto:sales@automotioncomponents.co.uk)  
 Fax: 01483 26 67 75 Web: [automotioncomponents.co.uk](http://automotioncomponents.co.uk)

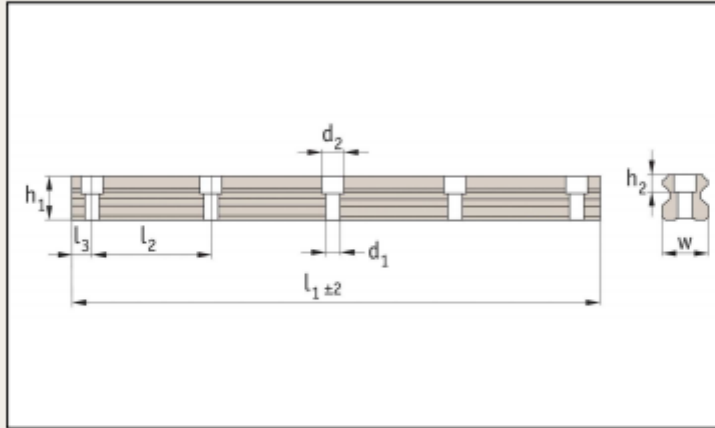
**AUTOMOTION<sup>®</sup>**  
**COMPONENTS**

## Appendix D: Linear Guide Rail

### 15mm Linear Guide Rail

standard

Linear Guideways



**L1016.15**

**Material**  
Hardened and ground steel (typically 60 HRC).

For carriages to suit the required load see part nos. L1016.F (flanged) and L1016.U (unflanged).  
Other rail lengths on request.  
Weight: 1,4 Kg/m.

**Tips**  
Plastic screw covers issued with the rails to protect screw holes from debris.

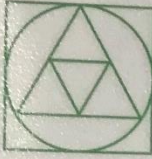
**Technical notes**

Order No.	Rail size	$l_1$	$l_2$	$l_3$	$h_1$	$h_2$	w	$d_1$	$d_2$	For screws
L1016.15-0160	15	160	60	20	13,0	6,0	15	4,5	7,5	M4
L1016.15-0220	15	220	60	20	13,0	6,0	15	4,5	7,5	M4
L1016.15-0280	15	280	60	20	13,0	6,0	15	4,5	7,5	M4
L1016.15-0340	15	340	60	20	13,0	6,0	15	4,5	7,5	M4
L1016.15-0400	15	400	60	20	13,0	6,0	15	4,5	7,5	M4
L1016.15-0460	15	460	60	20	13,0	6,0	15	4,5	7,5	M4
L1016.15-0520	15	520	60	20	13,0	6,0	15	4,5	7,5	M4
L1016.15-0580	15	580	60	20	13,0	6,0	15	4,5	7,5	M4
L1016.15-0640	15	640	60	20	13,0	6,0	15	4,5	7,5	M4
L1016.15-0700	15	700	60	20	13,0	6,0	15	4,5	7,5	M4
L1016.15-0760	15	760	60	20	13,0	6,0	15	4,5	7,5	M4
L1016.15-0820	15	820	60	20	13,0	6,0	15	4,5	7,5	M4
L1016.15-0880	15	880	60	20	13,0	6,0	15	4,5	7,5	M4
L1016.15-0940	15	940	60	20	13,0	6,0	15	4,5	7,5	M4
L1016.15-1000	15	1000	60	20	13,0	6,0	15	4,5	7,5	M4
L1016.15-1060	15	1060	60	20	13,0	6,0	15	4,5	7,5	M4
L1016.15-1120	15	1120	60	20	13,0	6,0	15	4,5	7,5	M4
L1016.15-1180	15	1180	60	20	13,0	6,0	15	4,5	7,5	M4
L1016.15-1240	15	1240	60	20	13,0	6,0	15	4,5	7,5	M4
L1016.15-1300	15	1300	60	20	13,0	6,0	15	4,5	7,5	M4
L1016.15-1360	15	1360	60	20	13,0	6,0	15	4,5	7,5	M4
L1016.15-1420	15	1420	60	20	13,0	6,0	15	4,5	7,5	M4
L1016.15-1480	15	1480	60	20	13,0	6,0	15	4,5	7,5	M4
L1016.15-1540	15	1540	60	20	13,0	6,0	15	4,5	7,5	M4
L1016.15-1600	15	1600	60	20	13,0	6,0	15	4,5	7,5	M4
L1016.15-1660	15	1660	60	20	13,0	6,0	15	4,5	7,5	M4
L1016.15-1720	15	1720	60	20	13,0	6,0	15	4,5	7,5	M4
L1016.15-1780	15	1780	60	20	13,0	6,0	15	4,5	7,5	M4
L1016.15-1840	15	1840	60	20	13,0	6,0	15	4,5	7,5	M4
L1016.15-1900	15	1900	60	20	13,0	6,0	15	4,5	7,5	M4
L1016.15-1960	15	1960	60	20	13,0	6,0	15	4,5	7,5	M4

Tel: 0333 207 4498 Email: [sales@automotioncomponents.co.uk](mailto:sales@automotioncomponents.co.uk)  
 Fax: 01483 26 67 75 Web: [automotioncomponents.co.uk](http://automotioncomponents.co.uk)



## Appendix E: Calibration Certificate of Force Transducer



**APPLIED MEASUREMENTS LTD.**  
 3 Mercury House, Calleva Park, Aldermaston, Berkshire, RG7 8PN  
 Tel: +44 (0) 1189 817339 | Web: [www.appmeas.co.uk](http://www.appmeas.co.uk)  
 Fax: +44 (0) 1189 819121 | Email: [info@appmeas.co.uk](mailto:info@appmeas.co.uk)

### CALIBRATION CERTIFICATE

#### Calibration of Transducer with Instrumentation

**Customer:**  
 Newcastle University  
 Invoices  
 PO Box 268  
 Sheffield  
 S98 1QY

**Date:** 26th February 2018  
  
**Customer Ref:** 4200538439  
  
**AML Order Ref:** 109455

Transducer Type:	DDE-10kN-002-000	Serial Number:	47063
Instrumentation Type:	SGA/A	Serial Number:	17173410
Supply Voltage:			110 - 240 Vac
Instrumentation Calibration Engineering Units:			kN
Number of Decimal Places:			Three
Calibration Carried Out By:			B.A.D
AML Reference Standard:		Asset No: TE150 - AML DBBSME-30kN - Traceable to UKAS Certificate No: 1710054, Calibration date: 26th October 2017	

Calibration Results:

Load Applied kN	Analogue Output Vdc	
	Tension	Compression
0	0.000	0.000
2	1.983	-2.022
4	3.984	-4.028
6	5.988	-6.026
8	7.998	-8.025
10	10.006	-10.022
0	0.003	-0.003

Electrical Connections:

<u>DDE-10kN Cable (2m)</u>		<u>SGA Input Terminal J2</u>
Blue	-ve Exc	(-) Strain Excite
Red	+ve Exc	(+) Strain Excite (10V)
Screen		Shield (0V)
N/A		Ref (2.5V/5V)
Green	-ve Sig	(-) Strain Input
Yellow	+ve Sig	(+) Strain Input

Applied Measurements Limited hereby certifies that the above items have been inspected, tested and calibrated - using UKAS traceable test equipment - in all respects with the requirements of the customer's order.

## Appendix F: Tufnol Sheet (Whale grade)



### Tufnol Whale

SRBF - Synthetic resin Bonded Fabric

Medium weave cotton/phenolic resin laminate

Colour: Natural (brown)

Density: 1.36(sheet) 1.35(rod)/cm<sup>3</sup>

## Material Data Sheet

Mechanical Properties	Value	Unit
Cross breaking strength	130	MPa
Charpy impact strength (notched)	11.5	kJ/m <sup>2</sup>
Compressive strength (flatwise)	310	MPa
Compressive strength (edgewise)	200	MPa
Shear strength (flatwise)	90	MPa
Tensile strength	68	MPa
Young's modulus	6.3	GPa

Thermal Properties	Value	Unit
Maximum working temperature – continuous	120	°C
Maximum working temperature – intermittent	130	°C
Thermal classification	E	
Thermal conductivity through laminae	0.32	W/(mK)
Thermal expansion in plane of laminae	2.2	X10 <sup>-5</sup> /K
Specific heat	1.5	kJ/(kgK)

Electrical properties	Value	Unit
Insulation resistance after immersion in water	1 x 10 <sup>8</sup>	Ω (ohms)
Electric strength (edgewise in oil @ 90°C)	12	kV
Electric strength (flatwise in oil @ 90°C) 1.6mm thk.	4.5	MV/m
Electric strength (flatwise in oil @ 90°C) 3mm thk.	2.6	MV/m
Electric strength (flatwise in oil @ 90°C) 6mm thk.	2.0	MV/m

Other Properties	Value	Unit
Water absorption 1.6mm thk.	90	Mg
Water absorption 3mm thk.	105	Mg
Water absorption 6mm thk.	130	Mg
Water absorption 12mm thk.	160	Mg
Water absorption (rod)	3.3	Mg/cm <sup>2</sup>

Sheet - BS EN 60893-3-4 Type PF CC 203

Rod - BS EN 61212-3-3 Type PF CC 42



Direct Plastics Ltd. Unit 14 Portland Business Park, Richmond Park Road, Sheffield, S13 8HS

The following information corresponds with our current knowledge and indicates our products and possible applications. We cannot give a legally binding guarantee of certain properties or the suitability for a specific application. Existing commercial patents must be observed. A definitive quality guarantee is given in our general conditions of sales. Unless otherwise stated, these values represent averages taken from injection moulding samples.

We reserve the right of technical alterations.

## Appendix G: Neodymium-Iron-Boron Magnet (N42H)



### N42H

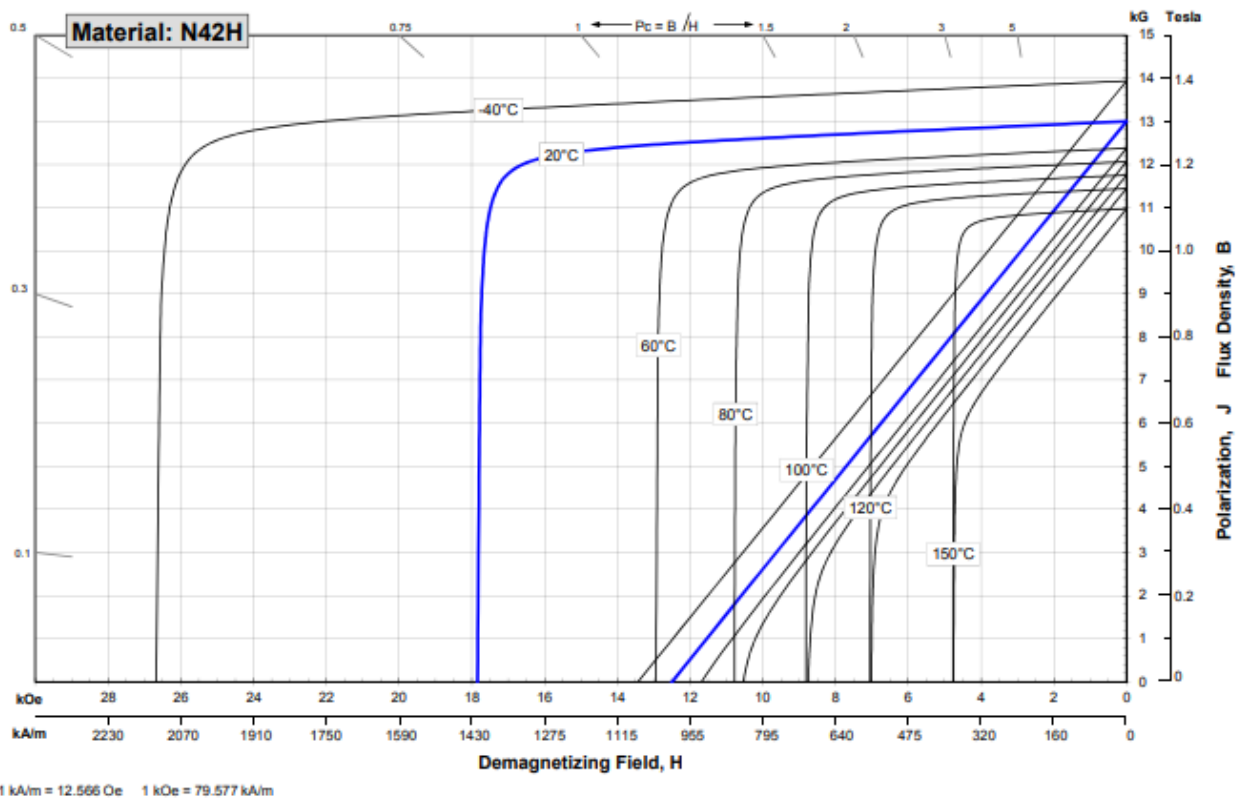
#### Sintered Neodymium-Iron-Boron Magnets

These are also referred to as "Neo" or NdFeB magnets. They offer a combination of high magnetic output at moderate cost. Please contact Arnold for additional grade information and recommendations for protective coating. Assemblies using these magnets can also be provided.

Characteristic	Units	Magnetic Properties		
		min.	nominal	max.
<b>Br</b> Residual Induction	Gauss	12,800	13,000	13,200
	mT	1280	1300	1320
<b>H<sub>CB</sub></b> Coercivity	Oersteds	12,000	12,300	12,800
	kA/m	955	979	1003
<b>H<sub>cJ</sub></b> Intrinsic Coercivity	Oersteds	17,000		
	kA/m	1,353		
<b>BHmax</b> , Maximum Energy Product	MGOe	40	42	43
	kJ/m <sup>3</sup>	318	330	342

Characteristic	Units	C #	C I	
Thermal Properties	Reversible Temperature Coefficients <sup>(1)</sup>			
	of Induction, α(Br)	%/°C	-0.120	
	of Coercivity, α(HcJ)	%/°C	-0.605	
	Coefficient of Thermal Expansion <sup>(2)</sup>	ΔL/L per °C×10 <sup>-4</sup>	7.5	-0.1
	Thermal Conductivity	W / (m · K)	7.6	
Specific Heat <sup>(3)</sup>	J / (kg · K)	460		
Curie Temperature, T <sub>c</sub>	°C	310		
Other Properties	Flexural Strength	psi	41,300	
		MPa	285	
	Density	g/cm <sup>3</sup>	7.5	
	Hardness, Vickers	Hv	620	
	Electrical Resistivity, ρ	μΩ · cm	180	

Notes: (1) Coefficients measured between 20 and 120 °C  
 (2) Between 20 and 200 °C  
 (3) Between 20 and 140 °C



**Notes** The material data and demagnetization curves shown above represent typical properties that may vary due to product shape and size. Magnets can be supplied thermally stabilized or magnetically calibrated to customer specifications. Additional grades are available. Please contact the factory for information.

## Appendix H: Stator and translator lamination (M270-35A)

### Typical data for SURA® M270-35A

T	W/kg at 50 Hz	VA/kg at 50 Hz	A/m at 50 Hz	W/kg at 100 Hz	W/kg at 200 Hz	W/kg at 400 Hz	W/kg at 1000 Hz	W/kg at 2500 Hz
0,1	0,03	0,06	30,0	0,04	0,09	0,21	0,99	4,10
0,2	0,07	0,17	39,6	0,16	0,37	0,92	3,67	14,9
0,3	0,13	0,29	46,0	0,34	0,79	1,99	7,63	30,7
0,4	0,22	0,44	52,0	0,55	1,31	3,33	12,7	52,0
0,5	0,31	0,61	58,2	0,80	1,91	4,94	18,9	79,1
0,6	0,43	0,81	65,2	1,06	2,61	6,84	26,4	113
0,7	0,54	1,04	73,3	1,38	3,39	9,00	35,4	156
0,8	0,68	1,31	83,1	1,73	4,26	11,4	46,0	209
0,9	0,83	1,63	95,5	2,10	5,23	14,2	58,4	274
1,0	1,01	2,04	112	2,51	6,30	17,3	73,0	353
1,1	1,20	2,58	136	2,98	7,51	20,9	90,1	
1,2	1,42	3,38	178	3,51	8,88	24,9		
1,3	1,70	4,90	272	4,15	10,5	29,5		
1,4	2,12	9,64	596	4,97	12,5	35,4		
1,5	2,47	28,0	1700	5,92	14,9	41,8		
1,6	2,80	72,3	3880					
1,7	3,05	149	7160					
1,8	3,25	264	11600					

Loss at 1.5 T , 50 Hz, W/kg	2,47
Loss at 1.0 T , 50 Hz, W/kg	1,01
Anisotropy of loss, %	10
Magnetic polarization at 50 Hz	
H = 2500 A/m, T	1,54
H = 5000 A/m, T	1,65
H = 10000 A/m, T	1,77
Coercivity (DC), A/m	40
Relative permeability at 1.5 T	700
Resistivity, $\mu\Omega\text{cm}$	52
Yield strength, N/mm <sup>2</sup>	450
Tensile strength, N/mm <sup>2</sup>	565
Young's modulus, RD, N/mm <sup>2</sup>	185 000
Young's modulus, TD, N/mm <sup>2</sup>	200 000
Hardness HV5 (VHN)	215

RD represents the rolling direction  
 TD represents the transverse direction  
 Values for yield strength (0.2 % proof strength)  
 and tensile strength are given for the rolling direction



# Appendix I: Soft Magnetic Composite (SMC) Material



## Somaloy® 700HR 5P

600 MPa

General			
<b>Base material:</b> Somaloy 700HR 5P	<b>Additive(s):</b> 0.3% 5P Lube	<b>Compaction:</b> Pressure: 600 MPa Die temperature: 100°C	<b>Heat treatment:</b> Atmosphere: Nitrogen Temperature: 650°C

Mechanical properties		Standards	
Transverse rupture strength/150°C	[MPa] 60/60	SS-ISO 3325	
Tensile strength/Yield strength	[MPa] 20/20	SS-EN 10002-1, ISO 2740	
Compressive Strength/Yield	[MPa] 530/110	ASTM E9-89a	
Young's modulus	[GPa] 150	ASTM E 1876-99	
Poisson's ratio	- 0.23	ASTM E 1876-99	
Impact Energy	[J] 1.7	SS-EN 10045, SS-EN 25754	

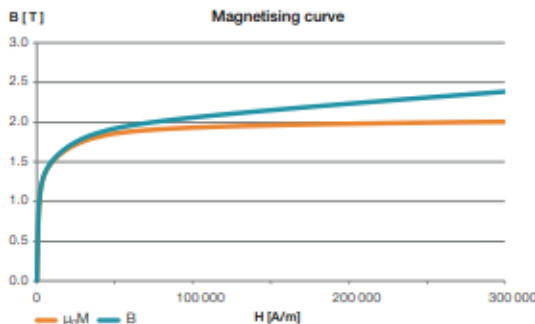
Physical properties		Standards	
Density	[g/cm³] 7.40	SS-ISO 2738	
Thermal expansion	[K⁻¹] 11 e-06	ASTM E 228/MPF 35	
Thermal conductivity	[W/m·K] 26	ISO 22007-2	
Resistivity	[µΩm] 600	Four point measurements on bars, size OD 50mm ID 45mm Height 5mm	

Magnetic properties		Standards	
B@4000A/m	[T] 1.28	IEC 60404-4	
B@10000A/m	[T] 1.52	IEC 60404-4	
H <sub>c</sub>	[A/m] 120	IEC 60404-4	
µ <sub>r</sub> -max	- 600	IEC 60404-4	

Powder properties		Standards	
Apparent density	[g/cm³] 3.30	ISO 3923/1	
Flow	[s/50g] 33	ISO 4490	
Green density	[g/cm³] 7.39	ISO 3927	
Green strength	[MPa] 13	ISO 3995	
Springback	[%] 0.14	ISO 4492, ISO 2740	
Heat treated dim. change	[%] -0.08	ISO 4492, ISO 2740	
Total dim. change	[%] 0.06	ISO 4492, ISO 2740	

### Magnetising curve

Data adjusted for use in Finite Element modelling



H[A/m]	µ <sub>0</sub> M[T]	B[T]	H[A/m]	µ <sub>0</sub> M[T]	B[T]
0	0.00	0.00	12476	1.54	1.56
63	0.03	0.03	26507	1.73	1.76
110	0.06	0.06	49591	1.85	1.91
197	0.12	0.12	74591	1.90	2.00
288	0.20	0.20	99591	1.93	2.05
559	0.43	0.43	124591	1.94	2.10
829	0.61	0.61	149591	1.96	2.15
1197	0.81	0.81	189591	1.97	2.21
1827	0.99	1.00	229591	1.98	2.27
3009	1.18	1.18	279591	2.00	2.35
5854	1.36	1.37	304591	2.002	2.39

Core loss													
[W/kg]	50/60 Hz	100 Hz	200 Hz	300 Hz	400 Hz	500 Hz	600 Hz	700 Hz	800 Hz	900 Hz	1000 Hz	2000 Hz	
0.5T	1.0/1.2	2.0	4.0	7.0	9.0	12	15	18	21	24	28	73	
1.0T	3.3/4.0	6.8	14	23	31	41	51	62	74	86	99	267	
1.5T	6.8/8.2	14	30	47	65	85	107	130	155	181	209	572	

Measured according to CEI/IEC 60404-6:2003 on ring sample (OD55 ID45 H5 mm).

Loss model			
K <sub>h</sub>	0.065	K <sub>ep</sub>	0.000032

$$P_{tot} = K_h * f * B^{1.75} + K_{ep} * f^2 * B^2 + \frac{B^2 * f^2 * d^2}{1.8 * \rho * resistivity * 1000} \quad [W/kg]$$

Model is verified up to 1.5T and 5000Hz.

- K<sub>h</sub> Hysteresis loss coefficient
- K<sub>ep</sub> In particle eddy current coefficient
- d Smallest cross section of component [mm]
- f Frequency [Hz]
- B Field strength [T]
- ρ Density [g/cm³]
- resistivity [µΩm]

[www.hoganas.com/electromagnetic](http://www.hoganas.com/electromagnetic)